UNIVERSITAT DE BARCELONA

Holographic Phase Transitions and Gravitational Waves

Mikel Sanchez Garitaonandia

Tesi doctoral

Holographic Phase Transitions and Gravitational Waves

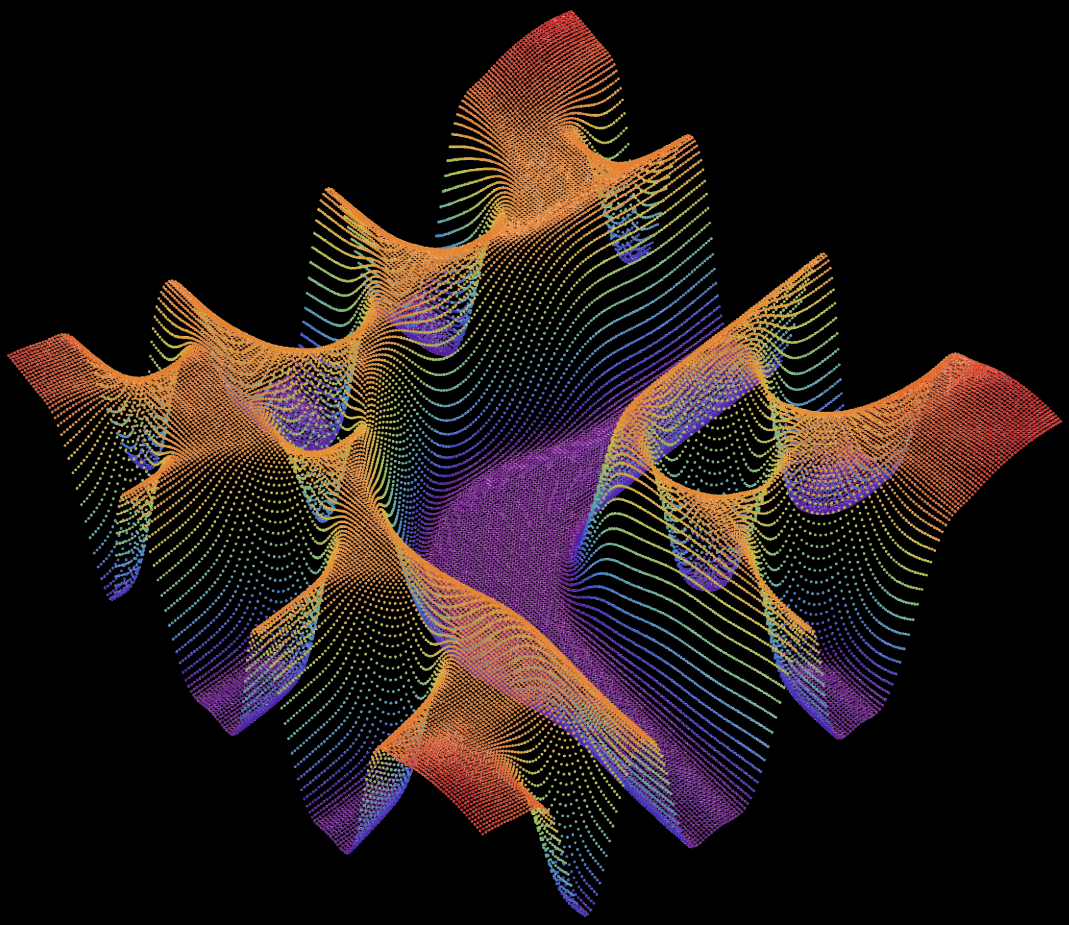

Mikel Sanchez Garitaonandia

UNIVERSITAT DE BARCELONA

Holographic Phase Transitions and Gravitational Waves

Memòria presentada per optar al grau de doctor per la Universitat de Barcelona

Programa de doctorat en Física

Autor: Mikel Sanchez Garitaonandia
Director: David Julian Mateos Solé
Tutor: Joan Soto Riera

UNIVERSITAT DE BARCELONA

Acknowledgements

My P.h.D. is compiled of more than just the last four years of my life. From the day I got actively interested in science the journey to where I am today every step has been important. This includes all my choices, from the one of becoming an engineer to eventually wanting something more and moving on to physics, but also people that crossed my path. When people is what we talk about, a number of them deserve to be mentioned, as this was not a journey I could have done on my own. Even if some of the people might not be around anymore, their effect on my life is certainly permanent.

I would like to start first with those that have been there from the beginning of my existence, my family. Both my mom and dad, for their unconditional love and support in every single way since the very beginning. Special mention goes for my mom, with whom I have connected even more over the last few years. Strong woman in character and mind but loving and caring like no one. My older brother Iñigo, who has always played such a role and made me feel like everything was going to be fine one way or the other. I have always looked up to you and today is not an exception. His wife Virginia, her family and the new recruitment Iñiguin, bringing joy and making home even more home. My grandma, that could only see the start of this thesis, but I know how proud she would be and I am surely proud of being her grandchild. Her sister, my uncle Javi with his curiosity for physics and his family. All of you deserve nicer words than what my skills allow me to express and I will always be grateful for being part the family I belong to.

Over the years in the field I had the chance of meeting very unique people.I could not start with any one else than David, my advisor, mentor and much more than that. You have guided me through the field, always had nice words for me and your support has been essential for my success. You have showed me how to think in simple terms about very complicated physics and taught me important lessons about academia too. I am very glad to have shared four years of my live with you and I really hope we continue exploring physics together for many more years. Jorge, who I consider my co-mentor, also supporting me when I needed it. Your way of viewing physics, sometimes orthogonal to David's, has brought very rich and fun discussions from which I could not have benefited more and I would love to continue doing so. Special thanks go also to Yago, who I see as my old brother in the field and whose presence in Barcelona was extremely helpful during my first year, while I was still trying to understand what was going on. Even today you still offer yourself to help me with anything. Oscar, for all the support and knowledge about numerical relativity I got from you. Roberto, whose love for explaining made me feel like what I was saying about black holes was not an atrocity (even if it was) and for your support even when you did not know me that well. Tomeu and Enric, my first contacts in the field, for being always very encouraging as they looked convinced that I could make it. Miguel, for teaching me the rest of what I know about numerics and giving me the chance to spend a wonderful month in Lisbon. Mark, Niko, Oscar and the whole Finnish group, who taught me a lot about phase transitions and made my stay in Finland a bit warmer, if such a thing is possible. And how could I forget the rest of the people that contributed in one way or another to my development and a good group environment: Jaume, Xandre, Antonia, Aron, Jorge, Federico, Ryotaku, Benson, Chris and Jacob, thank you all.

I could not refer to this as acknowledgements if I forget about the many people with whom I have spent my free time and have provided me with a way of resting my brain from physics with joy, fun and support too. From all of them I must start with my friends from San Sebastian: Ignacio, Goñi Martin, Manu, Xabi, Yago, Asier, Pablo, Miguel, Sesio, Julen, Gaizka, Josue, Kourt, Maria, Andrea, Ane and Eva. I feel very lucky to know you for so long. You always

make me forget the worst I can be going through with randomness, laughs and insane meals. For many years already and many to come.

Since I left my home town I met a series of people who also made a difference. Guillermo, Iñigo, Diego, Cristian, Ivan, Paula, Aniol, Marc, Carlos, Thanasis, Sascha, Fabian, Lais, Robert, Rafa, Julieta, Jairo, Javi, Alan, Nikos, Albert, Ana, Quim and Jordi, all of you are very different but each of you have brought your own speciality to my life. I also bring with me the names Zoran and Zorica, always so warm and welcoming for the cheap price of getting fatter eating delicious food while listening to bad jokes.

I am already starting to run out of names but there is one left before the end, probably because I do not really know how to write words out of what I feel. You have taught me in every possible sense of life, including physics. Your intensity in feelings when you are happy, angry, sad, compassionate and empathic, all define the unique person you are and how you have impacted me. All the absurd discussions we had about almost everything, all the impulsive fun, all the love and tender you gave me and even all the fights are moments that I will look back to with the warmest of feelings. Many things that you already know could be said, but one that you might not seems very appropriate right now. At the time that I was sick and upset with the world, determined to leave the field once the thesis was done it was you that insisted time and again until you finally pushed me back to enjoying physics as I used to do when I firstly moved into the field. Knowing myself no one but you could have made it. Only time will decide whether I make it in this field, but for the moment you are one of the main persons to blame for me being where I am standing today. Hvala ti puno, Marija.

Resumen

En esta tesis doctoral nos centramos en el estudio de la física asociada a las transiciones de fase y la emisión de ondas gravitacionales en el universo primitivo en teorías cuánticas de campos fuertemente acopladas. El estudio se realiza mediante la dualidad AdS/CFT, traduciendo los problemas de teoría cuántica de campos a problemas de gravedad clásica y dinámica de agujeros negros.

Para ello comenzamos introduciendo Jecco: la herramienta de programación desarrollada durante la tesis y que realiza simulaciones de evolución temporal en una teoría de gravedad deformada con un campo escalar que introduce transiciones de fase.

Una vez explicado el algoritmo empleado, comenzamos a estudiar la física asociada a las transiciones de fase. En el capítulo 3 encontramos el espacio de soluciones inhomogéneas presentes en toda transición de fase de primer orden a volumen finito, estableciendo la preferencia termodinámica. En el capítulo 4 estudiamos la dinámica de colisiones de un tipo de solución inhomogénea encontrada previamente, dominios de fase. Mediante simulaciones con diferentes velocidades de colisión encontramos tres regímenes diferentes según incrementamos la velocidad: colisión con estado cuasi-estático previo, colisión y relajación del dominio resultante sin estado cuasi-estático y, finalmente, colisión y desfragmentación del dominio resultante.

El capítulo 5 pone su atención en el estudio de la dinámica de burbujas, de crucial importancia en la emisión de ondas gravitacionales en la colisión de estas. Obtuvimos la burbuja crítica y la velocidad terminal de la burbuja para distintas temperaturas de nucleación. Con este estudio observamos una relación lineal sencilla para la velocidad terminal de gran interés y de difícil obtención mediante otros métodos de cálculo.

Finalmente, el capítulo 6 estudia el escenario en el que la nucleación de burbujas está suprimida y en donde la dinámica sigue otra vía, la de la inestabilidad espinodal. Realizamos la simulación completa de dicha inestabilidad y computamos el espectro de emisión de ondas gravitacionales. Llegamos a la conclusión de que dicho espectro es muy diferente del de la colisión de burbujas, pudiendo identificar correctamente el origen de la posible detección de ondas gravitacionales en los interferómetros de próxima generación.

Abstract

Cosmological thermal first-order phase transitions are assumed to proceed via the nucleation of bubbles and subsequent expansion and collision. The out-of-equilibrium physics involved during the collision of bubbles is expected to emit Gravitational Waves (GW) detectable by future generation interferometers like the Laser Interferometer Space Antenna (LISA). The Standard Model of Particle Physics (SM) as we know it does not exhibit any first order thermal phase transitions, meaning that the detection of such GW emission would imply the direct observation of new physics beyond the SM. For this reason, a good theoretical understanding of the features of the GW spectrum emitted during first order thermal phase transitions, together with an exploration of possible alternative mechanisms to bubble collisions is needed more than ever. An accurate study of such emission implies knowing out-of-equilibrium properties of the underlying Quantum Field Theory, which is known to be challenging even at weak coupling.

In this thesis we will employ the AdS/CFT, which has proven to be very useful in the study of out-of-equilibrium physics at strong coupling, to investigate the properties of first order thermal phase transitions and its application to the emission of GW in the early universe.

We start in by introducing Jecco, a program written in Julia and freely available. It evolves in time Einstein's Equations in a gravity theory with a simple scalar field that provides with first order thermal phase transitions. The simulations are done in 3+1 dynamical dimensions and, therefore the dual Quantum Field Theory has dynamics in 2+1. Jecco has been crucial for the results shown in chapters 5 and 6.

Chapter 3 studies the space of non-uniform states at finite volume in a theory with a first order thermal phase transition. This family of solutions is expected in generic first order transitions. We studied their thermodynamic properties and dominance in different thermodynamic ensembles. We additionally studied their dynamical (in-)stability and obtained the end state of the time evolutions. We additionally observed that in the infinite volume limit the dominant states tend to the well-known phase separated configurations.

In chapter 4 we went ahead and study the collision dynamics of phase domains. These collisions where first observed in the full-time evolution of the spinodal instability. In this chapter we set as initial data two identical phase domains with some velocity that we varied. For low speeds we observed that the domains enter a quasi-static regime in which they moved almost undeformed. Eventually the collision takes place, and the result is a larger phase domain that relaxes by oscillating. For larger velocities the quasistatic regime disappears and for large enough speeds the collision leads to a fragmentation. The eventual end state of all collisions is a phase separated configuration.

Chapter 5 analyzes bubbles, their expansion and the critical one. We observed that the late time expanding bubble profile is self-similar, and that hydrodynamics is applicable everywhere but at the walls. Furthermore, we observed a possible simple relation for the wall velocity, challenging to compute from first principles and important to estimate the GW emission in collisions. We also obtained the critical bubble for a given nucleation temperature, relevant for the nucleation temperature.

Finally in chapter 6 we argued that for theories with enough bubble nucleation probability suppression, the universe might get into the unstable, spinodal branch before nucleating bubbles. At this point the exponential growth of unstable modes dominates the dynamics. We performed the full-time evolution of the instability and computed the sourced GW spectrum. The resulting spectrum seems qualitatively different to the bubble collision one and opens the exciting possibility of being distinguishable in future interferometers.

Contents

Chapter 1

Introduction

Little of what was lying ahead was suspected when a fundamental force of nature was successfully quantized for the first time. Humans came up with more than just Quantum Electro Dynamics (QED): a methodology for quantizing classical field theories was engineered, which subsequently gave rise to the framework of Quantum Field Theory (QFT). As a result, the twentieth century turned out to be one of the most exciting eras in physics. In a matter of a hundred years, human kind went from discovering the electron[1] all the way to the discovery of the Higgs boson back in 2012 [1], the last missing piece of the well-known Standard Model of Particle Physics (SM). During this period, theory and experiments walked along hand to hand producing success after success. Theoretical physicists would not stop coming with predictions while experimentalists learned that smashing particles against each other at speeds practically that of the light would allow them to uncover a whole universe of new particles.

With the completion of the SM, this frenetic era seems to have taken a break. Experiments currently conducted at the Large Hadron Collider (LHC) do not seem to spot radical deviations from the theory. Even if some of the data indicates that we might be in front of new physics (like the recent muon $g-2$ anomaly [2])), a big discovery comparable to the direct observation of a new particle is not expected any time soon. Nevertheless, that the SM has been completed does not mean that we are done with fundamental physics. Among other unsolved questions we find: the Higgs mass naturalness problem, the need to account for neutrino masses, dark matter and dark energy, matter-antimatter asymmetry and, last but not least, the quantization of gravity. Even within the SM, important questions remain unanswered. A clear example is our ignorance about the phase structure of Quantum Chromodynamics (QCD), the theory of strong interactions. This means, for instance , that we cannot say much about the state of the universe around 10^{-6} after the Big Bang.

This is the context in which two new type of experiments are creating a lot of excitement in the field. These are the Heavy Ion Collision (HIC) and Gravitational Wave (GW) detection. The former hopes to explore the properties of the QCD matter in extreme conditions while the latter will hopefully give us information about some regions of the QCD diagram as well as directly observing new physics beyond the SM.

1.1 QCD in extreme conditions

The theory of strong interactions as we know it was developed during the 70s, being an extension of the Yang-Mills theory [3]. The main qualitative difference with QED is the fact that the force carriers, the gluons, are charged under the same force. In more technical terms, QCD is a non-Abelian theory, which has important consequences, as we will see. The Lagrangian for this this

[1] Although this discovery was a pre-QED one

theory with a single quark looks very simple,

$$\mathcal{L} = \sum_{i,j=1}^{3} \bar{\psi}_i i\gamma^\mu \left(\partial_\mu \delta_{ij} - ig(T_a)_{ij} A^a_\mu\right) \psi_j - m\bar{\psi}_i\psi_i - \sum_{a=1}^{8} \frac{1}{4} G^a_{\mu\nu} G^{\mu\nu}_a, \tag{1.1}$$

with ψ being the quark field, A^a_μ the gluon ones, with field strength $G^a_{\mu\nu}$. The coupling constant is g while i and a are color charge index for the quark and the gluon respectively. The gluon quark indices run from 1 to 8 when the number of colors $N_c = 3$ because they belong to a different representation of the $SU(N_c)$ symmetry group. For general N_c, quarks will have N_c color degrees of freedom while gluons $N_c^2 - 1$.

In spite of its apparent simplicity, obtaining meaningful results from this Lagrangian has proven to be a great challenge. The theory becomes strongly coupled for low energies, so perturbation theory is not helpful. Perturbation theory is one of the few approaches with which we know how to extract results out of QFTs, and it is based on the possibility of thinking of the theory as a set of asymptotically free particles that come closer to feebly interact and produce another set of asymptotically free particles. Mathematically, everything boils down to the possibility of performing an expansion around $g = 0$.

At high energies, the coupling g becomes smaller and tends to zero and perturbation theory becomes a good approximation for energy scales considerably bigger than the characteristic scale QCD possess, $\Lambda_{QCD} = 210\text{MeV}$[2]. This scale is small enough to study the high energy collisions at accelerators with perturbation theory, whose predictions have been well corroborated by the data. As a consequence, QCD became a huge success and was accepted as the theory to explain strong interactions, beating string theory along the way[3].

Despite the success at colliders, some of the interesting physics encoded in (1.1), expected to happen at around Λ_{QCD}, is yet to be uncovered fifty years after its formulation.

1.1.1 Phase Diagram

It is said that the universe today is a cold place. Cold for whom? The center of the sun, with a temperature of $T_{sun} \sim 10^7 K$, looks like an extremely hot place. For nuclear matter,

$$T_{sun} \ll T_{QCD} = \frac{\Lambda_{QCD}}{k_B} \sim 10^{12} K, \tag{1.2}$$

the center of the sun is a freezing spot. As a consequence, all quarks and gluons of the universe are confined inside hadrons, like protons and neutrons, unable of setting themselves free. This, however, was not the case throughout the history of our universe. Looking back, the universe was denser and hotter and, at sufficiently early times, its temperature was comparable to T_{QCD}. Around this temperature, a transition that sets the quarks and gluons free from the nucleons is expected, also known as deconfinement. The motivation to think so is that at very high temperatures thermal fluctuations are strong enough to break apart the hadrons, deconfining the quarks and gluons inside, and the transition should happen somewhere near Λ_{QCD}. This high temperature soup of deconfined quarks and gluons was baptised Quark-Gluon-Plasma (QGP).

A very interesting question is how did the universe cool down from a QGP phase to a hadronic one. Was it smooth or abrupt, i.e. was there any phase transition? And if so, what kind of phase transition was it? More generally one could ask how does the QCD phase diagram look like. Perturbation theory cannot say much because most of the transitions are expected to happen when either the temperature or the baryon charge is of the order of Λ_{QCD}, for which

[2] This scale, not present in (1.1), appears when quantizing the theory and its value has to is extracted from experiments. It is present even for the Yang-Mills theory, where there is no energy scale present in its Lagrangian. The appearance of Λ_{QCD} is the reason why g will change with the energy scale of interest even if it is dimensionless

[3] Of course string theory became much more than an attempt to study strong interactions

$g \gtrsim 1$. There are two more tools to try to tackle this issue. We either use effective theories, which will be not covered here, or one turns to a lattice formulation of QCD. This formulation of QCD, or simply Lattice QCD, is simple in spirit. We just take the QCD Lagrangian and perform the path integral in euclidean signature,

$$\mathcal{Z} = \int \mathcal{D}\psi\mathcal{D}A \exp\left[-\int_0^\beta d\tau d^3x \mathcal{L}^E_{QCD}\right], \tag{1.3}$$

with discretized spatial directions. Here τ is the compactified euclidean time with period related to the temperature, $\beta = 1/T$. We can view this formula as a sum over all possible field configurations whose probability is given by the exponential term. Discretization maps field configurations to a finite set of randomly generated variables following said probability distribution. This approach is completely valid as long as we consider vanishing baryonic chemical potential, μ_B. Turn it on and we need to add a term to the action that can evaluate to complex values in euclidean signature, so we can no longer interpret the exponential of the action as a probability distribution. This is essentially the sign problem. Nevertheless, the community is able of computing observables at finite baryon charge perturbatively in μ_B/T by obtaining high order derivatives with respect to μ_B for $\mu_B = 0$.

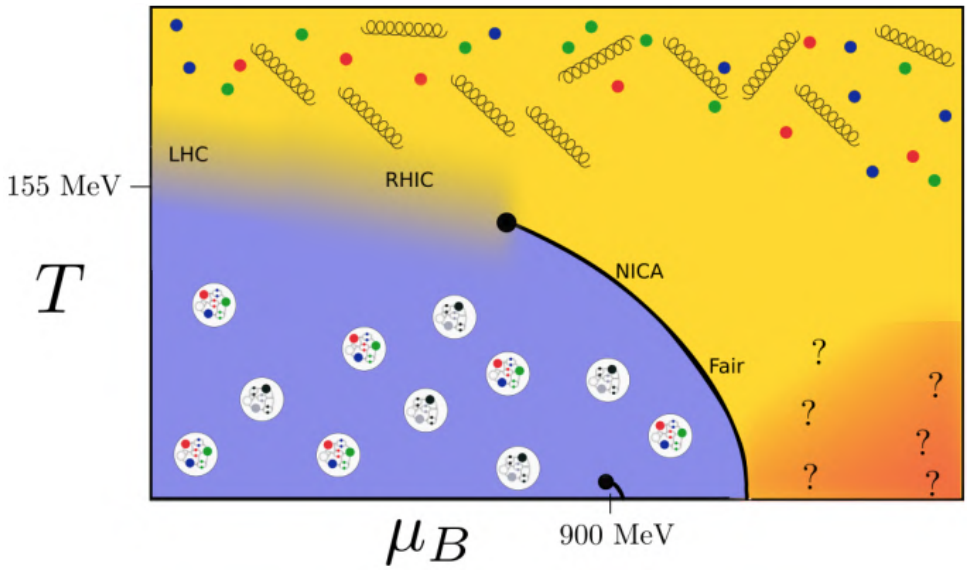

Figure 1.1: Hypothesized QCD phase diagram, taken from [4]. At low temperatures and baryon densities we find hadrons, while at high temperatures and densities we transition to the QGP. In the cold but dense region the phase present in the inside of neutron stars is expected.

With this tool the transition for small baryon charge was computed and a crossover was discovered, as shown in Fig. 1.1. Breaking up the proton into its constituents is a rapid but smooth process. For slightly larger baryonic chemical potential a more rapid crossover is found, suggesting a possible second order phase transition at finite μ_B. Additional intuition from other models [5] suggest that there is a critical point from where a first order phase transition line arises. Observable signatures of the critical point are expected to become relevant when matter is in the vicinity of it, see e.g. [6, 7], so experiments that try to generate conditions nearby the critical point are of high interest.

How do we get to such hot and dense conditions? In a similar way to how we uncovered a whole spectrum of subatomic particles, by smashing particles against each other in colliders. However, a phase is a thermodynamic concept, meaning that its properties manifest themselves when considering a large enough amount of particles; indeed, we cannot even define a temperature when considering a handful of them. In practice, heavy ions are collided, where a

larger amount of particles take part per collision, and the baryonic charge can be controlled by controlling the energy at the collision. At high energies the valence quarks, the baryon number carriers, barely interact with each other while the virtual sea of gluons and quark anti-quark pairs are the ones that collide, giving rise to a QGP at very low baryon density. As the energy at the collision drops the valence quarks interact more strongly, increasing the baryonic charge of the resulting QGP. Evidence of the discovery of a QGP-like phase was announced at the Relativistic Heavio Ion Collider (RHIC) back in the early 2000s.

The RHIC Beam energy scan is already producing higher μ_B collisions and the Nuclotron-based Ion Collider fAcility (NICA), Compressed Baryonic Matter Experiment (CBM) and the J-PARC heavy ion project (J-PARC-HI) will also produce high μ_B collisions that will hopefully allow us to observe the predicted critical point together with the first order phase transition line.

Finally, the reader might be wondering how could we explore the high charge density, low temperature regime if in collisions a lot of energy is deposited ino the QGP by construction. The answer is that gravity does the job by creating neutron stars out of certain dying stars. Neutron stars are known to consist of neutrons in their crust, but many hypothesis turn around the core state of matter, whose conditions are more or less where the question marks lie in Fig. 1.1. The challenge relies in extracting information out of the core of a neutron star. Fortunately, gravity has the answer again.

In 2015, the first ever detection of Gravitational Waves was announced at the Laser Interferometer Gravitational-Wave Observatory (LIGO) [8]. This detection came from the merger of two black holes. Later, in 2017, a new kind of detection was made, namely one sourced by a neutron star binary system [9], and not long ago a black hole neutron star merger was observed [10]. Detections like this will help us determine the properties of the core of neutron stars.

1.2 Gravitational Waves from Cosmological Phase Transtitions

The huge hype that the advent of Gravitational Wave astronomy has brought is not only due to study of astrophysical processes; there is also chance of directly discovering new physics. While direct evidence of new physics at colliders in the traditional way (by new particle observation) possibly means building a collider of unknown scale, the early universe naturally offers a high energy state. In the previous section we mentioned the hadron deconfinement in the early universe, but any other similar transition could have happened in other sectors of matter at even earlier times.

The difficulty relies in accessing the information of the early universe. The Cosmic Microwave Background (CMB) represents the oldest light that we can receive. Earlier in time the universe was too hot for atoms to form and photons were insatiably scattered, so the universe was opaque. Hence, the farthest we can look back is the time of the CMB. Back then the universe was at a temperature of $T_{CMB} \sim 0.25eV$, which is a very low temperature for QCD, even lower for the Electro-Weak (EW) sector ($T_{EW} \sim 100$GeV) and ridiculously low for some proposed new physics. Hence, the CMB does not contain what we look for[4]. Gravitational Waves, on the contrary, can travel from the time of emission all the way to us in the present even if they were sourced in the very early universe. The limit is presumably when the universe temperature was at the Planck scale, $T_p \sim 10^{19}$GeV.

Some cosmological events might be capable of producing a stochastic gravitational wave background. One such event is thermal first order phase transitions.

[4]Gravitational waves can leave an imprint in the polarization of the CMB light, but this corresponds to a restricted amount of the information they carry

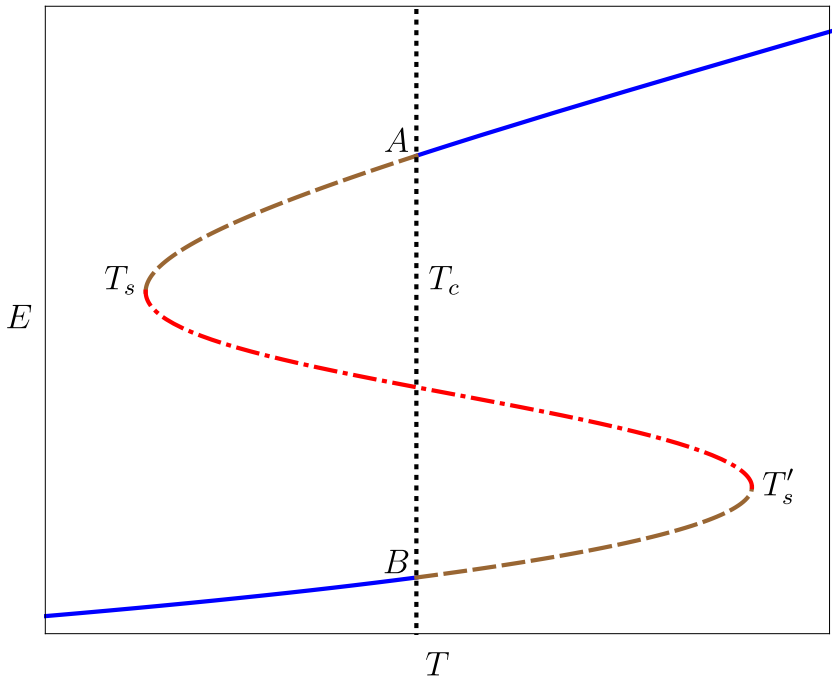

Figure 1.2: Schematic temperature dependence of the energy for a generic theory with a first order thermal phase transition. For $T_s < T < T'_s$ the energy is multivalued. In solid-blue we have the thermodynamically preferred states, in dashed-brown the metasteable states and in dash-dotted-red the thermodynamically unstable ones.

1.2.1 New physics from first order phase transition Gravitational Waves

Let us consider a generic theory with a thermal, first order phase transition. Fig. 1.2 shows the typical relation between the energy of the different thermodynamic states and their temperature. The transition comes from the fact that, for a given temperature between T_s and T'_s, the system has more than a single available state. The state that thermodynamically dominates for each temperature is the one with lowest free energy. Such analysis leads to the conclusion that at high temperatures high energy states are favored while at low temperatures the low energy states are preferred. In solid-blue we represent the thermodynamically preferred states. In dashed-brown we depict those states that are locally stable but not globally, i.e. metastable, and in dash-dotted-red those that are additionally locally unstable. The transition happens at a critical temperature T_c in a discontinuous way, jumping from A to B.

Now assume the universe was cooling down following the high energy branch in Fig. 1.2. At some temperature $T_c < T < T'_s$, the universe has two locally stable states available. This idea is clearly seen in the concept of the effective potential, which is a function that depends in some (family of) parameter that distinguishes among phases and its extrema correspond to the different equilibrium states of our system. The parameter can be an order parameter or some thermal expectation value that takes different values in different phases. The two minima are the high and low energy phases at a given temperature while the maxima is the intermediate, locally unstable one. At the equilibrium points the value of the potential coincides with the free energy.

For $T_c < T < T'_s$, the effective potential looks like the blue curve in Fig. 1.3, the universe being in the high energy branch, or the global minima. As the universe continues expanding it cools down locally, the difference in free energy between both minima diminishes and eventually acquires the same value at T_c. From this moment on, the universe no longer finds itself in the

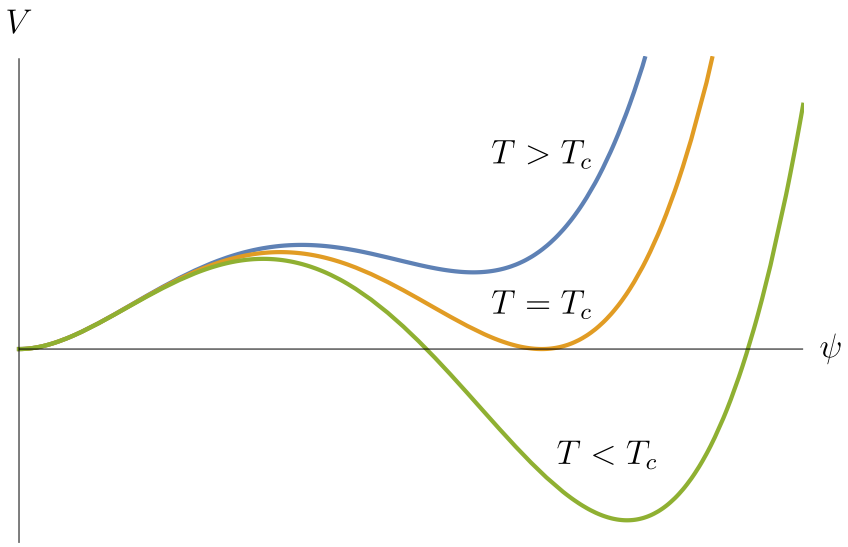

Figure 1.3: Effective potential for the theory Fig. 1.2 different temperatures. At $T = T_c$ the both minima are equally favoured and for lower T the second minima is preferred.

global minima, as seen in the green curve in Fig. 1.3.

Due to the local stability of the state, small thermal fluctuations will not take the universe out of the local minima, they will be reabsorbed. However, given enough time the fluctuation will be large enough to surpass the barrier in between the two minima. These fluctuations are bubbles, and the minimal fluctuation that overcomes the barrier is called the critical bubble. Anything smaller will collapse while bigger ones will drive the universe out of the metastable state towards the global minima. The critical bubble is an unstable solution then.

The probability of such fluctuation happening is exponentially suppressed. To be more precise, the probability per unit time and volume for the critical bubble to be nucleated is[5] [11],

$$\frac{\Gamma}{V} \sim T^4 e^{-S_{CB}(T)}, \tag{1.4}$$

where S_{CB} is the action of the critical bubble configuration at temperature T. The exponent can be interpreted as the difference in free energies between the bubble and the metastable state of same temperature.

The relevant question is, can at least one bubble nucleate , for a given characteristic cooling rate given by the Hubble constant $H \sim T^2/M_p$. We will take a close look into it in chapter 6

If nucleation occurs, some bubbles will expand while others collapse. Those expanding will accelerate and grow in size until the terminal velocity, imposed by the friction outside the wall, is reached. This process is, despite small fluctuations, spherically symmetric and no gravitational wave emission is expected. However, whenever two or more bubbles encounter each other and collide, the symmetry of the fluid motion breaks sourcing a large amount of gravitational waves.

Studying bubble collisions from first principles is a great challenge, but one can hope that, due to the big size of bubbles in a typical collision, gradients are very diluted and hydrodynamics is applicable. By simulating the bubble collisions one can take use the hydrodynamic stress tensor and use it as a source for linearized gravity equations. See a recent example in [12] together with videos of the simulations in https://vimeo.com/showcase/5968055 .

With the intuition acquired from hydrodynamic simulations, a model that allows for fast estimation of the gravitational wave spectrum given some parameters of the theory can be found in equation (8.24) of [11]. We do not need to display it here for our purposes. We just want to point out that all required parameters but one, the bubble wall velocity, are equilibrium

[5] In $\hbar = k_B = c = 1$ units for the rest of the chapter

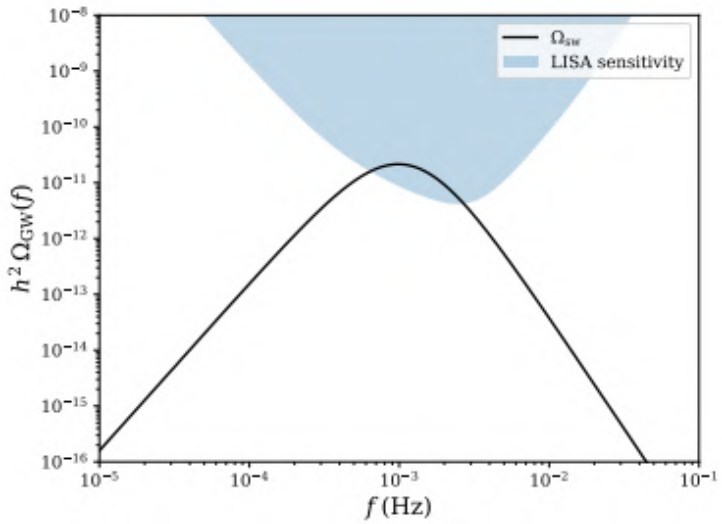

Figure 1.4: Estimation GW spectrum emitted by the bubble collision and comparison with LISA sensitivity. The spectrum is peaked at the relevant macroscopic scale, the mean bubble separation at the time of collision. Figure taken from [18].

properties. Determination of the wall velocity is difficult even at weak coupling [13–15]. The fact that the spectrum is specially sensitive to it (see e.g. [16, 17]) makes its computation not just challenging but pressing. Moreover, the determination of a heuristic, simple relation between the velocity and equilibrium properties of the theory could be of substantial help when performing estimations.

The qualitative shape of the spectrum is shown in Fig. 1.4. It grows with a certain power law until a peak and then it falls with a different power law. A spectrum consisting on two different power laws is denoted a broken power law. The peak location is set by the main macroscopic scale of the problem, the mean bubble separation at the time of collision. This quantity can be computed estimating the density of bubbles in the universe using the nucleation rate (1.4), see (7.21) in [11] for details.

Where does the new physics come around in all of this story? From the fact that the Standard Model as we know it exhibits no phase transition at all. We already saw that hadronization happens smoothly for low μ_B while Fig. 1.5 shows that for the value of the Higgs mass we measure, $m_H \sim 125$GeV, the Electro-Weak transition is a smooth one too. Therefore, if any stochastic background coming from a first-order phase transition is detected it must be from physics beyond the Standard Model.

The sector responsible for the phase transition may range from an extension of the Standard Model to a hidden sector coupled only gravitationally to the former. In the first case, the transition could take place at any scale between the Electroweak scale and the Planck scale $\sim 10^{19}$ GeV. For example, the Electroweak crossover turns into a first-order phase transition even in minimal extensions of the Standard Model [19–29], resulting in a GW frequency in the mHz range potentially observable by LISA [18]. In the second case, the transition could take place virtually at any scale. As an example, string theory compactifications often feature a large number of hidden sectors that are only gravitationally coupled to the Standard Model degrees of freedom. Phase transitions in these sectors can lead to a sizeable gravitational wave background [30–33] whose frequency can span the whole range of parameter space that will be explored by current and future interferometers. This includes the high-frequency range $\gtrsim$ 30 kHz, where new technologies are necessary [34], but also where conventional astrophysical foregrounds are absent.

One can rightfully wonder if the inevitability of bubble nucleation means that the story we

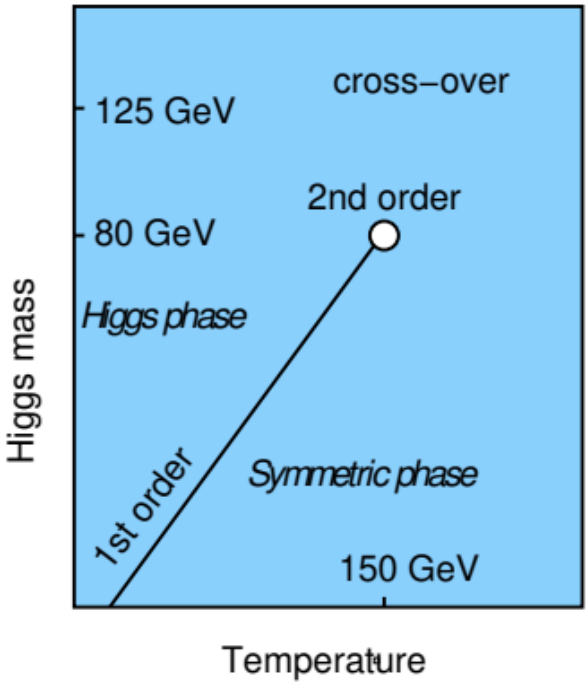

Figure 1.5: Electro-Weak phase diagram. For a the value of the Higgs meassured the transition was a smooth crossover. Figure taken from [11].

just told is the only possible fate of the universe as it cools down across a first order phase transition. The answer lies once again in how fast the universe cools down and if it can get out of the metastable branch while bubbles did not have time to grow enough. If that is the case, the instability of the red branch in Fig. 1.2 will dictate the resulting dynamics. This instability is called the spinodal instability. For this to happen is easy to believe that the nucleation rate should be highly suppressed. This is the main motivation for chapter 6 and we will go into details there. The conclusion for now is that there is an alternative way in which a phase transition can occur in the early universe, that it also sources gravitational waves and that it is important to know if it can be distinguished from the spectrum of colliding bubbles shown in Fig. 1.4.

1.3 Why Holography?

So far it has become clear that trustworthy theoretical predictions for next generation experiments require the knowledge of out-of-equilibrium properties of QFTs. Obtaining them is intrinsically difficult even at weak coupling and in the case of HIC experiments, strong coupling cannot be overlooked. Perturbation theory fails at strong coupling while Lattice QCD is finding a big obstacle with the sign problem. New approaches are welcome.

Fortunately, a duality of particular interest for our purposes was spotted around twenty years ago [35], the AdS/CFT duality. Roughly speaking the duality is between string theory in Anti de Sitter (AdS) spacetime, of constant negative curvature, in $d+1$ dimensions[6] and $\mathcal{N}=4$ $SU(N_c)$ Super-Yang-Mills theory in d dimensions, a supersymmetric generalization of the Yang-Mills theory mentioned earlier. The latter is a theory known as a Conformal Field Theory (CFT), a QFT with no intrinsic scales. At this stage it might not look very useful for our purposes, the theories we are interested in are neither string theory nor CFTs. Even before

[6] $\mathrm{AdS}_{d+1} \times S^5$, but we will forget about the sphere from now on. We can imagine we did dimensional reduction of the sphere and the result is a tower of massive fields that live in AdS_{d+1}.

getting to that point, we do not really know how to deal with strings in AdS.

The relation between the parameters in both sides of the duality is,

$$g^2 N_c \sim \left(\frac{\ell}{\ell_s}\right)^4, \qquad g^2 \sim 4\pi g_s, \tag{1.5}$$

where g_s is the string coupling, ℓ_s its length, ℓ the radii of AdS and g the SYM coupling. By taking $g \to 0$ but $N_c \to \infty$ in such a way that $g^2 N_c \to \infty$, the string theory dual corresponds to weakly interacting strings of size much smaller than the AdS radius. This limit of string theory is a classical theory of gravity[7]. In other words, we are considering a strongly coupled CFT with a large number of colors as to be described by General Relativity in a higher spacetime dimension. We already start seeing the potential of such duality. We can map out-of-equilibrium problems of a quantum theory to a classical one. Everything boils down to time evolving Einstein Equations with appropriate asymptotic conditions, which, fundamentally speaking, should not be an obstacle. In mathematical terms, the duality means that the partition function of each side of the duality matches,

$$\mathcal{Z}_{CFT}[J] = \mathcal{Z}_{gravity}[\phi|_{\partial AdS} = J] \sim \exp\left\{-S^{on-shell}_{gravity}[\phi|_{\partial AdS} = J]\right\}. \tag{1.6}$$

Sources J on the CFT side are identified with the boundary conditions of fields $\phi|_{\partial AdS}$ on the gravity set up (ϕ is a generic field, not necessarily a scalar one) and we use the saddle point approximation in the last step.From the equation we can also interpret that the CFT lives on the AdS boundary. We can obtain point functions of the boundary theory by making variations with respect to its sources, the boundary conditions for the fields living in the gravity side (the bulk),

$$\langle T_{\mu\nu} \rangle = -\frac{2}{\sqrt{-g_0}} \frac{\delta S^{on-shell}_{gravity}}{\delta g_0^{\mu\nu}}, \tag{1.7}$$

where the 0 subscript means the boundary value. Specific expressions will be given in chapter 2, but one can imagine how we could compute arbitrary point functions of boundary operators.

An immediate question is, what are black hole states dual to? From the bulk perspective, black holes are thermal states that have huge entropy. A deconfined state on the CFT has $N_c^2 - 1 \sim N_c^2$ color degrees of freedom (recall gluons), which is also enormous in our limit. It is then tempting to say that black holes are dual to deconfined thermal states. The computation leads to,

$$S \sim N_c^2 T^3, \qquad \langle T_{\mu\nu} \rangle \sim N_c^2 T^4, \tag{1.8}$$

for a black hole of temperature T. The temperature and entropy are not computed as the rest of the quantities, they are identified with the horizon properties. These results are what we expect for a $SU(N_c)$ CFT, where the only energy scale is the temperature of the state. This is true for very large black holes compared to ℓ, which is our case, as we will work in the so called Poincare patch. In this patch black holes do not look compact, they are black branes that extend indefinitely along the boundary directions.

We are now in position of computing out-of-equilibrium properties of a CFT. We just need to consider classical black brane dynamics. And how do we break conformal invariance? We add classical matter fields to our gravity theory, bringing the scale to the setup. We will do it in a phenomenological way, meaning that we will deform the bulk gravity theory by adding matter in the simplest possible way so that the resulting theory exhibits a desired property. These kind of models are referred to as bottom-up models. In this thesis we only add a scalar field that breaks the conformal symmetry (details in chapter 2), but one can add other type of fields, like Maxwell fields, which turn on a chemical potential on the boundary.

[7] Supergravity to be precise.

One should note that the community has already applied the duality to study all sorts of strongly coupled QFT setups: HIC [36–45], neutron stars [46–54], confinement and its possible diagnosis [55], RG flows [56–58], the QCD critical point models [59, 60], hydrodynamics in the presence of phase transitions [36, 61–65] and condensed matter systems among others [66–74].

1.3.1 Just a tool?

Despite treating the duality as a tool so far, one should avoid thinking of AdS/CFT in such way; after all it contains a universe in itself. AdS/CFT is a precise realization of a more general, and diffuse principle known as holography. Holography is the principle stating that the fundamental degrees of freedom of gravity are encoded in a lower dimensional surface. A simple place where motivation for this principle can be found is in the Bekenstein-Hawking entropy formula for a black hole of area A,

$$S_{BH} = \frac{A}{4G}, \tag{1.9}$$

which suggests that the information hidden by black holes scale with their area instead of their volume, as we are used to.

We could very well spend the rest of this thesis discussing holography, but that would be beyond our purposes. In few words we can say that holography is a quantum theory of gravity. It has helped us understand many non-classical features of gravity. As an example, new progress has been made recently in the black hole information paradox, the interpretation of quantum gravity as an ensemble average of theories or information about dynamically formed singularities, see e.g. [75–78].

The content of this thesis is distributed as follows. In chapter 2 we will introduce the technical details we use to evolve in time Einstein's Equations and a motivation for the model we use will be given, based on section section 2 of [79], where our newly developed code `Jecco` is introduced. We will then proceed to study the physics of phase transitions with this model. We start by discussing families of inhomogeneous solutions in chapter 3 [80] and then move to study the collision dynamics of phase domains in chapter 4 [81], an important inhomogeneous configuration in theories with phase transitions. We will then move into the realm of gravitational waves from cosmological phase transitions. We will start by discussing the dynamics bubbles in 5, namely its expansion and wall velocity and the determination of the critical bubble. This chapter is based on the work in [82] and section 3 of [79]. Finally, in chapter 6, we will explain in detail the possibility of getting gravitational waves out of an alternative process in theories with first order phase transitions and we will obtain such spectrum out of our time evolution [83]. Finally, we will give some general conclusions together with some possible interesting future directions.

Chapters 3 and 4, and section 5.4.1 study setups with dynamics along one spatial dimension. For them, `Jecco`'s predecessor, `SWEC`, was used. It was already existing at the time this thesis began and only the gravity model had to be slightly modified. Its time evolution algorithm is analogous to what will be exposed in chapter 2.

Chapter 2

Holographic model and time evolution algorithm: Jecco

In this chapter we will introduce both the holographic model we will use throughout the thesis together with the techniques that are employed to do full, non-linear time evolution of the Einstein's Equations. We will start by motivating the family of models under consideration and we will then move on to describe how to derive the equations of motion, what possible redefinitions are needed and a rough view of the details needed to numerically implement these equations. We will also provide with the expressions that one gets when applying the holographic dictionary to obtain the boundary one point functions in terms of the bulk metric and fields on our coordinates. The resulting numerical code arising from this chapter was named `Jecco` and can be found at github `https://github.com/mzilhao/Jecco.jl` and Zenodo [84].

The explanation given here intends to be a conceptual framework of the procedure we follow so that the picture of what `Jecco` does is clear. More detailed explanation can be found in [79].

We will work in the Poincare patch of AdS and we will use the so called characteristic formulation. This formulation is different to the usual Cauchy one in the sense that we will provide initial data on a null slice instead of a space-like one. Given some initial data, plus the usual boundary data required in AdS-like spacetimes, we will evolve in time from null slice to null slice, each of them attached at a different time coordinate of the boundary. See Fig. 2.1 for a schematic representation of the process. The boundary is located at $r = \infty$.

The advantage of this formulation is double fold. First, the equations end up in a very nice nested structure of radial Ordinary Differential Equations (ODE) for each grid point (x, y) where we can almost sequentially solve for the different functions. Second, our initial data includes a few bulk functions plus some boundary ones and no constraint has to be satisfied, in contrast with Cauchy formulations. The drawback is that the Characteristic formulation tends to form caustics (light rays that cross each other in two points) under time evolution..

Our black holes are non-compact, they are black branes, and whatever happens beyond the event horizon is of little interest as it is causally disconnected from the outside. We will cut out and not consider anything beyond some $r_{min} < r_{EH}$, where the latter is the event horizon position. Instead of the Event Horizon (EH) , which is of tautological definition, we will consider the Apparent Horizon (AH), which is always inside the EH under classical evolution. We will only consider a patch like the one in brown in Fig. 2.1. One could expect that under reasonable conditions, caustics will tend to form deep beyond the horizon, which is precisely not described by our numerical grid. As a consequence, the Characteristic formulation is widely used for applied holography problems while abandoned for other numerical relativity ones. Caustics do not seem to be putting up any problems. Nevertheless, it might be that for more unconventional evolutions caustics end up forming within the grid.

By giving some initial data in the null t_0-slice of Fig. 2.1, together with boundary conditions for all boundary times (like the boundary background metric) we perform the numerical time

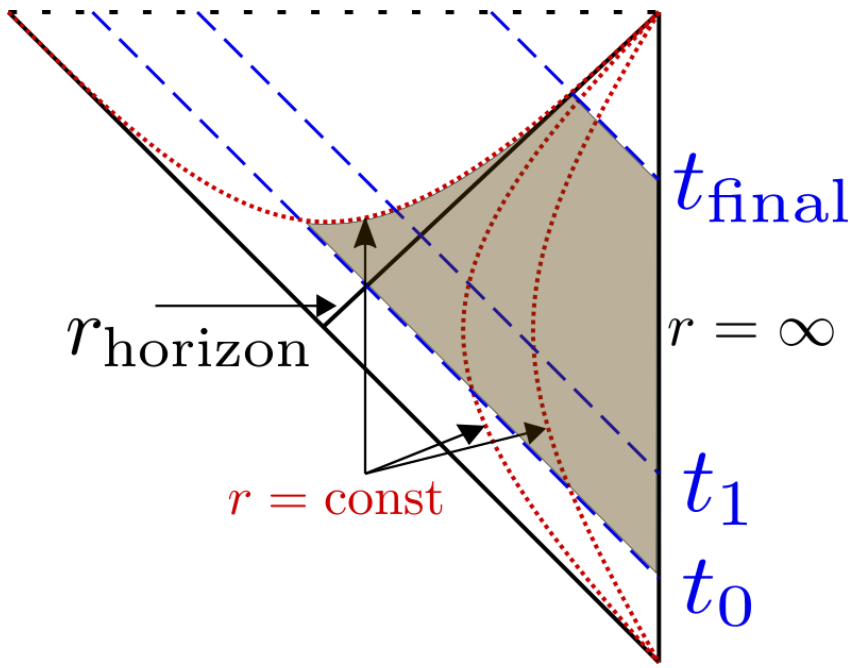

Figure 2.1: Penrose diagram of the evolution procedure, at constant x, y slices. The shaded region represents the region covered by the computational domain.

integration of the Einstein's Equations and use the holographic dictionary to obtain the desired one point functions at the boundary theory as a function of (t, x, y). The expression we will find are well defined regardless of our system being out-of-equilibrium. Our approach is similar to that of [85] and generalises the code presented in [38] to the 3+1 dimensional case.

In what follows we will go into the details of how to implement this procedure and the equations in question. Tests for our code are also summarized here. We use $G = c = \hbar = k_B = 1$ units throughout.

2.1 Model

We consider a five-dimensional action (3+1 boundary theory) consisting of gravity coupled to a scalar field ϕ with a non-trivial potential $V(\phi)$. The action for this Einstein-scalar model is

$$S = \frac{2}{\kappa_5^2} \int d^5x \sqrt{-g} \left[\frac{1}{4} R - \frac{1}{2} (\partial\phi)^2 - V(\phi) \right], \tag{2.1}$$

where κ_5^2 is the 5D gravitational coupling constant, $\kappa_5^2 = 8\pi$. Our potential $V(\phi)$ comes from a superpotential $W(\phi)$ with the form

$$\ell W(\phi) = -\frac{3}{2} - \frac{\phi^2}{2} + \lambda_4 \, \phi^4 + \lambda_6 \, \phi^6 \,, \tag{2.2}$$

being ℓ is the AdS_5 radius. The existence of a superpotential is not mandatory and it was considered here as it brings technical conveniences, namely the horizonless problem reduces to first order ODEs. The potential is then derived via

$$V = -\frac{4}{3} W^2 + \frac{1}{2} W'^2,$$

resulting in

$$\ell^2 V(\phi) = -3 - \frac{3}{2}\phi^2 - \frac{1}{3}\phi^4 + \left(\frac{4\lambda_4}{3} + 8\lambda_4^2 - 2\lambda_6\right)\phi^6 + \left(-\frac{4\lambda_4^2}{3} + \frac{4}{3}\lambda_6 + 24\lambda_4\lambda_6\right)\phi^8 + \left(18\lambda_6^2 - \frac{8}{3}\lambda_4\lambda_6\right)\phi^{10} - \frac{4}{3}\lambda_6^2\,\phi^{12}\,. \tag{2.3}$$

In these equations λ_4 and λ_6 are freely specifiable dimensionless parameters related to the parameters ϕ_M and ϕ_Q used in e.g. [58, 80] through

$$\lambda_4 = -\frac{1}{4\phi_M^2}\,, \qquad \lambda_6 = \frac{1}{\phi_Q}\,. \tag{2.4}$$

The dual gauge theory is a non-conformal theory obtained by deforming a conformal field theory (CFT) with a dimension-three scalar operator $\mathcal{O}_\phi$ of source Λ,

$$S_{4D} \sim S_{CFT} + \int d^4x \Lambda \mathcal{O}_\phi \tag{2.5}$$

The source Λ is an intrinsic energy scale for the gauge theory that will set the characteristic scale of much of the physics of interest. On the gravity side, Λ appears as a boundary condition for the scalar ϕ (we will refer to it as ϕ_0). When setting $\lambda_6 = 0$, the sextic term in W is absent and the model reduces to that studied in the past in [36, 61, 63].

The motivation for our choice of model is that it is possibly the simplest one with a number of desirable features. The presence of the scalar ϕ breaks conformal invariance. The first two terms in the superpotential are fixed by the asymptotic AdS radius and by the dimension of the dual scalar operator, $\mathcal{O}$. The quartic term in the superpotential is the simplest addition that will allow for thermal phase transition in the gauge theory (for appropriate values of λ_4 and λ_6). The sextic term in the superpotential guarantees that the five-dimensional geometry is regular even in the zero-temperature limit.

Throughout this work we will set $\lambda_6 = 0.1$ for convenience and we will play with the value of λ_4. This provides us with a full family of theories with a critical value of λ_4, $\lambda^* \simeq -0.17$. When $\lambda_4 < \lambda^*$ the theory manifests a first order phase transition, for $\lambda_4 > \lambda^*$ the transitions is a crossover and precisely at $\lambda_4 = \lambda^*$ the transition is second order. As it will become clear in the following chapters, different choices of λ_4 within the first range give raise to manifestly different first order phase transitions. This differences are both quantitative and qualitative and the set up under consideration will motivate us to take different values for λ_4.

Let us point out that even if we will always make use of the particular potential (2.3), the code implementation is such that more generic potentials can be used provided that, for low values of the scalar field, they behave as

$$\ell^2 V(\phi) = -3 - \frac{3}{2}\phi^2 - \frac{\phi^4}{3} + \mathcal{O}\left(\phi^6\right). \tag{2.6}$$

The constant term is fixed by the 4+1 dimensional AdS asymptotics and the quadratic one is in correspondence with the scaling dimension of the dual scalar operator $\mathcal{O}_\phi$. The quartic term, determined by the other two in our case, ensures the absence of a conformal anomaly, which would give rise to logarithms in the asymptotic expansions. A change in this near boundary behaviour of the potential would alter the hard-coded asymptotic expansions together wit the convenient variable redefinition introduced later.

Unless otherwise stated let us set $\ell = 1$ from now on.

2.2 Equations of motion and characteristic formulation

The dynamical equations of motion resulting from (2.1) read,

$$\begin{aligned} E_{\mu\nu} &\equiv R_{\mu\nu} - \frac{R}{2} g_{\mu\nu} - 8\pi T_{\mu\nu} = 0, \\ \Phi &\equiv \Box\phi - \partial_\phi V(\phi) = 0, \end{aligned} \tag{2.7}$$

where

$$8\pi T_{\mu\nu} = 2\partial_\mu\phi\partial_\nu\phi - g_{\mu\nu}\left(g^{\alpha\beta}\partial_\alpha\phi\partial_\beta\phi + 2V(\phi)\right).$$

As usual we need an ansatz in order to solve the problem. We will work in ingoing Edington-Finkestein (EF) coordinates. The reader should be aware that we will denote the ingoing null direction by t, instead of the usual v. The reason is that t coincides with a boundary observer time. The ansatz looks as follows,

$$\begin{aligned} ds^2 = g_{\mu\nu}dx^\mu dx^\nu = -Adt^2 + 2dt\left(dr + F_x dx + F_y dy\right) + S^2\Big[e^{-B_1-B_2}\cosh(G)dx^2 \\ + e^{B_1-B_2}\cosh(G)dy^2 + 2e^{-B_2}\sinh(G)dxdy + e^{2B_2}dz^2\Big], \end{aligned} \tag{2.8}$$

where all functions depend on the radial coordinate r, t and transverse directions x and y. Nothing depends on the coordinate z, so this is effectively a 3+1 system. From the boundary point of view, $r = \infty$, the functions only depend on (t, x, y), so we have a system with 2+1 dynamics. The (x, y, z) part of the metric, $dt = dr = 0$, might look cumbersome but it has a motivation. It is the shape it acquires once we impose that S should capture the volume of this slices,

$$\sqrt{g|_{dt,dr=0}} = S^3.$$

In chapters 3 and 4 we will restrict ourselves to dynamics in 2+1 (1+1 at the boundary). This is achieved by setting,

$$\begin{aligned} &F_y = G = 0, \quad B_1 = \frac{3}{2}B, \qquad B_2 = \frac{1}{2}B, \qquad \text{or} \\ &F_x = G = 0, \quad B_1 = -\frac{3}{2}B, \quad B_2 = \frac{1}{2}B, \end{aligned} \tag{2.9}$$

for non-trivial dependence only along the x or y direction respectively. If we now denote the dynamical direction as z and use Σ for S we make contact with the notation in [38]. There is still a residual diffeomorphism, or gauge, symmetry that will play an important role,

$$\begin{aligned} r &\to \bar{r} = r + \xi(t, x, y)\,, \\ S &\to \bar{S} = S\,, \\ B_1 &\to \bar{B}_1 = B_1\,, \\ B_2 &\to \bar{B}_2 = B_2\,, \\ A &\to \bar{A} = A + 2\partial_t\xi(t, x, y)\,, \\ F_x &\to \bar{F}_x = F_x - \partial_x\xi(t, x, y)\,, \\ F_y &\to \bar{F}_y = F_y - \partial_y\xi(t, x, y)\,. \end{aligned} \tag{2.10}$$

This corresponds to radially shifting r-constant slices in a different way for each x and y. It will be useful to set the AH at a constant r coordinate for convenience. Upon substitution of

ansatz (2.8) in the equations of motion (2.7), we obtain a set of coupled radial ODEs for the functions to solve and their dotted version, defined as,

$$\dot{f} \equiv \left(\partial_t + \frac{A}{2}\partial_r\right) f. \tag{2.11}$$

If we solve them we could use this definition to immediately obtain the ∂_t of all required functions and evolve to the next time step. However, by taking specific combinations of the equations, shown in Table 2.1, we can decouple the equations to great extent. This is the nested structure we were mentioning earlier, equations are fairly decoupled and can be solved sequentially. Each of the equations is a linear ODE that looks like,

$$\Big[\mathcal{A}(t,u,x,y)\,\partial_u^2 + \mathcal{B}(t,u,x,y)\,\partial_u + \mathcal{C}(t,u,x,y)\Big]\, f(t,u,x,y) = -\mathcal{S}(t,u,x,y), \tag{2.12}$$

where $u \equiv 1/r$, f is the corresponding function to be solved for and the coefficients $\mathcal{A}$, $\mathcal{B}$, $\mathcal{C}$ and $\mathcal{S}$ are fully known at each step of the nested scheme.

Table 2.1: Nested structure of the equations of motion.

Function(s)	Combination
S	E_{rr}
F_x	$E_{rx} - g_{tx}E_{rr}$
F_y	$E_{ry} - g_{ty}E_{rr}$
$\dot{S}$	$E_{tr} - \frac{1}{2}g_{tt}E_{rr}$
$\dot{\phi}$	Φ
A	$\frac{E_{zz}}{g_{zz}} + \left(g^{ry}g_{ty} + g^{rx}g_{tx}\right)E_{rr} + 2g^{rx}\left(E_{rx} - g_{tx}E_{rr}\right) + 2g^{ry}\left(E_{ry} - g_{ty}E_{rr}\right)$ $-4\left(E_{tr} - \frac{1}{2}g_{tt}E_{rr}\right) + 2\frac{E_{xy}}{g_{xy}} + g_{xx}g^{xx}\left(\frac{E_{yy}}{g_{yy}} + \frac{E_{xx}}{g_{xx}} - 2\frac{E_{xy}}{g_{xy}}\right)$
$\dot{B}_2$	E_{zz}
$\dot{G}$	E_{xy}
$\dot{B}_1$	E_{yy}
$\ddot{S}$	$E_{tt} - \frac{1}{2}g_{tt}E_{tr} - \frac{1}{2}g_{tt}\left(E_{tr} - \frac{1}{2}g_{tt}E_{rr}\right)$
$\dot{F}_x$	$E_{tx} - \frac{1}{2}g_{tt}E_{rx} - g_{tx}\left(E_{tr} - \frac{1}{2}g_{tt}E_{rr}\right)$
$\dot{F}_y$	$E_{ty} - \frac{1}{2}g_{tt}E_{ry} - g_{ty}\left(E_{tr} - \frac{1}{2}g_{tt}E_{rr}\right)$

Those equations that are grouped in pairs are coupled and have to be solved simultaneously for both functions. The only difference will be that in (2.12), the coefficients will become matrices.

The explicit form of the equations is not illuminating and are very long, so they are collected at the appendix, see (A.2-A.10).

2.2.1 Near the boundary

As it is customary in asymptotically AdS spacetimes, we are interested in how the metric and matter fields behave near the AdS boundary. In the first place because the way different functions approach the boundary will give us the field theory observables and, secondly, because some of the functions vanish and others blow up at the boundary, which is not numerically convenient. We will expand in powers of u and solve order by order the differential equations. This will give us the relations between coefficients, which ones are truly independent and what constraints are they forced to obey. With this we will later obtain the boundary one point functions and we will perform appropriate variable redefinitions so that functions that diverge or vanish at the boundary are replaced by others that remain always of order one.

The resulting boundary expansions are,

$$A(t,u,x,y) = \frac{1}{u^2} + \frac{2}{u}\xi + \xi^2 - 2\partial_t\xi - \frac{2\phi_0^2}{3} + u^2 a_4 - \frac{2}{3}u^3\left(3\xi a_4 + \partial_x f_{x2} + \partial_y f_{y2} + \phi_0\partial_t\phi_2\right) + \mathcal{O}\left(u^4\right), \tag{2.13a}$$

$$B_1(t,u,x,y) = u^4 b_{14} + \mathcal{O}\left(u^5\right), \tag{2.13b}$$

$$B_2(t,u,x,y) = u^4 b_{24} + \mathcal{O}\left(u^5\right), \tag{2.13c}$$

$$G(t,u,x,y) = u^4 g_4 + \mathcal{O}\left(u^5\right), \tag{2.13d}$$

$$S(t,u,x,y) = \frac{1}{u} + \xi - \frac{\phi_0^2}{3}u + \frac{1}{3}\xi\phi_0^2 u^2 + \frac{1}{54}u^3\left(-18\xi^2\phi_0^2 + \phi_0^4 - 18\phi_0\phi_2\right) + \frac{\phi_0}{90}u^4\left(30\xi^3\phi_0 - 5\xi\phi_0^3 + 90\xi\phi_2 - 24\partial_t\phi_2\right) + \mathcal{O}\left(u^5\right), \tag{2.13e}$$

$$F_x(t,u,x,y) = \partial_x\xi + u^2 f_{x2} - \frac{2}{15}u^3\left(15\xi f_{x2} + 6\partial_x b_{14} + 6\partial_x b_{24} - \partial_y g_4 - 2\phi_0\partial_x\phi_2\right) + \mathcal{O}\left(u^4\right), \tag{2.13f}$$

$$F_y(t,u,x,y) = \partial_y\xi + u^2 f_{y2} - \frac{2}{15}u^3\left(15\xi f_{y2} - 6\partial_y b_{14} + 6\partial_y b_{24} - \partial_x g_4 - 2\phi_0\partial_y\phi_2\right) + \mathcal{O}\left(u^4\right), \tag{2.13g}$$

$$\phi(t,u,x,y) = \phi_0 u - \xi\phi_0 u^2 + u^3\left(\xi^2\phi_0 + \phi_2\right) + u^4\left(\partial_t\phi_2 - 3\xi\phi_2 - \xi^3\phi_0\right) + \mathcal{O}\left(u^5\right), \tag{2.13h}$$

$$\dot{B}_1(t,u,x,y) = -2b_{14}u^3 + \mathcal{O}\left(u^4\right), \tag{2.13i}$$

$$\dot{B}_2(t,u,x,y) = -2b_{24}u^3 + \mathcal{O}\left(u^4\right), \tag{2.13j}$$

$$\dot{G}(t,u,x,y) = -2g_4 u^3 + \mathcal{O}\left(u^4\right), \tag{2.13k}$$

$$\dot{S}(t,u,x,y) = \frac{1}{2u^2} + \frac{\xi}{u} + \frac{\xi^2}{2} - \frac{\phi_0^2}{6} + \frac{1}{36}u^2\left(10a_4 - 5\phi_0^4 + 18\phi_0\phi_2\right) + \mathcal{O}\left(u^3\right), \tag{2.13l}$$

$$\dot{F}_x(t,u,x,y) = \partial_t\partial_x\xi - u f_{x2} + \mathcal{O}\left(u^2\right), \tag{2.13m}$$

$$\dot{F}_y(t,u,x,y) = \partial_t\partial_y\xi - u f_{y2} + \mathcal{O}\left(u^2\right), \tag{2.13n}$$

$$\dot{\phi}(t,u,x,y) = -\frac{\phi_0}{2} + u^2\left(\frac{\phi_0^3}{3} - \frac{3}{2}\phi_2\right) + \mathcal{O}\left(u^3\right). \tag{2.13o}$$

Note that ϕ_0 is a constant, freely specifiable, while the remaining variables in this expansion are functions of (t,x,y). By knowing ξ, a_4, ϕ_2, f_{x2}, f_{y2}, b_{14}, b_{24} and g_4 all asymptotic series are determined. Furthermore, these quantities are all we need to determine the boundary

expectation values. They are not fully independent, bounded to fulfill,

$$\partial_t a_4 = -\frac{4}{3}\left(\partial_x f_{x2} + \partial_y f_{y2} + \phi_0 \partial_t \phi_2\right), \tag{2.14a}$$

$$\partial_t f_{x2} = -\frac{1}{4}\partial_x a_4 - \partial_x b_{14} - \partial_x b_{24} + \partial_y g_4 + \frac{1}{3}\phi_0 \partial_x \phi_2, \tag{2.14b}$$

$$\partial_t f_{y2} = -\frac{1}{4}\partial_y a_4 + \partial_y b_{14} - \partial_y b_{24} + \partial_x g_4 + \frac{1}{3}\phi_0 \partial_y \phi_2, \tag{2.14c}$$

which is dual to the stress energy conservation on the boundary theory.

2.2.2 Redefinitions and boundary conditions

As advanced before, it is useful to redefine variables. We will split our holographic numerical grid into two kind of grids: inner and outer. Inner means to close to the boundary, where some functions diverge or vanish and it is good to look at the asymptotic behavior of the functions to create redefine variables $g1$ that will remain finite. For the outer grid functions evaluate to reasonable values, so minimal redefinitions useful to keep track of the AH are needed and will be assigned the $g2$ subscript.

The redefinitions are,

$$\begin{aligned}
A(t,u,x,y) &= \frac{1}{u^2} + \frac{2}{u}\xi(t,x,y) + \xi^2(t,x,y) - 2\partial_t \xi(t,x,y) - \frac{2\phi_0^2}{3} + u^2 A_{g1}(t,u,x,y) \\
&= -2\partial_t \xi(t,x,y) + A_{g2}(t,u,x,y) \\
B_1(t,u,x,y) &= u^4 B_{1g1}(t,u,x,y) \\
&= B_{1g2}(t,u,x,y), \\
B_2(t,u,x,y) &= u^4 B_{2g1}(t,u,x,y) \\
&= B_{2g2}(t,u,x,y), \\
G(t,u,x,y) &= u^4 G_{g1}(t,u,x,y) \\
&= G_{g2}(t,u,x,y), \\
S(t,u,x,y) &= \frac{1}{u} + \xi(t,x,y) - \frac{\phi_0^2}{3}u + \frac{1}{3}\xi\phi_0^2 u^2 + u^3 S_{g1}(t,u,x,y) \\
&= S_{g2}(t,u,x,y), \\
F_x(t,u,x,y) &= \partial_x \xi(t,x,y) + u^2 F_{xg1}(t,u,x,y) \\
&= \partial_x \xi(t,x,y) + F_{xg2}(t,u,x,y), \\
F_y(t,u,x,y) &= \partial_y \xi(t,x,y) + u^2 F_{yg1}(t,u,x,y) \\
&= \partial_y \xi(t,x,y) + F_{yg2}(t,u,x,y), \\
\phi(t,u,x,y) &= \phi_0 u - \xi(t,x,y)\phi_0 u^2 + u^3 \phi_0^3 \phi_{g1}(t,u,x,y) \\
&= \phi_{g2}(t,u,x,y), \\
\dot{B}_1(t,u,x,y) &= u^3 \dot{B}_{1g1}(t,u,x,y) \\
&= \dot{B}_{1g2}(t,u,x,y),
\end{aligned}$$

$$
\begin{aligned}
\dot{B}_2(t,u,x,y) &= u^3 \dot{B}_{2g1}(t,u,x,y) \\
&= \dot{B}_{2g2}(t,u,x,y), \\
\dot{G}(t,u,x,y) &= u^3 \dot{G}_{g1}(t,u,x,y) \\
&= \dot{G}_{g2}(t,u,x,y), \\
\dot{S}(t,u,x,y) &= \frac{1}{2u^2} + \frac{\xi(t,x,y)}{u} + \frac{\xi^2(t,x,y)}{2} - \frac{\phi_0^2}{6} + u^2 \dot{S}_{g1}(t,u,x,y) \\
&= \dot{S}_{g2}(t,u,x,y), \\
\dot{\phi}(t,u,x,y) &= -\frac{\phi_0}{2} + u^2 \phi_0^3 \dot{\phi}_{g1}(t,u,x,y) \\
&= \dot{\phi}_{g2}(t,u,x,y).
\end{aligned}
$$

The boundary conditions for the inner grid become,

$$S_{g1}|_{u=0} = \frac{1}{54}\left(-18\xi^2\phi_0^2 + \phi_0^4 - 18\phi_0\phi_2\right), \tag{2.15a}$$

$$\partial_u S_{g1}|_{u=0} = \frac{\phi_0}{90}\left(30\xi^3\phi_0 - 5\xi\phi_0^3 + 90\xi\phi_2 - 24\partial_t\phi_2\right), \tag{2.15b}$$

$$F_{xg1}|_{u=0} = f_{x2}, \tag{2.15c}$$

$$\partial_u F_{xg1}|_{u=0} = -\frac{2}{15}\left(15\xi f_{x2} + 6\partial_x b_{14} + 6\partial_x b_{24} - \partial_y g_4 - 2\phi_0\partial_x\phi_2\right), \tag{2.15d}$$

$$F_{yg1}|_{u=0} = f_{y2}, \tag{2.15e}$$

$$\partial_u F_{yg1}|_{u=0} = -\frac{2}{15}\left(15\xi f_{y2} + 6\partial_y b_{14} + 6\partial_y b_{24} - \partial_x g_4 - 2\phi_0\partial_y\phi_2\right), \tag{2.15f}$$

$$\dot{S}_{g1}|_{u=0} = \frac{1}{36}\left(10a_4 - 5\phi_0^4 + 18\phi_0\phi_2\right), \tag{2.15g}$$

$$\dot{B}_{1g1}|_{u=0} = -2b_{14}, \tag{2.15h}$$

$$\dot{B}_{2g1}|_{u=0} = -2b_{24}, \tag{2.15i}$$

$$\dot{G}_{g1}|_{u=0} = -2g_4, \tag{2.15j}$$

$$\dot{\phi}_{g1}|_{u=0} = \frac{1}{3} - \frac{3\phi_2}{2\phi_0^3}, \tag{2.15k}$$

$$A_{g1}|_{u=0} = a_4, \tag{2.15l}$$

$$\partial_u A_{g1}|_{u=0} = -\frac{2}{3}\left(3\xi a_4 + \partial_x f_{x2} + \partial_y f_{y2} + \phi_0\partial_t\phi_2\right). \tag{2.15m}$$

which are obtained upon identification of the redefined variables with the expansions in (2.13). For the outer grid we simply impose continuity and differentiability at the boundary between inner and outer grids.

2.2.3 Fixing the location of the AH

So far we have not mentioned what criteria we want to follow to fix the free parameter $\xi(t,x,y)$. We will demand that the AH lies, at all times, at a constant radial coordinate $u = u_{AH}$, making everything very comfortable. How do we do this? We could very well impose, at each time

step, that the outgoing congruence of light rays has vanishing expansion, θ_l (see Appendix B for information about the AH finder), and then switch to coordinates in which $u = u_{AH}$, from where $\xi(t, x, y)$ would get determined. This is not efficient. It is better to do what was described for the initial time and then impose an evolution equation for $\xi(t, x, y)$ that ensures that the AH will remain at $u = u_{AH}$ in the next time step. We achieve it by imposing the diffusion equation,

$$\partial_t \Theta + \kappa \Theta = 0 \tag{2.16}$$

for the expansion of null rays for the hypersurface $u = u_{AH}$, $\Theta = \theta_l|_{u_{AH}=const}$. The explicit expression can be found in Appendix B. The free parameter κ that plays the role of the diffusion constant. (2.16) has the virtue that $\Theta = 0$ is a stable fixed point. If we start with $\Theta = 0$ at the specified $u = u_{AH}$, then (2.16) keeps the AH location where it is. If for any reason, the AH location changes, the equation will push it back to $u = u_{AH}$ as time progresses.

An evolution equation for ξ is obtained from (2.16) by expanding (2.16) and using (B.6) together with the equations of motion for both $\ddot{S}$ and $\dot{F}_{x,y}$. Then we substitute all the variables by their outer grid redefinitions, $g2$, and evaluate them at constant $u = u_{AH}$.The end point is a Partial Differential Equation (PDE) of the type,

$$\left(\mathcal{A}^{(\xi)}_{xx}\partial_x^2 + \mathcal{A}^{(\xi)}_{xy}\partial_x\partial_y + \mathcal{A}^{(\xi)}_{yy}\partial_y^2 + \mathcal{B}^{(\xi)}_{x}\partial_x + \mathcal{B}^{(\xi)}_{y}\partial_y + \mathcal{C}^{(\xi)}\right)\partial_t\xi(t, x, y) = -\mathcal{S}^{(\xi)}\,, \tag{2.17}$$

whose solution allow us to evolve ξ to the next time step ensuring that the AH is being pushed to the location we specified.

2.2.4 Evolution procedure

The procedure in which we can perform the time evolution is quite straight forward.

We start with some initial bulk data, consisting of B_1, B_2, G and ϕ for all (u, x, y) and some $t = t_0$. No constraint is needed, only that the asymptotic expansion of these functions is compatible with AdS, i.e. with (2.13). At the boundary we need to specify the functions a_4, f_{x2}, f_{y2} and some $\xi(t_0, x, y)$.

With this we can solve the nested scheme to obtain all the bulk variables, and with it find the location of the AH. We update ξ to the value for which the AH lies at the specified $u = u_{AH}$.

We solve again the nested scheme and use (2.11) to obtain the time derivative bulk functions. We additionally solve (2.14) and (2.17) to get the time derivative of the boundary functions.

We evolve the functions needed as initial data to the next time step t_1 and repeat the whole process to move forward in time. The only exception is that we do not need to locate the AH again.

2.2.5 Boundary one point functions

The gauge theory expectation values can be obtained from the asymptotic behaviour of the bulk variables in a way similar to [38]. The result is:

$$\begin{aligned}
\mathcal{E} = \tfrac{\kappa_5^2}{2\ell^3}\langle T^{tt}\rangle &= -\frac{3}{4}a_4 - \phi_0\phi_2 + \left(\frac{7}{36} - \lambda_4\right)\phi_0^4, \\
\mathcal{P}_x = \tfrac{\kappa_5^2}{2\ell^3}\langle T^{xx}\rangle &= -\frac{a_4}{4} - b_{14} - b_{24} + \frac{\phi_0\phi_2}{3} + \left(\frac{-5}{108} + \lambda_4\right)\phi_0^4, \\
\mathcal{P}_{xy} = \tfrac{\kappa_5^2}{2\ell^3}\langle T^{xy}\rangle &= -g_4, \\
\mathcal{P}_y = \tfrac{\kappa_5^2}{2\ell^3}\langle T^{yy}\rangle &= -\frac{a_4}{4} + b_{14} - b_{24} + \frac{\phi_0\phi_2}{3} + \left(\frac{-5}{108} + \lambda_4\right)\phi_0^4, \\
\mathcal{P}_z = \tfrac{\kappa_5^2}{2\ell^3}\langle T^{zz}\rangle &= -\frac{a_4}{4} + 2b_{24} + \frac{\phi_0\phi_2}{3} + \left(\frac{-5}{108} + \lambda_4\right)\phi_0^4, \\
\mathcal{J}_x = -\tfrac{\kappa_5^2}{2\ell^3}\langle T^{tx}\rangle &= f_{x2}, \\
\mathcal{J}_y = -\tfrac{\kappa_5^2}{2\ell^3}\langle T^{ty}\rangle &= f_{y2}, \\
\mathcal{V} = \tfrac{\kappa_5^2}{2\ell^3}\langle \mathcal{O}_\phi\rangle &= -2\phi_2 + \left(\frac{1}{3} - 4\lambda_4\right)\phi_0^3.
\end{aligned} \tag{2.18}$$

For a $SU(N_c)$ gauge theory the prefactor $\kappa_5^2/2\ell^3$ typically scales as N_c^{-2}, whereas the stress tensor scales as N_c^2. The rescaled quantities are therefore finite in the large-N_c limit. The stress tensor and the expectation of the scalar operator are related through the Ward identity

$$\langle T^\mu_\mu\rangle = -\Lambda\langle\mathcal{O}\rangle, \tag{2.19}$$

which can be seen as a measure of the magnitude of conformal symmetry breaking.

2.3 Numerical implementation

In this section we will briefly summarize the numerical implementation that allows for solving the time evolution problem. The goal is not to give a very precise picture of the numerics, but to provide with a good enough conceptual picture. For more details the reader is asked to check the detailed information we offer at [79].

Jecco is a numerical time evolution code writen in Julia from scratch. Julia is a fairly new programming language that looks promising given its good performance while being intuitive to code in. Our code is divided into two main parts. On the one hand, we have all the model independent infrastructure, consisting of modules that build the spatial numerical grid, the corresponding derivative operator matrices, the input/output routines etc. On the other hand we have all the model dependent modules. These include the specific equations to use, the scalar potential, the initial data routines, the AH finder, the specific variables to be considered, etc. As a result it is very simple to change among theories by implementing small changes to the code.

2.3.1 Radial ODEs

In order to solve the nested scheme we start by imposing periodic boundary conditions on x and y, a.k.a. our boundary a torus. We discretize our three dynamical spatial directions distinguishing between the holographic u grid and the gauge ones x and y.

We will discretize the latter by using a uniform grid, where derivatives are computed using finite difference methods, while for the holographic direction we will employ a *Lobatto-Chebyshev* grid. The *Lobatto-Chebyshev* is a non-uniform grid where points are mapped from a uniform grid through

$$u_i = \frac{u_{max}+u_{min}}{2} - \frac{u_{max}-u_{min}}{2}\cos\left(\frac{\pi i}{N_u}\right) \qquad (i=1,\ldots,N_u). \tag{2.20}$$

The resulting grid is one in which a big portion of the points are located near the boundaries and convergence is known to be very good. Derivative matrices are computed by approximating the functions in a basis of Chebyshev polynomials.

Once the grids are created, we can transform the ODEs into matrix equations by replacing the functions of u by an array of points where the entries correspond to the value of the functions at the grid points. We get an equation per boundary grid point (x,y). Therefore, given a grid of $N_u \times N_x \times N_y$ each ODE transforms into $N_x N_y$ matrix equations of dimension $N_u \times N_u$. In order to get the matrix we simply substitute the differential operators in (2.12) by their matrix counterparts.

For the case of the PDE, the idea is almost identical, we just need to be a bit mroe careful. Upon discretization, a function of (x,y) became a matrix of dimensions $N_x \times N_y$. To convert this matrix into a variable of a PDE, we flatten the matrix into an array as follows,

$$\mathcal{A}_{vec} = \begin{pmatrix} \mathcal{A}_{1,1} \\ \mathcal{A}_{2,1} \\ . \\ . \\ . \\ \mathcal{A}_{N_x,1} \\ \mathcal{A}_{1,2} \\ . \\ . \\ . \\ \mathcal{A}_{Nx,Ny} \end{pmatrix}, \tag{2.21}$$

and the appropriate derivative operators are then constructed by taking Kronecker products of the derivative operators that act in each of the grids x or y separately,

$$\begin{aligned} \hat{\mathcal{D}}_x &= \mathbb{I}_{N_y\times N_y}\otimes\mathcal{D}_x, & \hat{\mathcal{D}}_y &= \mathcal{D}_y\otimes\mathbb{I}_{N_x\times N_x}, \\ \hat{\mathcal{D}}_{xx} &= \mathbb{I}_{N_y\times N_y}\otimes\mathcal{D}_{xx}, & \hat{\mathcal{D}}_{yy} &= \mathcal{D}_{yy}\otimes\mathbb{I}_{N_x\times N_x}, \end{aligned} \tag{2.22}$$

where $\hat{\mathcal{D}}_{xy} = \hat{\mathcal{D}}_x\hat{\mathcal{D}}_y$. The result is that (2.17) becomes another matrix equation, this time of dimension $N_xN_y \times N_xN_y$. Due to the big amount of vanishing entries on the derivative operators it is useful to use the Julia package `SparseArrays`, where all zero entries will not be stored and a considerable amount of memory can be saved.

Once we have all relevant equations in matrix form, we can solve them fast by direct inversion of matrices. `Jecco` does this by LU decomposing the matrix operator and performing a left division operation. The fact that the nested scheme has to be solved for each (x,y) grid point independently prompts parallelization.

2.3.2 Time evolution

Performing time evolution is simple. Our problem is of the kind,

$$\frac{\partial v}{\partial t} = f(v,x,y), \tag{2.23}$$

where $f(v, x, y)$ is a very complicated function, consisting in solving all the nested scheme in the way described earlier given the initial bulk and boundary data at t. Problems like the current one can be solved by using a time evolution method like Runge-Kutta. Specifically we use the Juliaa routine `ODEProblem` from DifferentialEquations.jl package. The only thing that we need to do is to cast all of our variables to be evolved in a single vector v.

Only one additional issue remains, high order modes of too short wavelength to be properly described by our grid spacing. Once again we discriminate among grids. For the finite difference grids we make use of Kreiss-Oliger dissipation [86], while for the spectral grid we directly damp high frequency modes by multiplying their Fourier coefficients by an exponential factor that decays with the momenta k.

2.4 Testing the code

Testing an implementation is crucial for obvious reasons. Of course most of the applications of the code will involve non-linear physics that is very hard to check explicitly. However, we can at least check the code where there is a benchmark coming from other methods, either analytical or numerical. The tests performed are collected in Appendix A of [79], and they will be briefly summarized here.

We started by studying equilibrium, uniform black branes. The easiest setup, in which analytic expressions are obtainable is the conformal case. For that we simply turn off our scalar source $\phi_0 = 0$ and the equations take care of the rest. Moreover we added a small sinusoidal perturbation to the fall-off a_4 and let the system relax back to the uniform black brane. The results matched the analytic expressions and convergence with increasing number of points along the radial direction u was as expected.

Next step was to jump into the non-conformal tests. For that we can no longer rely on analytic expressions as reference. We obtained the thermodynamic properties of equilibrium uniform black branes for the theory with $\lambda_4 = -0.25$ and $\lambda_6 = 0.1$, for which there is a first order thermal phase transition. We initialized the code with a configuration close to equilibrium, let it relax, and measure the properties of the black brane at late times. We then compared these results with the ones obtained by numerically integrating the ODEs that arise when assuming static, black brane ansatz. The results were good once again.

For out of equilibrium tests we proposed two complementary ones: Quasi Normal Modes (QNM) and Hydrodynamics.

The QNM test was engineered by initializing the code with all equilibrium properties but the bulk scalar field profile and non vanishing, constant B_1 and B_2. The deviation from equilibrium is independent of x and y. As we will deal with the relaxation of a perturbation of momenta $k = 0$ it must be a QNM. We let the system relax and extracted the frequency ω of the perturbation, which evolves like $e^{i\omega t}$. We then compared the measured valued with the one that is obtained using the `QNMspectral` Mathematica package [87] for the late time geometry. The results where compatible.

Finally, we performed a test using first order hydrodynamics. Knowing the dual of a theory we can compute, independently of `Jecco`, the first order transport coefficients (viscosities) easily. We initialize `Jecco` in an equilibrium configuration on top of which we add a long wave length perturbation, $k/T \ll 1$. This is the regime in which hydrodynamics should be applicable. We let the system relax back to equilibrium and, by reading off the boundary stress tensor as a function of (t, x, y), we checked that the evolution is compatible to a great precision with the transport coefficients we obtained by other means.

All of this tests show the robustness of the code and that it is ready to be used.

Chapter 3

Crossing a Large-N Phase Transition at finite volume

Phase coexistence is an essential feature of systems with a first-order phase transition. Consider for example Fig. 3.1. This shows the energy density as a function of the temperature, in the infinite-volume limit, for the four-dimensional gauge theory that we will study in this paper. The blue curve indicates homogeneous states with energy density $\overline{\mathcal{E}}$, which we measure in units of the microscopic scale in the gauge theory Λ. In the canonical ensemble there is a first-order phase transition at a critical temperature T_c indicated by the dashed, vertical line. The thermodynamically preferred, lowest-free energy states at $T > T_c$ lie on the upper branch and have energies above that of point D. Similarly, at $T < T_c$ the preferred states are on the lower branch with energies below that of point E. States between points A and D, and between B and E, are locally but not globally thermodynamically stable. Finally, states between points A and B are locally thermodynamically unstable. The region between A and B is known as the "spinodal region".

In the canonical ensemble, setting $T = T_c$ does not select a unique state. For this reason, it is convenient to work in the microcanonical ensemble, in which the control parameter is the energy instead of the temperature. In this case the preferred, maximum-entropy configuration for energy densities between points D and E is well understood in the infinite-volume limit: it is a phase-separated state in which part of the volume is in the phase associated to point D and the other part is in the phase associated to point E (see Sec. 3.1.4). The fraction of volume occupied by each phase is determined by the average energy density $\overline{\mathcal{E}}$, which lies between D and E. The two phases are separated by a universal interface, i.e. by an interface whose spatial profile is independent of the way in which the phase-separated configuration is reached. Since the temperature is constant and equal to T_c across the entire volume, these states lie on the red, vertical segment DE in Fig. 3.1. We conclude that, at infinite volume in the microcanonical ensemble, the sequence of preferred states as the energy density decreases is that indicated by the black arrows in Fig. 3.1.

The thermodynamic statements above have dynamical counterparts. Since the total energy is conserved under time evolution, it is again convenient to think of the system in the microcanonical ensemble. Imagine preparing the system in a homogeneous state. If the energy density lies above point D or below point E then this state is dynamically stable against small or large perturbations. If instead the energy density is between points A and D or between B and E then we expect the system to be dynamically stable against small perturbations but not against large ones. This means that, if subjected to large enough a perturbation, the system will dynamically evolve to a phase-separated configuration. The average energy density in this inhomogeneous configuration will be the same as in the initial, homogenous state, but the entropy will be higher. Finally, if the initial energy density is between A and B then the state is dynamically unstable even against small perturbations. This instability, known as "spinodal instability", implies that

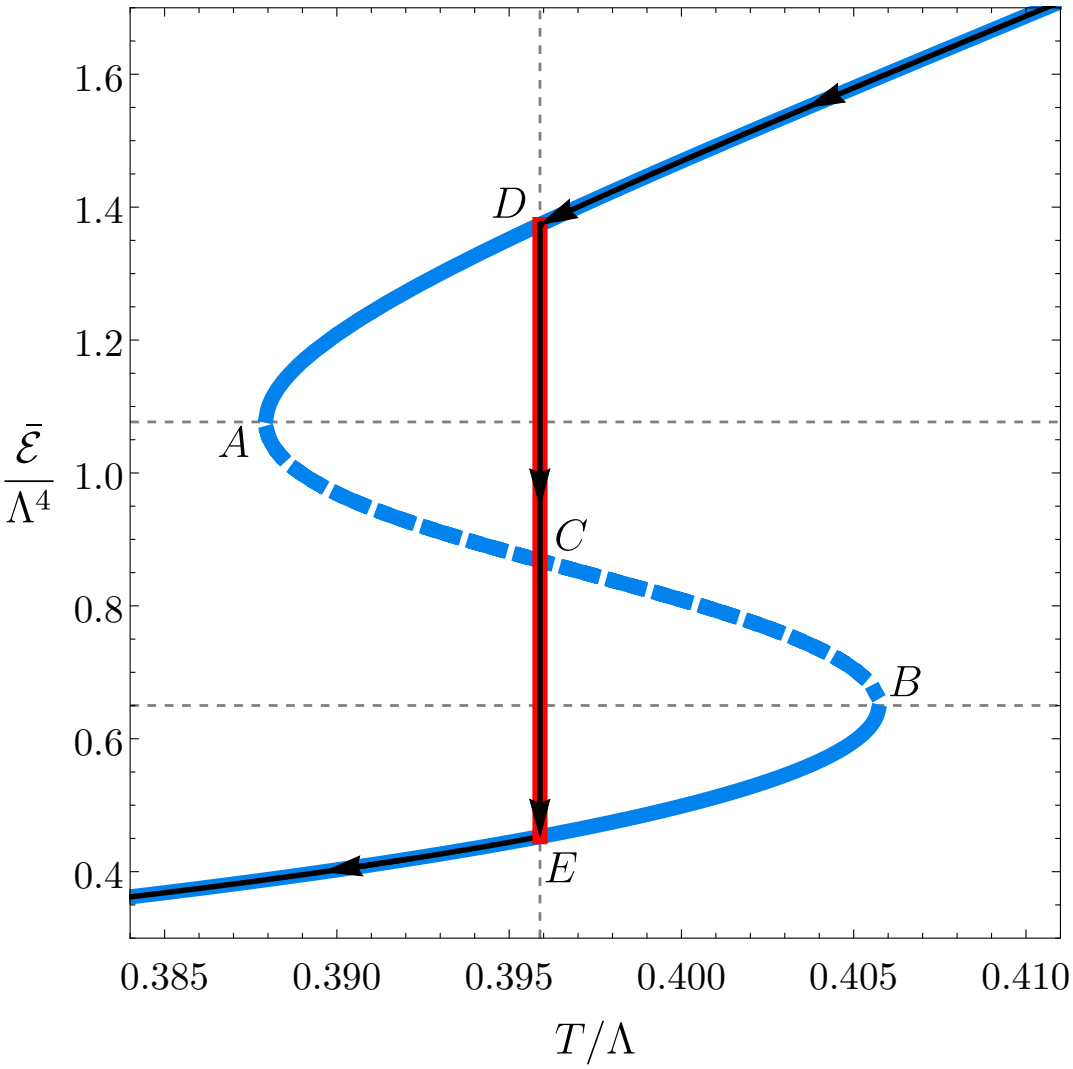

Figure 3.1: Phase diagram in the infinite-volume limit. The dashed, vertical line indicates the critical temperature $T = T_c$. The blue curve corresponds to homogeneous states. The red line corresponds to inhomogeneous, phase-separated states. Solid segments indicate locally dynamically stable states; dashed segments indicate unstable ones. The black curves with arrows indicate the sequence of maximum-entropy states as the average energy density $\bar{\mathcal{E}}$ decreases. In the canonical ensemble there is one first-order phase transition at which the system jumps betweens points D and E. In the microcanonical ensemble there are two second-order phase transitions at points D and E between homogeneous and inhomogeneous states.

the slightest perturbation will trigger an evolution towards a phase-separated configuration of equal average energy but higher entropy.

If the system of interest is an interacting, four-dimensional quantum field theory then following the real-time evolution from an unstable homogeneous state to a phase-separated configuration can be extremely challenging with conventional methods. For this reason, in [61, 63] holography was used to study this evolution in the case of a four-dimensional gauge theory with a gravity dual (see also [88, 89] for a case in which the gauge theory is three-dimensional). In order to regularise the problem, Refs. [61, 63] considered the gauge theory formulated on $\mathbb{R}^{1,2} \times S^1$ with periodic boundary conditions on a circle of size L. For simplicity, translational invariance along the non-compact spatial directions was imposed, thus effectively reducing the dynamics to a 1+1 dimensional problem along time and the compact direction. The compactness of the circle makes the spectrum of perturbations discrete and simplifies the technical treatment of the problem. Ref. [61] provided a first example of the time evolution from a homogeneous state to an inhomogeneous one. A systematic study was then performed in [63]. In this reference the focus was on the infinite-volume limit, understood as the limit in which L is much larger than any other scale in the problem such as the microscopic gauge theory scale Λ, the size of the interface, etc. It was shown that, if slightly perturbed, an initial homogeneous state with energy density between A and B always evolves towards a phase-separated configuration, and that the latter is dynamically stable.

In addition to its implications for gauge theory dynamics, the spinodal instability of states between A and B is interesting also on the gravity side, where it implies that the corresponding black branes are afflicted by a long-wavelength dynamical instability. Although this is similar [90–92] to the Gregory-Laflamme (GL) instability of black strings in spacetimes with vanishing cosmological constant [93], there is an important difference: In the GL case all strings below a certain mass density are unstable, whereas in our case only states between points A and B are unstable. Having clarified this, since the term "GL-instability" is familiar within part of the gravitational community, in this paper we will use the terms "spinodal instability" and "GL-instability" interchangeably to refer to the dynamical instability between points A and B.

The purpose of this paper is to extend the analysis of the equilibrium states summarised in Fig. 3.1, as well as the systematic analysis of their dynamical stability properties of [63], to the case of finite volume. In particular, we would like to: (i) classify all possible states, homogeneous or inhomogeneous, available to the system; (ii) determine which ones are thermodynamically preferred; (iii) establish the local dynamical stability or instability of each state; and (iv) investigate the time evolution from unstable states to stable ones. For this purpose we will place the system in a box, impose translational invariance along two of its directions and vary the size L of the third direction. We will then see that the results depend on the value of L compared to a hierarchy of length scales

$$L_K < L_{\Sigma_1} < L_{\Sigma_2} \,. \tag{3.1}$$

These three scales are an intrinsic property of the system at finite volume that cannot be determined through an infinite-volume analysis. Depending on the ratio of L to these scales we will uncover: (i) a large configuration space of inhomogeneous states, both stable and unstable; (ii) a rich set of first- and second-order thermodynamic phase transitions between them; and (iii) the possible time evolutions from dynamically unstable to dynamically stable states. Note that the existence of phase transitions is not in contradiction with the finite volume of the gauge theory because we work in the planar limit, $N_c \to \infty$, which effectively acts as a thermodynamic limit.

3.1 Nonconformal lumpy branes: nonlinear static solutions

3.1.1 Setup of the physical problem and general properties of the system

During the following section let us recover ℓ in the expressions. We will choose the values $\lambda_6 = 0.1$ and $\lambda_4 = -1/4$ for the potential 2.3. The reason for this choice is that the resulting model exhibits a first order thermal phase transition where all quantities are order 1 in units of Λ, in contrast to the large hierarchies that where found when studying models with vanishing $\lambda_6 = 0$, see [36, 61, 63]. For this specific choice of parameters, the potential (2.3) and the superpotential (2.2) take the form shown in Fig. 3.2. In this case both functions have a minimum

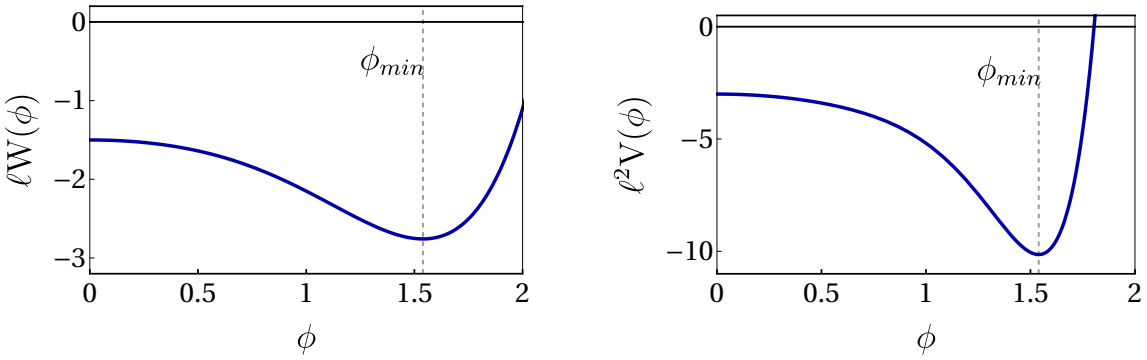

Figure 3.2: Superpotential (left) and potential (right) of our model.

at $\phi_{\rm min} \approx 1.54$, corresponding to an infrared (IR) fixed point of the gauge theory. The potential has an additional maximum at $\phi_{\rm max} \approx 3.65$ and diverges negatively, i.e. $V(\phi) \to -\infty$, as $\phi \to +\infty$. However, values of ϕ larger than ϕ_{min} will play no role in our analysis.

We are interested in finding static, "lumpy" black brane solutions of (2.1) that can break translational invariance along a spatial gauge theory direction $\tilde{x}$ while being isometric along the remaining two spatial directions x_2 and x_3 directions. The most general ansatz compatible with such symmetries is

$$\begin{aligned} \mathrm{d}s^2 =& -Q_1(\tilde{x},Z)\mathrm{d}t^2 + Q_2(\tilde{x},Z)\mathrm{d}Z^2 + 2Q_3(\tilde{x},Z)\mathrm{d}\tilde{x}\mathrm{d}Z + Q_4(\tilde{x},Z)\mathrm{d}\tilde{x}^2 \\ &+ Q_5(\tilde{x},Z)\mathrm{d}x_2^2 + Q_6(\tilde{x},Z)\mathrm{d}x_3^2 + 2\,Q_7(\tilde{x},Z)\mathrm{d}x_2\mathrm{d}x_3\,, \end{aligned} \tag{3.2a}$$

$$\phi = Q_8(\tilde{x},Z)\,, \tag{3.2b}$$

where Z is the holographic coordinate. We shall be interested in solutions which are isotropic in x_2 and x_3, so we take $Q_5 = Q_6$ and $Q_7 = 0$. To fix the gauge completely we demand $Q_3 = 0$,

and

$$Q_1(\tilde{x},z) = \frac{\ell^2 q_1(\tilde{x},Z)^2}{Z^2}\left(1-\frac{Z^4}{Z_+^4}\right), \tag{3.3a}$$

$$Q_2(\tilde{x},Y) = \frac{\ell^2}{Z^2\, q_2(\tilde{x},Z)}\left(1-\frac{Z^4}{Z_+^4}\right)^{-1}, \tag{3.3b}$$

$$Q_4(\tilde{x},Y) = \frac{\ell^2}{Z^2} q_2(\tilde{x},Z)\, q_3(\tilde{x},Z), \tag{3.3c}$$

$$Q_6(\tilde{x},Y) = \frac{\ell^2}{Z^2\, q_1(\tilde{x},Z)}, \tag{3.3d}$$

$$Q_8(\tilde{x},Y) = \frac{Z}{\ell}\, q_4(\tilde{x},Z), \tag{3.3e}$$

together with the condition

$$q_1(\tilde{x},Z_+)^2\, q_2(\tilde{x},Z_+) = \alpha_\Lambda, \tag{3.3f}$$

where $\alpha_\Lambda > 0$ is a positive constant whose physical significance will be discussed later; see (3.23). The coordinate $\tilde{x}$ is periodic with period L, and we take $\tilde{x} \in [-L/2, L/2]$ and $Z \in [0, Z_+]$. The translationally invariant directions $x_{2,3}$ have arbitrary periods L_2 and L_3. These will play essentially no role in our discussion, since only densities per unit area in the 23-plane will matter. Thus we will take them to be the same, i.e. $L_2 = L_3 \equiv \mathcal{L}$ and $x_{2,3} \in [0, \mathcal{L}]$.

We shall also be interested in solutions which are $\mathbb{Z}_2$-symmetric around $\tilde{x} = 0$, which means that we can restrict our domain of integration to $\tilde{x} \in [0, L/2]$, at the expense of imposing $\partial_{\tilde{x}} q_j|_{\tilde{x}=0} = 0$, for $j = 1, 2, 3, 4$. In order to vary L in a numerically efficient manner, we further change to a new coordinate

$$x = \frac{2\tilde{x}}{L}, \tag{3.4}$$

and take all functions to take values in $x \in [0, 1]$. Note that our ansatz (3.5) together with our periodicity conditions further imply that $\partial_x q_j|_{x=1} = 0$ $(j = 1, 2, 3, 4)$.

Putting everything together brings (3.2) to the following simplified form

$$\begin{aligned} \mathrm{d}s^2 &= \frac{\ell^2}{Z^2}\Bigg[-q_1(x,Z)^2\left(1-\frac{Z^4}{Z_+^4}\right)\mathrm{d}t^2 + \frac{1}{q_2(x,Z)}\left(1-\frac{Z^4}{Z_+^4}\right)^{-1}\mathrm{d}Z^2 \\ &\qquad + \left(\frac{L}{2}\right)^2 q_2(x,Z)\, q_3(x,Z)\mathrm{d}x^2 + \frac{1}{q_1(x,Z)}\left(\mathrm{d}x_2^2 + \mathrm{d}x_3^2\right)\Bigg], \\ \phi &= \frac{Z}{\ell}\, q_4(x,Z). \end{aligned} \tag{3.5}$$

Our gauge choice is such that the determinant of the metric along the Killing directions (t, x_2, x_3) is fixed and defines the radial (holographic) direction Z. The conformal boundary is located at $Z = 0$ where we demand

$$q_1 = q_2 = q_3 = 1. \tag{3.6}$$

In this sense we can denote this gauge choice as the "double Wick rotation Schwarzschild gauge" and, as far as we are aware, this is the first time it is introduced. The advantage of this gauge choice (at least in the present system) is that the fields q_j $(j = 1, 2, 3, 4)$ have an asymptotic power law decay without irrational powers (nor logarithmic terms; more below), unlike e.g. the DeTurck gauge.[1]

[1] This feature is particularly important when finding q_j numerically using pseudospectral collocation methods

Our gauge choice — condition (3.3f) — reveals that $Z = Z_+$ is a null hypersurface, where the norm of the Killing vector field $\partial/\partial t$ vanishes.[2] Thus, $Z = Z_+$ is a Killing horizon, and α_Λ controls its associated surface gravity or, equivalently, temperature. In fact, we find

$$T = \frac{\sqrt{\alpha_\Lambda}}{\pi}\frac{1}{Z_+}\,. \tag{3.7}$$

Our solutions have two important scaling symmetries. The first one is

$$\{t, Z, x_i\} \to \{\lambda_1 t, \lambda_1 Z, \lambda_1 x_i\}, \quad \{q_{1,2,3}, q_4\} \to \{q_{1,2,3}, \lambda_1^{-1} q_4\}, \quad \{\ell, Z_+\} \to \{\lambda_1 \ell, \lambda_1 Z_+\} \tag{3.8}$$

where $x_i = \{x, x_2, x_3\}$. This leaves the equations of motion and scalar field invariant and rescales the line element as $\mathrm{d}s^2 \to \lambda_1^2\,\mathrm{d}s^2$, namely $g_{\mu\nu} \to \lambda_1^2\, g_{\mu\nu}$. It follows that we can use this scaling symmetry to fix the AdS radius to $\ell \equiv 1$. In other words, under the scaling $g_{\mu\nu} \to \lambda_1^2\, g_{\mu\nu}$, the affine connection $\Gamma^\gamma{}_{\mu\nu}$, and the Riemann ($R^\alpha{}_{\beta\mu\nu}$) and Ricci ($R_{\mu\nu}$) tensors are left invariant. It follows from the trace-reversed equations of motion that the AdS radius must scale as $\ell \to \lambda_1 \ell$ and we can use this scaling symmetry to set $\ell \equiv 1$.

The second scaling symmetry (known as a dilatation transformation, one of the conformal transformations) is

$$\{t, Z, x_i\} \to \{\lambda_2 t, \lambda_2 Z, \lambda_2 x_i\}, \quad \{q_{1,2,3}, q_4\} \to \{q_{1,2,3}, \lambda_2^{-1} q_4\}, \quad \{\ell, Z_+\} \to \{\ell, \lambda_2 Z_+\}\,. \tag{3.9}$$

This leaves the metric, scalar field and equations of motion invariant. It follows that we can use this symmetry to set the horizon radius at $Z = Z_+ \equiv 1$ or, equivalently, the temperature (3.7) to

$$T = \frac{\sqrt{\alpha_\Lambda}}{\pi}\,. \tag{3.10}$$

We will see below that this is just a convenient choice of units with no effect on the physics.

Let us turn now our attention to the scalar field. It follows from (2.6) that the scalar field has a mass $\mu^2 = V''(0) = -3/\ell^2$. According to AdS/CFT, the conformal dimension of the dual operator is simply given by

$$\Delta_\pm = 2 \pm \sqrt{4 + \mu^2 \ell^2} \quad \Leftrightarrow \quad \Delta_- = 1 \text{ or } \Delta_+ = 3, \tag{3.11}$$

and these give the two independent asymptotic decays $Z^{\Delta_\pm}$ of the scalar field. Actually, since $\Delta_\pm$ are integers, the nonlinear equations of motion might also generate logarithmic decays of the form $\sum_{n=3} c_n Z^n \ln Z$ where the coefficients c_n depend exclusively on the amplitude of the two independent terms. When this is the case, the conserved charges depend on c_3. However, for the potential we use (only with even powers of ϕ and double Wick rotation Schwarzschild gauge choice) it turns out that logarithmic terms are not generated by the equations of motion. So, for our system, the scalar field decays asymptotically as

$$\phi\Big|_{Z\to 0} \sim \Lambda Z^{\Delta_-} + \phi_2 Z^{\Delta_+} + \cdots = Z\left(\Lambda + \phi_2 Z^2\right) + \cdots \tag{3.12}$$

where Λ and ϕ_2 are two arbitrary integration constants and $\cdots$ represent higher order powers of Z (with no logarithms) whose coefficients are fixed in terms of Λ and ϕ_2 by the equations of motion. The fact that $\Delta_- = 1$ motivates our choice of ansatz for the scalar field in (3.5).

to discretize the numerical grid, as we will do. Due to the absence of the irrational powers near the conformal boundary, the numerical scheme will exhibit exponential convergence when reading asymptotic charges. This is unlike e.g. the DeTurck gauge that has power law decays also with irrational powers and therefore does not have exponential convergence in the continuum limit [94, 95].

[2] Strictly speaking, in order to prove this we need to introduce regular coordinates at the horizon located at $Z = Z_+$. This can be achieved if we use ingoing (or outgoing) Eddington-Finkelstein coordinates of the Schwarzschild brane.

The Breitenlöhner-Freedman (BF) bound of the system is $\mu^2_{\rm BF}\ell^2 = -4$ and thus $\mu^2\ell^2 = -3$ coincides precisely with the unitarity bound $\mu^2_{\rm BF}\ell^2+1$. It follows that only the mode Z^{Δ_+} with the faster fall-off is normalizable. In the AdS/CFT correspondence, the non-normalizable mode Λ is the source of a boundary operator $\mathcal{O}_\phi$ since it determines the deformation of the boundary theory action. On the other hand, the normalizable modes ϕ_2 are identified with states of the theory with ϕ_2 being proportional to the expectation value $\langle\mathcal{O}_\phi\rangle$ of the boundary operator (in the presence of the source Λ). $\Delta_+ = 3$ is then the (mass) conformal dimension of the boundary operator $\mathcal{O}_\phi$ dual to ϕ. Under the scaling symmetries (3.8)-(3.9) the scalar source transforms as $\Lambda \to \lambda_1\lambda_2\Lambda$. As a consequence, the ratio T/Λ is left invariant by these scalings. Since the physics only depends on this ratio, setting $T = \sqrt{\alpha_\Lambda}/\pi$ as we did above is just a convenient choice of units with no effect on the physics. In general, throughout this paper we will measure all dimensionful physical quantities in units of Λ.

The undeformed boundary theory — a CFT — corresponds thus to the Dirichlet boundary condition $\Lambda = 0$, and we have a pure normalizable solution. For this reason the planar AdS_5 Schwarzschild solution (3.5) with $q_{1,2,3} = 1$, $q_4 = 0$ is often denoted as the (uniform) "conformal" brane of the theory (2.1). In contrast, if we turn-on the source the dual gauge theory is no longer conformal. In particular, there are such solutions (3.5) with $q_{1,2,3,4}(Z,x) = q_{1,2,3,4}(Z)$ (and $q_4(0) = \Lambda$) that are translationally invariant along x, x_2, x_3. These are often denoted as the "uniform nonconformal" branes of the theory. This is one family of solutions that we will construct in this manuscript. Still with $\Lambda \neq 0$, we can then have solutions that break translational invariance along x (while keeping the isometries along the other two planar directions). Our main aim is to construct these nonuniform solutions, which we denote as "lumpy nonconformal branes", and study their thermal competition with the uniform nonconformal branes in a phase diagram of static solutions of (2.1), both in the micro-canonical and canonical emsembles. Of course there are also nonconformal branes that break translation invariance along the other two directions $x_{2,3}$. These are cohomogeneity-4 solutions that we will not attempt to construct. Fortunately, the cohomogeneity-2 lumpy branes that we will find seem to already allow us to understand the key properties of the most general system.

3.1.2 Setup of the boundary-value problem

Finding the nonconformal brane solutions necessarily requires resorting to numerical methods. For that, we find it convenient to change our radial coordinate into

$$y = \frac{Z^2}{Z_+}\,, \quad \text{and define} \quad y_+ \equiv \frac{1}{Z_+}\,, \tag{3.13}$$

so that the ansatz (3.5) now reads

$$\begin{aligned} {\rm d}s^2 &= \frac{1}{y}\Bigg[-y_+^2\, q_1(x,y)^2(1-y^2){\rm d}t^2 + \frac{1}{q_2(x,y)}\frac{{\rm d}y^2}{4y(1-y^2)} \\ &\qquad + \left(\frac{L}{2}\right)^2 y_+^2\, q_2(x,y)\, q_3(x,y){\rm d}x^2 + \frac{y_+^2}{q_1(x,y)}\left({\rm d}x_2^2+{\rm d}x_3^2\right)\Bigg], \\ \phi &= \frac{\sqrt{y}}{y_+}\, q_4(x,y)\,, \end{aligned} \tag{3.14}$$

with compact coordinates $y \in [0,1]$ and $x \in [0,1]$. The horizon is located at $y = 1$ and the asymptotic boundary at $y = 0$. Note, that we used the two scaling symmetries (3.8)-(3.9) to set $\ell \equiv 1$ and $y_+ \equiv 1$.

In these conditions we now need to find the minimal set of Einstein-scalar equations — the equations of motion (EoM) — that allows us to solve for all $q_j(x,y)$ while closing the full

system of equations, $g_{\mu\nu} = T_{ab}$ and $\Box\phi = 0$, of the action (2.1). This is a nested structure of PDEs. This structure motivates also in part our original choice of gauge in the ansätze (3.5) and (3.14). For this reason, rather than presenting the final EoM, it is instructive to explain their origin and nature. Prior to any gauge choice and symmetry assumptions, the differential equations that solve (2.1) are second order for all the fields. The symmetry requirements we made fix some of these fields. Additionally, the fact that we have chosen to fix the gauge freedom of the system using the 'double Wick rotation Schwarzschild' gauge means that our system of equations should have the structure of an ADM-like system but with the spacelike coordinate x playing the role of "time". Of course, our problem is ultimately an elliptic problem. However, it is instructive to analyse our EoM adopting the above "time-dependent" viewpoint. In doing so, one expects that the equations of motion take a nested structure of PDEs that include a subset of "evolution" equations (to be understood as evolution in the x-direction) but also a subset of non-dynamical ("slicing" and "constraint") equations. We now describe in detail this nested structure.

We have a total of five equations of motion. Two of these EoM are dynamical *evolution* equations for q_1 and q_4. The main building block of these equations is the Laplacian operator $\partial_x^2 + \partial_y^2$ (acting either on q_1 or q_4) that describes the spatial dynamics as the system evolves in x. With respect to the familiar ADM time evolution in the Schwarzschild gauge, this Laplacian replaces the wave operator $\partial_t^2 - \partial_y^2$. Additionally, we have two (first-order) *slicing* EoM for $\partial_y q_2$ and $\partial_y q_3$ that can be solved at each constant-x spatial slice for q_2 and q_3. Besides depending on $\partial_y q_{2,3}$ and $q_{2,3}$ — but, quite importantly, not on $\partial_x q_{2,3}$ — these equations also depend on $q_{1,4}$ (that are determined "previously" by the evolution equations) and on their first derivatives (both along x and y). This means that we can integrate the slicing equations of motion along the radial direction to find $q_{2,3}$ at a particular constant-x slice. Finally, the EoM still includes a fifth PDE that expresses $\partial_x q_2$ as a function of $(q_{1,2,3,4}, \partial_x q_{1,4}, \partial_y q_{1,4})$. Let us schematically denote it as $\mathcal{C}(x,y) = 0$. This is a *constraint* equation. To see this note that, after using the evolution and slicing EoM and their derivatives, the Bianchi identity $\nabla^\mu(R_{\mu\nu} - g_{\mu\nu}R/2) = 0$ implies the constraint evolution relation[3]

$$\partial_y\left(\sqrt{-g}\,\mathcal{C}\right) + F(x,y)\sqrt{-g}\,\mathcal{C} = 0\,, \tag{3.15}$$

where $F(x,y)$ is a function that is regular at the horizon whose further details are not relevant.[4] It follows from this constraint evolution relation that if the constraint equation is obeyed at a given y, say at the horizon $\mathcal{C}(x,y)\big|_{y=1} = 0$, then it is obeyed at any other $y \in [0,1]$. In practice, this means that we just need to impose the constraint as a *boundary condition* at $y = 1$, say. It is then preserved into the rest of the domain.

Altogether, the strategy to solve the EoM is thus the following. There are effectively four EoM, two second order PDEs for $q_{1,4}(x,y)$ and two second order PDEs for $q_{2,3}(x,y)$. We need to solve these equations for $q_{1,2,3,4}(x,y)$ as a boundary-value problem. One of the boundary conditions is imposed at the horizon and takes the form $\mathcal{C}(x,y)\big|_{y=1} = 0$, whereas the others are the physically motivated boundary conditions discussed next.

Our integration domain is a square bounded in the radial direction by $y = 0$ (the asymptotic boundary) and $y = 1$ (the horizon). Along the x-direction the boundaries are at $x = 0$ and $x = 1$. The angular coordinate x is periodic in the interval $[0,1]$. We can thus use this symmetry

[3] Note that in standard ADM *time*-evolution problems the constraint relation that must vanish involves the *time* derivative, i.e. it is schematically of the form $\partial_t\left(\sqrt{-g}\,\tilde{\mathcal{C}}\right) + \tilde{F}(t,y)\sqrt{-g}\,\tilde{\mathcal{C}} = 0$, where y is a radial coordinate. Interestingly, in our 'double Wick rotation of the ADM gauge' — where x is the evolution coordinate — it is the radial derivative ∂_y (and *not* ∂_x) that appears in the vanishing constraint relation.

[4] Let $\hat{\mathcal{C}} \equiv \sqrt{-g}\,\mathcal{C}$. Solving $\partial_y\hat{\mathcal{C}} + F(x,y)\,\hat{\mathcal{C}} = 0$ yields $\hat{\mathcal{C}}(x,y) = \hat{\mathcal{C}}(x,1)\exp\left(\int_1^y F(x,Y)dY\right)$ which converges if $F(x,y)$ is regular at the horizon $y = 1$.

to impose Neumann boundary conditions for all q_j at $x = 0$ and $x = 1$:

$$\partial_x q_j(x,y)\big|_{x=0} = 0\,, \quad \text{for } j = 1,2,3,4\,, \tag{3.16}$$
$$\partial_x q_j(x,y)\big|_{x=1} = 0\,, \quad \text{for } j = 1,2,3,4. \tag{3.17}$$

Consider now the asymptotic UV boundary at $y = 0$. The invariance of the EoM under dilatations (3.9) guarantees that asymptotically our PDEs are of the Euler type and thus $y = 0$ is a regular singular point. The order of our PDE system (two second-order and two first-order PDEs) is 6. It follows that we have a total of 6 free UV independent parameters. We have explicitly checked that, for our gauge choice and scalar potential, all our functions q_j admit a Taylor expansion in integer powers of y (in particular, without logarithmic terms) that contains precisely 6 independent parameters. In this Taylor expansion, at a certain order (as expected due to the fact that we fixed the gauge and our system is cohomogeneity-2) we need to use a differential relation that is ultimately enforced by the Bianchi identity:

$$q_2^{(1,2)}(x,0) = \frac{8}{3}\,\Lambda\, q_4^{(1,1)}(x,0). \tag{3.18}$$

The requirement that our nonconformal branes asymptote to AdS fixes two of the six UV integration constants to unity, namely $q_1(x,0)$ and $q_3(x,0)$ at the boundary (it then follows directly from the EoM that $q_2(x,0) = 1$). We complement these boundary conditions with a Dirichlet boundary condition for the scalar field function q_4 which introduces the source Λ. This will be a running parameter in our search for solutions. Altogether we thus impose the boundary conditions at the UV boundary:

$$q_j(x,y)\big|_{y=0} = 1\,, \quad \text{if } j = 1,2,3; \qquad q_4(x,y)\big|_{y=0} = \Lambda. \tag{3.19}$$

Finally, we discuss the boundary conditions imposed at the horizon, $y = 1$. It follows directly from the four equations of motion that $q_{1,2,3,4}(x,1)$ are free independent parameters and $q_{1,2,3,4}$ must obey a set of four mixed conditions that fix their first radial derivative as a function of $q_{1,2,3,4}(x,1)$ and $\partial_x q_{1,2,3,4}(x,1)$ that is not enlightening to display. When assuming a power-law Taylor expansion for

$$q_j(x,y)\big|_{y\sim 1} = \sum_{k=0} c_{j(k)}(x)(1-y)^k \tag{3.20}$$

we are already imposing boundary conditions that discard two integration constants that would describe contributions that diverge at the horizon.

Having imposed the boundary conditions, we must certify that we have a well-defined elliptic (boundary-value) problem. For that, we need to confirm that the number of free parameters at the UV boundary matches the IR number of free parameters. Recall that, before imposing boundary conditions, we have 6 integration constants at the UV and another 6 in the IR. A power-law Taylor expansion about the asymptotic boundary,

$$q_j(x,y)\big|_{y\sim 0} = \sum_{k=0} a_{j(k)}(x) y^k\,, \tag{3.21}$$

concludes that, after imposing the boundary conditions (3.19) that fix $a_{1(0)} = 1, a_{3(0)} = 1$ and $a_{4(0)} = \Lambda$ ($a_{2(0)}$ is not a free parameter since it is fixed by the equations of motion), we are left with three free UV parameters, namely $a_{1(2)}(x), a_{2(2)}(x), a_{4(1)}(x)$. Note that we will give Λ as an input parameter so the boundary-value problem will not have to determine it. As we shall find later, the energy density depends on these three parameters, whereas the expectation value of the dual operator sourced by Λ is proportional to $a_{4(1)}(x)$. On the other hand, at the horizon, after imposing the aforementioned boundary conditions that eliminate two integration constants, one finds that there are 4 free IR parameters.

So we have 3 UV free parameters but 4 IR free parameters. In order to have a well-defined boundary value problem (BVP) the number of free UV parameters must match the IR number. Note however that in our discussion of the boundary conditions we have not yet imposed the constraint equation $\mathcal{C}(x,y)=0$. As described above we just need to impose it at the horizon $y=1$, where $\mathcal{C}(x,1)=0$ simply reads

$$2q_2(x,1)\partial_x q_1(x,1)^2+q_1(x,1)\partial_x q_2(x,1)=0\,. \tag{3.22}$$

This is solved by $q_1(x,1)=\sqrt{\alpha_\Lambda}/\sqrt{q_2(x,1)}$ where α_Λ is a constant to be fixed below. It follows that, if we impose this Dirichlet condition together with the three aforementioned mixed conditions for $q_{2,3,4}$ at the horizon

$$q_1(x,y)\big|_{y=1}=\frac{\sqrt{\alpha_\Lambda}}{\sqrt{q_2(x,1)}}\,;\qquad \partial_y q_j\big|_{y=1}=\partial_y q_j\left(q_{1,2,3,4},\partial_x q_{1,2,3,4}\right)\big|_{y=1}\quad \text{if } j=2,3,4, \tag{3.23}$$

then we have just three free IR parameters, namely $q_{2,3,4}(x,1)$. We fix the value of α_Λ as follows. For a given source Λ, the lumpy nonconformal branes that we seek merge with the *uniform* nonconformal branes at the onset of the Gregory-Laflamme-type instability of the latter. We use this merger (where the fields of the two solutions must match) to fix the constant α_Λ to be the value of $q_1(y)^2q_2(y)\big|_{y=1}$ (no x-dependence) of the nonuniform solution when it merges with the uniform brane.

This discussion can be complemented as follows (which also allows us to set the IR boundary condition we impose to search for the uniform branes). Note that when looking for *uniform* branes, the PDE system of EoM reduces to an ODE system without any x-dependence. In particular, the constraint equation $\mathcal{C}(x,1)=0$ reduces to $\mathcal{C}(1)=0$ and is trivially obeyed, since all of its terms involve terms with partial derivatives in x. So when searching for uniform branes we use the IR boundary conditions (3.23) but with the first condition replaced by the Dirichlet condition $q_1(y)\big|_{y=1}=1$:

$$q_1(y)\big|_{y=1}=1\,;\qquad \partial_y q_j\big|_{y=1}=\partial_y q_j\left(q_{2,4}\right)\big|_{y=1}\quad \text{if } j=2,3,4;\qquad \text{(if uniform branes)}. \tag{3.24}$$

This is a choice of normalization that does not change physical thermodynamic quantities. Solving the EoM for a given source Λ we then find, in particular, the value of $q_2(y)$ at $y=1$. We can then read the constant $\alpha_\Lambda=q_1(y)^2q_2(y)\big|_{y=1}=q_2(y)\big|_{y=1}$ of the uniform brane with source Λ. This value of $\alpha_\Lambda(\Lambda)$ is then the one we plug in the boundary condition (3.23) to find the *non*-uniform branes with the same source Λ. The UV boundary conditions for the uniform branes is still given by (3.19) (with the replacement $q_j(x,y)|_{y=0}\to q_j(y)|_{y=0}$).

3.1.3 Thermodynamic quantities

Having found the nonconformal solutions (3.14) that obey the boundary conditions (3.16)-(3.23), we will now implement the holographic renormalization procedure in order to obtain the relevant thermodynamic quantities (recall that $\ell\equiv 1$ and $y_+\equiv 1$). Our (non)uniform branes are asymptotically AdS_5 solutions with a scalar field with mass $\mu^2=-3$. In these conditions, the holographic renormalization procedure to find the holographic stress tensor $\mathcal{T}_{ab}$ and expectation value $\langle\mathcal{O}_\phi\rangle$ of the operator dual to the scalar field ϕ was developed in [96, 97]. We apply it to our system. We first need to introduce the Fefferman-Graham (FG) coordinates (z,χ) that are such that the asymptotic boundary is at $z=0$ and $g_{zz}=1/z^2$ and $g_{za}=0$ (with $a=t,\chi,w_{2,3}$) at all orders in a Taylor expansion about $z=0$. In terms of the radial and planar coordinates (y,x) of (3.14) the FG coordinates are

$$\begin{aligned} y&=z^2+\frac{\Lambda^2}{3}z^4+\frac{1}{12}z^6\left(\Lambda^4-3+\frac{3}{2}q_2^{(0,2)}(\chi,0)\right)+\mathcal{O}(z^8);\\ x&=\chi-\frac{q_2^{(1,2)}(\chi,0)}{96L^2}\,z^6+\mathcal{O}(z^8). \end{aligned} \tag{3.25}$$

The expansion of the gravitational and scalar fields around the boundary up to the order that contributes to the thermodynamic quantities is then

$$ds^2 = \frac{1}{z^2}\left[dz^2 + ds_\partial^2 + z^2\, ds_{(2)}^2 + z^4\, ds_{(4)}^2 + \mathcal{O}(z^6)\right] \tag{3.26}$$

where

$$\begin{aligned}
ds_\partial^2 &= g_{ab}^{(0)}\mathrm{d}x^a\mathrm{d}x^b = -dt^2 + L^2 d\chi^2 + dx_2^2 + dx_3^2,\\
ds_{(2)}^2 &= g_{ab}^{(2)}\mathrm{d}x^a\mathrm{d}x^b = -\frac{\Lambda^2}{3}\, ds_\partial^2\,,\\
ds_{(4)}^2 &= g_{ab}^{(4)}\mathrm{d}x^a\mathrm{d}x^b = \frac{1}{36}\left(27 - \Lambda^4 - 36\, q_1^{(0,2)}(\chi,0) + \frac{9}{2}\, q_2^{(0,2)}(\chi,0)\right) dt^2\\
&\quad + \frac{L^2}{36}\left(9 - 7\Lambda^4 + \frac{27}{2}\, q_2^{(0,2)}(\chi,0) - 72\,\Lambda\, q_4^{(0,1)}(\chi,0)\right) d\chi^2\\
&\quad + \frac{1}{36}\left(9 + \Lambda^4 - 18\, q_1^{(0,2)}(\chi,0) - \frac{9}{2}\, q_2^{(0,2)}(\chi,0)\right)\left(dx_2^2 + dx_3^2\right);
\end{aligned} \tag{3.27}$$

$$\phi = \Lambda\, z + \phi_2\, z^3 + \mathcal{O}(z^5)\,, \tag{3.28}$$

$$\phi_2 = \left(\frac{\Lambda^3}{6} + q_4^{(0,1)}(\chi,0)\right). \tag{3.29}$$

The holographic quantities can now be computed using the holographic renormalization procedure of Bianchi-Freedman-Skenderis [96, 97].[5] At the end of the day, for our system, the expectation value of the holographic stress tensor is given by

$$\langle \mathcal{T}_{ab}\rangle = \frac{2\ell^3}{\kappa^2}\left[g_{ab}^{(4)} + g_{ab}^{(0)}\left(\Lambda\,\phi_2 - \frac{\Lambda^4}{18} + \lambda_4\Lambda^4\right)\right], \tag{3.30}$$

where the metric components $g_{ab}^{(0)}$, $g_{ab}^{(4)}$ and the scalar decay ϕ_2 can be read directly from (3.26)-(3.29), and we recall that λ_4 is a parameter of the superpotential (2.2) that we will eventually set to
$lambda_4 = -1/4$. Similarly, the expectation value of the dual operator sourced by Λ is

$$\langle \mathcal{O}_\phi\rangle = \frac{2\ell^3}{\kappa^2}\Big(-4\lambda_4\Lambda^3 - 2\phi_2\Big). \tag{3.31}$$

The trace of the expectation value yields the expected Ward identity associated to the conformal anomaly

$$\langle \mathcal{T}_a{}^a\rangle = -\Lambda\langle\mathcal{O}_\phi\rangle\,, \tag{3.32}$$

which reflects the fact that our branes are not conformal.[6] Furthermore, after using the Bianchi relation (3.18), we confirm that the expectation value of the holographic stress tensor is conserved, i.e.

$$\nabla^a\langle\mathcal{T}_{ab}\rangle = -\langle\mathcal{O}_\phi\rangle\nabla_b\Lambda = 0\,. \tag{3.33}$$

In (3.30) and (3.31) we have reinstated the appropriate power of ℓ in order to remind the reader that, as seen in the previous chapter, the prefcator in the expectation values of the boundary

[5] Note however that we use different conventions for the Riemann curvature, that is to say, with respect to [96, 97] our action (2.1) has the opposite relative sign between the Ricci scalar $\mathcal{R}$ and the scalar field kinetic term $(\nabla\phi)^2$.

[6] Note that the holographic gravitational conformal anomaly contribution $\mathcal{A}_{\text{grav}}$ [96, 97] and the scalar conformal anomaly contribution $\mathcal{A}_{\text{scalar}}$ vanish for our system.

theory typically scales as N_c^2. In the rest of the paper we will work with rescaled quantities obtained by multiplying the stress tensor and the scalar operator by the inverse of this factor. In other words, we will measure boundary expectation values in units of N_c^2.

Evaluating (3.30) explicitly we find the following expressions for the energy density $\mathcal{E}$, the longitudinal pressure P_L (along the inhomogenous direction x) and the transverse pressure P_T (along the homogenous directions x_2 and x_3):

$$\mathcal{E}(\chi) = \frac{\Lambda^4}{4}\left(-4\lambda_4 - \frac{5}{9}\right) + \frac{1}{4}\left(3 - 4\,q_1^{(0,2)}(\chi,0) + \frac{1}{2}\,q_2^{(0,2)}(\chi,0)\right) - \Lambda\,q_4^{(0,1)}(\chi,0)\,, \tag{3.34}$$

$$P_L = \frac{\Lambda^4}{4}\left(-4\lambda_4 + \frac{1}{3}\right) - \frac{1}{4}\left(1 + 3\,q_2^{(0,2)}(\chi,0)\right) + \Lambda\,q_4^{(0,1)}(\chi,0)\,, \tag{3.35}$$

$$P_T(\chi) = \frac{\Lambda^4}{4}\left(-4\lambda_4 - \frac{5}{9}\right) - \frac{1}{4}\left(1 - 4\,q_1^{(0,2)}(\chi,0) - q_2^{(0,2)}(\chi,0)\right) - \Lambda\,q_4^{(0,1)}(\chi,0)\,. \tag{3.36}$$

Note that P_L is the pressure conjugate to the dimensionful coordinate $\tilde{x}$, not to the dimensionless coordinate x. Moreover, for static configurations, conservation of the stress tensor implies that P_L is constant along the inhomogeneous direction, i.e. independent of χ. The temperature T and the entropy density s of the nonconformal branes can be read simply from the surface gravity and the horizon area density of the solutions (3.14), respectively:

$$\begin{aligned} T &= \frac{\sqrt{\alpha_\Lambda}}{\pi}\,, \\ s &= \pi\sqrt{\alpha_\Lambda}\,\sqrt{q_3(\chi,1)}\Big(q_1(\chi,1)\Big)^{-2}\,, \end{aligned} \tag{3.37}$$

where have already used the boundary condition (3.23) that introduces the constant α_Λ (that we read from the uniform solutions; see discussion below (3.23)). The Helmoltz free energy density is $\mathcal{F} = \mathcal{E} - Ts$. The total energy E, entropy S and free energy F are obtained by integrating over the total volume:

$$E = \mathcal{L}^2\,L\int_0^1 d\chi\,\mathcal{E}(\chi)\,, \qquad S = \mathcal{L}^2\,L\int_0^1 d\chi\,s(\chi)\,, \qquad F = \mathcal{L}^2\,L\int_0^1 d\chi\,\mathcal{F}(\chi)\,, \tag{3.38}$$

where we have made use of the fact that the system is homogeneous in the transverse directions. It will also be useful to define average densities by dividing the integrated quantities by the total volume:

$$\overline{\mathcal{E}} = \frac{E}{L\mathcal{L}^2}\,, \qquad \overline{s} = \frac{S}{L\mathcal{L}^2}\,, \qquad \overline{f} = \frac{F}{L\mathcal{L}^2}\,. \tag{3.39}$$

For uniform branes these averages coincide with the corresponding densities, since the latter are constant, but for nonuniform branes they do not. A quantity that will play a role below is an analogous integral for the expectation value of the scalar operator:

$$\mathcal{O} = \mathcal{L}^2\,L\int_0^1 d\chi\,\langle\mathcal{O}_\phi\rangle(\chi)\,. \tag{3.40}$$

Because of the translational invariance in the transverse directions it will also be convenient to work with densities in the transverse plane, namely with quantities that are only integrated along the inhomogeneous direction. Thus we define the energy, the entropy, the free energy and the expectation value densities per unit area in the transverse plane as

$$\rho = \frac{E}{\mathcal{L}^2}\,, \qquad \sigma = \frac{S}{\mathcal{L}^2}\,, \qquad f = \frac{F}{\mathcal{L}^2}\,, \qquad \vartheta = \frac{\mathcal{O}}{\mathcal{L}^2}\,. \tag{3.41}$$

We will refer to these type of quantities as “area densities" or “Killing densities". In order to write the first law we will also need the integral of the transverse pressure along the inhomogeneous direction. We therefore define

$$\mathfrak{p}_L = P_L\,, \qquad \mathfrak{p}_T = L\int_0^1 d\chi\,P_T(\chi)\,. \tag{3.42}$$

Note that $\mathfrak{p}_L$ and $\mathfrak{p}_T$ have mass dimension 4 and 3, respectively. Finally, we will choose to measure all dimensionful quantities in units of the only gauge theory microscopic scale Λ. We will use a "$\hat{}$" symbol to denote the corresponding dimensionelss quantity obtained by multiplying or dividing a dimensionful quantity by the appropriate power of Λ, thus:

$$\hat{L} = \Lambda L\,, \qquad \hat{T} = \frac{T}{\Lambda}\,, \qquad \hat{\mathcal{E}} = \frac{\mathcal{E}}{\Lambda^4}\,, \qquad \hat{\overline{\mathcal{E}}} = \frac{\overline{\mathcal{E}}}{\Lambda^4}\,, \qquad \hat{\rho} = \frac{\rho}{\Lambda^3}\,, \qquad \hat{f} = \frac{f}{\Lambda^3}\,, \qquad \text{etc.} \tag{3.43}$$

We are now ready to write down the first law. In order to do this, we first note that the extensive thermodynamic variables of the system are the total energy E, the total entropy S, the scalar source Λ, and the three lengths L, $L_2 \equiv \mathcal{L}$, $L_3 \equiv \mathcal{L}$ of the planar directions. It follows that the first law for the total charges of the system is:

$$\mathrm{d}E = T\,\mathrm{d}S + \mathcal{O}\,\mathrm{d}\Lambda + \mathfrak{p}_L\,\mathcal{L}^2\,\mathrm{d}L + 2\,\mathfrak{p}_T\,\mathcal{L}\,\mathrm{d}\mathcal{L}\,. \tag{3.44}$$

We see that T, $\mathcal{O}$, $\mathfrak{p}_L\mathcal{L}^2$ and $\mathfrak{p}_T\mathcal{L}$ are the potentials (intensive variables) conjugate to S, Λ, L and $\mathcal{L}$, respectively. Since the system is translationally invariant along the x_2 and x_3 directions, under the associated scale transformation $x_{2,3} \to \lambda_0\, x_{2,3}$ the energy transforms as $E(x_{2,3}) \to \lambda_0^2 E(x_{2,3})$ and thus it is a homogeneous function of λ_0 of degree 2. This means that for any value of λ_0 one has:

$$E\left(\lambda_0^2\, S, \Lambda, L, \lambda_0\, L_2, \lambda_0\, L_3\right) = \lambda_0^2\, E\left(S, \Lambda, L, L_2, L_3\right). \tag{3.45}$$

We can now apply Euler's theorem for homogeneous functions to write the energy as a function of its partial derivatives:[7]

$$2S\frac{\partial E}{\partial S} + L_2\frac{\partial E}{\partial L_2} + L_3\frac{\partial E}{\partial L_3} = 2E\left(S, \Lambda, L, L_2, L_3\right). \tag{3.46}$$

The relevant partial derivatives in (3.46) can be read from (3.44) and, recalling that we are taking $L_2 = L_3 \equiv \mathcal{L}$, this yields the Smarr relation for the total charges of the system

$$E = TS + \mathfrak{p}_T\mathcal{L}^2\,. \tag{3.47}$$

Dividing by $\mathcal{L}^2$ we obtain a Smarr relation for the area densities along the transverse plane:

$$\rho = T\sigma + \mathfrak{p}_T\,. \tag{3.48}$$

Rewriting the first law (3.44) in terms of these densities and using (3.48) we find the first law for the area densities:

$$\mathrm{d}\rho = T\,\mathrm{d}\sigma + \mathfrak{p}_L\,\mathrm{d}L + \vartheta\,\mathrm{d}\Lambda\,. \tag{3.49}$$

Since we will measure all dimensionful quantities in units of Λ, it will be useful to find a first law and a Smarr relation for the dimensionless densities $\hat{\rho}, \hat{\sigma}$, etc. In order to do this we first use the dilatation transformation (3.9). Under this scale transformation $x^\mu \to \lambda_2\, x^\mu$ the energy density ρ transforms as $\rho(x^\mu) \to \lambda_2^3\,\rho(x^\mu)$ and thus it is a homogeneous function of λ_2 of degree 3, i.e.

$$\rho\left(\lambda_2^2\,\sigma, \lambda_2\,\Lambda, L/\lambda_2\right) = \lambda_2^3\,\rho\left(\sigma, \Lambda, L\right). \tag{3.50}$$

Applying Euler's theorem for homogeneous functions we get

$$2\sigma\frac{\partial\rho}{\partial\sigma} + \Lambda\frac{\partial\rho}{\partial\Lambda} - L\frac{\partial\rho}{\partial L} = 3\rho\left(\sigma, \Lambda, L\right). \tag{3.51}$$

[7] Essentially, in the present case, Euler's theorem amounts to take a derivative of the homogeneous relation (3.45) with respect to λ_0 and then sending $\lambda_0 \to 1$.

Reading the associated derivatives from the first law (3.49) we find (another) Smarr relation for the dimensionful densities:

$$3\,\rho = 2\,T\,\sigma - \mathfrak{p}_L\,L + \vartheta\,\Lambda\,. \tag{3.52}$$

Dividing this relation by Λ^3 we get the Smarr relation for the dimensionless densities:

$$3\,\hat{\rho} = 2\,\hat{T}\,\hat{\sigma} - \hat{\mathfrak{p}}_L\,\hat{L} + \hat{\vartheta}\,. \tag{3.53}$$

Finally, we can now rewrite the first law (3.49) in terms of the dimensionless area densities and use (3.53) to find the desired first law

$$\mathrm{d}\hat{\rho} = \hat{T}\,\mathrm{d}\hat{\sigma} + \hat{\mathfrak{p}}_L\,\mathrm{d}\hat{L} \tag{3.54}$$

that nonconformal branes with two Killing planar directions $x_{2,3}$ must obey. In a traditional thermodynamic language the first law (3.54) and the Smarr relation (3.53) are also known as the Gibbs-Duhem and Euler relations, respectively. In our case they provide valuable tests of our numerical results. Moreover, they will be useful to discuss the dominant thermal phases in the microcanonical and canonical ensembles. Indeed, in the microcanonical ensemble the dominant phase will be the one that maximises $\hat{\sigma}$ for fixed values of $\hat{\rho}$ and $\hat{L}$. Similarly, in the canonical ensemble the dominant phase will be the one that minimises $\hat{f}$ for fixed $\hat{T}$ and $\hat{L}$.

3.1.4 Perturbative construction of lumpy branes

In the previous sections we have setup the BVP that will allow us to find the uniform and nonuniform nonconformal branes (3.14) that obey the boundary conditions (3.16)-(3.23). This nonlinear BVP can be solved in full generality using numerical methods. In the uniform case we have a system of coupled quasilinear ODEs that can be solved without much effort. However, in the nonuniform case the ODEs are replaced by PDEs and it is harder to solve the system. We will do this numerically in Sec. 3.1.5. In the present section we will complement this full numerical analysis with a perturbative nonlinear analysis that finds lumpy branes in the region of the phase diagram where they merge with the uniform branes. This perturbative analysis will already provide valuable physical properties of the system. Additionally, these perturbative results will also be important to test the numerical results of Sec. 3.1.5. We solve the BVP in perturbation theory up to an order in the expansion parameter where we can distinguish the thermodynamics of the uniform and nonuniform branes.

We follow a perturbative approach that was developed in [98] (to find vacuum lattice branes) and that has its roots in [99–101] (to explore the existence of vacuum nonuniform black strings). More concretely, our strategy to find perturbatively the lumpy branes has three main steps:

1. The first step is to construct the uniform branes.

2. Then, at linear ($n = 1$) order in perturbation theory, we find the locus in the space of uniform branes where a zero-mode, namely a mode that is marginally stable, exists. We will refer to this mode as the GL-mode. In practice, we will identify this locus by finding the critical length $L = L_{\rm GL}$ (wavenumber $k_{\rm GL} = 2\pi/L_{\rm GL}$) above (below) which uniform branes become locally unstable (stable). As expected from the discussion in in the introduction of the current chapter, this critical length only exists for energy densities between points A and B.

3. The third step is to extend perturbation theory to higher orders, $n \geq 2$, and construct the nonuniform (lumpy) branes that bifurcate (in a phase diagram of solutions) from the GL merger curve of uniform branes.

We describe in detail and complete these three steps in the next three subsections.

Uniform branes: $\mathcal{O}(0)$ solution

The first step is to construct the uniform branes. We solve the system of four coupled ODEs for $q_j(x,y) \equiv Q_j(y)$ (here and below, $j = 1,\ldots,4$) subject to the boundary conditions (3.19) and (3.24), as described in Sec. 3.1.2. This can be done only numerically: we use the numerical methods detailed in the review [102].

There is a 1-parameter family of uniform nonconformal branes. We can take this parameter to be the scalar field source Λ. This is actually how we construct these solutions since Λ is an injective parameter: we give the source Λ via the boundary condition (3.19) and find the associated brane; then we repeat this for many other values of Λ. The dimensionless energy density $\hat{\mathcal{E}} = \mathcal{E}/\Lambda^4$ decreases monotonically as Λ grows, so this procedure maps out all possible uniform branes. Recall that, once we have found $q_j(x,y) \equiv Q_j(y)$, the thermodynamic quantities of the solution follow straightforwardly from Sec. 3.1.2.

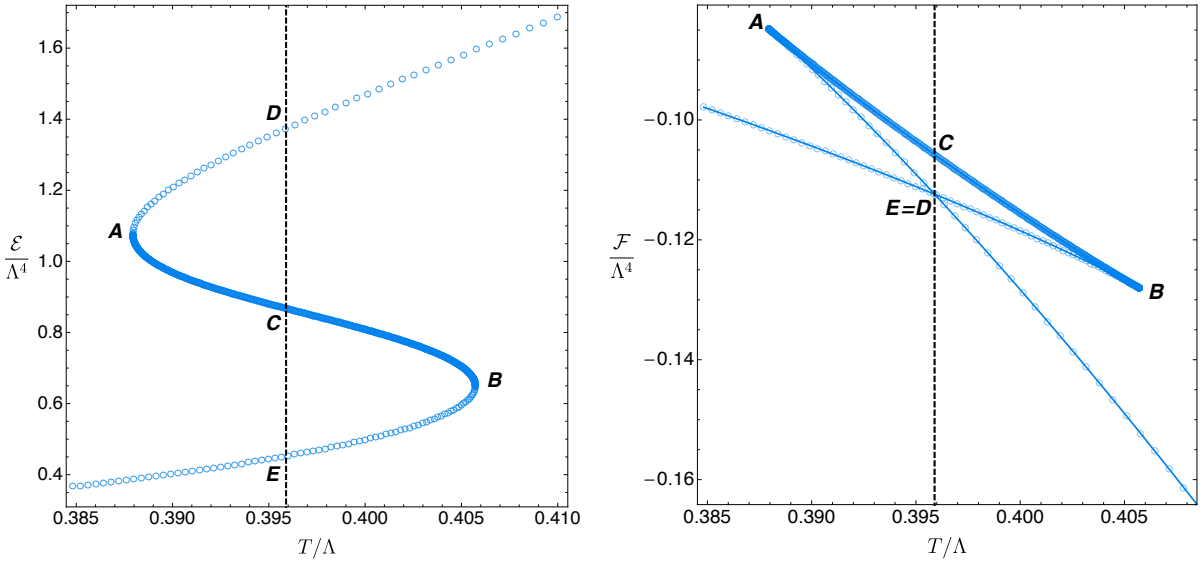

Figure 3.3: Dimensionless energy density (left) and free energy density (right) as a function of the dimensionless temperature for uniform nonconformal branes in our model. The curve between A and B is the spinodal region and we will refer to it as the "intermediate branch". At $\hat{T}_c \simeq 0.3958945$ (vertical dashed line) there is a first order phase transition in the canonical ensemble (see right panel). For reference here and in future plots, $(\hat{T},\hat{\mathcal{E}})_A \simeq (0.387944, 1.076417)$, $(\hat{T},\hat{\mathcal{E}})_B \simeq (0.405724, 0.650227)$, $(\hat{T},\hat{\mathcal{E}})_C \simeq (0.3958945, 0.867956)$, $(\hat{T},\hat{\mathcal{E}})_D \simeq (0.3958945, 1.37386)$ and $(\hat{T},\hat{\mathcal{E}})_E \simeq (0.3958945, 0.452754)$.

The properties of uniform branes are summarized in Figs. 3.3 and 3.4. In the left panel of Figs. 3.3 we plot the dimensionless energy density $\hat{\mathcal{E}} \equiv \mathcal{E}/\Lambda^4$ as a function of the dimensionless temperature $\hat{T} \equiv T/\Lambda$. We see the familiar S-shape associated to the multivaluedness of a first-order phase transition. Specifically, for a given temperature $\hat{T}$ in the window of temperatures $\hat{T}_A \leq T/\Lambda \leq \hat{T}_B$ there are three distinct families or branches of uniform branes with different values of $\hat{\mathcal{E}}$. We will refer to these families as the "heavy", "intermediate" and "light" branches. The heavy branch (with higher energy density) starts in the conformal $T/\Lambda \to \infty$ limit and then extends through point D all the way down to point A as the temperature $\hat{T}$ decreases. The intermediate branch extends from point A, passes though point C, towards point B. This branch has negative specific heat and is both thermodynamically and dynamically locally unstable. A general discussion of these features can be found in Sec. 2 of Ref. [63]. In the present paper we will analyse the zero-mode properties of this instability in Sec. 3.1.4, and its timescale in Sec. 3.1.7. Finally, the light branch (with lower energy density) starts at point B, passes thought

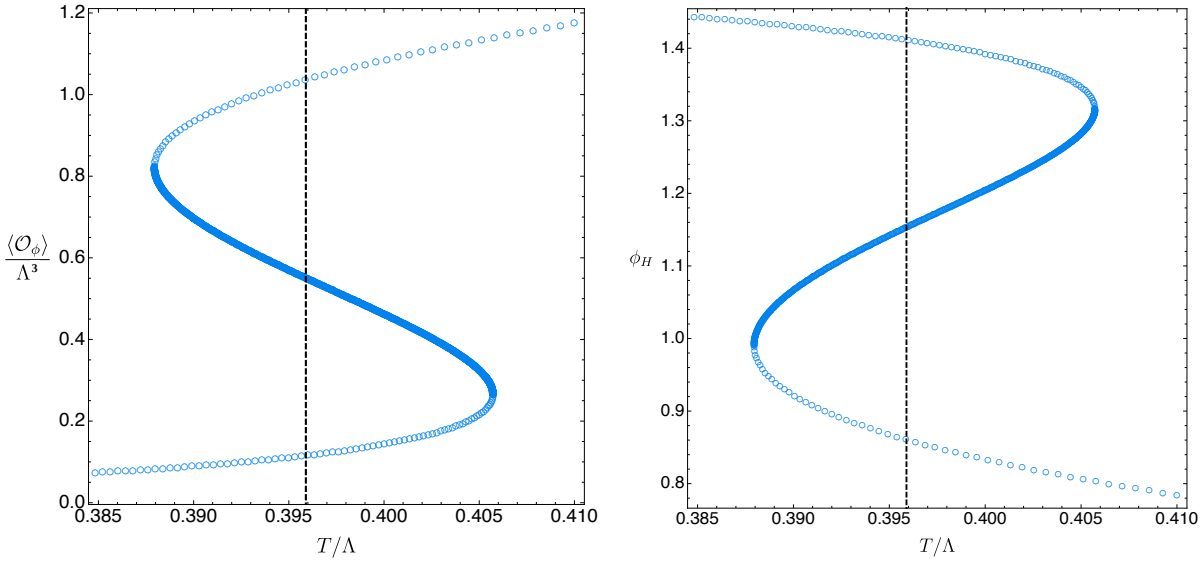

Figure 3.4: (Left) Dimensionless expectation value $\langle \mathcal{O}_\phi \rangle / \Lambda^3$ of the operator with source Λ as a function of the dimensionless temperature $\hat{T}$ of the uniform branes. (Right) Value of the scalar field of the uniform branes at the horizon ϕ_H as a function of $\hat{T}$.

point E and extends all the way down towards $T/\Lambda \to 0$. We do not show the plots of $\hat{s}(\hat{T})$ and $\hat{\mathfrak{p}}_{L,T}(\hat{T})$ because they are qualitatively similar to the plot of $\hat{\mathcal{E}}(\hat{T})$.

The relevant phase diagram for the canonical ensemble, namely the dimensionless free energy $\hat{\mathcal{F}} \equiv \mathcal{F}/\Lambda^4$ as a function of the dimensionless temperature $\hat{T}$, is displayed in the right panel of Fig. 3.3, where we see the expected swallow-tail shape. For a given $\hat{T}$, the solution with lowest $\hat{\mathcal{F}}$ is the preferred thermal phase. So, as anticipated above, there is a first-order phase transition at $\hat{T} = \hat{T}_c \approx 0.3958945$. This critical temperature is indicated with a vertical dashed line in the plots of Figs. 3.3 and 3.4, as well as in subsequent ones whenever appropriate. For $\hat{T} < \hat{T}_c$ the light uniform branch (the lower branch in the left panel of Fig. 3.3) is the preferred thermal phase, while for fixed $\hat{T} > \hat{T}_c$ the heavy uniform branch (the upper branch in the left panel) dominates the canonical ensemble. In particular, the intermediate uniform branch (between A and B) is never the preferred thermal phase.

For completeness, in Fig. 3.4 we show how the dimensionless expectation value $\langle \mathcal{O}_\phi \rangle / \Lambda^3$ of the operator with source Λ changes with the dimensionless temperature $\hat{T}$ (left panel) and how the value of the scalar field at the horizon ϕ_H varies with $\hat{T}$ (right panel).

In the microcanonical ensemble, the relevant phase diagram is the average entropy density $\hat{\bar{s}} \equiv \bar{s}/\Lambda^3$ as a function of the average energy density $\hat{\bar{\mathcal{E}}} \equiv \bar{\mathcal{E}}/\Lambda^4$. It is important to consider averaged quantities (which involve integration along the x direction) because inhomogeneous state will play a role. The qualitative form of the function $\hat{\bar{s}}(\hat{\bar{\mathcal{E}}})$ is shown in Fig. 3.5. The key features are as follows. $\hat{\bar{s}}$ is convex ($\hat{\bar{s}}'' > 0$) in the region between A and B. This indicates local thermodynamical instability, since the system can increase its total entropy by rising the energy slightly in part of its volume and lowering in another so as to keep the total energy fixed. In the regions EB and AD the entropy function is concave ($\hat{\bar{s}}'' < 0$) but there are states with the same total energy and higher total entropy, namely phase-separated configurations in which the phases E and D coexist at the critical temperature. These states are characterised by the fractions $0 \leq \nu, (1-\nu) \leq 1$ of the total volume occupied by each phase, so their total entropy is of the form $\hat{s}_E + (\hat{s}_D - \hat{s}_E)\nu$, as indicated by the red segment in Fig. 3.5. Therefore the regions EB and AD are locally but not globally thermodynamically stable. Finally, all states outside the region ED are globally stable. For our system, these qualitative features are difficult to

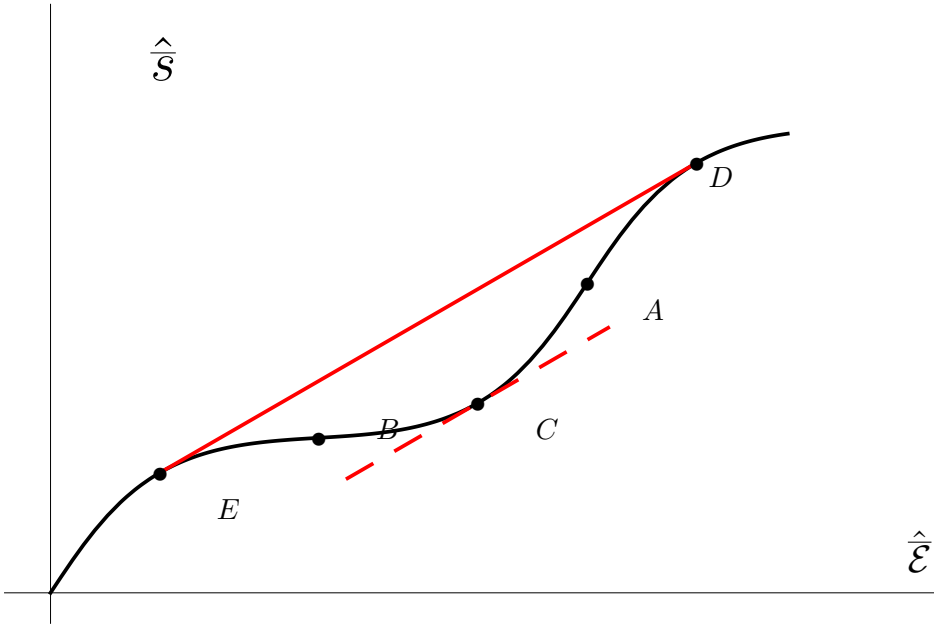

Figure 3.5: Qualitative form of the entropy density in the microcanonical ensemble. The solid red segment corresponds to the average entropy density of phase-separated configurations, as explained in the text. The dashed red segment indicates that the slope of the tangent at point C is the same as that of the solid red segment. This follows from the fact that the temperature at point C is precisely T_c.

appreciate directly on a plot of $\hat{s}$ versus $\hat{\mathcal{E}}$ because the curve $\hat{s}(\hat{\mathcal{E}})$ is very close to a straight line. For this reason we show the convexity/concavity property (the second derivative) in Fig. 3.6(left) and the difference between the phase-separated configurations and the homogeneous solutions in Fig. 3.6(right).

Gregory-Laflamme physics: $\mathcal{O}(1)$ solution and the spinodal zero-mode

The intermediate uniform branes with $\hat{\mathcal{E}}_B < \hat{\mathcal{E}} < \hat{\mathcal{E}}_A$ (see left panel of Fig. 3.3), and only these, can be Gregory-Laflamme (GL) unstable. Roughly speaking, we expect this to happen if their dimensionless length $L\,\Lambda$ (along the x direction) is bigger than the dimensionless thermal scale Λ/T of the system. This linear instability is ultimately responsible for the nonlinear existence of the lumpy solutions. Therefore, our second step is to consider *static* perturbations about the uniform branes, $q_j(x,y) = Q_j(y) + \epsilon\, q_j^{(1)}(x,y)$, that break the $U(1)$ symmetry along x (see Sec. 3.1.7 for time-dependent perturbations). Here, $\epsilon \ll 1$ is the amplitude of the linear perturbation and, ultimately, it will be the expansion parameter of our perturbation theory to higher order.

We adopt a perturbation scheme that is consistent with our nonlinear ansatz (3.14) — where we recall that $x \in [0,1]$ — since we want to simply linearize the nonlinear equations of motion that we already have (Sec. 3.1.2) to get the perturbative EoM. In this perturbation scheme we assume an ansatz for the perturbation of the form[8]

$$q_j^{(1)}(x,y) = \mathfrak{q}_j^{(1)}(y)\cos(\pi\, x). \tag{3.55}$$

This means that the length L of the periodic coordinate x is given in terms of the wavenumber k of the perturbation by $L = 2\pi/k$, and it will *change* as we climb the perturbation ladder (this

[8]The superscript $^{(n)}$ here and henceforth always denotes the order n of the perturbation theory, not order of derivatives.

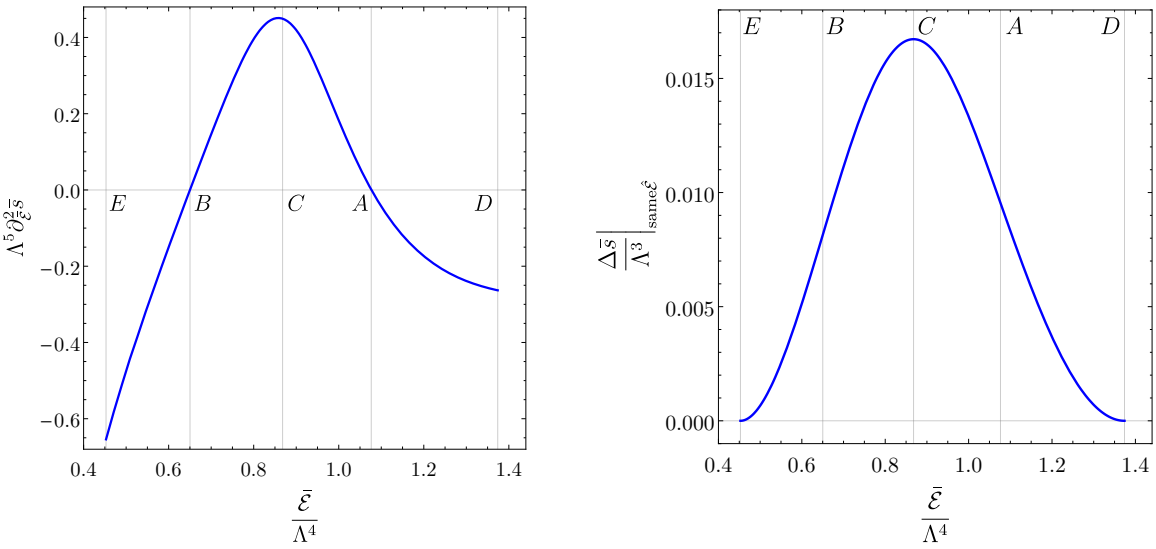

Figure 3.6: (Left) Second derivative $\hat{\bar{s}}''(\hat{\bar{\mathcal{E}}})$ of the entropy density with respect to the energy density, showing the convexity/concavity properties discussed in the text. (Right) Difference between the average entropy density of the phase-separated configurations and the entropy density of the homogeneous solutions, showing that the former are preferred in the region between A and B.

is because k, and thus L, will be corrected at each order; see Sec. 3.1.4). Since the EoM depend on L, this relation $L = 2\pi/k$ introduces the zero mode wavenumber k in the problem.[9]

Under these circumstances the linearized EoM become a simple eigenvalue problem in k^2 of four coupled ODEs. Henceforth, we denote this *leading-order* wavenumber by $k_{\rm GL}$. So we need to solve our eigenvalue problem to find the eigenvalue $k_{\rm GL}$ as well as the associated four eigenfunctions $q_j^{(1)}(y)$. Note however that we "just" need to solve an ODE system of four coupled equations (not PDEs) subject to the *linearized versions* of the boundary conditions (3.19)-(3.23). For example, when we linearize (3.19) using $q_j|_{y=0} = Q_j|_{y=0} + \epsilon\, q_j^{(1)}|_{y=0}$ we find that the linear perturbations $\mathfrak{q}_j^{(1)}(y)$ must obey the UV Dirichlet boundary conditions $\mathfrak{q}_j^{(1)}\big|_{y=0} = 0$. On the other hand, linearizing the IR boundary conditions (3.23) we find that the linear perturbations $\mathfrak{q}_j^{(1)}(y)$ must obey the condition $\mathfrak{q}_1^{(1)}\big|_{y=1} = \frac{1}{2\alpha_\Lambda}\mathfrak{q}_2^{(1)}\big|_{y=1}$ and mixed boundary conditions for $\mathfrak{q}_{2,3,4}^{(1)}\big|_{y=1}$. Of course, in this linearization procedure about the uniform brane, we insert the boundary conditions (3.19) and (3.24) of the leading solution; in particular, we impose $Q_1\big|_{y=1} = 1$ and $Q_2\big|_{y=1} = \alpha_\Lambda$.

Summarizing this second step, the above perturbation procedure at $\mathcal{O}(\epsilon)$ finds the critical zero mode of the Gregory-Laflamme (GL) instability of uniform branes with energy densities $\hat{\mathcal{E}}_B < \hat{\mathcal{E}} < \hat{\mathcal{E}}_A$. That is to say, it finds the dimensionless critical wavenumber $\hat{k}_{\rm GL} = k_{\rm GL}/\Lambda$ for the onset of the GL instability, and thus the minimum length $L_{\rm GL}\Lambda = 2\pi/\hat{k}_{\rm GL}$ above which

[9] We have some freedom in the choice of the perturbation scheme. For example, an *alternative* perturbation scheme would be to keep the length L *fixed* by absorbing the L factor in the metric component g_{xx} of the ansatz (3.14) into a new coordinate $\tilde{x}$. That is to say, we would change the $x \in [0,1]$ coordinate of (3.14) into $\tilde{x} = x\frac{L}{2} \in [0, \frac{L}{2}]$. In this case, the $U(1)$ dependence of the perturbation would be $\cos(k\,\tilde{x})$ which would introduce the wavenumber $k = \frac{2\pi}{L}$ in the problem. These two schemes are equivalent. This follows from the observation that the two sets of Fourier modes are equivalent: $\cos(\eta\, k\,\tilde{x}) = \cos\left(\eta \frac{2\pi}{L}\frac{L}{2}x\right) = \cos(\eta\,\pi\,x)$. Further recall from the discussion above (3.5) that our solutions have $\mathbb{Z}_2$ symmetry: the solution in $\tilde{x} \in [-L/2, 0[$ can be obtained by simply flipping our solution over the $x = 0$ axis (computationally this is useful/efficient since we deploy a given number of grid points to study the range $[0, L/2]$ instead of $[-L/2, L/2]$). This is why we have just a factor of π and not 2π in the arguments of our Fourier cosines.

the uniform brane is unstable. This critical value $\hat{k}_{\rm GL} = \hat{k}_{\rm GL}(\hat{T})$ is only a function of the dimensionless temperature $\hat{T} = T/\Lambda$ and is plotted in Fig. 3.7. We see that $\hat{k}_{\rm GL} = 0$ at the endpoints A and B of the *intermediate* uniform branch where $\hat{T} = \hat{T}_A$ and $\hat{T} = \hat{T}_B$. These two branes are effectively stable since $\hat{L}_{\rm GL} \to \infty$ at these two temperatures. However, intermediate branes with $\hat{T}_A \leq \hat{T} \leq \hat{T}_B$ are unstable if their length satisfies $\hat{L} > \hat{L}_{\rm GL} = 2\pi/\hat{k}_{\rm GL}$.

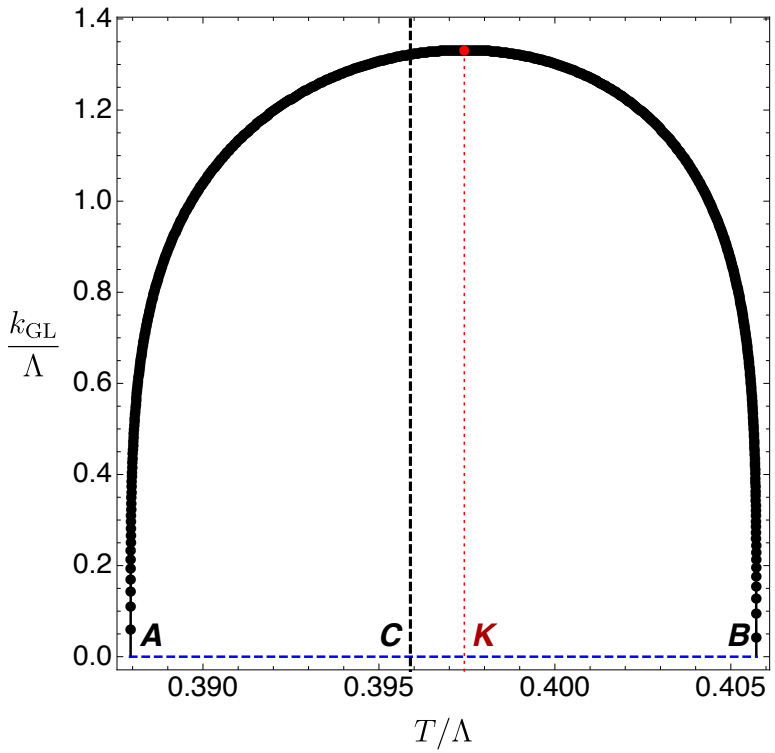

Figure 3.7: Zero mode of the GL or spinodal instability, i.e. its onset wavenumber $\hat{k}_{\rm GL}$ as a function of the temperature $\hat{T}$. For reference $(\hat{T}, \hat{k}_{\rm GL}, \hat{L}_{\rm GL})_C \simeq (0.3958945, 1.322508, 4.750961)$, and the maximum of the instability occurs for $(\hat{T}, \hat{k}_{\rm GL}, \hat{L}_{\rm GL})_K \simeq (0.397427, 1.332306, 4.716021)$.

So $\hat{L}_{\rm GL}$ is parametrized by $\hat{T}$, and the energy density of uniform branes is also only a function of the temperature, $\hat{\mathcal{E}} = \hat{\mathcal{E}}(\hat{T})$. It follows that we can identify the onset GL curve of uniform branes in a plot $\hat{\mathcal{E}}$ *vs* $\hat{L}$. This is done in Fig. 3.8. This plot is effectively a stability phase diagram for the uniform branes since the black dotted GL onset curve separates the region where the uniform branes are unstable — namely, the parabola-like shaped interior region $\hat{\mathcal{E}}_B < \hat{\mathcal{E}} < \hat{\mathcal{E}}_A$ with $\hat{L} > \hat{L}_{\rm GL}$ — from its complementary region where branes are stable against the spinodal instability. In this figure note that the energy density $\hat{\mathcal{E}} = \hat{\mathcal{E}}_A$ and $\hat{\mathcal{E}} = \hat{\mathcal{E}}_B$ corresponds to the energy densities of the uniform solutions A and B in Fig. 3.3 and note that $\hat{L}_{\rm GL} \to \infty$ when the energy density of the black dashed GL onset curve approaches $\hat{\mathcal{E}}_A$ or $\hat{\mathcal{E}}_B$.

To summarize, Fig. 3.8 shows that *intermediate* uniform branes with a given energy density $\hat{\mathcal{E}}_B < \hat{\mathcal{E}} < \hat{\mathcal{E}}_A$ are unstable if their dimensionless length is higher that the GL critical length, $\hat{L} > \hat{L}_{\rm GL}$. Not less importantly, in a phase diagram of solutions, the GL onset curve also signals a bifurcation to a new family of solutions that describes nonuniform or lumpy branes. That is to say, the GL onset curve is a *merger line* between the uniform and lumpy nonconformal branes. Perturbation theory at order $\mathcal{O}(\epsilon)$ identifies this merger or intersection line (see Fig. 3.8) of two distinct surfaces in a 3D phase diagram but it cannot describe the properties of the lumpy brane surface as we move away from the merger line (roughly speaking, it cannot describe the "slope of the lumpy surface" in a 3D phase diagram). For that, we need to proceed to higher order $\mathcal{O}(\epsilon^n)$ in the perturbation theory, as we do in in the next subsection.

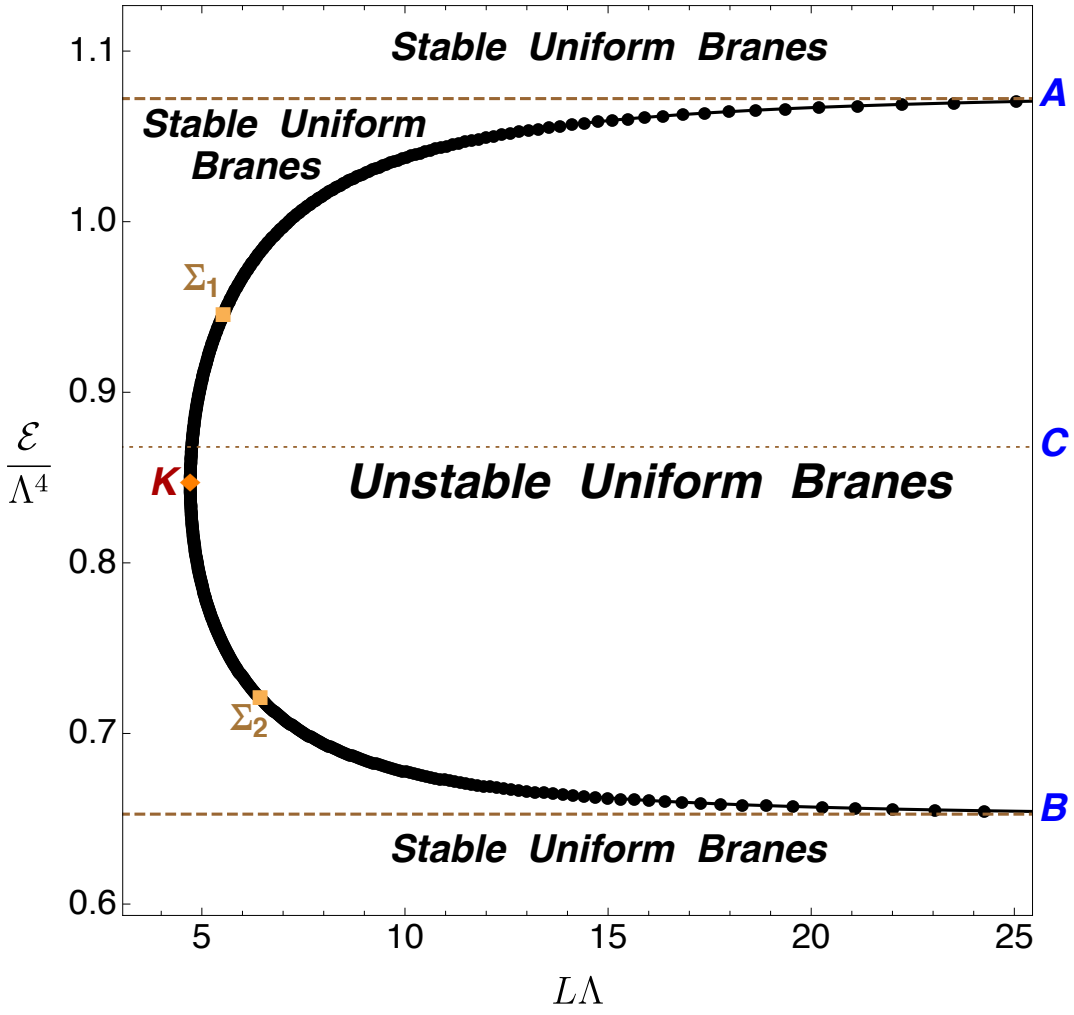

Figure 3.8: Stability diagram for uniform nonconformal branes. The interpretation of the two yellow square points Σ_1 and Σ_2 will be given when discussing Fig. 3.10. For reference, $(\hat{T}, \hat{L}_{\rm GL}, \hat{\mathcal{E}})_{\Sigma_1} \simeq (0.390817, 5.618133, 0.950579)$ and $(\hat{T}, \hat{L}_{\rm GL}, \hat{\mathcal{E}})_{\Sigma_2} \simeq (0.404645, 6.592316, 0.717060)$ and $(\hat{T}, \hat{L}_{\rm GL}, \hat{\mathcal{E}})_{K} \simeq (0.397427, 4.716021, 0.846337)$.

Lumpy branes: perturbative solution at $\mathcal{O}(n)$

To find the solution at order $\mathcal{O}(\epsilon^n)$ we expand the metric functions and wavenumber in powers of ϵ:

$$q_j(x,y) = Q_j(y) + \sum_{n=1}^{\infty} \epsilon^n \, q_j^{(n)}(x,y); \tag{3.56a}$$

$$k = \sum_{n=1}^{\infty} \epsilon^{n-1} k^{(n-1)} \equiv k_{\rm GL} + \sum_{n=2}^{\infty} \epsilon^{n-1} k^{(n-1)}, \quad \text{with } L = \frac{2\pi}{k}. \tag{3.56b}$$

In this expansion we have made the identification $k^{(0)} \equiv k_{\rm GL}$ and we have already found the $n=1$ contribution in the previous section. Recall that this $\{k_{\rm GL}, q_j^{(1)}\}$ contribution was found by solving a *homogeneous* eigenvalue problem for $k_{\rm GL}$. The expansion (3.56) is such that at order $\mathcal{O}(\epsilon^n)$ we solve the BVP to find the coefficients $\{k^{(n-1)}, q_j^{(n)}\}$.

Further note that, as explained above, our choice of perturbation scheme is such that the length L is corrected at each order n (see also footnote 9). That is, one has

$$L = L_{\rm GL} + \sum_{n=2}^{\infty} \epsilon^{n-1} L^{(n-1)} \,, \tag{3.57}$$

where the coefficients $L^{(n-1)}$ can be read straightforwardly from (3.56b). This also means that in our choice of scheme, the periodicity of the x circle allows us to introduce a separation ansatz for the perturbation coefficients $q_j^{(n)}(x,y)$ whereby they are expressed as a sum of Fourier modes (with harmonic number η) in the x direction as

$$q_j^{(n)}(x,y) = \sum_{\eta=0}^{n} \mathfrak{q}_j^{(n,\eta)}(y) \cos(\eta \, \pi \, x). \tag{3.58}$$

So here and onwards, $0 \leq \eta \leq n$ identifies a particular Fourier mode (harmonic) of our expansion at order $\mathcal{O}(\epsilon^n)$.

At order $n \geq 2$, the perturbation EoM are no longer homogeneous. Instead, they describe an *inhomogeneous* boundary value problem with a source $\mathcal{S}^{(n,\eta)}$. Not surprisingly, this source is a function of the lower order solutions $\{k^{(i-1)}, q_j^{(i)}\}$, $i = 1, \ldots, n-1$ (and their derivatives): $\mathcal{S}^{(n,\eta)}(k^{(i-1)}, q_j^{(i)})$. This source can always be written as a sum of Fourier modes of the system. We find that at order $n \geq 2$, the maximum Fourier mode harmonic that is excited in the source is $\eta = n$. This is due to the fact that at linear order we start with the single $\eta = 1$ Fourier mode and the $n^{\rm th}$ polynomial power of this linear mode, after using trigonometric identities to eliminate powers of trigonometric functions, can be written as a sum of Fourier modes with the highest harmonic being $\eta = n$. This property of our source implies that the solution of the $\mathcal{O}(n)$ EoM can only excite harmonics up to $\eta = n$ and this explains why we capped the sum in (3.58) at $\eta = n$.

To proceed, at each order $\mathcal{O}(n)$, we have to distinguish the Fourier modes $\eta = 1$ from the other, $\eta \neq 1$. This is because this particular Fourier mode $\eta = 1$ is the only one that is already excited at linear order $n = 1$.

Start with the generic case $\eta \neq 1$. Then the differential operator — call it $\mathcal{L}_H$ — that describes the associated homogeneous system of equations, $\mathcal{L}_H \, \mathfrak{q}_j^{(n,\eta)} = 0$, is the same at each order n and for any Fourier mode η: it only depends on the uniform brane $Q_j(y)$ we expand about and $k_{\rm GL}$. The ODE system of 4 inhomogeneous equations is thus of the form

$$\mathcal{L}_H \, \mathfrak{q}_j^{(n,\eta)} = \mathcal{S}^{(n,\eta)}, \quad \text{if } n \geq 2 \text{ and } \eta \neq 1. \tag{3.59}$$

It follows that the complementary functions of the homogeneous system are the same at each order $n \geq 2$ and η. But, we also need to find the particular integral of the inhomogeneous system and this is different for each pair (n, η) since the sources $\mathcal{S}^{(n,\eta)}$ differ. The general solution $\mathfrak{q}_j^{(n,\eta)}(y)$ is found by solving (3.59) subject to vanishing UV Dirichlet boundary conditions $\mathfrak{q}_j^{(n,\eta)}\big|_{y=0} = 0$ — since the full solution (3.56) must obey (3.19) — and regularity at the horizon $y = 1$. This gives mixed boundary conditions for $\mathfrak{q}_{2,3,4}^{(n,\eta)}$ and a Dirichlet condition for $\mathfrak{q}_1^{(n,\eta)}$, all of which follow from (3.23).

Consider now the exceptional case $\eta = 1$. In this case, at order $n \geq 2$, our BVP becomes a (non-conventional[10]) eigenvalue problem in $k^{(n-1)}$. That is to say, the ODE system of 4 inhomogeneous equations is now of the form

$$\mathcal{L}_H\, \mathfrak{q}_j^{(n,1)} = k^{(n-1)} \frac{k_{\rm GL} K_{jm} \mathfrak{q}_m^{(1)}}{2y(1-y^2)Q_2^2 Q_3} + \mathcal{S}^{(n,1)}, \quad \text{if } n \geq 2 \text{ and } \eta = 1. \tag{3.60}$$

where K_{jm} is a diagonal matrix whose only non-vanishing components are $K_{11} = 1 = K_{44}$. Recall that $\mathcal{L}_H$ is an operator that describes two second-order ODEs for $\mathfrak{q}_1$, $\mathfrak{q}_4$ and two first-order ODEs for $\mathfrak{q}_2$, $\mathfrak{q}_3$ and this justifies the presence of this particular K_{jm} in our eigenvalue term. We now have to solve (3.60) (subject to boundary conditions that are motivated as in the $\eta \neq 1$ case) to find the eigenvalue $k^{(n-1)}$ and the eigenfunctions $\mathfrak{q}_j^{(n,1)}(y)$.

To have a full understanding of the EoM of our perturbation problem one last observation is required. As pointed out above, the highest Fourier harmonic that is excited in our system at order $\mathcal{O}(\epsilon^n)$ is $\eta = n$. This is because the $n^{\rm th}$ polynomial power of the single Fourier mode that is present at linear order, after using trigonometric identities to eliminate powers of trigonometric functions, can be written as a sum of Fourier modes with the highest harmonic being $\eta = n$. But this trigonometric operation also indicates (as we explicitly confirmed) that *not* all Fourier modes with $\eta \leq n$ are excited. More concretely, for *even* $n \geq 2$ we find that *only even* $0 \leq \eta \leq n$ modes are present in our system. And for any *odd* $n \geq 3$, *only odd* $0 \leq \eta \leq n$ modes are excited. Therefore, up to order $n = 5$ we find that the modes that are excited in our system are:

$$q_j^{(2)}(x,y) = \mathfrak{q}_j^{(2,0)}(y) + \mathfrak{q}_j^{(2,2)}(y)\cos(2\,\pi\,x), \tag{3.61a}$$

$$q_j^{(3)}(x,y) = \mathfrak{q}_j^{(3,1)}(y)\cos(\pi\,x) + \mathfrak{q}_j^{(3,3)}(y)\cos(3\,\pi\,x), \tag{3.61b}$$

$$q_j^{(4)}(x,y) = \mathfrak{q}_j^{(4,0)}(y) + \mathfrak{q}_j^{(4,2)}(y)\cos(2\,\pi\,x) + \mathfrak{q}_j^{(4,4)}(y)\cos(4\,\pi\,x), \tag{3.61c}$$

$$q_j^{(5)}(x,y) = \mathfrak{q}_j^{(5,1)}(y)\cos(2\,\pi\,x) + \mathfrak{q}_j^{(5,3)}(y)\cos(3\,\pi\,x) + \mathfrak{q}_j^{(5,5)}(y)\cos(5\,\pi\,x). \tag{3.61d}$$

This last property of our system, together with the previous observation — see the discussion of (3.60) — that Fourier modes with $\eta = 1$ are those that give the wavenumber correction $k^{(n-1)}$ at order n, immediately allows us to conclude that $k^{(n-1)} = 0$ if n is even. At even n order the $\cos(\pi\,x)$ Fourier mode is not excited by the source and thus the only solution of (3.60) is the trivial solution.

Finally, note that the $\eta = 0$ harmonics are of particular special interest. Indeed note that modes with $\eta \neq 0$ do not contribute (since the integral of a cosine vanishes) to the total thermodynamic quantities of the solution such as the energy E, the entropy S, etc. It follows from the discussion of (3.61) that odd order n modes do not contribute to correct these thermodynamic quantities.

We can finally summarize the key aspects of the general flow of our perturbation theory as the order n grows:

1. even orders $\mathcal{O}(\epsilon^n)$ introduce perturbative corrections to thermodynamic quantities like energy, entropy, pressure, etc., but they do not correct the wavenumber, $k^{(n-1)} = 0$ (and thus do not correct L).

[10] It is not a standard eigenvalue problem because the eigenvalue $k^{(n-1)}$ is not multiplying the unknown eigenfunction $\mathfrak{q}_j^{(n,\eta)}$. Instead, it multiplies an eigenfunction that was already determined at previous $n = 1$ order.

2. odd orders $\mathcal{O}(\epsilon^n)$ give the wavenumber corrections $k^{(n-1)}$ but do not change the energy, entropy and pressure.

We complete this perturbation scheme up to order $\mathcal{O}(\epsilon^5)$: this is the order required to find a deviation between the relevant thermodynamics of the lumpy branes and the uniform phase.

Once we have found all the Fourier coefficients $\mathfrak{q}_j^{(n,\eta)}(y)$ and wavenumber corrections $k^{(n-1)}$ up to $n=5$, we can reconstruct the four fields $q_j(x,y)$ using (3.56). We can then substitute these fields in the thermodynamic formulas of Sec. 3.1.2 to obtain all the thermodynamic quantities of the system up to $\mathcal{O}(\epsilon^5)$. We find that all of them, as well as the wavenumber, have an even expansion in ϵ^n, with the only exception of the temperature that is simply given by (3.37).

Now that we have the thermodynamic description of lumpy branes up to $\mathcal{O}(\epsilon^5)$, we can compare it against the thermodynamics of uniform branes and find which of these two families is the preferred phase. We are particularly interested in the microcanonical ensemble, so the dominant phase is the one that has the highest $\hat{\sigma}$ for a given pair $(\hat{L},\hat{\rho})$. Let $Q_{\rm u}$ and $Q_{\rm nu}$ denote thermodynamic quantities Q for the uniform and nonuniform branes, respectively. When comparing these two solutions in the microcanonical ensemble, one must have

$$\hat{L}_{\rm nu}=\hat{L}_{\rm u}, \quad \text{and} \quad \hat{\rho}_{\rm nu}=\hat{\rho}_{\rm u}. \tag{3.62}$$

Given a lumpy brane with $(\hat{L}_{\rm nu},\hat{\rho}_{\rm nu})$ we must thus identify a uniform brane whose Killing density $\hat{\rho}_{\rm u}$ satisfies (3.62). Equivalently, we can impose that the energy density of the uniform brane obeys

$$\mathcal{E}_{\rm u}=\frac{\hat{\rho}_{\rm nu}}{\hat{L}_{\rm nu}}\,. \tag{3.63}$$

Both sides of this equation are known as a perturbative expansion in ϵ. This is because the energy density $\mathcal{E}_{\rm u}$ is a function of the dimensionless temperature $\hat{T}_{\rm u}$ which is corrected at each order as $\hat{T}_{\rm u}=\hat{T}_0+\epsilon^2\,\hat{T}_{(2)}+\epsilon^4\,\hat{T}_{(4)}+\mathcal{O}(\epsilon^6)$ in our perturbation expansion. Similarly, the Killing energy density $\hat{\rho}_{\rm nu}(\epsilon)$ and the length $\hat{L}_{\rm nu}(\epsilon)$ of lumpy branes are also known as a Taylor expansion in ϵ. Therefore, in practice equation (3.63) becomes

$$\mathcal{E}_{\rm u}(\hat{\tau}_0)+\epsilon^2\,\hat{\tau}_{(2)}\,\mathcal{E}'_{\rm u}(\tau_0)+\epsilon^4\left(\hat{\tau}_{(4)}\,\mathcal{E}'_{\rm u}(\tau_0)+\frac{1}{2}\,\hat{\tau}^2_{(2)}\,\mathcal{E}''_{\rm u}(\tau_0)\right)+\mathcal{O}(\epsilon^6)=\frac{\hat{\rho}_{\rm nu}(\epsilon)}{\hat{L}_{\rm nu}(\epsilon)}\,. \tag{3.64}$$

Taking the Taylor expansion of $\rho_{\rm u}(\hat{T}_{\rm u})$ we must impose

$$\rho_{\rm nu}=\rho_{\rm u}(\hat{T}_0)+\epsilon^2\,\hat{T}_{(2)}\,\rho'_{\rm u}(T_0)+\epsilon^4\left(\hat{T}_{(4)}\,\rho'_{\rm u}(T_0)+\frac{1}{2}\,\hat{T}^2_{(2)}\,\rho''_{\rm u}(T_0)\right)+\mathcal{O}(\epsilon^6)\,, \tag{3.65}$$

Given a lumpy brane with known $\hat{L}_{\rm nu}(\epsilon)$ and $\hat{\rho}_{\rm nu}(\epsilon)$, equation (3.65) allows us to find the temperature coefficients $T_{(i)}$ of the uniform brane that has the same length and Killing energy density as the lumpy solution, i.e. the temperature of the uniform brane $\hat{T}_{\rm u}$ up to $\mathcal{O}(\epsilon^n)$ that satisfies (3.62).

Having this $\hat{T}_{\rm u}$ we can now compute the entropy density of the uniform brane $\hat{s}_{\rm u}(T_{\rm u})$ and the Killing entropy density $\hat{\sigma}_{\rm u}(T_{\rm u})=\hat{L}_{\rm u}\,\hat{s}_{\rm u}(T_{\rm u})$. More concretely, a Taylor expansion in ϵ of this equality yields

$$\begin{aligned}\hat{\sigma}^{(0)}_{\rm u}+\epsilon^2\,\hat{\sigma}^{(2)}_{\rm u}+\epsilon^4\,\hat{\sigma}^{(4)}_{\rm u}+\mathcal{O}(\epsilon^6)=&\left[\hat{L}_{{\rm nu}(0)}+\epsilon^2\,\hat{L}_{{\rm nu}(2)}+\epsilon^4\,\hat{L}_{{\rm nu}(4)}+\mathcal{O}(\epsilon^6)\right]\\ &\times\left[\hat{s}_{\rm u}(\hat{T}_0)+\epsilon^2\,\hat{T}_{(2)}\,\hat{s}'_{\rm u}(T_0)+\epsilon^4\left(\hat{T}_{(4)}\,\hat{s}'_{\rm u}(T_0)+\frac{1}{2}\,\hat{T}^2_{(2)}\,\hat{s}''_{\rm u}(T_0)\right)+\mathcal{O}(\epsilon^6)\right],\end{aligned} \tag{3.66}$$

which allows us to find the entropy correction coefficients $\hat{\sigma}^{(i)}_{\rm u}$ and thus the Killing entropy density $\hat{\sigma}_{\rm u}(\hat{T}_{\rm u})$ up to order $\mathcal{O}(\epsilon^6)$ of the uniform brane that has the same $(\hat{L},\hat{\rho})$ as the particular lumpy brane we selected. This procedure (3.62)-(3.65) can now be repeated for all lumpy branes.

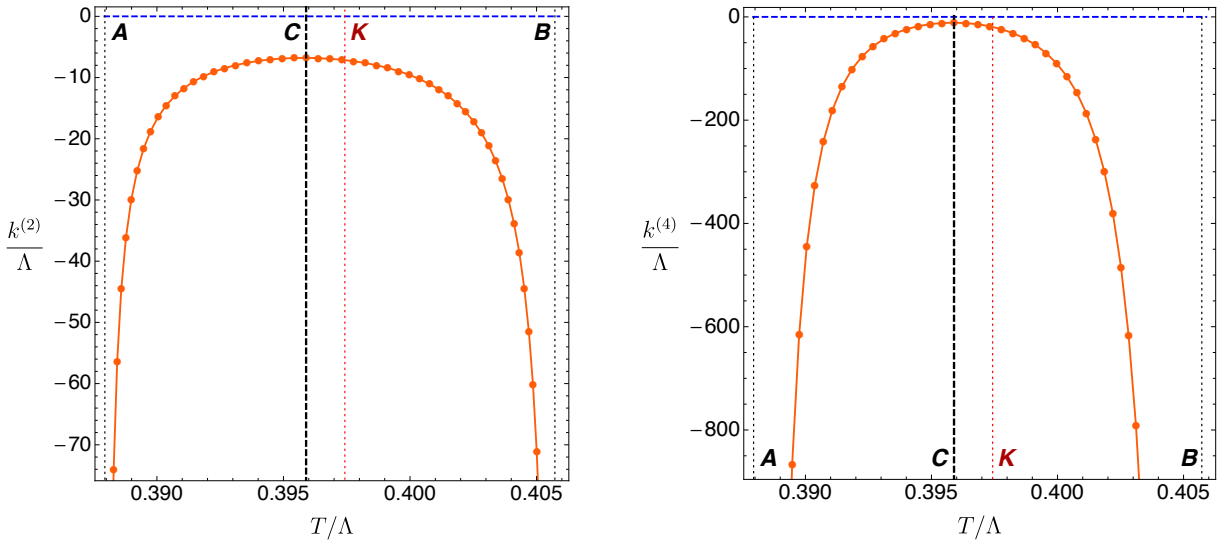

Figure 3.9: Wavenumber corrections $k^{(2)}$ (left panel) and $k^{(4)}$ (right panel), as defined in (3.56b), as a function of the uniform brane temperature. For reference, $\hat{T}_C \simeq 0.3958945$ and the maximum of the instability occurs for $\hat{T}_K \simeq 0.397427$.

We are now ready to discuss our higher-order perturbative findings. First, in Fig. 3.9 we plot the wavenumber corrections $k^{(2)}$ (left panel) and $k^{(4)}$ (right panel), as defined in (3.56b). The fact that these higher order quantities grow large as one approaches $\hat{T}_A$ and $\hat{T}_B$ tells us that our perturbation theory breaks down in these regions. We will come back to this below.

Second, in order to determine the dominant phase, we are interested in the entropy difference between a nonuniform and a uniform brane when the two have the same length $\hat{L}$ and Killing energy density $\hat{\rho}$. This is given by

$$\begin{aligned}\Delta\hat{\sigma}(\epsilon)\big|_{\text{same }\hat{L},\hat{\rho}} &= \left[\hat{\sigma}_{\rm nu}(\epsilon)-\hat{\sigma}_{\rm u}(\epsilon)\right]_{\text{same }\hat{L},\hat{\rho}} \\ &= \left(\hat{\sigma}^{(0)}_{\rm nu}-\hat{\sigma}^{(0)}_{\rm u}\right)+\epsilon^2\left(\hat{\sigma}^{(2)}_{\rm nu}-\hat{\sigma}^{(2)}_{\rm u}\right)+\epsilon^4\left(\hat{\sigma}^{(4)}_{\rm nu}-\hat{\sigma}^{(4)}_{\rm u}\right)+\mathcal{O}(\epsilon^6) \\ &\equiv \Delta\hat{\sigma}^{(0)}+\epsilon^2\Delta\hat{\sigma}^{(2)}+\epsilon^4\Delta\hat{\sigma}^{(4)}+\mathcal{O}(\epsilon^6)\,.\end{aligned} \tag{3.67}$$

By construction $\Delta\hat{\sigma}^{(0)} \equiv 0$ since the leading order of our perturbation theory describes the merger line of lumpy branes with uniform branes. Moreover, the first law for the Killing densities (3.54) can be rewritten, in the perturbative context, as $\partial_\epsilon\hat{\rho} = \hat{T}\,\partial_\epsilon\hat{\sigma} + \hat{\mathfrak{p}}_L\,\partial_\epsilon\hat{L}$ and has itself an expansion in ϵ that must be obeyed at each order. The leading-order term of this expansion implies that $\Delta\hat{\sigma}^{(2)} \equiv 0$, a condition that we actually use to test our numerical results. Therefore the first non-trivial contribution to $\Delta\hat{\sigma}(\epsilon)$ occurs at fourth order, namely

$$\Delta\hat{\sigma}(\epsilon)\big|_{\text{same }\hat{L},\hat{\rho}} = \left[\hat{\sigma}_{\rm nu}(\epsilon)-\hat{\sigma}_{\rm u}(\epsilon)\right]_{\text{same }\hat{L},\hat{\rho}} = \epsilon^4\Delta\hat{\sigma}^{(4)}+\mathcal{O}(\epsilon^6)\,. \tag{3.68}$$

This is the reason why we have to extend our perturbation analysis up to $\mathcal{O}(\epsilon^5)$.

We conclude that, for given $(\hat{L},\hat{\rho})$, if $\Delta\hat{\sigma}^{(4)} > 0$ then the lumpy branes are the preferred phase; otherwise the uniform branes are the dominant phase. We should thus plot the coefficient $\Delta\hat{\sigma}^{(4)}$ of (3.67) as a function of $\hat{L}$ and $\hat{\rho}$. However, we find it clearer to plot instead $\Delta\hat{\sigma}^{(4)}$ as a function of the temperature $\hat{T}_{\rm u}$ of the uniform brane that has the same $(\hat{L},\hat{\rho})$ as the lumpy brane we compare it with. This is done in Fig. 3.10. Recall that uniform branes can be GL-unstable only in the range $\hat{T}_A \le \hat{T} \le \hat{T}_B$ and $\hat{\mathcal{E}}_B < \hat{\mathcal{E}} < \hat{\mathcal{E}}_A$, see Fig. 3.3. It follows that lumpy branes bifurcate from the uniform branch at the GL zero mode for temperatures in the range

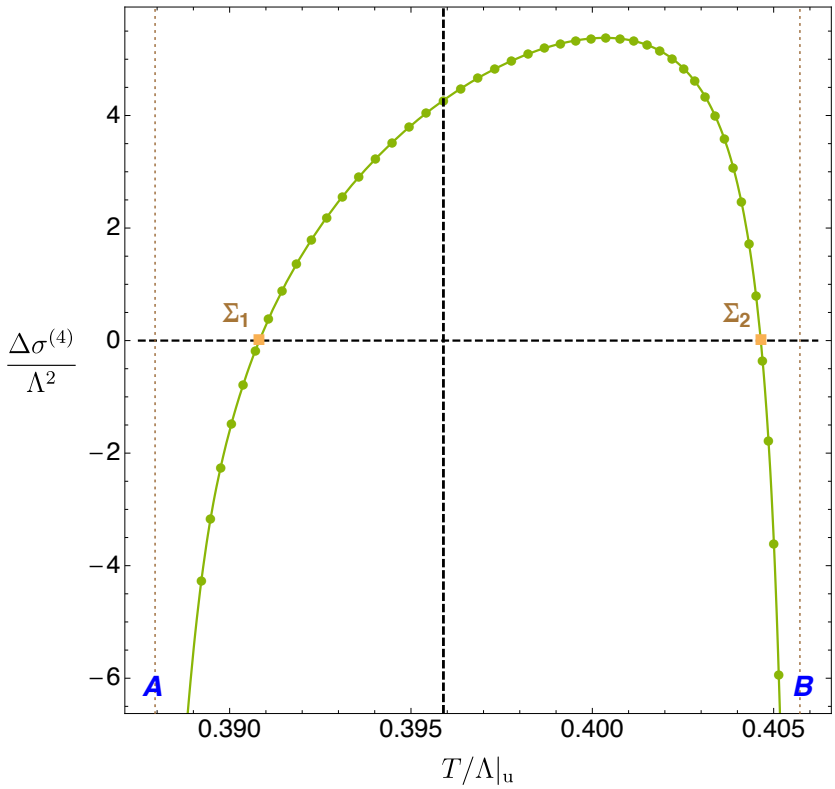

Figure 3.10: Perturbative identification of the dominant microcanonical phase. The horizontal axis shows the temperature $\hat{T}_{\rm u}$ of the uniform brane that has the same $(\hat{L}, \hat{\rho})$ as the lumpy brane we compare it with. The vertical axis shows the difference between the Killing entropy densities of the lumpy and the uniform branes. Thus lumpy branes (uniform branes) dominate if $\Delta\hat{\sigma}^{(4)} > 0$ ($\Delta\hat{\sigma}^{(4)} < 0$). For reference, $\hat{T}_{\rm c} \simeq 0.3958945$ (vertical black dashed line), $(\hat{T}, \hat{\mathcal{E}}, \hat{L}_{\rm GL})_{\Sigma_1} \simeq (0.390817, 0.950579, 5.618133)$ and $(\hat{T}, \hat{\mathcal{E}}, \hat{L}_{\rm GL})_{\Sigma_2} \simeq (0.404645, 0.717060, 6.592316)$.

$\hat{T}_A \leq \hat{T} \leq \hat{T}_B$. Fig. 3.10 plots this range of temperature and shows that for $\hat{T}_{\Sigma_1} < \hat{T} < \hat{T}_{\Sigma_2}$, where the values of $\hat{T}_{\Sigma_1}$ and $\hat{T}_{\Sigma_2}$ are identified in the caption, the lumpy branes are the preferred thermodynamic phase since $\Delta\hat{\sigma}^{(4)} > 0$. However, for $\hat{T}_A < \hat{T} < \hat{T}_{\Sigma_1}$ and $\hat{T}_{\Sigma_2} < \hat{T} < \hat{T}_B$, we have $\Delta\hat{\sigma}^{(4)} < 0$ and thus uniform branes dominate over the lumpy phase when they have the same dimensionless length $\hat{L}$ and Killing energy density $\hat{\rho}$. Going back to Fig. 3.8, for completeness we have also identified these points Σ_1 and Σ_2 in the associated GL merger curve.

Figs. 3.9 and 3.10 also illustrate the regime of validity of our perturbative expansion. For example, in Fig. 3.10 we see that $\Delta\hat{\sigma}^{(4)}$ grows arbitrarily negative as we approach the endpoints A and B of the *intermediate* branes with temperature $\hat{T}_A \simeq 0.387944$ and $\hat{T}_B \simeq 0.405724$ (see also Fig. 3.3). But once the associated entropy correction becomes of the order of our expansion parameter, $\Delta\hat{\sigma}^{(4)}\epsilon^4 \sim \epsilon$, perturbation theory breaks down. So we should not trust our perturbative results close to the endpoints A and B.

Even away from $\hat{T}_A$ and $\hat{T}_B$, our perturbation theory is certainly valid only for $\epsilon \ll 1$. Therefore we expect it to describe accurately the properties of lumpy branes close to their GL merger line with the uniform branes (where $\epsilon = 0$) but not far away from this merger. To learn what happens further away, we need to solve the full nonlinear BVP using numerical methods. This is what we do in the next subsection.

3.1.5 Full nonlinear solutions and phase diagram of nonconformal branes

To find accurately the lumpy branes and thus their thermodynamics in the full phase space where they exist, one needs to resort to numerical methods to solve nonlinearly the associated BVP, which was set up in Sec. 3.1.2. It consists of a coupled set of four quasilinear PDEs — two second-order PDEs for $q_{1,4}(x, y)$ and two second-order PDEs for $q_{2,3}(x, y)$ — that allow us to find the brane solutions (3.14) that obey the boundary conditions (3.16)-(3.23).

We solve our BVP using a Newton-Raphson algorithm. For the numerical grid discretization we use a pseudospectral collocation with a Chebyshev-Lobatto grid and the Newton-Raphson linear equations are solved by LU decomposition. These methods are reviewed and explained in detail in the review [102] and used in e.g. [103–107]. As explained in Sects. 3.1.1 and 3.1.2 (see in particular footnote 1 and the associated discussion) our gauge was judiciously chosen to guarantee that our solutions have analytical polynomial expansions at all the boundaries of the integration domain. In these conditions the pseudospectral collocation guarantees that our numerical results have exponential convergence with the number of grid points. We further use the first law and the Smarr relations (3.54)-(3.53) to check our numerics. In the worst cases, our solutions satisfy these relations with an error that is smaller than 1%. As a final check of our full nonlinear numerical results, we compare them against the perturbative expansion results of Sec. 3.1.4.

As usual, to initiate the Newton-Raphson algorithm one needs an educated seed. We use the perturbative solutions of Sec. 3.1.4 as seeds for the lumpy branes near the GL merger line with the uniform branes. The uniform branes are a 1-parameter family of solutions parametrized by the dimensionless temperature T/Λ. In contrast, the lumpy branes are a 2-parameter family of solutions that we can take to be T/Λ and the dimensionless length $L\Lambda$. This means that we need to scan a 2-dimensional parameter space. Our strategy to do so follows two routes. In one of them we follow lines of constant-temperature lumpy branes as their length $L\Lambda$ changes. The temperature T is given by (3.37) where the constant α_Λ and Λ (to build the dimensionless ratio T/Λ) are read from the uniform solution at the GL merger. The minimum length of these branes is the GL length $\hat{L}_{\rm GL}$ computed in Sec. 3.1.4, and constant-temperature branes exist for arbitrarily large $L\Lambda$. In a second route, we generate curves of lumpy branes that have fixed dimensionless length $L\Lambda$. In this path the temperature T/Λ of the branes changes but at the GL merger with the uniform branes, see e.g. Fig. 3.7, we know both the temperature $\hat{T}$ and the associated GL length $\hat{L}_{\rm GL}(\hat{T})$. Altogether these two solution-generating procedures allow us to construct a grid of two "orthogonal-like" lines of solutions that span the phase space of lumpy

branes. Further, recall that once we have the numerical solutions $q_j(x,y)$, the thermodynamic quantities of the lumpy branes are read straightforwardly from the expressions discussed in Sec. 3.1.3.

After these preliminaries we are ready to discuss our numerical nonlinear findings. A first important plot is shown in Fig. 3.11, where we show the dimensionless average energy density $\hat{\overline{\mathcal{E}}} = \overline{\mathcal{E}}/\Lambda^4$ as a function of the dimensionless temperature $\hat{T} = T/\Lambda$. Recall that for uniform branes $\hat{\overline{\mathcal{E}}}$ coincides with the dimensionless energy density, $\hat{\mathcal{E}}$, which is constant across the entire system. This plot contains again the uniform-brane spinodal curve (blue circles) already shown in Fig. 3.3 but this time we also show some representative examples of lumpy brane solutions (all other lines/curves).

As illustrated in Fig. 3.11, a first non-trivial conclusion of our study is that lumpy branes exist *only* in the temperature window $\hat{T}_A \leq \hat{T} \leq \hat{T}_B$ where $\hat{T}_A \simeq 0.387944$ and $\hat{T}_B \simeq 0.405724$. That is, they exist only in the temperature range where the GL-unstable, intermediate branch of uniform solutions (the curve ACB) exists. Of course, we should have anticipated that lumpy branes merge with the uniform branes of the *intermediate* branch and thus in the window $\hat{T}_A \leq \hat{T} \leq \hat{T}_B$. However, it was a logical possibility that, away from this merger, lumpy branes might exist also for temperatures outside the range $\hat{T} \in [\hat{T}_A, \hat{T}_B]$. We have generated considerably more solutions than those shown in Fig. 3.11 in order to test this possibility and, as stated above, we have found that it is not realised.

To continue interpreting Fig. 3.11, it is convenient to discuss separately the regions $\hat{T}_A \leq \hat{T} < \hat{T}_{\rm c}$ and $\hat{T}_{\rm c} < \hat{T} \leq \hat{T}_B$, i.e. the regions to the left and to the right, respectively, of the vertical dashed line DCE. Recall that this auxiliary line identifies the critical temperature $\hat{T} = \hat{T}_{\rm c}$ at which the first-order phase transition for uniform branes takes place (see right panel of Fig. 3.3).

So consider first lumpy branes that exist in the window $\hat{T}_A \leq \hat{T} < \hat{T}_{\rm c}$:

1. For a given temperature $\hat{T}$ in this range, lumpy branes exist with a dimensionless length that satisfies $\hat{L}_{\rm GL} \leq \hat{L} \leq \infty$. In particular, the vertical lines of orange circles of Fig. 3.11 are lumpy branes at constant $\hat{T}$ that have $\hat{L} = \hat{L}_{\rm GL}(\hat{T})$ when they bifurcate from the *intermediate* uniform-brane branch AC. Then they extend for arbitrarily large $\hat{L}$. More precisely, for $\hat{T} < \hat{T}_{\rm c}$, constant-$\hat{T}$ lumpy branes extend upwards (i.e. towards higher $\hat{\overline{\mathcal{E}}}$) as $\hat{L}$ grows. However, we find that for a given step increase in $\hat{L}$, the increase in $\hat{\overline{\mathcal{E}}}$ gets smaller and smaller as $\hat{L}$ grows, i.e. $(\partial\hat{\overline{\mathcal{E}}}/\partial\hat{L})|_{\hat{T}}$ is a monotonically decreasing function of $\hat{L}$. This is explicitly observed in the vertical lines that we display: *away* from the merger each two consecutive orange circles are separated by the *same* step in $\hat{L}$ but the step increase in $\hat{\mathcal{E}}$ is significantly decreasing as we move upwards. Due to the large hierarchy of scales that develops it is difficult to construct lumpy branes with $\hat{L} \to \infty$. But the above behaviour strongly suggests that lumpy branes with $\hat{T} < \hat{T}_{\rm c}$ are precisely bounded by the *heavy* uniform branch segment AD when $\hat{L} \to \infty$, i.e. we conjecture that

$$\lim_{\hat{L}\to\infty} \frac{\partial\hat{\mathcal{E}}}{\partial\hat{L}}\Big|_{\hat{T}} \to 0 \qquad \text{and} \qquad \lim_{\hat{L}\to\infty} \hat{\mathcal{E}}\Big|_{\text{const }\hat{T}} \to \hat{\mathcal{E}}_{\rm u}^{AD}(\hat{T})\,. \tag{3.69}$$

2. The other six curves (with $\triangledown, \diamond, \square, \bigcirc, \triangle, \otimes$) in Fig. 3.11, that intersect the vertical lines, describe six families of lumpy branes at constant $\hat{L}$. Concretely, the chosen fixed $\hat{L}$ increases as the curves go from the bottom to the top (for $\hat{T} < \hat{T}_{\rm c}$), i.e. $\hat{L}_{\triangledown} < \hat{L}_{\diamond} < \hat{L}_{\square} < \hat{L}_{\bigcirc} < \hat{L}_{\triangle} < \hat{L}_{\otimes}$. We find that constant-$\hat{L}$ lumpy branes *always* bifurcate from the *intermediate* uniform brane branch AC at a temperature/point that matches the temperature already found *independently* in Fig. 3.7, $\{\hat{T}, \hat{L}\} = \{\hat{T}, \hat{L}_{\rm GL}(\hat{T})\}$. This is thus a test of our numerics. In particular, curves with (constant) higher $\hat{L}$ bifurcate from the *intermediate* uniform brane with lower $\hat{T}$, i.e. the merger is closer to the endpoint A. In the limit $\hat{L} \to \infty$, this bifurcation occurs exactly at $\{\hat{T}, \hat{\mathcal{E}}\} = \{\hat{T}_A, \hat{\mathcal{E}}_A\}$ i.e. at point A, *in*

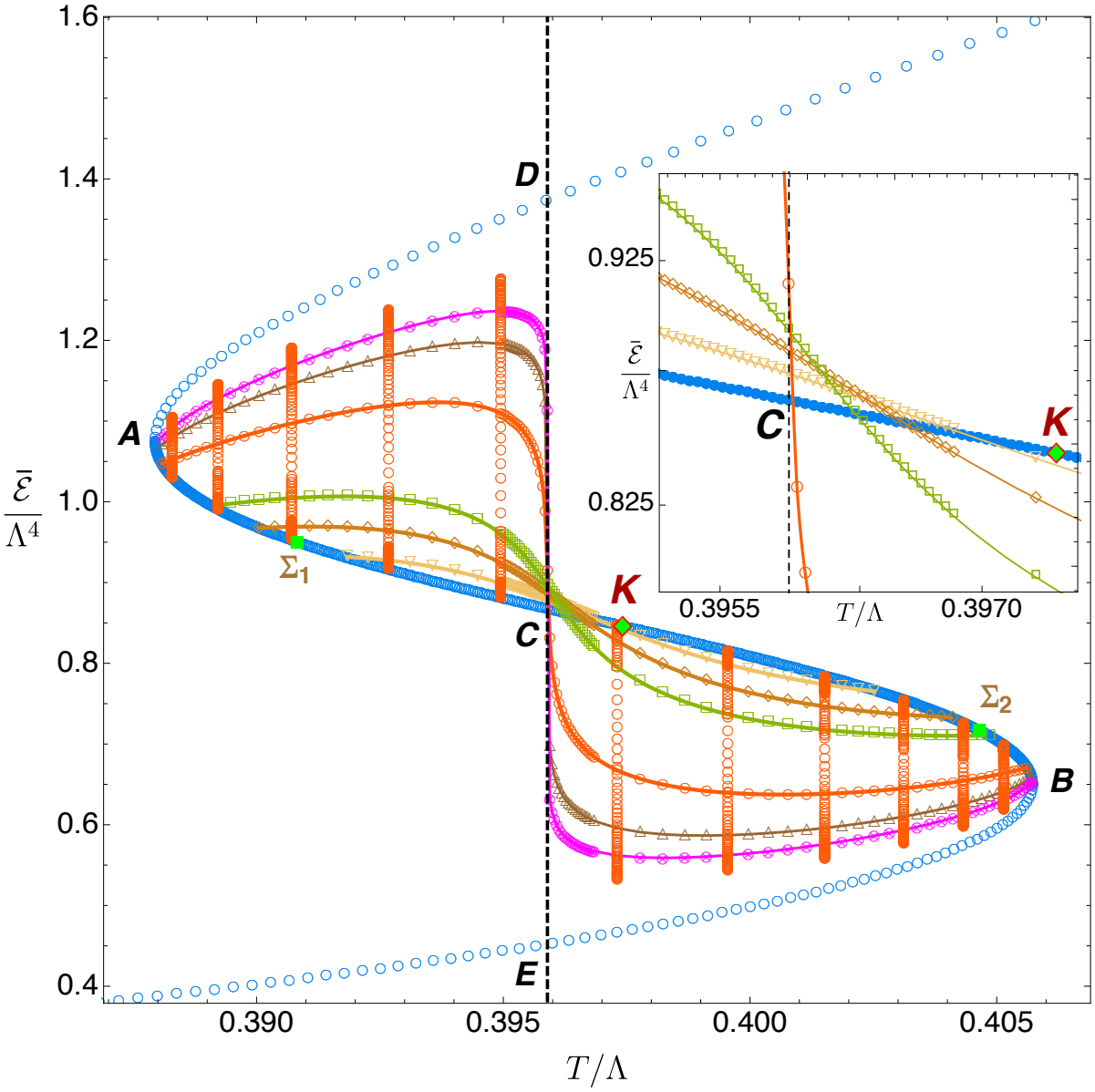

Figure 3.11: Phase diagram of Fig. 3.3 now with both uniform branes (blue circles) and some nonuniform brane solutions at constant temperature $\hat{T}$ (orange circles) or constant length $\hat{L}$. The eleven constant-temperature vertical lines have (from left to the right): $\hat{T} \simeq \{0.388292, 0.389219, 0.390711, 0.392677, 0.394948, 0.397308, 0.399547, 0.401511, 0.403112, 0.404320, 0.405141\}$. The six lumpy-brane curves at constant $\hat{L}$ have (from bottom to top on the left): $\hat{L}_\triangledown \simeq 5.299674$, $\hat{L}_\diamond \simeq 6.004224$, $\hat{L}_\square \simeq 6.900924$, $\hat{L}_\bigcirc \simeq 11.501849$, $\hat{L}_\triangle \simeq 17.906849$, $\hat{L}_\otimes \simeq 24.311849$. The inset plot is a zoom in around the region that contain C and K (see also Fig. 3.7) and here we plot the uniform-brane curve and just the four constant-$\hat{L}$ curves $\{\hat{L}_\triangledown, \hat{L}_\diamond, \hat{L}_\square, \hat{L}_\bigcirc\}$. For reference, $(\hat{T}, \hat{\mathcal{E}})_{\Sigma_1} \simeq (0.390817, 0.950579)$, $(\hat{T}, \hat{\mathcal{E}})_{\Sigma_2} \simeq (0.404645, 0.717060)$ and $(\hat{T}, \hat{\mathcal{E}})_K \simeq (0.397427, 0.846337)$.

agreement with the GL linear results of Fig. 3.7. As $\hat{L}$ decreases, the bifurcation occurs at temperatures that are increasingly closer to $\hat{T} = \hat{T}_c$. For $\hat{T} < \hat{T}_c$, constant-$\hat{L}$ curves do not intersect further the uniform branch AC.

Let us now follow these constant-$\hat{L}$ curves as they flow into the second relevant region, namely $\hat{T} > \hat{T}_c$. Fig. 3.11 shows that, if this was not already happening for smaller $\hat{T}$, all these curves have a drop in their $\hat{\mathcal{E}}$ as they approach $\hat{T}_c$ from the left. For very large $\hat{L}$ this drop is dramatic with an almost vertical slope (see e.g. the magenta, $\otimes$ curve). Therefore, as best illustrated in the inset plot of Fig. 3.11 that zooms in the region around point C, all constant-$\hat{L}$ curves pile up around point C in a way such that:

1. As $\hat{T} \to \hat{T}_c^-$ (approaching from the left) all curves have $\hat{\mathcal{E}} > \hat{\mathcal{E}}_C$. In particular, this means that these curves do not intersect the uniform branch AC near C.

2. Once at $\hat{T} > \hat{T}_c$, *all* constant-$\hat{L}$ curves that bifurcated from the uniform branes in the trench AC cross the uniform brane branch curve between C and K. Recall that K describes the uniform brane solution that has the largest GL wavenumber $k_{\rm GL}$ or, equivalently, that has the lowest $\hat{L}_{\rm GL} = 2\pi/k_{\rm GL}$; see Fig. 3.7. After this crossing, the constant-$\hat{L}$ lumpy branes keep extending to higher $\hat{T}$ with an energy density lower that the *intermediate* uniform brane with the same $\hat{T}$. This keeps happening until they merge again with the uniform brane in the trench KB at a critical temperature that is again the one predicted by the GL zero-mode analysis, i.e. at the highest $\hat{T}$ that satisfies the condition $\hat{L} = \hat{L}_{\rm GL}(\hat{T})$, see again Fig. 3.7. Lumpy-brane curves with higher constant $\hat{L}$ merge with the uniform branch KB at a point that is closer to B. In the limit where $\hat{L} \to \infty$ this merger occurs precisely at point B in Fig. 3.11, in agreement with the GL linear results of Fig. 3.7.

3. There are constant-$\hat{L}$ lumpy branes with very small $\hat{L}$ that bifurcate from the uniform brane branch *only* in the trench CK (*instead* of AC). Then they extend to higher $\hat{T}$, initially with $\hat{\mathcal{E}}$ higher that the uniform branes with same $\hat{T}$ before they cross the uniform branch CK at a temperature $\hat{T} < \hat{T}_K$ and proceed to higher $\hat{T}$ below point K until they merge again with the uniform brane branch but this time in the trench KB (at a point very close to K). This happens for fixed-$\hat{L}$ branes whenever $\hat{L}_{\rm GL}(\hat{T}_K) < \hat{L} < \hat{L}_{\rm GL}(\hat{T}_C)$.

The three features of the lumpy branes just listed are compatible with the following interpretation that merges our nonlinear findings, summarized in Fig. 3.11, with the GL linear results of Sec. 3.1.4, summarized in Fig. 3.7. Indeed, let us go back to Fig. 3.7 and consider an auxiliary horizontal line at constant $\hat{k}_{\rm GL}$, i.e. at constant $\hat{L}_{\rm GL}$. This line intersects the curve $\hat{k}_{\rm GL}(\hat{T})$ at two points. These are the two merger points of constant $\hat{L}$ lumpy branes with the uniform brane that we identify in Fig. 3.11. One of the mergers — let us denote it simply as the "left" merger — has $\hat{T}_A \leq \hat{T} \leq \hat{T}_K$ and the other — the "right" merger — has $\hat{T}_K \leq \hat{T} \leq \hat{T}_B$. Since the maximum of the GL wavenumber occurs at a temperature that is higher than the one of the first-order phase transition of the uniform system, $\hat{T}_K > \hat{T}_c$, it follows that the "left" mergers of lumpy branes with constant $\hat{L}_{\rm GL}(\hat{T}_K) < \hat{L} < \hat{L}_{\rm GL}(\hat{T}_C)$ are in the trench CK of Fig. 3.11. But, for $\hat{L} > \hat{L}_{\rm GL}(\hat{T}_C)$, the "left" merger is located in the trench AC, with the $\hat{L} \to \infty$ "left" merger being at A. On the other hand, the "right" merger is always located in the trench KB of Fig. 3.11, with the "right" merger of the $\hat{L} \to \infty$ lumpy branes being at B. Our nonlinear results summarized in Fig. 3.11 further conclude that there are no lumpy branes with $\hat{L} < \hat{L}_{\rm GL}(\hat{T}_K)$. As $\hat{L}$ approaches $\hat{L}_{\rm GL}(\hat{T}_K)$ from above, lumpy branes exist only in a small neighbourhood around point K in Fig. 3.11, with the characteristics described in item 3 in the list above.[11]

[11] Note that for other values of the (super)potential parameters ϕ_M and ϕ_Q in (2.2) (we have picked $\phi_M = 1$

We stress again that lumpy branes exist only in the temperature range $\hat{T}_A \leq \hat{T} \leq \hat{T}_B$. Our nonlinear results of Fig. 3.11 give strong evidence that constant-$\hat{T} < \hat{T}_c$ branes extend to arbitrarily large $\hat{L}$ with

$$\lim_{\hat{L}\to\infty} \hat{\mathcal{E}}\big|_{\text{const}\,\hat{T}} \to \hat{\mathcal{E}}_{\rm u}^{AD}(\hat{T})\,, \tag{3.70}$$

see the *heavy* uniform brane trench AD in Fig. 3.11. On the other hand, our results also strongly indicate that constant-$\hat{T} > \hat{T}_c$ branes extend to arbitrarily large $\hat{L}$ with

$$\lim_{\hat{L}\to\infty} \hat{\mathcal{E}}\big|_{\text{const}\,\hat{T}} \to \hat{\mathcal{E}}_{\rm u}^{EB}(\hat{T})\,, \tag{3.71}$$

see the *light* uniform brane trench ED in Fig. 3.11. Moreover, as $\hat{L}$ grows arbitrarily large, the constant-$\hat{L}$ lumpy branes intersect (without merging with) the *intermediate* uniform brane branch AB at a point that is arbitrarily close (from the right) to point C in Fig. 3.11 and with a slope $(\partial\hat{\bar{\mathcal{E}}}/\partial\hat{T})|_{\hat{T}_c}$ that grows unbounded, that is

$$\lim_{\hat{L}\to\infty} \left.\frac{\partial\hat{\bar{\mathcal{E}}}}{\partial\hat{T}}\right|_{\hat{T}_c} \to \infty\,. \tag{3.72}$$

In the limit $\hat{L}\to\infty$ we thus conjecture that lumpy branes are limited by the curve $ADCEB$ with two cusps connected by the vertical DCE line in Fig. 3.11. To argue further in favour of this conjecture, it is important to explore better the properties of the system in this $\hat{L}\to\infty$ limit and the associated limiting curve $ADCEB$. For that it is instructive to look at the energy density profile $\hat{\mathcal{E}}(x)$ of the lumpy branes as a function of the inhomogeneous direction x.

In Fig. 3.12 we first consider lumpy branes with the same $\hat{T}$ but different lengths $\hat{L}$.[12] In the left panel we have the profile of 3 lumpy branes with $\hat{T}\simeq 0.394948 < \hat{T}_c$; in the middle panel we have the profile of 3 lumpy branes with $\hat{T}\simeq 0.395894 \lesssim \hat{T}_c$ (i.e. almost at $\hat{T}_c\simeq 0.3958945$); and, finally, in the right panel we show the profile of 3 lumpy branes with $\hat{T}\simeq 0.397308 > \hat{T}_c$. In all panels, the blue diamond lines have a length only slightly above $\hat{L}_{\rm GL}(\hat{T})$. Therefore, the profile of these lumpy branes is almost flat and very close to the horizontal dashed line that represents the *intermediate* uniform brane with $\hat{\mathcal{E}}_{\rm u}^{AC}(\hat{T})$ (left/middle panels) or $\hat{\mathcal{E}}_{\rm u}^{CB}(\hat{T})$ (right panel). Then, the green square curves have a length of roughly $\hat{L}\sim 1.25\hat{L}_{\rm GL}(\hat{T})$. We see that the profile starts becoming considerably deformed with one of the "halves" pulling well above (below) the uniform brane profile with the same $\hat{T}$. Finally, the red disk curves represent lumpy branes that have a length $\hat{L}(\hat{T})$ that is considerably higher than $\hat{L}_{\rm GL}(\hat{T})$ (exact values in the caption). We see that the profile of lumpy branes with $\hat{T}\simeq 0.394948 < \hat{T}_c$ (left panel) is, in a wide range of x ($x\lesssim 0.7$), very flat with $\hat{\mathcal{E}}(x)\sim\hat{\mathcal{E}}_{\rm u}^{AD}(\hat{T})$, i.e. with an energy density that is the same as the one of the *heavy* uniform brane in the trench AD that has the same $\hat{T}$ (upper horizontal dashed line). Then, for $x\gtrsim 0.7$, $\hat{\mathcal{E}}(x)$ falls considerably towards the energy density $\hat{\mathcal{E}}_{\rm u}^{light}(\hat{T})$ of the *light* uniform brane that has the same temperature (lower horizontal dashed line). Still in Fig. 3.12, the middle panel shows that as $\hat{T}$ approaches $\hat{T}_c$ and for large $\hat{L}$ (red disks), the profile $\hat{\mathcal{E}}(x)$ describes a domain-wall solution that interpolates between $\hat{\mathcal{E}}_{\rm u}^{AD}(\hat{T})$ (for small x) and $\hat{\mathcal{E}}_{\rm u}^{light}(\hat{T})$ (for large x). On the other hand, for $\hat{T}\simeq 0.397308 > \hat{T}_c$ (right panel of Fig. 3.12) the roles of the *heavy* and *light* uniforms get reversed: for $x\lesssim 0.7$ the red disk

and $\phi_Q = 10$), or in similar spinodal systems, it might well be the case that $\hat{T}_c > \hat{T}_K$ or, for a fine-tuned choice of potential, even $\hat{T}_c = \hat{T}_K$. If that is the case our conclusions should still apply with the appropriate shift of K to the left of C in Figs. 3.7 and 3.11. Note that for this exercise we only need to find the uniform branes of the system and solve for static linear perturbations of these branes which determine the zero-mode GL wavenumber and thus the location of its maximum K with respect to $\hat{T}_c$. That is to say, we just need to complete the tasks described in sections 3.1.4 and 3.1.4.

[12] When interpreting these figures recall, from the discussion above (3.5), that our solutions have $\mathbb{Z}_2$ symmetry: the range $x\in[0,1]$ describes only the brane's half $\tilde{x} = xL/2 \in [0, L/2]$. To get the other half extension, $\tilde{x}\in[-L/2, 0]$, we just need to flip the profiles of Figs. 3.12-3.13 along their vertical axis.

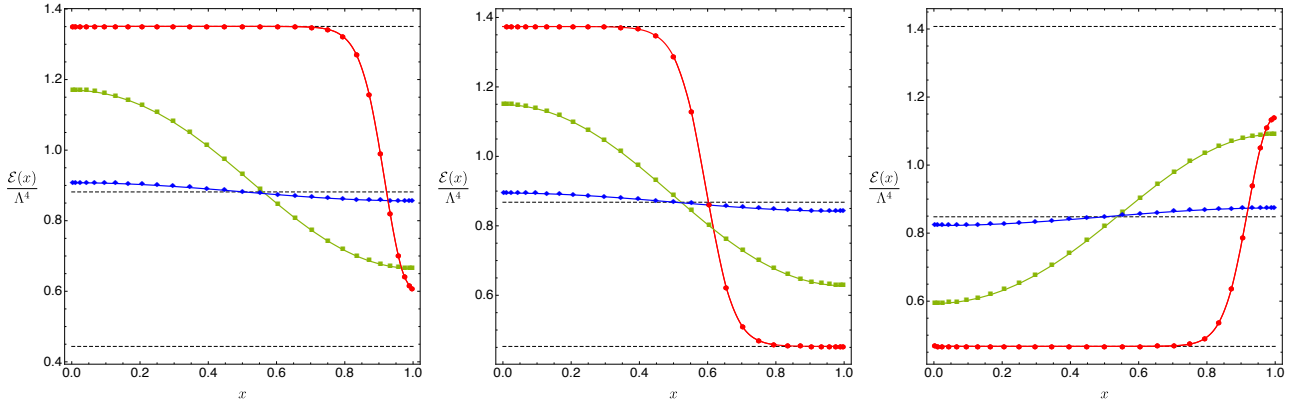

Figure 3.12: Energy density profile $\hat{\mathcal{E}}(x)$ for three lumpy branes at the same temperature $\hat{T}$.[12] (Left) Lumpy branes at constant $\hat{T} \simeq 0.394948$ (this is the first vertical line of orange circles to the left of C in Fig. 3.11). For reference, at the merger the lumpy brane with this temperature has $\hat{L} = \hat{L}_{\rm GL} \simeq 4.808993$ and $\hat{L}_{\blacklozenge} \simeq 4.819793$, $\hat{L}_{\blacksquare} \simeq 5.996993$, $\hat{L}_{\bullet} \simeq 37.208993$. For this temperature the heavy, intermediate and light uniform branes have energy densities $\hat{\mathcal{E}}^{heavy} \simeq 1.350615$, $\hat{\mathcal{E}}^{inter} \simeq 0.881537$ and $\hat{\mathcal{E}}^{light} \simeq 0.443756$, respectively. These energy densities are indicated by the dashed horizontal lines in the plot. (Middle) Lumpy branes at constant $\hat{T} \simeq 0.395894 \lesssim \hat{T}_c$ (so, very close to $\hat{T}_c \simeq 0.3958945$). For reference, $\hat{L} = \hat{L}_{\rm GL} \simeq 4.750995$ and $\hat{L}_{\blacklozenge} \simeq 4.761845$, $\hat{L}_{\blacksquare} \simeq 5.944495$, $\hat{L}_{\bullet} \simeq 46.523495$, and the energy densities of the relevant uniform branes (dashed horizontal lines) are $\hat{\mathcal{E}}^{heavy} \simeq 1.373843$, $\hat{\mathcal{E}}^{inter} \simeq 0.867966$, $\hat{\mathcal{E}}^{light} \simeq 0.452747$. (Right) Lumpy branes at constant $\hat{T} \simeq 0.397308$ (this is the first vertical line of orange circles to the right of C in Fig. 3.11). For reference, at the merger the lumpy brane with this temperature has $\hat{L} = \hat{L}_{\rm GL} \simeq 4.716232$ and $\hat{L}_{\blacklozenge} \simeq 4.727157$, $\hat{L}_{\blacksquare} \simeq 5.917982$, $\hat{L}_{\bullet} \simeq 34.759982$, and the energy densities of the relevant uniform branes (dashed horizontal lines) are $\hat{\mathcal{E}}^{heavy} \simeq 1.407521$, $\hat{\mathcal{E}}^{inter} \simeq 0.848014$, $\hat{\mathcal{E}}^{light} \simeq 0.467119$.

lumpy curve is almost flat with an energy density close to the one of the *light* uniform brane with the same $\hat{T}$, $\hat{\mathcal{E}}(x) \sim \hat{\mathcal{E}}_{\rm u}^{EB}(\hat{T})$ (lower horizontal dashed line), while for $x \gtrsim 0.7$, $\hat{\mathcal{E}}(x)$ starts increasing towards the energy density $\hat{\mathcal{E}}_{\rm u}^{heavy}(\hat{T})$ of the *heavy* uniform brane with the same $\hat{T}$ (upper dashed horizontal line).

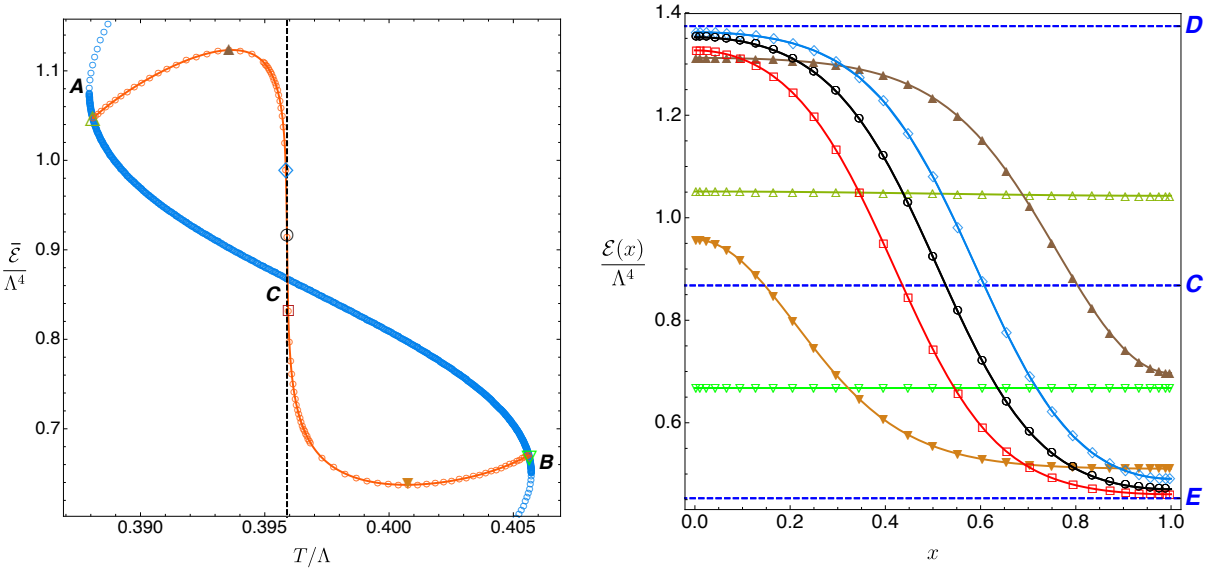

Figure 3.13: Lumpy branes at constant $\hat{L} \simeq 11.501849$. (Left) $\hat{\mathcal{E}}$ as a function of $\hat{T}$. This figure reproduces Fig. 3.11 but this time it singles out only the relevant lumpy brane with $\hat{L} = \hat{L}_{\bigcirc} \simeq 11.501849$ (orange circles) and the uniform branes (blue circles) and zooms in on the relevant region. It also identifies 7 solutions whose energy density profiles are then plotted on the right panel. From left to right these are given by: $(\hat{T}, \hat{\mathcal{E}})_{\triangle} \simeq (0.388085, 1.047078)$, $(\hat{T}, \hat{\mathcal{E}})_{\blacktriangle} \simeq (0.393560, 1.123216)$, $(\hat{T}, \hat{\mathcal{E}})_{\diamond} \simeq (0.395846, 0.988820)$, $(\hat{T}, \hat{\mathcal{E}})_{\bigcirc} \simeq (0.3958945, 0.914833)$, $(\hat{T}, \hat{\mathcal{E}})_{\square} \simeq (0.395941, 0.831460)$, $(\hat{T}, \hat{\mathcal{E}})_{\blacktriangledown} \simeq (0.400765, 0.637410)$, $(\hat{T}, \hat{\mathcal{E}})_{\triangledown} \simeq (0.405648, 0.667817)$. (Right) Energy density profile $\hat{\mathcal{E}}(x)$ for the 7 lumpy branes pinpointed in the left panel.[12] The same shape/colour code is used.

The $\hat{L} \to \infty$ limit of lumpy branes and its association with the limiting curve $ADCEB$ is further revealed when we complement Fig. 3.12 with an analysis of the energy density profile $\hat{\mathcal{E}}(x)$ of a constant-$\hat{L}$ family of branes for different values of the temperature. One such analysis is done in Fig. 3.13 where we fix $\hat{L} \simeq 11.501849$: this picks the fourth constant-$\hat{L}_{\bigcirc}$ curve (from bottom-left) in the plot of Fig. 3.11. For clarity we single out this curve and reproduce it — this time only the relevant zoomed in region of Fig. 3.11 — in the left panel of Fig. 3.13. We pinpoint a total of seven solutions with seven different temperatures (each one with its own distinctive plot marker shape and colour). The first ($\triangle$) and the last ($\triangledown$) solutions are the two mergers with the *intermediate* uniform brane, the second ($\blacktriangle$) and sixth ($\blacktriangledown$) solutions are the two extrema of $\hat{\mathcal{E}}(\hat{T})\big|_{\hat{L}}$, and the third ($\diamond$), fourth ($\bigcirc$) and fifth ($\square$) plot markers identify three solutions with $\hat{T}$ at or very close to $\hat{T}_{\rm c}$. As in Fig. 3.12, we see that the profile of the two lumpy branes at the merger is flat: they coincide with the uniform branes. As we move to the "extrema" solutions with plot markers $\blacktriangle$ and $\blacktriangledown$ we see, like for similar solutions in Fig. 3.12, that the profile is considerably deformed. More important for our purposes are the solutions with $\hat{T} \sim \hat{T}_{\rm c}$, e.g. $\diamond$, $\bigcirc$, $\square$. We see that for such cases the profile reaches its maximum deformation in the sense that the solution clearly interpolates between to regions that are fairly flat. Importantly, the small-x flat region is approaching the energy density $\hat{\mathcal{E}}_{\rm u}^{D}(\hat{T}_{\rm c})$ of the *heavy* uniform brane that has $\hat{T} = \hat{T}_{\rm c}$ (see the upper, horizontal, dashed, blue line labelled by D). Similarly, the large-x flat region is approaching the energy density $\hat{\mathcal{E}}_{\rm u}^{E}(\hat{T}_{\rm c})$ of the *light* uniform brane that has $\hat{T} = \hat{T}_{\rm c}$ (see the lower, horizontal, dashed, blue curve labelled by E). We further see that the closer we are to

$\hat{T}_c^-$ ($\hat{T}_c^+$), the closer we get to $\hat{\mathcal{E}}_u^D(\hat{T})$ ($\hat{\mathcal{E}}_u^E(\hat{T})$). The plot of Fig. 3.13 is for a moderate value of $\hat{L}$. Combined with the findings of the discussion of Fig. 3.12 we conclude that as $\hat{L}$ grows large and $\hat{T} \to \hat{T}_c$, the flat regions get more extended in x and the domain wall that interpolates between them at $\hat{\mathcal{E}} \sim \hat{\mathcal{E}}_u^D(\hat{T}_c)$ and $\hat{\mathcal{E}} \sim \hat{\mathcal{E}}_u^E(\hat{T}_c)$ gets narrower.

Altogether, the findings summarized in Fig. 3.12 and Fig. 3.13 lead to the following conclusion/conjecture. In the double limit $\hat{L} \to \infty$ and $\hat{T} \to \hat{T}_c$ our results support the conjecture that

$$\lim_{\hat{L}\to\infty} \left.\frac{\partial \hat{\mathcal{E}}}{\partial \hat{T}}\right|_{\hat{T}_c} \to \infty \,. \tag{3.73}$$

That is, in this double limit we have a family of lumpy branes that fills up the segment DCE of Fig. 3.11. All this segment describes infinite-length lumpy branes that are sharp/narrow domain wall solutions interpolating (along $0 \leq \tilde{x} \leq \infty$) between two flat regions: one with $\hat{\mathcal{E}}(\tilde{x}) = \hat{\mathcal{E}}_u^D(\hat{T}_c)$ and the other with $\hat{\mathcal{E}}(\tilde{x}) = \hat{\mathcal{E}}_u^E(\hat{T}_c)$. These are the phase-separated configurations discussed above. As we move up from C to D, the region of $\tilde{x}$ with $\hat{\mathcal{E}}(\tilde{x}) = \hat{\mathcal{E}}_u^D$ increases while as we move down from C to E, the region of $\tilde{x}$ with $\hat{\mathcal{E}}(\tilde{x}) = \hat{\mathcal{E}}_u^E$ increases. We have infinite domain wall solutions that interpolate between the two uniform phases of the system at $T = T_c$. Moreover, keeping the limit $\hat{L} \to \infty$, but relaxing the condition $\hat{T} \to \hat{T}_c$, the results summarized in Figs. 3.12 and 3.13 give evidence to conjecture that infinite-length lumpy branes exist only for $\hat{T}_A \leq \hat{T} \leq \hat{T}_B$ and are exactly at the line $ADCEB$ of Fig. 3.11.

We will now discuss the thermal competition between lumpy and uniform nonconformal branes in the microcanonical ensemble. Recall that we keep the dimensionless length $\hat{L}$ and the Killing energy density $\hat{\rho}$ fixed and the relevant thermodynamic potential is the Killing entropy density $\hat{\sigma}$. Again, uniform and lumpy branes co-exist for temperatures $\hat{T}_A \leq \hat{T} \leq \hat{T}_B$. So in the microcanonical ensemble, given a lumpy brane with $(\hat{L}, \hat{\rho})$, our first task is to find the uniform brane (i.e. the temperature $\hat{T}$ which parametrizes this family) that has the same $(\hat{L}, \hat{\rho})$ as the chosen lumpy brane. Once this is done, we can compare the Killing entropy densities $\hat{\sigma}$ of the two solutions at the same selected $(\hat{L}, \hat{\rho})$ pair. As for the perturbative analysis of Sec. 3.1.4 — see e.g. the discussion of (3.67) — we compute the entropy difference between the two phases when they have the same $\hat{L}$ and $\hat{\rho}$:

$$\Delta\hat{\sigma}\big|_{\text{same } \hat{L},\hat{\rho}} = \left[\hat{\sigma}_{\text{nu}} - \hat{\sigma}_{\text{u}}\right]_{\text{same } \hat{L},\hat{\rho}} \,. \tag{3.74}$$

As before, the subscript "nu" stands for the nonuniform (lumpy) brane and "u" denotes the uniform brane. From our perturbative analysis recall that at the merger curve (ACB in Fig. 3.11 or the black dotted line in Fig. 3.8) between uniform and lumpy branes one must have $\Delta\hat{\sigma}\big|_{\text{same } \hat{L},\hat{\rho}} = 0$. Moreover, in the perturbative analysis leading to Fig. 3.10 we found that lumpy branes that bifurcate from uniform branes in the trench $\Sigma_1\Sigma_2$ of Figs. 3.11 or 3.8 do so with a positive entropy difference slope. In other words, slightly away from the merger curve we have $\Delta\hat{\sigma}\big|_{\text{same } \hat{L},\hat{\rho}} > 0$. This means that lumpy branes emanating from the GL merger dominate over the uniform branes with the same $\hat{L}, \hat{\rho}$, at least "initially". On the other hand, in the complement of $\Sigma_1\Sigma_2$, i.e. for lumpy branes bifurcating from $A\Sigma_1$ or $\Sigma_2 B$ in Fig. 3.11, the perturbative analysis of Fig. 3.10 shows that $\Delta\hat{\sigma}\big|_{\text{same } \hat{L},\hat{\rho}} < 0$. That is, in this case for a given $(\hat{L}, \hat{\rho})$ lumpy branes have less Killing entropy density than the uniform solutions and thus the latter are the preferred phase in the microcanonical ensemble.

Now that we have the full nonlinear solutions, our first task is to naturally compare these results with the perturbative results of Sec. 3.1.4 that led to Fig. 3.10. On the one hand this will check our numerical results. On the other hand it will identify the regime of validity of the perturbative analysis, i.e. how "far away" from the merger curve it holds. To illustrate this comparison, in Fig. 3.14 we show $\Delta\hat{\sigma}\big|_{\text{same } \hat{L},\hat{\rho}}$ as a function of $\hat{\rho}$ for a family of lumpy branes that have a fixed temperature $\hat{T}$. Note that, as $\hat{\rho}$ changes, so does $\hat{L}$ in order to keep $\hat{T}$ fixed (this

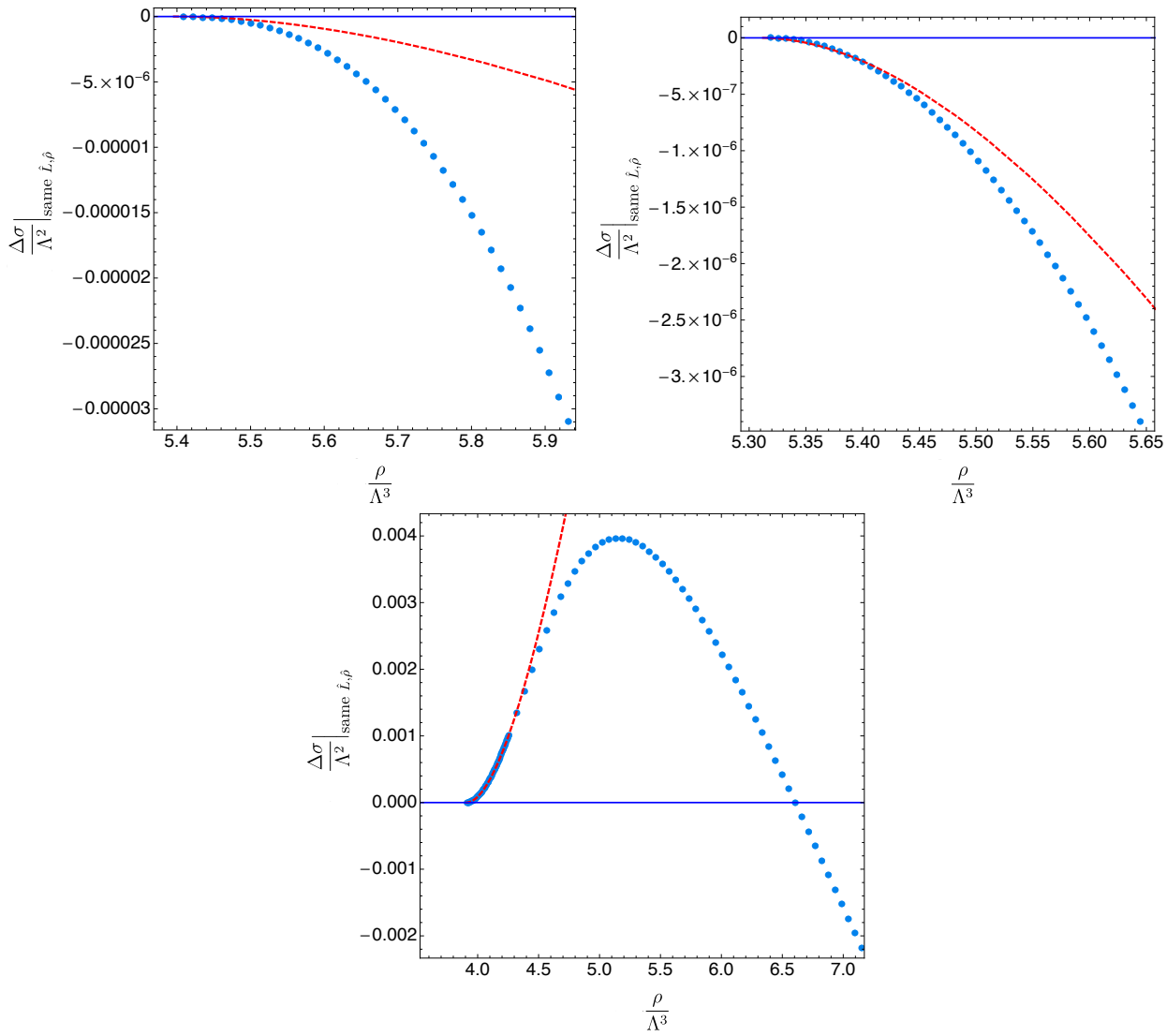

Figure 3.14: Difference $\Delta\hat{\sigma}|_{\text{same }\hat{L},\hat{\rho}}$ between the Killing entropy densities of lumpy and uniform branes with the same $(\hat{L},\hat{\rho})$ as a function of the Killing energy density $\hat{\rho}$ for three constant-$\hat{T}$ families of lumpy branes with $\hat{T}\simeq 0.390711<\hat{T}_{\Sigma_1}$ (top-left), $\hat{T}\simeq 0.405141>\hat{T}_{\Sigma_2}$ (top-right) and $\hat{T}_{\Sigma_1}<\hat{T}\simeq 0.399547<\hat{T}_{\Sigma_2}$ (bottom). Recall that $\hat{T}_{\Sigma_1}\simeq 0.390817$ and $\hat{T}_{\Sigma_2}\simeq 0.404645$. The blue dots are the numerical results for the lumpy branes. The dashed, red curves are the perturbative result (3.67). The horizontal blue line indicates the uniform-brane family.

effect is better illustrated in Fig. 3.15, as we explain below). The plots in the top row of Fig. 3.14 illustrate what happens for $\hat{T} < \hat{T}_{\Sigma_1}$ (left) and $\hat{T} > \hat{T}_{\Sigma_2}$ (right). In these cases the perturbative analysis summarized in Fig. 3.10 predicts that lumpy branes bifurcate from the GL merger with $\Delta\hat{\sigma}|_{\text{same } \hat{L},\hat{\rho}} < 0$, as indicated by the dashed red curves in Fig. 3.14. The numerical nonlinear results, shown as blue dots, indeed confirm this, and they are in excellent agreement with the perturbative results near the merger with the uniform brane. The numerical nonlinear results then show the regime where the perturbative analysis ceases to be valid and that $\Delta\hat{\sigma}|_{\text{same } \hat{L},\hat{\rho}}$ decreases monotonically with $\hat{\rho}$ (we have extended the computation to much higher values of ρ than those shown in the plot). The plot in the bottom row of Fig. 3.14 illustrates what happens for a constant-$\hat{T}$ lumpy brane family that bifurcates from an intermediate uniform brane with $\hat{T}_{\Sigma_1} < \hat{T} < \hat{T}_{\Sigma_2}$. In this case the perturbative analysis (see Fig. 3.10) tells us that the bifurcation occurs with $\Delta\hat{\sigma}|_{\text{same } \hat{L},\hat{\rho}} > 0$. Again the full nonlinear analysis confirms this is the case and is in excellent agreement with the perturbative results near the merger. However, in this case the nonlinear analysis provides new crucial information away from the merger: it shows that, although $\Delta\hat{\sigma}|_{\text{same } \hat{L},\hat{\rho}}$ initially grows away from the GL merger, at a certain point it reaches a maximum and then it starts to decrease until it becomes negative. We have extended the computation to much larger values of $\hat{\rho}$ than those shown in the plot and we have found that, beyond this point, $\Delta\hat{\sigma}|_{\text{same } \hat{L},\hat{\rho}}$ becomes more and more negative as $\hat{\rho}$ becomes larger and larger. Since both $\hat{\sigma}_{\text{nu}}$ and $\hat{\sigma}_{\text{u}}$ are non-negative, the reason for this is clearly that $\hat{\sigma}_{\text{u}}$ becomes arbitrarily large. In turn, this is due to the fact that, on a constant-T curve, $\hat{L}$ becomes larger and larger as $\hat{\rho}$ increases (see Fig. 3.15), which causes the integral over the x-direction of the entropy density $\hat{s}$ to diverge. At the value of $(\hat{\rho}, \hat{L})$ where $\Delta\hat{\sigma}$ crosses zero, there is a phase transition between lumpy and uniform branes. This is a first-order phase transition since, for example, the temperature changes discontinuously. We emphasize that, at the qualitative level, this behaviour is the same for all constant-$\hat{T}$ families of lumpy branes that bifurcate from uniform branes in between points Σ_1 and Σ_2 in Fig. 3.11.

To further understand this phase transition, in Figs. 3.15 and 3.16 we reproduce again the stability diagram of Fig. 3.8, but this time we also plot a few constant-$\hat{T}$ or constant-$\hat{L}$ lumpy branes that depart from the GL merger curve. We use two plot marker codes: The solid blue markers, no matter their shape, represent the trench where $\Delta\hat{\sigma}|_{\text{same } \hat{L},\hat{\rho}} > 0$, while the empty orange markers, no matter their shape, describe the region where $\Delta\hat{\sigma}|_{\text{same } \hat{L},\hat{\rho}} < 0$. For reference, recall that

$$\begin{aligned} (\hat{T}, \hat{L}_{\text{GL}}, \hat{\mathcal{E}})_{\Sigma_1} &\simeq (0.390817, 5.618133, 0.950579)\,, \\ (\hat{T}, \hat{L}_{\text{GL}}, \hat{\mathcal{E}})_{\Sigma_2} &\simeq (0.404645, 6.592316, 0.717060)\,, \\ (\hat{T}, \hat{L}_{\text{GL}}, \hat{\mathcal{E}})_{K} &\simeq (0.397427, 4.716021, 0.846337)\,. \end{aligned} \tag{3.75}$$

For brevity, henceforth we will use the notation

$$\hat{L}_{\Sigma_1} \equiv \hat{L}_{\text{GL}}|_{\Sigma_1}\,, \qquad \hat{L}_{\Sigma_2} \equiv \hat{L}_{\text{GL}}|_{\Sigma_2}\,, \qquad \hat{L}_{K} \equiv \hat{L}_{\text{GL}}|_{K}\,. \tag{3.76}$$

The main conclusions from Figs. 3.15 and 3.16 are as follows:

1. Recall that lumpy branes that bifurcate from the GL merger line at a temperature $\hat{T} < \hat{T}_{\Sigma_1}$ (i.e. above Σ_1 in the figures) or at a temperature $\hat{T} > \hat{T}_{\Sigma_2}$ (i.e. below Σ_2 in the figures) have $\Delta\hat{\sigma}|_{\text{same } \hat{L},\hat{\rho}} < 0$ no matter how large $\hat{L}$ is, as pointed out when discussing Fig. 3.14 (recall that Σ_1 and Σ_2 were introduced in Fig. 3.10). In Fig. 3.15 we display one family of lumpy branes in each of these classes. One has constant $\hat{T}_{\times} \simeq 0.390711 < \hat{T}_{\Sigma_1}$ and is always described by empty orange colour markers, which means that the solutions indeed have $\Delta\hat{\sigma}|_{\text{same } \hat{L},\hat{\rho}} < 0$. All the curves that bifurcate from the GL merger above Σ_1 have this feature and they always bifurcate towards higher $\hat{\mathcal{E}}$ and higher $\hat{L}$ with respect to the merger point $(\hat{\mathcal{E}}_{\text{GL}}, \hat{L}_{\text{GL}})$. The other family has constant $\hat{T}_{\otimes} \simeq 0.405141 > \hat{T}_{\Sigma_2}$ and is

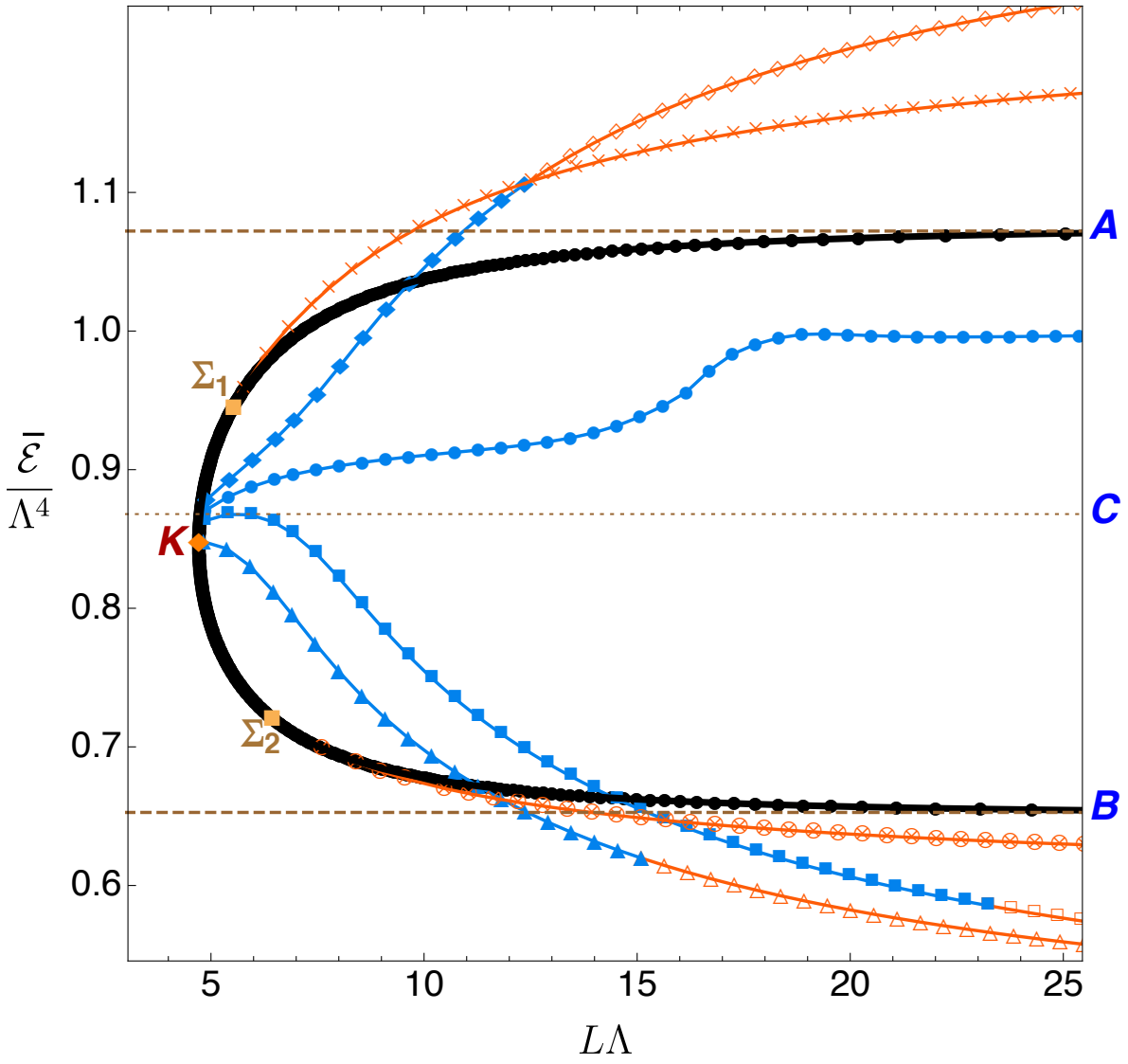

Figure 3.15: Same stability diagram as in Fig. 3.8 with the inclusion of some lumpy-brane curves that bifurcate from the GL merger curve. These curves have constant $\hat{T}$ given by $\{\hat{T}_\times, \hat{T}_\otimes, \hat{T}_\blacklozenge, \hat{T}_\bullet, \hat{T}_\blacksquare, \hat{T}_\blacktriangle\} \simeq \{0.390711, 0.405141, 0.395420, 0.395894, 0.396367, 0.397307\}$. Solid blue markers (empty orange markers), no matter their shape, indicate positive (negative) $\Delta\hat{\sigma}|_{\text{same } \hat{L},\hat{\rho}}$.

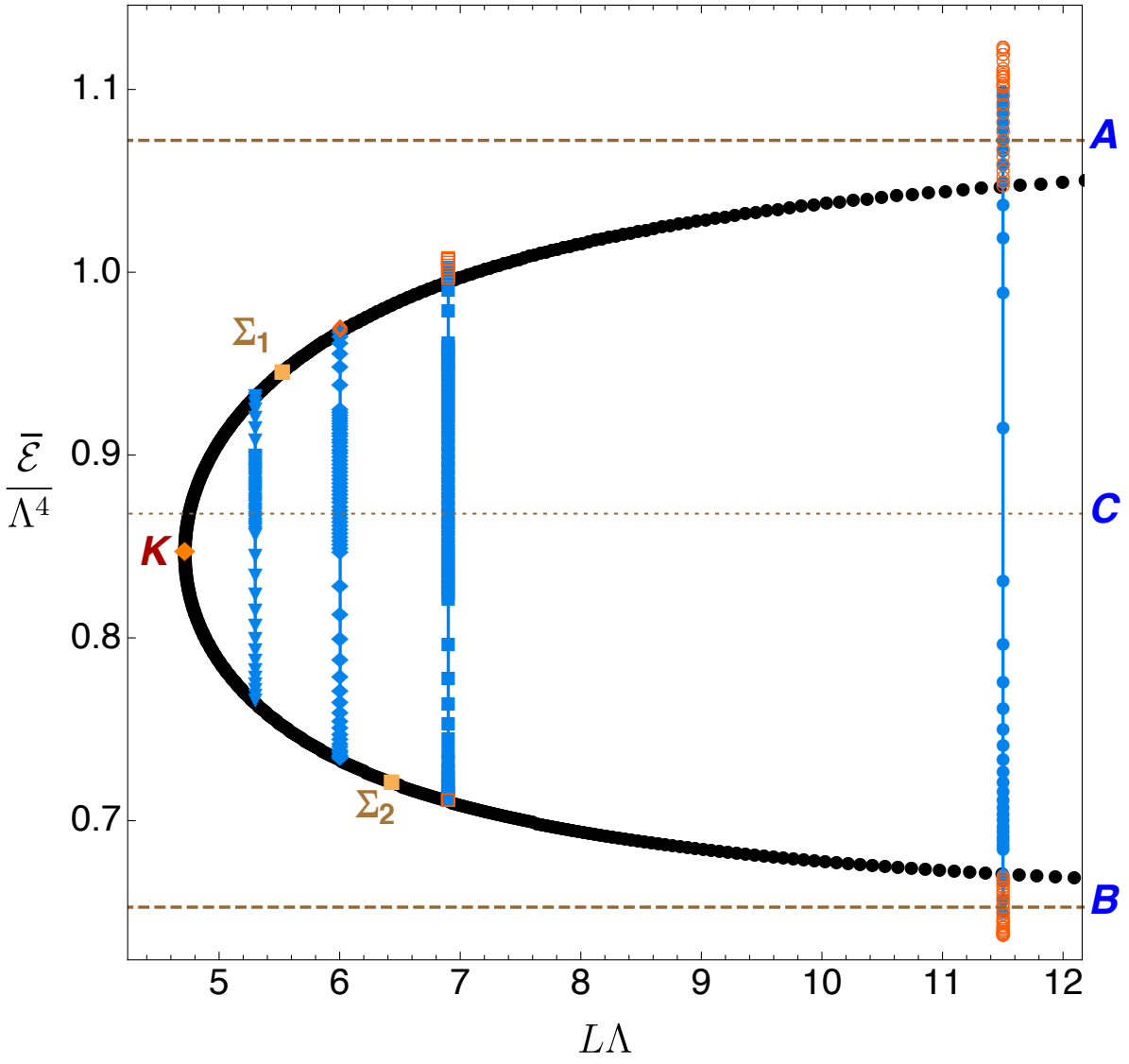

Figure 3.16: Same stability diagram as in Fig. 3.8 with the inclusion of some lumpy-brane lines that bifurcate from the GL merger curve. These lines have constant $\hat{L}$ given by $\{\hat{L}_{\blacktriangledown}, \hat{L}_{\blacklozenge}, \hat{L}_{\blacksquare}, \hat{L}_{\bullet}\} \simeq \{5.299674, 6.004224, 6.900924, 11.501849\}$. Solid blue markers (empty orange markers), no matter their shape, indicate positive (negative) $\Delta\hat{\sigma}\big|_{\text{same } \hat{L},\hat{\rho}}$. Note that some orange circles are on top of some blue disks. This describes the region around the cusps of Fig. 3.17 and 3.18.

again always described by empty orange markers, which means that the solutions indeed have $\Delta\hat{\sigma}\big|_{\text{same }\hat{L},\hat{\rho}} < 0$. All the curves that bifurcate from the GL merger below Σ_2 have this feature and they always bifurcate towards lower $\hat{\mathcal{E}}$ and higher $\hat{L}$ with respect to the merger point $(\hat{\mathcal{E}}_{\rm GL}, \hat{L}_{\rm GL})$.

2. The situation is less monotonous for lumpy branes that bifurcate from a point on the GL merger curve that lies between Σ_1 and Σ_2. Recall that these have, close to the merger, $\Delta\hat{\sigma}\big|_{\text{same }\hat{L},\hat{\rho}} > 0$. In Fig. 3.15 we display four curves in this class, namely: the family with constant $\hat{T}_{\blacklozenge} \simeq 0.395420 < \hat{T}_c$; the family with constant $\hat{T}_{\bullet} \simeq 0.395894 \lesssim \hat{T}_c$ (so, very close to $\hat{T}_c \simeq 0.3958945$); the family with constant $\hat{T}_{\blacksquare} \simeq 0.396367 > \hat{T}_c$; and the family with constant $\hat{T}_{\blacktriangle} \simeq 0.397307 > \hat{T}_c$ (slightly below $\hat{T}_K \simeq 0.397427$). These curves with $\hat{T}_{\Sigma_2} < \hat{T} < \hat{T}_{\Sigma_2}$ bifurcate towards $\hat{L} > \hat{L}_{\rm GL}$ with $\Delta\hat{\sigma}\big|_{\text{same }\hat{L},\hat{\rho}} > 0$. Then, if $\hat{T}_{\Sigma_1} < \hat{T} < \hat{T}_{\rm c}$ (e.g. the curve with diamond plot markers $\blacklozenge$) they typically move to higher $\hat{\bar{\mathcal{E}}}$ as $\hat{L}$ increases and $\Delta\hat{\sigma}\big|_{\text{same }\hat{L},\hat{\rho}}$ changes from positive into negative when the plot markers change from solid blue $\blacklozenge$ into empty orange $\diamond$. On the other hand, if $\hat{T}_{\rm c} < \hat{T} < \hat{T}_{\Sigma_2}$ (e.g. the curves initially with $\blacksquare$ and $\blacktriangle$), the constant $\hat{T}$-curves typically plunge into lower $\hat{\bar{\mathcal{E}}}$ as $\hat{L}$ increases and $\Delta\hat{\sigma}\big|_{\text{same }\hat{L},\hat{\rho}}$ changes from positive into negative when the plot markers change from solid blue into empty orange (i.e. $\blacksquare \to \square$ or $\blacktriangle \to \triangle$).

3. When $\hat{T} \sim \hat{T}_c$ the properties described in the two previous points hold but the constant-$\hat{T}$ curves do not escape to large $\hat{\bar{\mathcal{E}}}$ (if $\hat{T} \lesssim \hat{T}$) or small $\hat{\bar{\mathcal{E}}}$ (if $\hat{T} \gtrsim \hat{T}$) so quickly as $\hat{L}$ grows. A good example is given by the dotted ($\bullet$) curve with $\hat{T}_{\bullet} \simeq 0.395894 \lesssim \hat{T}_c$. The closer one is of $\hat{T}_{\rm c}$ the longer $\hat{L}$ must be for the constant-$\hat{T}$ curve to cross the GL merger line again and then acquire $\Delta\hat{\sigma}\big|_{\text{same }\hat{L},\hat{\rho}} < 0$. Our results suggest that in the exact limit $\hat{T} \to \hat{T}_{\rm c}$ the curve extends to $\hat{L} \to \infty$ without ever leaving the window of energy densities $[\hat{\mathcal{E}}_B, \hat{\mathcal{E}}_A]$.

To complete our understanding of the microcanonical phase diagram, in Fig. 3.17 we plot the Killing entropy density difference $\Delta\hat{\sigma}\big|_{\text{same }\hat{L},\hat{\rho}}$ between lumpy and uniform branes with the same $(\hat{L}, \hat{\rho})$ as a function of the Killing energy density $\hat{\rho}$ for three families of lumpy branes that have *constant* $\hat{L}$. Note that $\hat{L}_K < \hat{L}_{\Sigma_1} < \hat{L}_{\Sigma_2}$ (see e.g. Fig. 3.16). The three panels of Fig. 3.17 describe representative examples of the following three possible cases: (1) $\hat{L}_K < \hat{L} < \hat{L}_{\Sigma_1}$ (top-left panel), (2) $\hat{L}_{\Sigma_1} < \hat{L} < \hat{L}_{\Sigma_2}$ (top-right panel), and (3) $\hat{L} > \hat{L}_{\Sigma_2}$ (bottom panel). Together with those in Fig. 3.14, the plots in Fig. 3.17 are the most important ones in our analysis of the phase diagram. The three panels of Fig. 3.17 encode the following conclusions:

1. The top-left panel is for constant $\hat{L} \simeq 5.299674$ solutions and illustrates what happens in the three-dimensional microcanonical phase diagram $\Delta\hat{\sigma}\big|_{\text{same }\hat{L},\hat{\rho}}$ versus $(\hat{\rho}, \hat{L})$ when the lumpy branes have $\hat{L}_K < \hat{L} < \hat{L}_{\Sigma_1}$. We see that in this range of $\hat{L}$, lumpy branes (yellow inverted triangles) bifurcate from the uniform brane (blue line) at low $\hat{\rho}$ with $\Delta\hat{\sigma}\big|_{\text{same }\hat{L},\hat{\rho}} > 0$ and, as $\hat{\rho}$ increases, the entropy difference grows until it reaches a maximum and then it decreases monotonically until the lumpy brane merges again with the uniform brane at higher $\hat{\rho}$. Since in this range of $(\hat{L}, \hat{\rho})$ one always has $\Delta\hat{\sigma}\big|_{\text{same }\hat{L},\hat{\rho}} > 0$, lumpy branes are the preferred phase in the microcanonical ensemble.

2. The top-right panel is for constant $\hat{L} \simeq 6.004224$ solutions and illustrates what happens in the 3-dimensional microcanonical phase diagram $\Delta\hat{\sigma}\big|_{\text{same }\hat{L},\hat{\rho}}$ versus $(\hat{\rho}, \hat{L})$ when the lumpy branes have $\hat{L}_{\Sigma_1} < \hat{L} < \hat{L}_{\Sigma_2}$. As in the previous case, in this range of $\hat{L}$, lumpy branes (brown diamonds) also bifurcate from the uniform brane (blue line) at low $\hat{\rho}$ with $\Delta\hat{\sigma}\big|_{\text{same }\hat{L},\hat{\rho}} > 0$ and, as $\hat{\rho}$ increases, the entropy difference grows until it reaches a maximum. Then it again decreases monotonically but, this time, $\Delta\hat{\sigma}\big|_{\text{same }\hat{L},\hat{\rho}}$ becomes negative

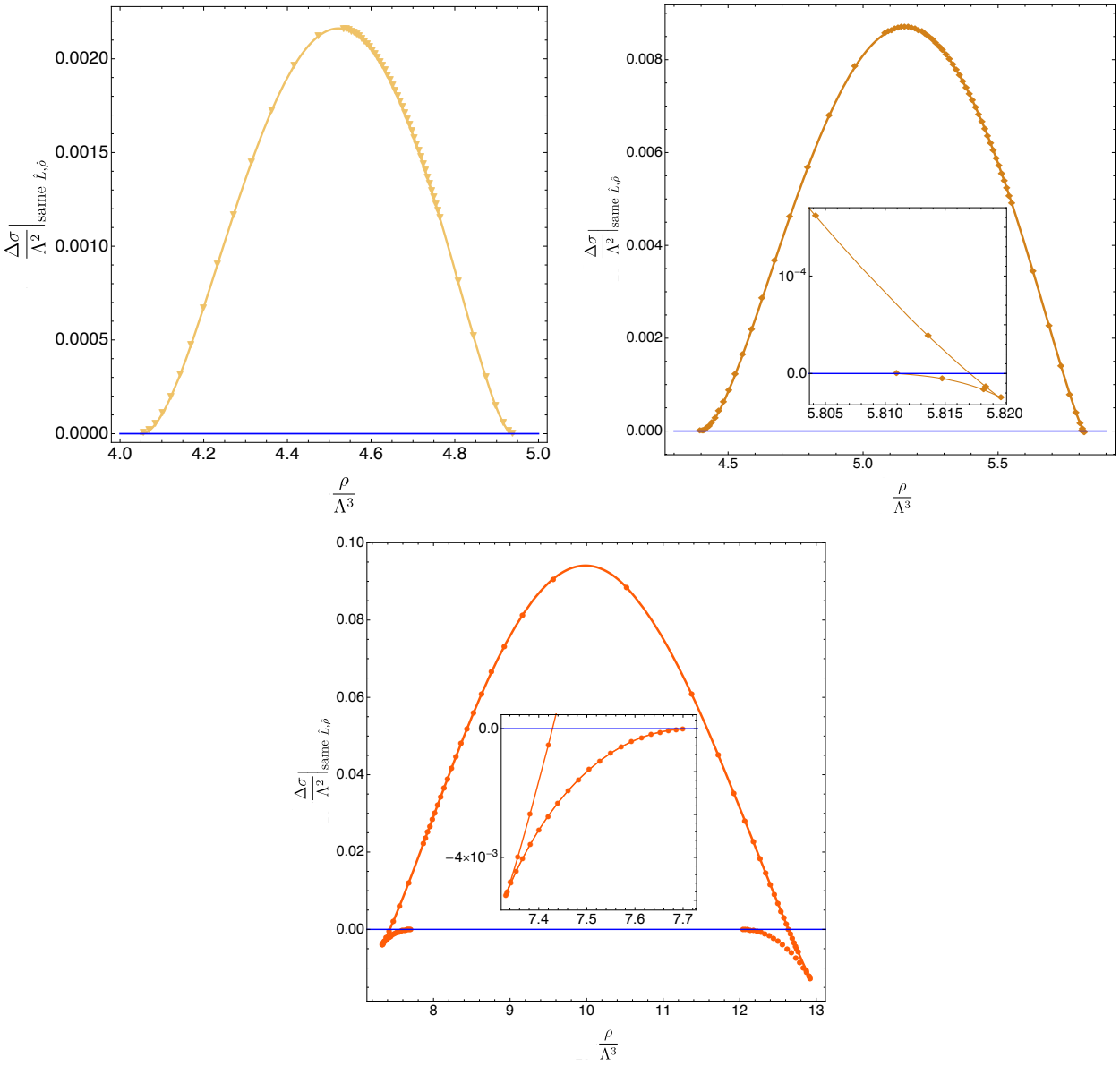

Figure 3.17: Microcanonical phase diagram: Killing entropy density difference $\Delta\hat{\sigma}\big|_{\text{same }\hat{L},\hat{\rho}}$ between lumpy and uniform branes with the same $(\hat{L},\hat{\rho})$ as a function of the Killing energy density $\hat{\rho}$ for 3 families of lumpy branes that have constant $\hat{L}$ given by $\hat{L}\simeq 5.299674<\hat{L}_{\Sigma_1}$ (top-left), $\hat{L}\simeq 6.004224$ which is in the range $\hat{L}_{\Sigma_1}<\hat{L}<\hat{L}_{\Sigma_2}$ (top-right) and $\hat{L}\simeq 11.501849>\hat{L}_{\Sigma_2}$ (bottom). For reference, $\hat{L}_{\Sigma_1}\simeq 5.618133$ and $\hat{L}_{\Sigma_2}\simeq 6.592316$. The three families are those with constant $\{\hat{L}_{\blacktriangledown},\hat{L}_{\blacklozenge},\hat{L}_{\bullet}\}$ already displayed in Fig. 3.11; we use the same shape/colour coding for the markers execpt that here they are all solid. The horizontal blue line with $\Delta\hat{\sigma}\big|_{\text{same }\hat{L},\hat{\rho}}=0$ describes the uniform brane family.

at a certain $\hat{\rho}$. This first-order phase transition point is best seen in the inset plot that zooms into this region. The entropy difference keeps decreasing as ρ grows until it reaches a cusp. Then, as $\hat{\rho}$ decreases, $\Delta\hat{\sigma}|_{\text{same } \hat{L},\hat{\rho}}$ becomes less negative until the lumpy brane with constant $\hat{L}$ merges again with the uniform brane.

3. Finally, the bottom panel is for constant $\hat{L} \simeq 11.501849$ solutions (whose energy density profile was discussed in Fig. 3.13). It illustrates how the 3-dimensional microcanonical phase diagram $\Delta\hat{\sigma}|_{\text{same } \hat{L},\hat{\rho}}$ versus $(\hat{\rho}, \hat{L})$ looks like when the lumpy branes have $\hat{L} > \hat{L}_{\Sigma_2}$. In this range of $\hat{L}$, at both GL mergers with the uniform brane (blue line), lumpy branes (orange disks) bifurcate with $\Delta\hat{\sigma}|_{\text{same } \hat{L},\hat{\rho}} < 0$. Then, as we move along the constant-$\hat{L}$ line away from the merger points, there are first two cusps (the left one is shown in more detail in the inset plot) and two first-order phase transition points where $\Delta\hat{\sigma}|_{\text{same } \hat{L},\hat{\rho}}$ changes sign and becomes positive. For $\hat{\rho}$ in between these two transition points, one has a lumpy brane with $\Delta\hat{\sigma}|_{\text{same } \hat{L},\hat{\rho}} > 0$ and thus these lumpy branes are the preferred microcanonical phase. Otherwise, uniform branes dominate the microcanonical ensemble.

To complement this discussion, it is useful to plot the Killing entropy density difference $\Delta\hat{\sigma}|_{\text{same } \hat{L},\hat{\rho}}$ between lumpy and uniform branes with the same $(\hat{L}, \hat{\rho})$ as a function of the average energy density $\hat{\bar{\mathcal{E}}}$ for some families of lumpy branes that have constant $\hat{L}$. Recall that the average energy density and the Killing energy density are related through $\hat{\bar{\mathcal{E}}} = \hat{\rho}/\hat{L}$. This means that comparing the entropy of uniform and nonuniform brane at the same $(\hat{L}, \hat{\rho})$ is the same as comparing them at the same $(\hat{L}, \hat{\bar{\mathcal{E}}})$. Fig. 3.18 shows this comparison for the four constant-$\hat{L}$ families $\{\hat{L}_\blacktriangledown, \hat{L}_\blacklozenge, \hat{L}_\blacksquare, \hat{L}_\bullet\}$ that were plotted in Fig. 3.16. Fig. 3.18, together with the projections to the $(\hat{L}, \hat{\bar{\mathcal{E}}})$-plane shown in Fig. 3.16, is the key figure to understand the microcanonical phase diagram because it provides four representative slices of this plot at constant $\hat{L}$. Gluing slices of this type together along the $\hat{\bar{\mathcal{E}}}$-axis one obtains the three-dimensional plot of $\Delta\hat{\sigma}|_{\text{same } \hat{L},\hat{\rho}}$ versus $(\hat{L}, \hat{\bar{\mathcal{E}}})$. The $\hat{L} \to \infty$ limit of the curves of Fig. 3.18 is the curve in Fig. 3.6(right).

So far we have discussed the lumpy branes only in the microcanonical ensemble. This is the most interesting ensemble because nonuniform branes can dominate this ensemble for certain windows of the parameter space and in a time evolution we typically fix the length and the average energy density of the solutions (i.e. the latter is conserved). But we may also ask about the role played by the lumpy branes in the canonical ensemble. In this case, we want to fix the length $L\Lambda$ and the temperature T/Λ of the solutions and the dominant solution is the one that has the lowest Killing free energy density f/Λ^3.

To address this question it is useful to first recall what happens when we consider only the uniform brane solutions. In the right panel of Fig. 3.3 we have already seen that the light uniform branch (the lower branch in the left panel of Fig. 3.3) is the preferred thermal phase for $\hat{T} < \hat{T}_c$, while for fixed $\hat{T} > \hat{T}_c$ the heavy uniform branch (the upper branch in the left panel of Fig. 3.3) dominates the canonical ensemble. The intermediate uniform branch (between A and B in Fig. 3.3) is never a preferred thermal phase of the canonical ensemble. For this reason it is sometimes stated in textbooks that, at $\hat{T} = \hat{T}_c \sim 0.3958945$, there is a first-order phase transition at which the system jumps discontinuously between the light and heavy uniform branes. However, at infinite volume there is actually a degeneracy of states at $\hat{T} = \hat{T}_c$ because the average free energy density of any phase separated state is the same as that of the homogeneous states at $\hat{T} = \hat{T}_c$. The reason for this is that the interface between the two phases in a phase-separated configuration gives a volume-independent contribution. This contribution is therefore subleading in the infinite-volume limit with respect to those of the two coexisting phases, whose free energy densities are equal to each other and to those of homogeneous states at $\hat{T} = \hat{T}_c$. Therefore, in the infinte-volume limit the system can transition between points D and E along a sequence of constant-temperature, constant free-energy, phase-separated states.

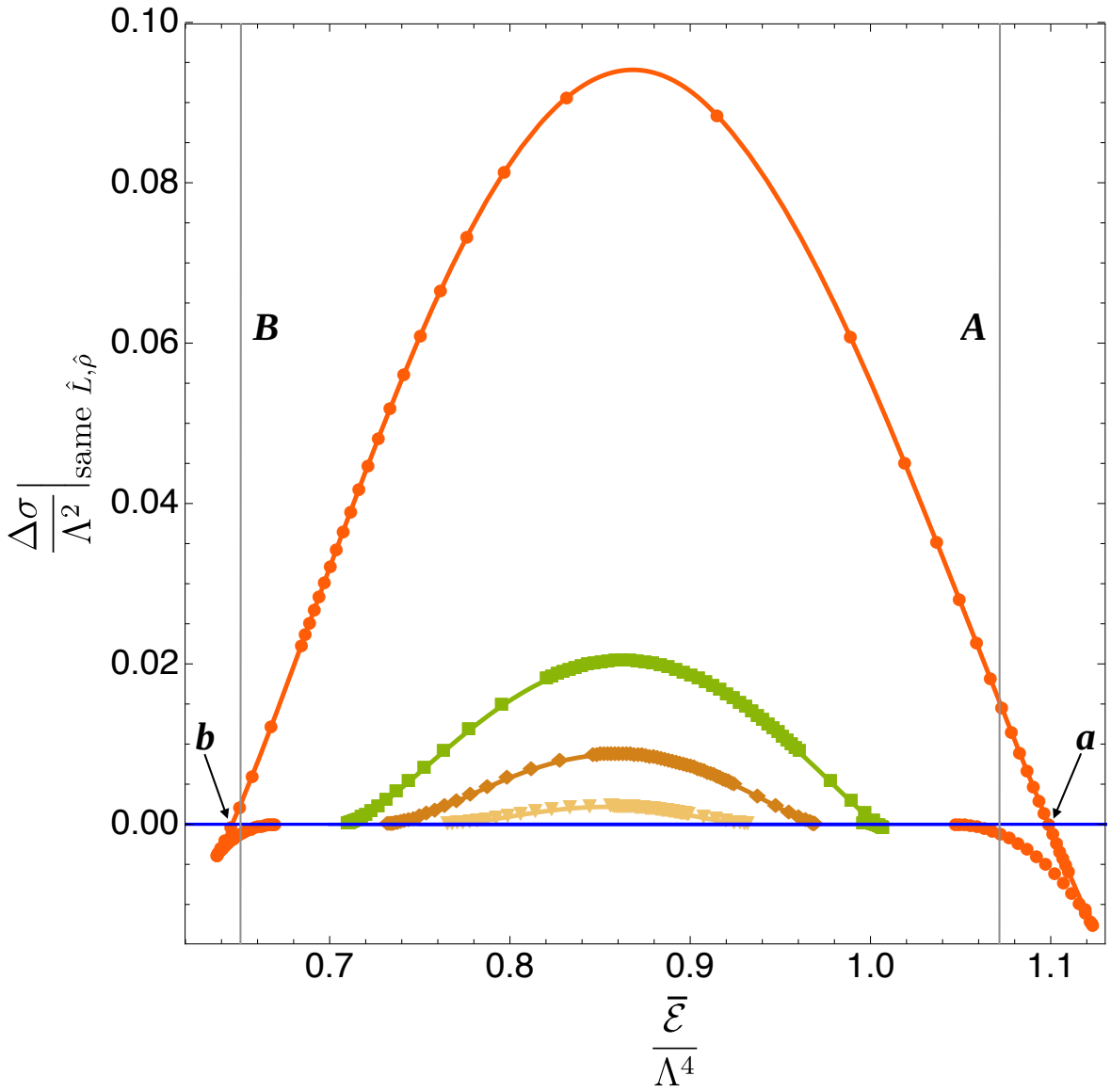

Figure 3.18: Killing entropy density difference $\Delta\hat{\sigma}|_{\text{same }\hat{L},\hat{\rho}}$ between lumpy and uniform branes with the same $(\hat{L},\hat{\rho})$ or, equivalently, with the same $(\hat{L},\hat{\bar{\mathcal{E}}})$, as a function of the average energy density $\hat{\bar{\mathcal{E}}}$. We show the same four families of lumpy branes with constant $\{\hat{L}_\blacktriangledown,\hat{L}_\blacklozenge,\hat{L}_\blacksquare,\hat{L}_\bullet\}\simeq\{5.299674,6.004224,6.900924,11.501849\}$ already displayed in Fig. 3.11. We use the same shape/colour coding for the markers as in Fig. 3.11 except that here they are all solid. The families with $\blacktriangledown,\blacklozenge,\bullet$ were also shown in Fig. 3.17, but the family $\blacksquare$ was not. The horizontal blue line with $\Delta\hat{\sigma}|_{\text{same }\hat{L},\hat{\rho}}=0$ describes the uniform brane family. The grey vertical lines indicate the turning points A and B in the phase diagram of Fig. 3.3. The labels "a" and "b" indicate the lumpy solutions with $\hat{L}_\bullet\simeq 11.501849$ that lie away from the merger curve but have the same entropy density as the corresponding uniform branes. In other words, these are the points away from the merger curve at which $\Delta\hat{\sigma}|_{\text{same }\hat{L},\hat{\rho}}$ crosses zero. The average energy densities at these points are $\hat{\bar{\mathcal{E}}}_a\simeq 1.09879>\hat{\bar{\mathcal{E}}}_A$ and $\hat{\bar{\mathcal{E}}}_b\simeq 0.645861<\hat{\bar{\mathcal{E}}}_B$.

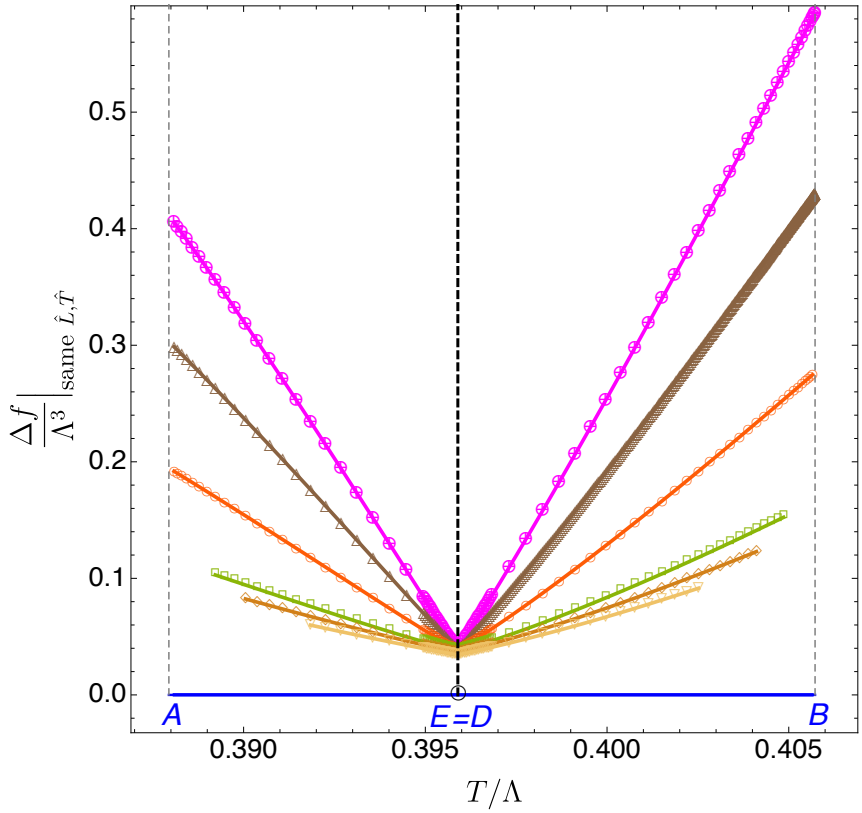

Figure 3.19: Canonical phase diagram: Dimensionless Killing free energy density difference $\Delta\hat{f}\big|_{\text{same } \hat{L},\hat{T}}$ as a function of the dimensionless temperature $\hat{T}$ for the six lumpy-brane families at constant $\hat{L}$ already shown in Fig. 3.11 (with the same colour/shape code). Namely, from the bottom to the top the length of the curves are: $\hat{L}_\triangledown \simeq 5.299674$, $\hat{L}_\diamond \simeq 6.004224$, $\hat{L}_\square \simeq 6.900924$, $\hat{L}_\bigcirc \simeq 11.501849$, $\hat{L}_\triangle \simeq 17.906849$, $\hat{L}_\otimes \simeq 24.311849$. The black dashed vertical line with $\hat{T} = \hat{T}_D = \hat{T}_E \equiv \hat{T}_c \sim 0.3958945$ represents the critical temperature first identified in the right panel of Fig. 3.3 and the grey vertical dashed lines represent $\hat{T} = \hat{T}_A \sim 0.387944$ and $\hat{T} = \hat{T}_B \sim 0.405724$ between which lumpy branes coexist with uniform branes. The horizontal blue line with $\Delta\hat{f} = 0$ represents the light uniform brane for $\hat{T} < \hat{T}_c$, and the heavy uniform brane for $\hat{T} > \hat{T}_c$.

The fact that all these states have the same free energy is the content of Maxwell's construction.

In contrast, at finite volume the inhomogenous, phase-separated states are never thermodynamically favoured. To show this, in Fig. 3.19 we compare the free energy of lumpy branes with the light uniform branes if $\hat{T} < \hat{T}_{\rm c}$, and with the heavy uniform branch if $\hat{T} > \hat{T}_{\rm c}$. More concretely, we compute the difference between the Killing free energy of the nonuniform brane $\hat{f}_{\rm nu}$ and the light (heavy) uniform Killing free energy $\hat{f}_{\rm u}$ when $\hat{T} < \hat{T}_{\rm c}$ ($\hat{T} > \hat{T}_{\rm c}$) that has the same length $L\Lambda$ and temperature T/Λ, i.e. $\Delta\hat{f}\big|_{\text{same } \hat{L},\hat{T}} = (\hat{f}_{\rm nu} - \hat{f}_{\rm u})_{\text{same } \hat{L},\hat{T}}$. Fig. 3.19 shows that for any temperature $\hat{T}_A \leq \hat{T} \leq \hat{T}_B$ where nonuniform branes exist, one always has $\Delta\hat{f}\big|_{\text{same } \hat{L},\hat{T}} > 0$. That is to say, the Killing free energy density of the lumpy branes is always higher than the free energy of the relevant (light or heavy) uniform brane and thus lumpy branes *never* dominate the canonical ensemble.[13]

3.1.6 Excited static lumpy branes: beyond the ground state solutions

So far we have discussed only the "ground state" lumpy branes of our spinodal system. The profile, for example that of the energy density $\mathcal{E}(x)$, of these fundamental branes has a single maximum and a single minimum, see Figs. 3.12 and 3.13. The phase diagram of the theory also contains infinitely many more lumpy brane phases whose profiles $\mathcal{E}(x)$ have η maxima and η minima for natural integer η. However, these are "excited states" of the theory in the sense that, as we will show below, for given $(\hat{L}, \hat{\rho})$ they always have lower Killing entropy density $\hat{\sigma}$ than the ground state lumpy branes that we have constructed above. In other words, lumpy branes with $\eta > 1$ are subdominant phases of the microcanonical ensemble. In particular, this suggests that they should be dynamically unstable and evolve towards the fundamental lumpy brane if slightly perturbed. In the case of large $\hat{L}$ this was explicitly verified in [63].

In principle, excited lumpy branes can be constructed using the perturbative method of Secs. 3.1.4 and 3.1.4. At linear order we would have to start with a Fourier mode that describes the $\eta^{\rm th}$ harmonic of the system, namely with

$$q_j^{(1)}(x,y) = \mathfrak{q}_j^{(1)}(y)\cos(\eta\,\pi\,x)\,, \quad \text{for } \eta = 2,3,4,\cdots \tag{3.77}$$

instead of the $\eta = 1$ case of (3.55). However, it is not necessary to perform this construction since the properties of these excited states can be obtained from those of the fundamental ones using extensivity.[14] Indeed, given a solution with $\eta = 1$ in a box of size $\hat{L}$ we can obtain a solution with $\eta > 1$ in a box of size $\eta\hat{L}$ by taking η copies of the initial solution. Once we know all solutions with $\eta = 1$ in boxes of any size, as we do, this procedure gives us all possible solutions with $\eta > 1$ maxima and minima in all possible boxes. Clearly, if the Killing energy and entropy densities of the initial solution are $\hat{\rho}$ and $\hat{\sigma}$, respectively, then those of the new solution are $\eta\hat{\rho}$ and $\eta\hat{\sigma}$. In contrast, the average energy density $\hat{\bar{\mathcal{E}}} = \hat{\rho}/\hat{L}$ remains invariant. We must now compare the Killing entropy density of the solution with η maxima and minima with that of the corresponding $\eta = 1$ brane in a box of size $\eta\hat{L}$. Since the average energy density is invariant when taking copies of the initial solution, this comparison is most easily done by considering $\hat{\sigma}$ as a function of $\hat{\bar{\mathcal{E}}}$ and $\hat{L}$. Therefore we must compare the entropy of the excited brane $\hat{\sigma}_\eta(\hat{\bar{\mathcal{E}}}, \eta\hat{L}) \equiv \eta \times \hat{\sigma}(\hat{\bar{\mathcal{E}}}, \hat{L})$ with that of the fundamental brane $\hat{\sigma}(\hat{\bar{\mathcal{E}}}, \eta\hat{L})$. It follows that if the entropy at fixed $\hat{\bar{\mathcal{E}}}$ grows with $\hat{L}$ faster than linearly then the fundamental brane always

[13] For completeness, we have verified that the Killing free energy density $\hat{f}$ of lumpy branes is always *lower* than the Killing free energy density of the *intermediate* branes AB, and that they become equal to one another precisely when the merger of these two branches occurs. In any case neither branch is ever preferred at finite volume in the canonical ensemble.

[14] Similar arguments where used to find the thermodynamics of excited nonuniform black strings of the original GL system [108, 109]). We can also start our linear order analysis with two (or more) harmonics with *different* amplitudes. This allows to construct lumpy branes with two (or more) maxima that have different amplitudes (in the spirit of [110]).

has higher entropy than the excited brane. This is indeed the case, as can be seen by taking constant-$\hat{\mathcal{E}}$ slices of Fig. 3.18. For example, in Fig. 3.20 we do this for $\hat{\mathcal{E}} = 0.85$ and we compare $\Delta\hat{\sigma}_{\eta=1}$ of the fundamental ($\eta = 1$) nonuniform brane (orange $\bullet$) against $\Delta\hat{\sigma}_{\eta=2}$ and $\Delta\hat{\sigma}_{\eta=3}$ of the $\eta = 2$ (blue $\blacklozenge$) and $\eta = 3$ (green $\blacksquare$) excited branes. For a given $(\hat{L}, \hat{\rho})$ or, equivalently, for a fixed $(\hat{L}, \hat{\mathcal{E}})$, we see that the Killing entropy density decreases as η grows: in agreement with the most naive intuition, the fundamental lumpy brane has the highest Killing entropy density and therefore it dominates the microcanonical ensemble over any excited brane.

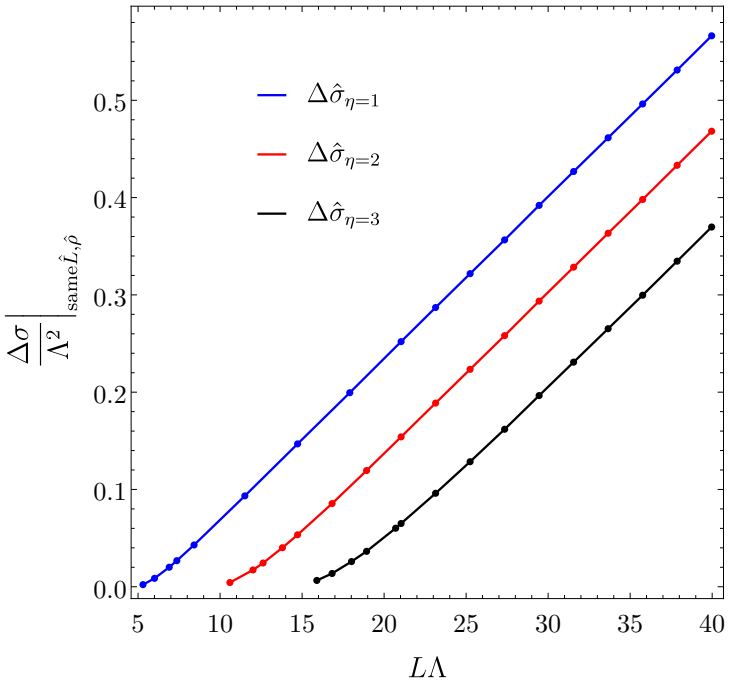

Figure 3.20: Killing entropy density difference $\Delta\hat{\sigma}|_{\text{same }\hat{L},\hat{\rho}}$ (between lumpy and uniform branes with the same $(\hat{L}, \hat{\rho})$) as a function of the length $\hat{L}$ for solutions with $\hat{\mathcal{E}} = 0.85$ for: (1) the fundamental ($\eta = 1$) lumpy brane (orange disks), (2) the $\eta = 2$ excited lumpy brane (blue diamonds), and (3) $\eta = 3$ excited lumpy branes (green squares).

The discussion above applies to excited states that can be obtained as copies of a single configuration. Therefore states of this type with η maxima and minima have a $\mathbb{Z}_\eta$ discrete symmetry. There exist more general excited states with maxima and minima of different heights, but we expect these to be subdominant too. In the case of large $\hat{L}$ this was explicitly verified in [63].

3.1.7 The spinodal (Gregory-Laflamme) timescale

In Sec. 3.1.4 we saw that intermediate uniform branes with $\hat{\mathcal{E}}_B < \hat{\mathcal{E}} < \hat{\mathcal{E}}_A$ (see left panel of Fig. 3.3) can be GL-unstable. To find when the instability appears, we took the uniform branes $Q_j(y)$ of section 3.1.4 and considered static Fourier perturbations of the form (3.55) about this background, namely $q_j(x, y) = Q_j(y) + \epsilon\, \mathfrak{q}_j^{(1)}(y) \cos(\pi x)$. This allowed us to find the minimum length $L_{\rm GL}\Lambda = 2\pi/\hat{k}_{\rm GL}$ (see Figs. 3.7 and 3.8) above which the uniform brane is unstable. This was enough for our purposes of Sec. 3.1, where we were just interested in finding the static lumpy branes. In particular, we found large regions of the microcanonical phase diagram where lumpy branes coexist with and are favoured over uniform branes. This suggests that, if we start with initial data that consists of a uniform brane that is GL unstable plus a perturbation, the system should evolve towards a lumpy brane with the same length $\hat{L}$ and Killing energy density

$\hat{\rho}$, and hence also the same $\hat{\bar{\mathcal{E}}} = \hat{\rho}/\hat{L}$. The initial stages of this time evolution should be well described by the linear GL frequencies. It is thus important to compute the GL timescales of the system.

Consider again the uniform branes constructed in Sec. 3.1.4 in the regime $\hat{\mathcal{E}}_B < \hat{\mathcal{E}} < \hat{\mathcal{E}}_A$ (see left panel of Fig. 3.3). Denote the collective fields by $\bar{\psi}(y) = \{\bar{g}_{\mu\nu}(y), \bar{\phi}(y)\}$. We will now allow for time-dependent perturbations of this background. More concretely, we will use the fact that ∂_t and $\partial_{\tilde{x}}$ are Killing vector fields of the uniform brane background to Fourier decompose the time dependent perturbations as

$$\psi(t, x, y) = \bar{\psi}(y) + \epsilon\, \delta\psi^{(1)}(y) e^{i\,k\,\tilde{x}} e^{-i\,\omega\,t}\,. \tag{3.78}$$

This introduces the wavenumber k conjugate to the spatial direction $\tilde{x} = x\frac{L}{2} \in [0, L/2]$ and the frequency ω of the perturbation. Let $\delta g_{\mu\nu} \equiv h_{\mu\nu}$ be the metric perturbations and $\delta\phi$ the scalar field perturbation. Perturbations $\delta\psi^{(1)}(y) = \{h_{\mu\nu}(y), \delta\phi(y)\}$ that break the symmetries indicated in (3.78) excite a total of 8 fields, namely: $\delta\phi$, h_{tt}, h_{ty}, $h_{t\tilde{x}}$ h_{yy}, $h_{\tilde{x}y}$, $h_{\tilde{x}\tilde{x}}$ and $h_{x_2x_2} = h_{x_3x_3}$.

We have not yet fixed the gauge freedom of the problem. Instead of doing so we construct two gauge invariant-quantities that encode the most general perturbations of the form (3.78) as described in [111]. The linearized Einstein equations then reduce to (and are closed by) a coupled system of two linear, second-order ODEs for these two gauge-invariant variables. The perturbations must be regular at the horizon in ingoing Eddington-Finkelstein coordinates and preserve the asymptotic AdS structure of the uniform background. This is a non-polynomial eigenvalue problem for the frequency ω where we give the uniform background and the wavenumber k and find ω. The GL modes of the uniform brane system have purely imaginary frequency.

In Fig. 3.21, as an illustrative example, we plot the dimensionless dispersion relation $\hat{\omega}(\hat{k})$

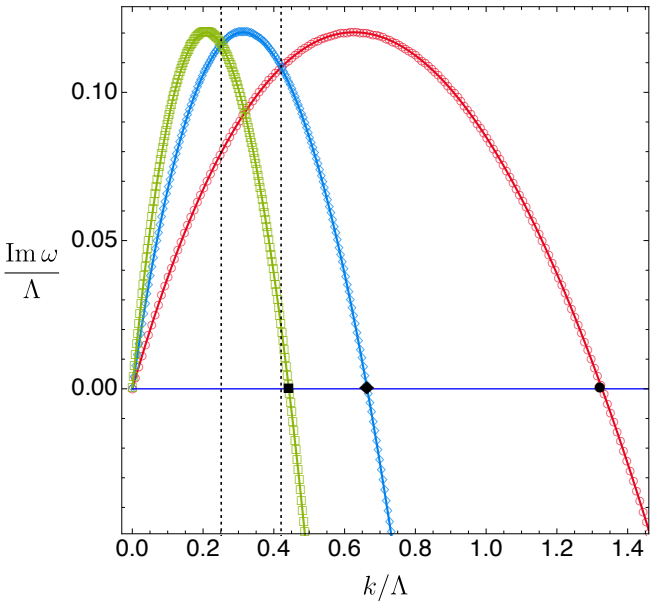

Figure 3.21: Dispersion relation of GL modes for a uniform brane with $(\hat{\tau}, \hat{\mathcal{E}}) \simeq (0.395894, 0.867966)$. Red circles, blue diamonds and green squares correspond to harmonics with $\eta = 1, 2$ and 3, respectively. For reference the maximum of the instability occurs for $(\hat{\tau}, \hat{k}_{\rm GL})_K \simeq (0.397427, 1.332306)$, i.e. $(\hat{\tau}, \hat{L}_{\rm GL})_K \simeq (0.397427, 4.716021)$. The GL zero mode was identified in Fig. 3.7.

for a particular uniform brane with $(\hat{\tau}, \hat{\mathcal{E}}) \simeq (0.395894, 0.867966)$ that is very close to point C

in Fig. 3.3, for which $(\hat{\tau}, \hat{\mathcal{E}})_C \simeq (0.3958945, 0.867956)$.[15] In Fig. 3.21, the red circle $\circ$ curve describes the dispersion relation of the fundamental harmonic $\eta = 1$. Not surprisingly, this curve starts at $(\hat{k}, \hat{\omega}) = (0, 0)$ and, as $\hat{k}$ increases, the dimensionless frequency $\mathrm{Im}\,\omega/\Lambda$ first grows until it reaches a maximum and then starts decreasing. Precisely at the GL critical wavenumber $\hat{k} = \hat{k}_{\rm GL} = 1.322499$, as computed independently in Fig. 3.7, one has $\mathrm{Im}\,\omega/\Lambda = 0$ and for $\hat{k} > \hat{k}_{\rm GL}$ the uniform brane is stable. For $0 < \hat{k} < \hat{k}_{\rm GL}$ the uniform brane is GL unstable and the maximum of the instability occurs at $(\hat{k}, \hat{\omega})|_{\rm max} \simeq (0.626902, 0.120249\, i)$.

Besides the fundamental GL mode, the uniform brane has an infinite tower of integer η spatial Fourier harmonics. Uniform branes are also unstable to these higher harmonics but the minimum unstable GL length $\hat{L}_{{\rm GL},\eta}$ for the $\eta^{\rm th}$ harmonic increases with η or, equivalently, the critical GL wavenumber $\hat{k}_{{\rm GL},\eta}$ decreases with η. As examples, in Fig. 3.21 we also plot two other curves that describe the dispersion relation of the second ($\eta = 2$, blue $\diamond$) and third ($\eta = 3$, green $\square$) harmonics. Note that the dispersion relation of these higher harmonics can be obtained straightforwardly from that of the fundamental harmonic. Indeed, note that we can unwrap the S^1 and change the periodicity of its coordinate $\tilde{x}$ from L to $L_\eta = \eta\, L$, for integer η [108, 109]. This also changes the wavenumber from $k = \frac{2\pi}{L}$ into $k_\eta = \frac{k}{\eta}$. Altogether this leaves the phase of the Fourier mode $e^{ik\tilde{x}}$ invariant. But this means that the frequency ω_η of the $\eta^{\rm th}$ harmonic is related to the frequency of the fundamental harmonic simply by $\omega_\eta(k) = \omega(k/\eta)$ and that the critical GL zero mode of the $\eta^{\rm th}$ harmonic is $\hat{L}_{{\rm GL},\eta} = \eta\, \hat{L}_{\rm GL}$ or $\hat{k}_{{\rm GL},\eta} = \hat{k}_{\rm GL}/\eta$. These properties, namely

$$\omega_\eta(k) = \omega(k/\eta)\,, \qquad \hat{k}_{{\rm GL},\eta} = \hat{k}_{\rm GL}/\eta\,, \tag{3.79}$$

are indeed observed in Fig. 3.21.

The linear results of Fig. 3.21 also provide a guide to the full nonlinear time evolution of nonconformal branes. In a microcanonical ensemble experiment, imagine that we start with a uniform brane in the regime $\hat{\mathcal{E}}_B < \hat{\mathcal{E}} < \hat{\mathcal{E}}_A$ where it can co-exist with lumpy branes, for example with $\hat{\mathcal{E}} \simeq 0.867966$. We want to perturb it to drive it towards a lumpy brane with the same $\hat{L}$ and $\hat{\rho}$ and thus same $\hat{\bar{\mathcal{E}}}$. What should we do? We certainly have to consider a Fourier perturbation with $\hat{k} < \hat{k}_{\rm GL}$ as read from Fig. 3.21 or from Figs. 3.7 and 3.8. In these circumstances we still have different options that will result in substantially different time evolutions. Indeed, if we start with a $\hat{k}_{{\rm GL},2} < \hat{k} < \hat{k}_{\rm GL}$ where only the fundamental harmonic is unstable then the system will evolve "quickly" towards an $\eta = 1$ lumpy brane (the quickest evolution should occur if $\hat{k} \sim \hat{k}|_{\rm max}$). More generically this will still be the case also for a $\hat{k} < \hat{k}_{{\rm GL},2}$ as long as it is higher than the critical $\hat{k} \sim 0.4205$ where the curves for $\eta = 1$ ($\bullet$) and $\eta = 2$ ($\diamond$) meet, see the right-most dotted vertical line in Fig. 3.21. (In this discussion we assume that the initial amplitudes of all modes are similar.) If instead $0.2513 \lesssim \hat{k} \lesssim 0.4205$, i.e. in between the two vertical dotted lines of Fig. 3.21, then the time evolution of the uniform brane should first approach an $\eta = 2$ lumpy brane before finally moving towards the fundamental $\eta = 1$ lumpy brane, which has a higher Killing entropy density. Finally, if the uniform brane is perturbed with a $\hat{k} \lesssim 0.2513$ mode then the system will first evolve towards an $\eta \geq 3$ lumpy brane before being driven towards its fundamental lumpy brane endpoint. These expectations were explicitly verified in the case of large boxes in [63].

3.2 Real-time dynamics

Above we have constructed inhomogeneous static solutions using purely static methods to solve the Einstein equations. We will now examine several aspects of these solutions using real-time dynamical methods. We will first reproduce the static solutions obtaining excellent agreement. Then we will use the dynamical methods to address two novel aspects not studied above: the

[15] This corresponds to the same temperature used in the lumpy branes of the top-right panel of Fig. 3.12 and in the disk lumpy curve $\hat{\bar{\mathcal{E}}}(\hat{L})$ of Fig. 3.15.

local dynamical stability of the inhomogeneous static solutions, and the full time evolution, including the end state, of the unstable solutions. The reader interested in the numerical methods that we use can consult e.g. [36, 61, 63, 112, 113].

3.2.1 Reproducing the static solutions from real-time dynamics

In Fig. 3.22 we compare the Killing entropy density of the static inhomogeneous solutions obtained with dynamical methods (black dots) and with static methods (orange dots) for a system with $\hat{L} \simeq 11.501849$. In Fig. 3.23 we compare the average energy density-versus-temperature relation. As is clear from the figures we find excellent agreement.

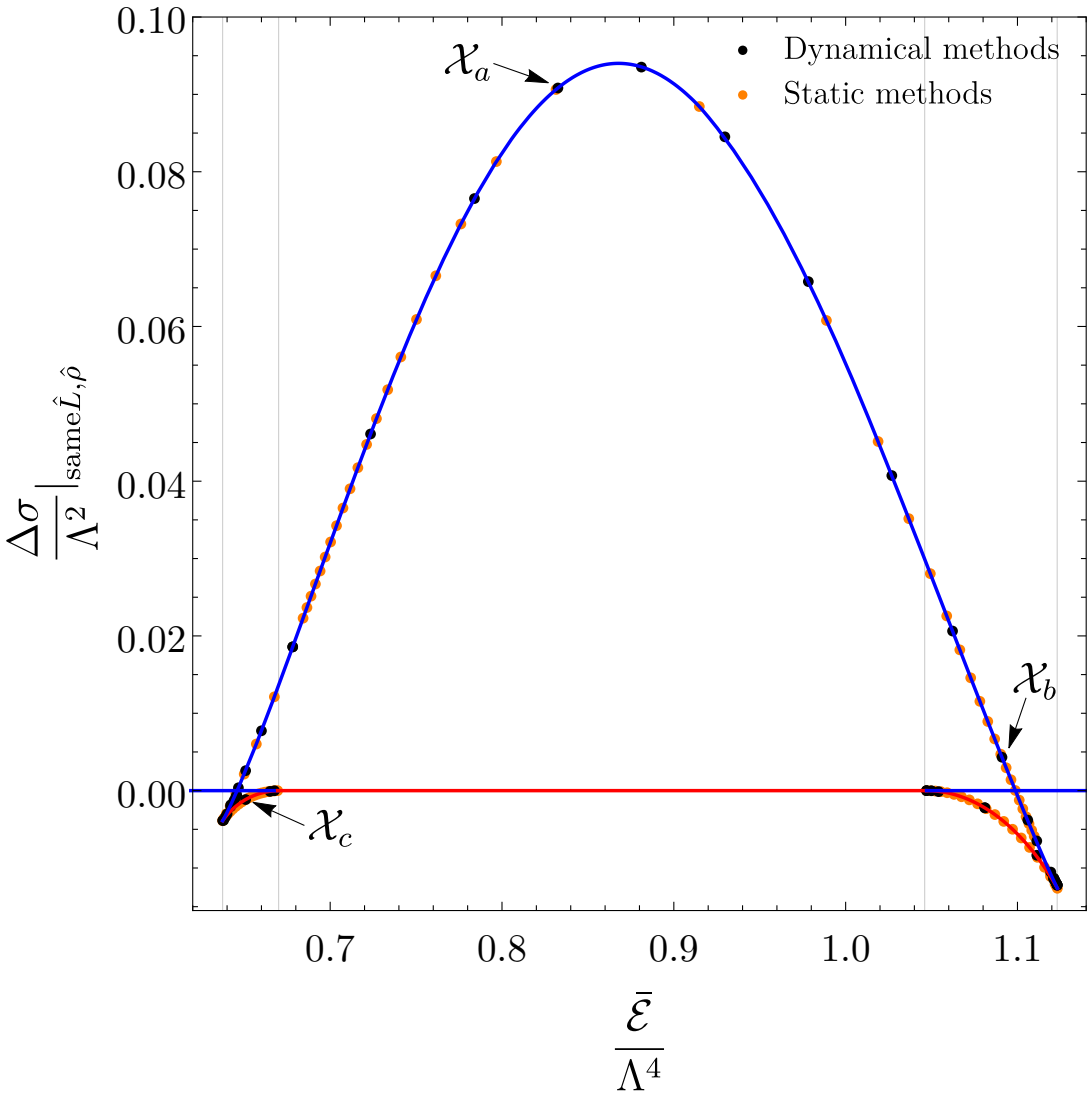

Figure 3.22: Comparison of the entropy density of the static inhomogeneous solutions obtained with dynamical methods (black dots) and with static methods (orange dots) for a system with $\hat{L} \simeq 11.501849$. Blue (red) curves indicate locally stable (unstable) solutions. Orange dots are exactly as in Fig. 3.17(bottom). Grey vertical lines indicate the location of the mergers and the cusps. The representative solutions $\mathcal{X}_a, \mathcal{X}_b$ and $\mathcal{X}_c$ have average energies $\hat{\bar{\mathcal{E}}}_a \simeq 0.831460$, $\hat{\bar{\mathcal{E}}}_b \simeq 1.091$ and $\hat{\bar{\mathcal{E}}} \simeq 0.651$, respectively.

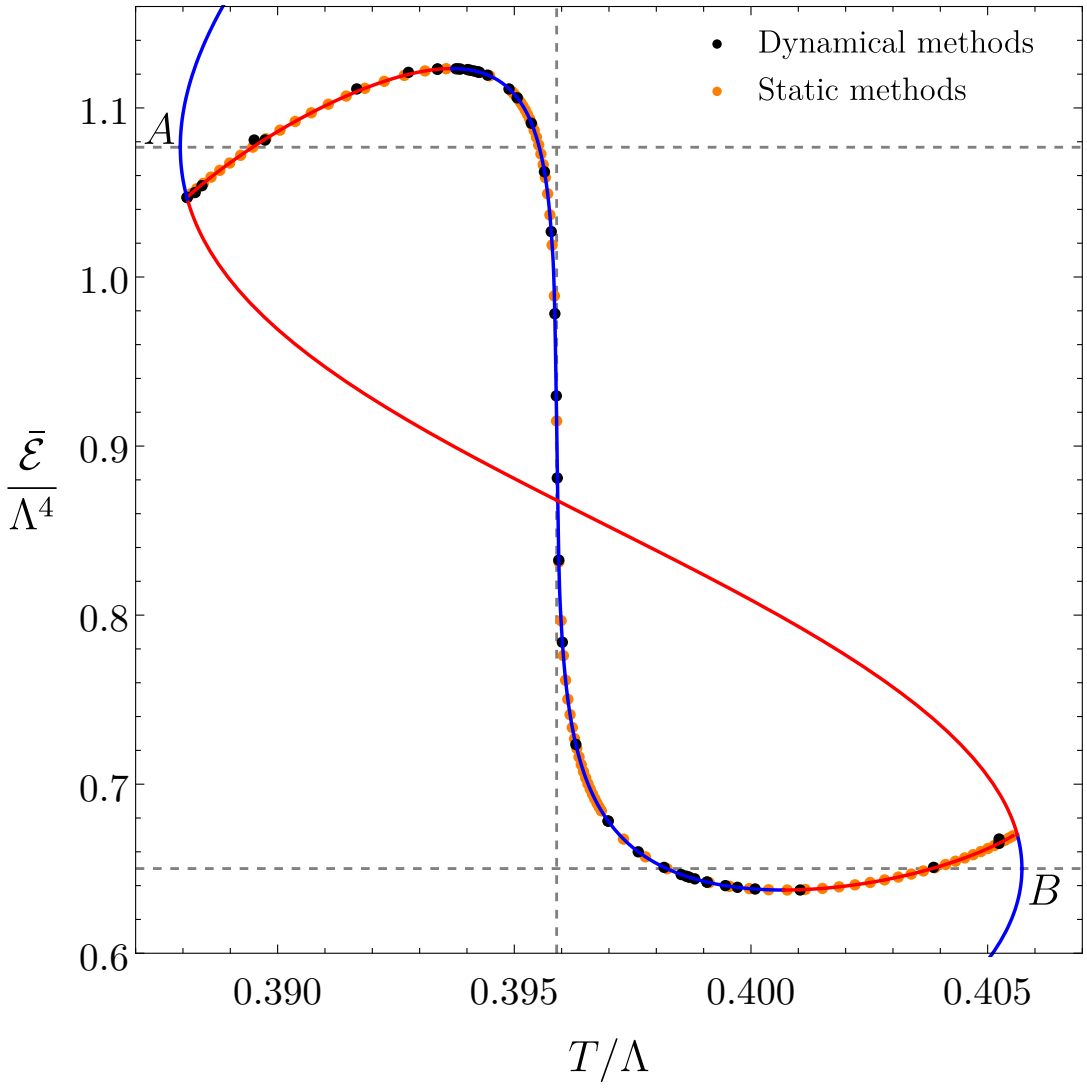

Figure 3.23: Average energy density versus temperature for static inhomogeneous solutions obtained with dynamical methods (black dots) and with static methods (orange dots) for a system with $\hat{L} \simeq 11.501849$. Blue (red) curves indicate locally stable (unstable) solutions. Orange dots are exactly as in Fig. 3.13(left).

The process that we follow to reproduce the static inhomogeneous solutions from real-time dynamical evolution makes it natural to distinguish three cases:

(I) Lumpy branes whose $(\hat{L},\hat{\rho})$ lies inside the GL merger curve of Figs. 3.15 and 3.16. An example is given by the solution labelled as $\mathcal{X}_a$ in Fig. 3.22.

(II) Lumpy branes that are outside the merger curve and have the largest entropy among lumpy branes with the same $(\hat{L},\hat{\rho})$. An example is given by the solution labelled as $\mathcal{X}_b$ in Fig. 3.22.

(III) Lumpy branes outside the merger curve with the smallest entropy for a given $(\hat{L},\hat{\rho})$. An example is given by the solution labelled as $\mathcal{X}_c$ in Fig. 3.22.

We follow different strategies to find each of these types of solutions. Solutions of type I are reproduced by following the full evolution of the spinodal instability, as in [61, 63]. The initial state is a homogeneous brane with the same $(\hat{L},\hat{\rho})$ of the lumpy brane that we want to obtain plus a small sinusoidal perturbation corresponding to the lowest Fourier mode that fits in the box. As this solution lies inside the GL merger, this perturbation is unstable and grows with time.[16] Upon dynamical evolution the system eventually enters the nonlinear regime and finally relaxes to the inhomogeneous solution. In Fig. 3.24 we show an example of one of these evolutions (top-left) and the comparison of the solution at asymptotically late times with the solution obtained via static methods (top-right), with excellent agreement.

The previous procedure fails to produce solutions of type II because the homogeneous system is locally stable, so small perturbations decay in time and the system returns to the initial homogeneous state. Indeed, we consider a uniparametric family of perturbations, not necessarily sinusoidal, with the parameter given by the amplitude $\mathcal{A}$ of the perturbation, and find that if $\mathcal{A}$ is smaller than a certain critical value $\mathcal{A}^*$ then the system evolves back to the homogeneous state. In order to obtain a lumpy brane as a final state we must start with a homogenous brane plus a perturbation that is so large that the system finds itself directly in the non-linear regime. This is indeed what happens if $\mathcal{A} > \mathcal{A}^*$. In this case the system evolves in time towards the globally preferred state, namely towards a lumpy brane like the one labelled $\mathcal{X}_b$ in Fig. 3.22. An example of this evolution is illustrated in Fig. 3.24(middle-left).

Finally, if the amplitude of the perturbation is tuned to be exactly $\mathcal{A}^*$ then the system evolves in time towards a type III solution like the one labelled as $\mathcal{X}_c$ in Fig. 3.22. An example of this evolution is illustrated in Fig. 3.24(bottom-left). The fact that $\mathcal{A}$ must be precisely tuned in order to reach the type III solution suggests that these solutions are locally dynamically unstable. We will verify this explicitly below. Since numerically it is impossible to tune $\mathcal{A}$ with infinite precision, this means that if we were to evolve the configuration in Fig. 3.24(bottom-left) for sufficiently long times we would see that either it falls back to the homogeneous state (if $\mathcal{A}$ is slightly smaller than $\mathcal{A}^*$) or it evolves towards a type II configuration (if $\mathcal{A}$ is slightly larger than $\mathcal{A}^*$). We will confirm this in Fig. 3.28.

3.2.2 Local stability

In this section we study the local stability of the static inhomogeneous solutions by using real-time dynamical methods. We consider an initial state given by the static inhomogeneous solution plus a small perturbation and study its time evolution. The system is said to be locally stable if all possible linear perturbations decay in time. If at least one of the perturbations grows in time, then the system is said to be locally unstable. In order to establish which is the case one must decouple, i.e. diagonalise, the full set of linearized equations around the inhomogeneous solution (note that all Fourier modes are indeed coupled to one another because the inhomogenous state

[16] There could be other unstable harmonics. However, by considering a sufficiently large amplitude for the first mode the system can always be driven to the fundamental lumpy brane with $\eta = 1$.

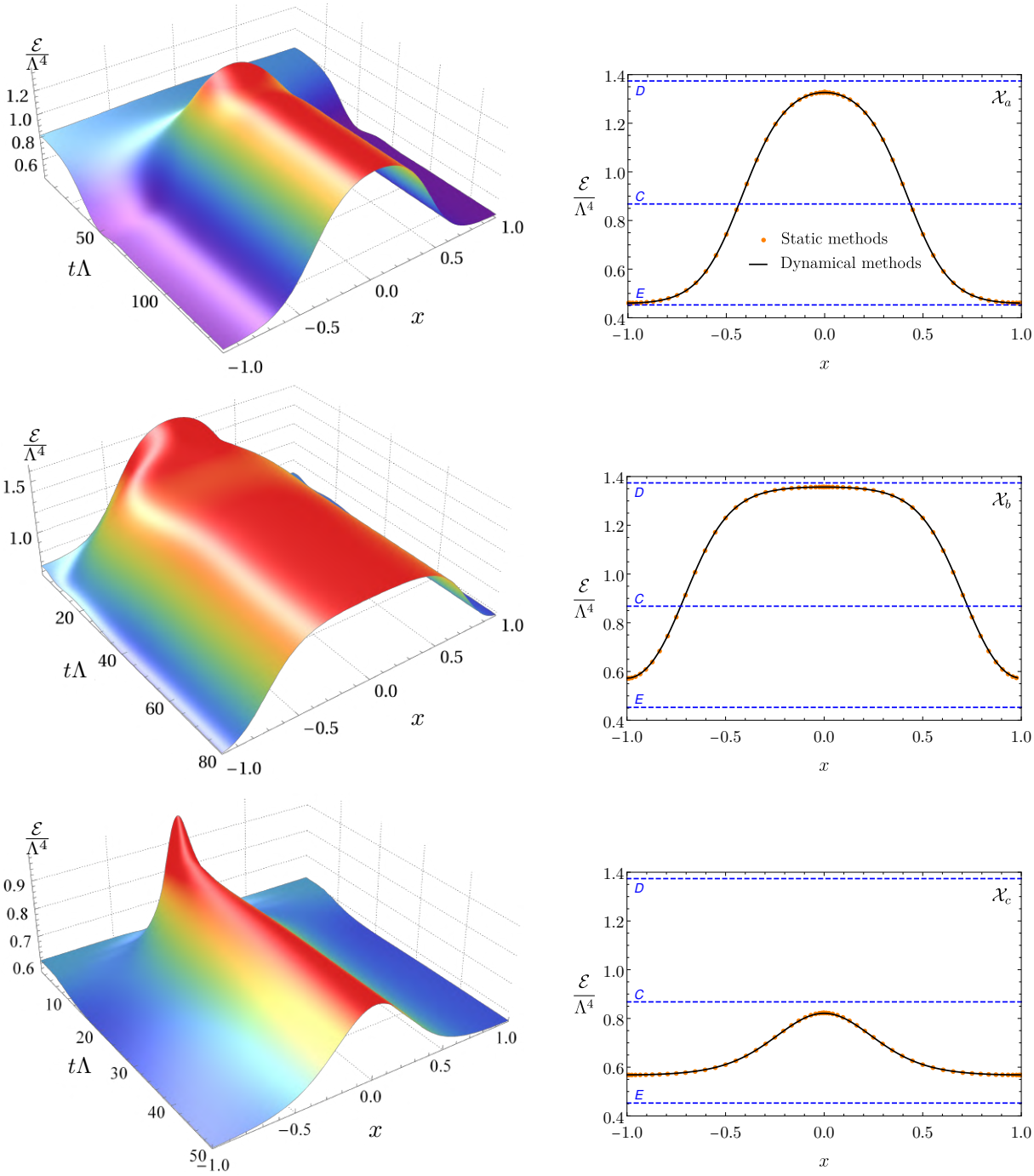

Figure 3.24: Real-time evolution leading to a type I (top-left), a type II (middle-left) and a type III (bottom-left) lumpy brane with $\hat{L} \simeq 11.501849$, labelled $\mathcal{X}_a, \mathcal{X}_b$ and $\mathcal{X}_c$ in Fig. 3.22, respectively. On the right panels we compare the energy density profiles at late times (continuous black lines) with those obtained by static methods (orange dots).

breaks translational invariance). Each eigenmode then evolves in time as $e^{-i\omega t}$, with ω the corresponding eigenfrequency. If the imaginary part of all the eigenfrequencies is negative the system is locally stable. If at least one of the eigenfrequencies has a positive imaginary part then it is locally unstable.

Rather than performing the exercise above, we will use our numerical code to obtain the time evolution of a generic small initial perturbation of the inhomogeneous state. Since the perturbation is generic we expect that it will be a linear combination of all the eigenmodes of the system. Thus, after some characteristic time, the eigenmode with the largest imaginary part of omega will dominate the evolution leading to a well defined exponential evolution. We have identified this region of exponential behaviour in all the time evolutions of the perturbed system that we have studied, and we have obtained the real and imaginary parts of omega for the dominant mode by performing fits. Note that this will not result in a mathematical proof of local stability. For example, our generic perturbations may accidentally have a very small projection on some unstable mode, or the positive imaginary part of the frequency of this mode may be exceedingly small and hence go unnoticed, etc. While these possibilities cannot be excluded with absolutely certainty, the detailed searches that we have performed, together with the consistent emergent physical picture, make us confident that they are highly unlikely.

Let us illustrate the procedure with the two examples in Fig. 3.25. The top panel corresponds to the relaxation to equilibrium at late times of the simulation presented in Fig. 3.24(top-left). Specifically, we take the spatial profile of the energy density at some late time, we subtract from it the profile of the inhomogeneous static solution (which we denoted as $\mathcal{X}_a$ in Fig. 3.22), and we decompose this difference into Fourier modes. The time-dependent amplitude of the first few of these Fourier modes is shown in Fig. 3.25(top). We see that all of these modes oscillate and decay exponentially in time with the same frequency. This is as expected since the evolution is dominated by the single eigenmode with the slowest decay. The fact that there is no growing mode indicates that the type I, inhomogeneous, static solution to which this configuration asymptotes at late times (namely, $\mathcal{X}_a$ in the current simulation) is locally dynamically stable.

The second example shown in Fig. 3.25(bottom) corresponds to the evolution presented in Fig. 3.24(bottom-left), but extended to longer times. Here we plot the Fourier modes corresponding to the difference between the spatial energy profile at a given time and the spatial energy profile of the inhomogeneous, static configuration that we denoted as $\mathcal{X}_c$ in Fig. 3.22. We observe a first relaxation in which the stable modes decay but, this time, at later times the system is dominated by an exponential growth of an unstable mode. This confirms that the type III lumpy branes such as $\mathcal{X}_c$ are locally dynamically unstable, as anticipated above. Recall that the initial state in this time evolution is a homogeneous brane plus a large perturbation of amplitude $\mathcal{A}$ that is tuned to be close to a critical value $\mathcal{A}^*$. This tuning is what suppresses the initial amplitude of the unstable mode, hence allowing the time evolution to drive the system close to $\mathcal{X}_c$ for some time. Thus, intuitively, this solution behaves like a saddle point in configuration space with some stable and some unstable directions (i.e. a metastable configuration).

We have performed a scan to determine the real and imaginary parts of omega for the dominant mode of static inhomogeneous solutions with $\hat{L} \simeq 11.501849$ and varying energy densities. The result is shown in Fig. 3.26. We find that type I and II solutions have negative imaginary parts of omega, and so they are locally stable, while the type III solutions have positive imaginary parts of omega, and so they are locally unstable. The imaginary part of omega crosses zero precisely at the "cusps" of Fig. 3.22, that is, at the static solutions lying precisely at the boundary between type II and III solutions. The real part of omega is non-vanishing in the locally stable cases, whereas it vanishes in the locally unstable cases, going to zero also at the cusps. In Figs. 3.22, 3.23 and 3.26 we show locally stable solutions in blue and locally unstable solutions in red.

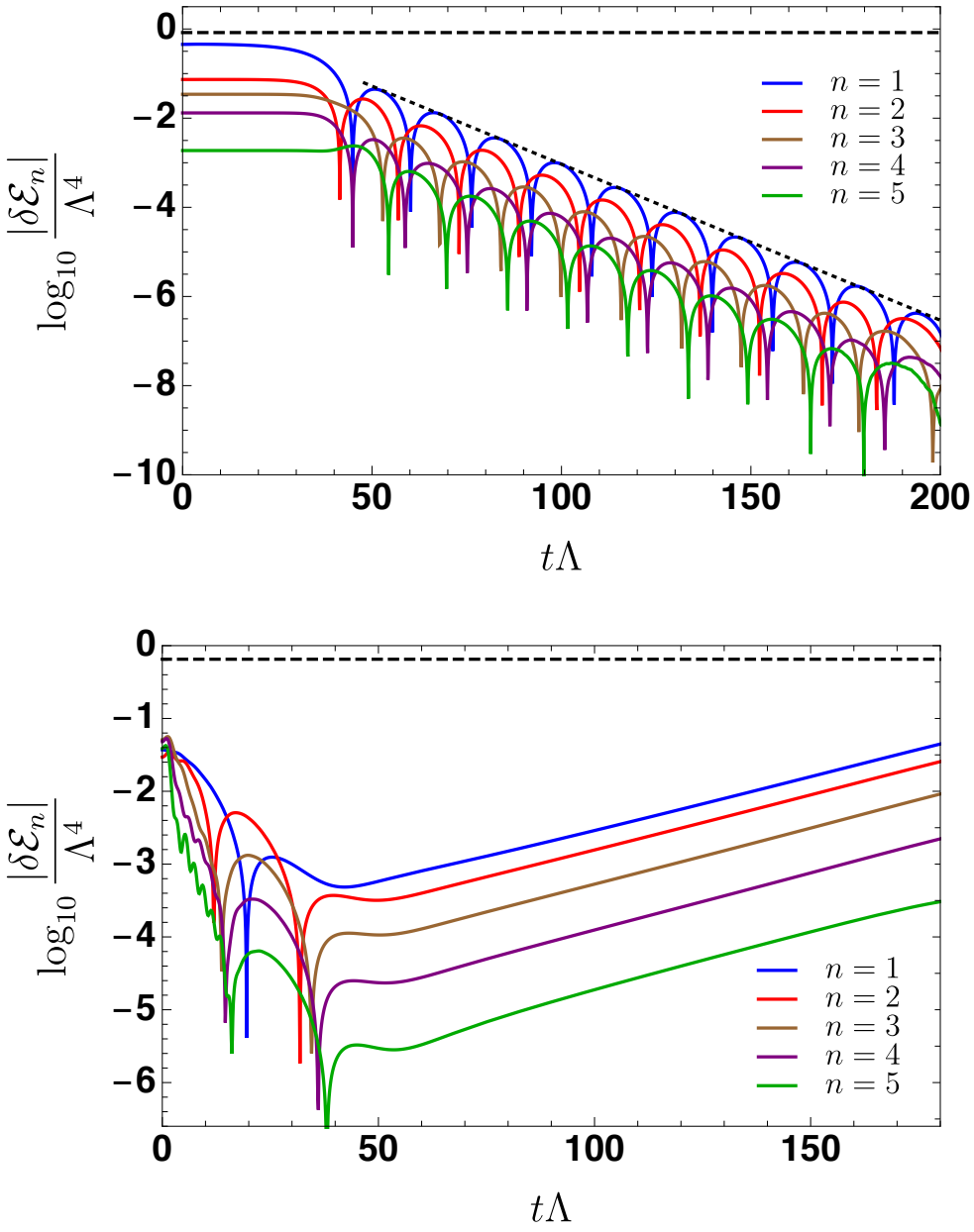

Figure 3.25: (Top) Time evolution of some Fourier modes of a perturbation around the type I, inhomogeneous, static configuration $\mathcal{X}_a$ of Fig. 3.24(top-right) with $\hat{\mathcal{E}} \simeq 0.831460$, $\hat{L} \simeq 11.501849$. The dashed horizontal line indicates the average energy density of the box. The region with clear exponentially damped oscillations corresponds to times where the subdominant modes have decayed sufficiently, and the dominant mode has leading amplitude. The dotted line corresponds to a fit to the envelope, from which we extract the imaginary part of omega. The fact that no mode grows in time indicates that $\mathcal{X}_a$ is locally dynamically stable. (Bottom) Time evolution of some Fourier modes of a perturbation around the type III, inhomogeneous, static configuration $\mathcal{X}_c$ of Fig. 3.24(bottom-right) with $\hat{\mathcal{E}} \simeq 0.651$, $\hat{L} \simeq 11.501849$. In this case the leading mode grows exponentially in time, indicating that $\mathcal{X}_c$ is locally dynamically unstable.

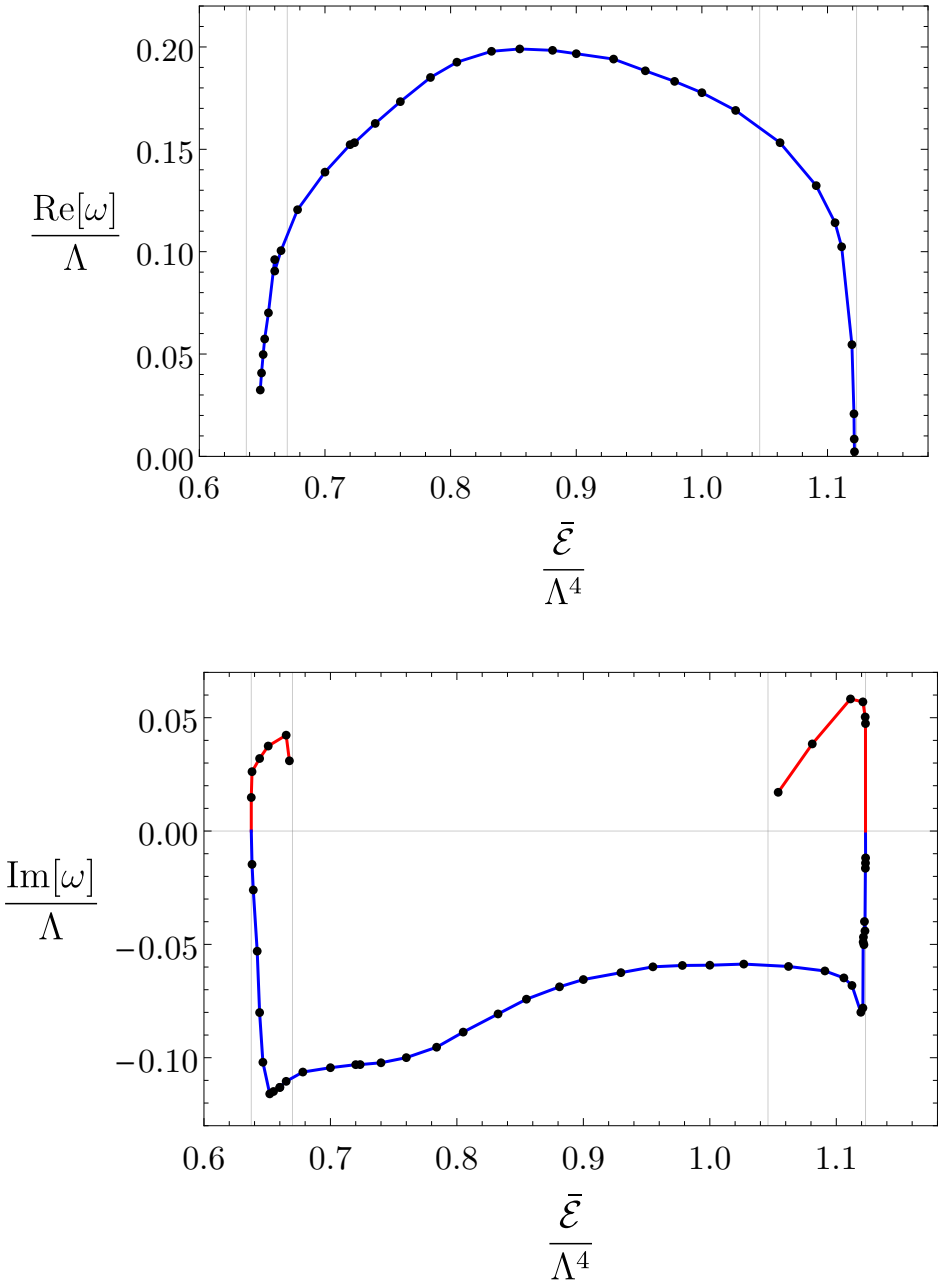

Figure 3.26: Real part (top) and imaginary part (bottom) of the frequency of the dominant linear mode of the perturbations around static inhomogeneous solutions with $\hat{L} \simeq 11.501849$ and varying energy densities. The real part of omega goes to zero at the cusps and vanishes for locally unstable solutions. The imaginary part of omega goes to zero at the cusps and at the mergers. Vertical lines indicate the location of the mergers and the cusps, as in Fig. 3.22. Blue (red) curves correspond to locally stable (unstable) solutions.

In this section we have discussed the (in)stability of what we called “ground-state" or “fundamental" solutions in Sec. 3.1.6, namely of solutions whose spatial energy density profile has a single maximum and a single minimum. Here we have not explicitly investigated the case of “excited" solutions, namely those with multiple maxima and minima. However, some configurations of this type were studied in [63], and in all cases they were found to be locally dynamically unstable. As discussed in Sec. 3.1.6 and Sec. 3.1.7 the reason is that the entropy density can be continuously increased by moving two of these maxima or minima towards each other. Since this seems to be a generic feature, we expect all excited configurations to be locally dynamically unstable.

3.2.3 Full time evolution of the unstable solutions

In the previous section we studied the local stability properties of the inhomogeneous static solutions, finding some regions of local instability. A natural question is therefore what is the end state of the evolution if these locally unstable solutions are perturbed. In this section we perform the full time evolution of the system and determine the end state.

Given a locally unstable solution there are two natural possibilities for the end state of the evolution. In Fig. 3.27 we present a concrete example where we show the three static solutions with the same $(\hat{L},\hat{\mathcal{E}}) \simeq (11.501849, 0.651)$: $\mathcal{X}_c$, $\mathcal{X}_d$ and $\mathcal{X}_e$, where $\mathcal{X}_c$ is the static solution presented in Fig. 3.24(bottom-right). For the locally unstable solution $\mathcal{X}_c$, the two possible candidates for the end state of the evolution are the homogeneous solution $\mathcal{X}_d$ and the inhomogeneous solution $\mathcal{X}_e$, since both of these have larger entropy than $\mathcal{X}_c$. By performing full

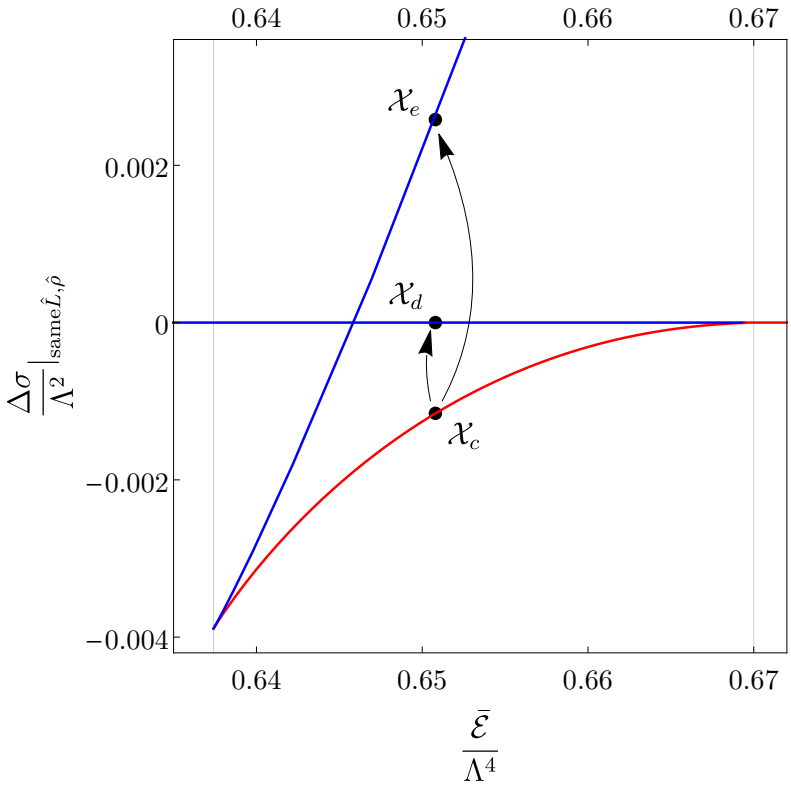

Figure 3.27: Zoom-in on the left region of Fig. 3.22, where $\hat{L} \simeq 11.501849$. $\mathcal{X}_c$, $\mathcal{X}_d$ and $\mathcal{X}_e$ are the three static solutions with the same average energy density $\hat{\bar{\mathcal{E}}} \simeq 0.651$. The nonlinear time evolution of Fig. 3.28(left) corresponds to an evolution from $\mathcal{X}_c$ to $\mathcal{X}_d$, and Fig. 3.28(right) corresponds to an evolution from $\mathcal{X}_c$ to $\mathcal{X}_e$.

time evolution we confirm that both solutions $\mathcal{X}_d$ and $\mathcal{X}_e$ can be the end state of the evolution,

and that which one is reached depends on the initial perturbation.

In order to illustrate this we essentially extend the range of the time evolution shown in Fig. 3.24(bottom-left). Recall that in that figure we dynamically generated a solution very close to $\mathcal{X}_c$ by fine-tuning the amplitude of the initial perturbation to be close to the critical value $\mathcal{A}^*$. Since the amplitude we choose is close but not exactly equal to $\mathcal{A}^*$, the result of this time evolution at intermediate times is not exactly the solution $\mathcal{X}_c$ but $\mathcal{X}_c$ plus a small perturbation. Since the perturbation is small the system spends a sizeable amount of time in a very slowly evolving configuration close to $\mathcal{X}_c$, as can be seen from the intermediate-time behaviour in Fig. 3.28. However, if the exact amplitude is slightly smaller than the critical one then further time evolution eventually drives the system back to the homogeneous solution labelled as $\mathcal{X}_d$ in Fig. 3.27. This is the case in Fig. 3.28(left). If instead the amplitude is slightly larger than the critical one then the system eventually evolves towards the stable, inhomogeneous solution labelled as $\mathcal{X}_e$ in Fig. 3.27. This is the case in Fig. 3.28(right). Note that the evolution from

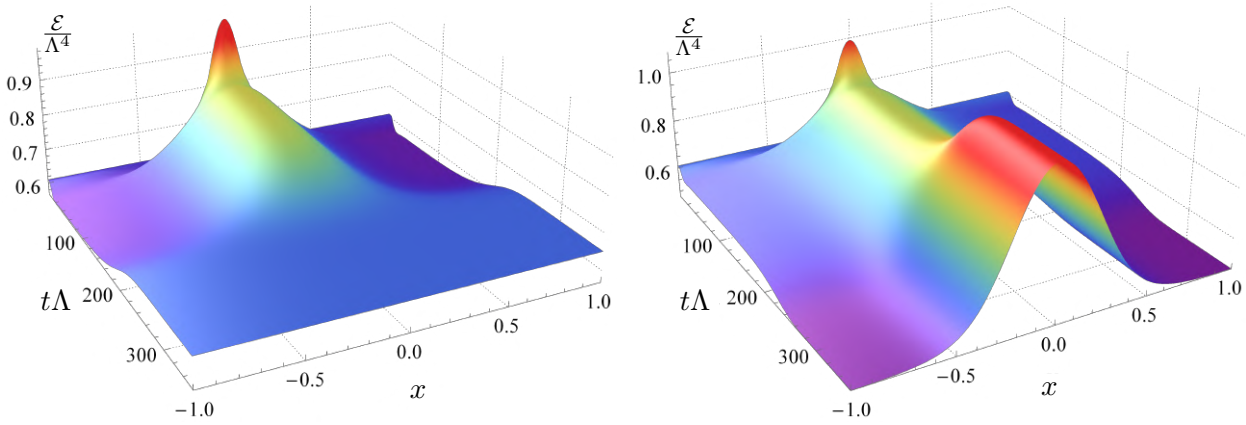

Figure 3.28: Extension to longer times of the time evolution shown in Fig. 3.24(bottom-left), whose initial state is a homogeneous configuration plus a large perturbation of amplitude $\mathcal{A}$. At intermediate times this generates the unstable solution $\mathcal{X}_c$ plus a small perturbation. (Left) If the amplitude of the initial perturbation $\mathcal{A}$ is slightly smaller than the critical value $\mathcal{A}^*$ then the system eventually evolves back to the homogeneous solution labelled as $\mathcal{X}_d$ in Fig. 3.27. (Right) If the amplitude of the initial perturbation $\mathcal{A}$ is slightly larger than the critical value $\mathcal{A}^*$ then the system eventually evolves towards the stable, inhomogeneous solution labelled as $\mathcal{X}_e$ in Fig. 3.27.

the unstable to the stable solutions can be viewed as a long, approximately linear regime (when the unstable solution is perturbed), followed by a fast non-linear regime, further followed by another long, approximately linear regime (when the system relaxes to the corresponding stable solution). We have verified that, at the qualitative level, these results apply to all the unstable solutions with $\hat{L} \simeq 11.501849$ and varying energy densities that we have studied.

3.3 Discussion

By placing our holographic model (2.1) in a box with translational invariance only along two boundary directions, we have varied the volume by changing the size $\hat{L} = \Lambda L$ of the third side, where Λ is the microscopic scale of the gauge theory. We have then constructed what we believe is the complete set of all possible homogeneous or inhomogeneous equilibrium states at finite $\hat{L}$. On the gravity side these correspond to uniform or lumpy branes, respectively. Although we do not have a mathematical proof that this set is indeed complete, we have found no evidence to the contrary in our extensive investigations based both on static and dynamical methods.

The first effect of the finite volume is that some homogeneous states between points A and B in Fig. 3.1 become locally dynamically stable, as illustrated in Fig. 3.8. The reason for this is that the spinodal instability is a long-wavelength instability. If $\hat{L}$ is below a certain energy-dependent value, then the potentially unstable mode does not fit in the box and the corresponding homogeneous state is actually stable. The unstable states are those in the region inside the parabola in Fig. 3.8. We see that as $\hat{L} \to \infty$ we recover the fact that all states with energy densities between A and B are unstable, but that at finite $\hat{L}$ some of them are stable. In particular, there is a value $\hat{L} = \hat{L}_K$ below which all homogeneous states are locally dynamically stable since none of them can accommodate an unstable mode.

The parabola in Fig. 3.8 is a curve of marginal stability. Therefore we expect a branch of static, inhomogeneous states to emanate from each point on this curve. One should think of the extra direction in which these branches emanate as the entropy relative to that of the homogeneous state, $\Delta\hat{\sigma}$. The union of all such inhomogeneous branches is therefore a surface in the three-dimensional space parametrized by the average energy density in the box $\overline{\mathcal{E}}$, the size of the box $\hat{L}$, and the entropy $\Delta\hat{\sigma}$. We will refer to this surface as the "entropy surface". The intersection of this surface with the $\hat{\overline{\mathcal{E}}}$-$\hat{L}$ plane contains the parabola in Fig. 3.8 (as well as other points such as the points a and b of Fig. 3.18). The curves in Fig. 3.15 are the projections on this plane of constant-$\hat{T}$ slices of the entropy surface. Similarly, the vertical lines in Fig. 3.16 are the projections on this plane of constant-$\hat{L}$ slices. The same slices projected onto the $\hat{\overline{\mathcal{E}}}$-$\hat{T}$ plane are shown in Fig. 3.11. This last figure makes it clear that inhomogeneous states only exist in the range of temperatures $\hat{T}_A \leq \hat{T} \leq \hat{T}_B$.

The structure of the entropy surface is most easily understood by thinking of it as the union of constant-$\hat{L}$ slices for all $\hat{L} > \hat{L}_K$. The shape of each of these slices as a function of the energy density is shown in Figs. 3.17 and 3.18. We see that, at the qualitative level, there are three possibilities depending on the value of $\hat{L}$ in relation to the following hierarchy

$$\hat{L}_K < \hat{L}_{\Sigma_1} < \hat{L}_{\Sigma_2} \,. \tag{3.80}$$

These three length scales are an intrinsic property of the theory at finite volume and their values are given in (3.75). If $\hat{L}_K < \hat{L} < \hat{L}_{\Sigma_1} < \hat{L}_{\Sigma_2}$, then $\Delta\hat{\sigma}$ is always positive for all the values of the energy for which inhomogeneous states exist. This is the case illustrated by Fig. 3.17(top-left) and by the bottom curve with beige inverted triangles in Fig. 3.18. If instead $\hat{L}_K < \hat{L}_{\Sigma_1} < \hat{L} < \hat{L}_{\Sigma_2}$ then the $\Delta\hat{\sigma}$ curve becomes negative and develops a cusp near its endpoint on the right-hand side. This is the case illustrated by Fig. 3.17(top-right) and by the second-from-the-bottom curve with brown diamonds in Fig. 3.18. Finally, if $\hat{L}_K < \hat{L}_{\Sigma_1} < \hat{L}_{\Sigma_2} < \hat{L}$ then the $\Delta\hat{\sigma}$ curve becomes negative and develops cusps near both of its endpoints. This is the case illustrated by Fig. 3.17(bottom) and by the two top curves with orange circles and green squares, respectively, in Fig. 3.18.

The shape of the entropy surface that we have just described determines the structure of phase transitions in the microcanonical ensemble. Recall that in the limit $\hat{L} \to \infty$ the set of globally preferred, maximum-entropy states are those indicated by the black curves (with arrows) in Fig. 3.1 (see also the discussion around Figs. 3.5 and 3.6). The direction of the arrows in Fig. 3.1 indicates what happens as the energy decreases from an arbitrarily high value. As the energy density decreases towards point D the preferred states are homogeneous branes of decreasing temperature. At D there is a phase transition into inhomogeneous states of constant temperature T_c. Since $\hat{L} \to \infty$ these are phase-separated configurations in which the homogeneous phases D and E coexist. At E there is another phase transition, in this case from inhomogeneous to homogeneous states. The fact that the fraction of the total volume occupied by each phase varies continuously between 0 and 1 as the energy density varies between D and E suggests that these transitions are continuous in the microcanonical ensemble. Continuity can also be seen more formally as follows. For fixed length and source, the first law (3.44) takes

the form

$$\frac{1}{T} = \frac{dS}{dE}\,. \tag{3.81}$$

In the microcanonical ensemble the total entropy S is the relevant thermodynamic potential, the total energy E is the control parameter and T is a derived quantity. At the points D and E the temperature is continuous, but its derivative dT/dE is not, because this is positive on the homogeneous branch but it vanishes on the inhomogeneous one.

This picture is modified at finite $\hat{L}$. Note that in this case the system may still exhibit phase transitions since the planar limit that we work in, $N_c \to \infty$, acts effectively as a thermodynamic limit. Consider first Fig. 3.29 which illustrates the structure of phase transitions for a length $\hat{L} \simeq 11.501849$ such that $\hat{L}_K < \hat{L}_{\Sigma_1} < \hat{L}_{\Sigma_2} < \hat{L}$ (this is the value corresponding to the orange circles in Fig. 3.11). In this case the preferred states lie on the homogeneous branch until the energy density reaches that of point a in Fig. 3.18. At this point a first-order phase transition takes place between the homogeneous state and the state a on the inhomogeneous branch, as indicated by the top horizontal arrow in Fig. 3.29. Note that this transition can take place before (as in the case of the orange circles in Fig. 3.11) or after (as in the case of the green squares Fig. 3.11) the turning point A is reached. The reason that this is a first-order transition is that the temperature changes discontinuously. As the energy decreases further, the preferred states are those on the inhomogeneous branch until the energy density reaches that of point b in Fig. 3.18. At this point another first-order phase transition takes place between the inhomogeneous state and a state on the homogeneous branch with the same average energy density, as indicated by the bottom horizontal arrow in Fig. 3.29. Note that this state is below the turning point B (i.e. $\hat{\bar{\mathcal{E}}}_b < \hat{\bar{\mathcal{E}}}_B$). As the energy is further decreased the preferred state remains on the homogenous branch.

Thinking of the infinite-volume case as the limit $\hat{L} \to \infty$ of the situation described in Fig. 3.29 sheds light on the order of the phase transition at infinite volume. As $\hat{L}$ increases the point a in Fig. 3.29 moves up and to the right. This means that the homogeneous and the inhomogeneous states between which the transition takes place become closer to one another. In the limit $\hat{L} \to \infty$ the point a tends to the point D (of Figs. 3.1 or 3.3) and the transition takes place between two states at the same temperature $\hat{T} = \hat{T}_c$. Since the discontinuity in $\hat{T}$ disappears the phase transition becomes second-order.

Consider now Fig. 3.30, which illustrates the structure of phase transitions for a length $\hat{L} \simeq 5.299674$ such that $\hat{L}_K < \hat{L} < \hat{L}_{\Sigma_1} < \hat{L}_{\Sigma_2}$ (this is the value corresponding to the inverted beige triangles in Fig. 3.11). In this case the preferred states lie on the homogeneous branch until the merger point with the inhomogeneous branch is reached. At this point a transition between the homogeneous and the inhomogeneous branches takes place. Since the transition happens at the merger point, the temperature is continuous and the transition is second-order. As the energy is further decreased the preferred states remain on the inhomogeneous branch until this merges again with the homogeneous branch. At this point another second-order phase transition takes place. Below this point the preferred state lies on the homogeneous branch.

In the intermediate range of lengths $\hat{L}_K < \hat{L}_{\Sigma_1} < \hat{L} < \hat{L}_{\Sigma_2}$ the structure of transitions is a hybrid between those described in Figs. 3.29 and 3.30. As the energy decreases there is first a first-order phase transition between the homogeneous branch and the inhomogeneous branch. In our model the point on the homogeneous branch lies between A and Σ_1, and the point on the inhomogeneous branch is the analog of point a in Fig. 3.29. As the energy is further decreased the preferred state remains on the inhomogeneous branch until this merges with the homogeneous one. At this point a second-order phase transition occurs in which the preferred state becomes the one on the homogeneous branch. This second transition is analogous to that in Fig. 3.30. Below this point the preferred state remains on this branch.

Finally, for lengths such that $\hat{L} < \hat{L}_K < \hat{L}_{\Sigma_1} < \hat{L}_{\Sigma_2}$, no inhomogeneous states exist and all the homogeneous ones are dynamically stable. In this case no phase transitions occur as the

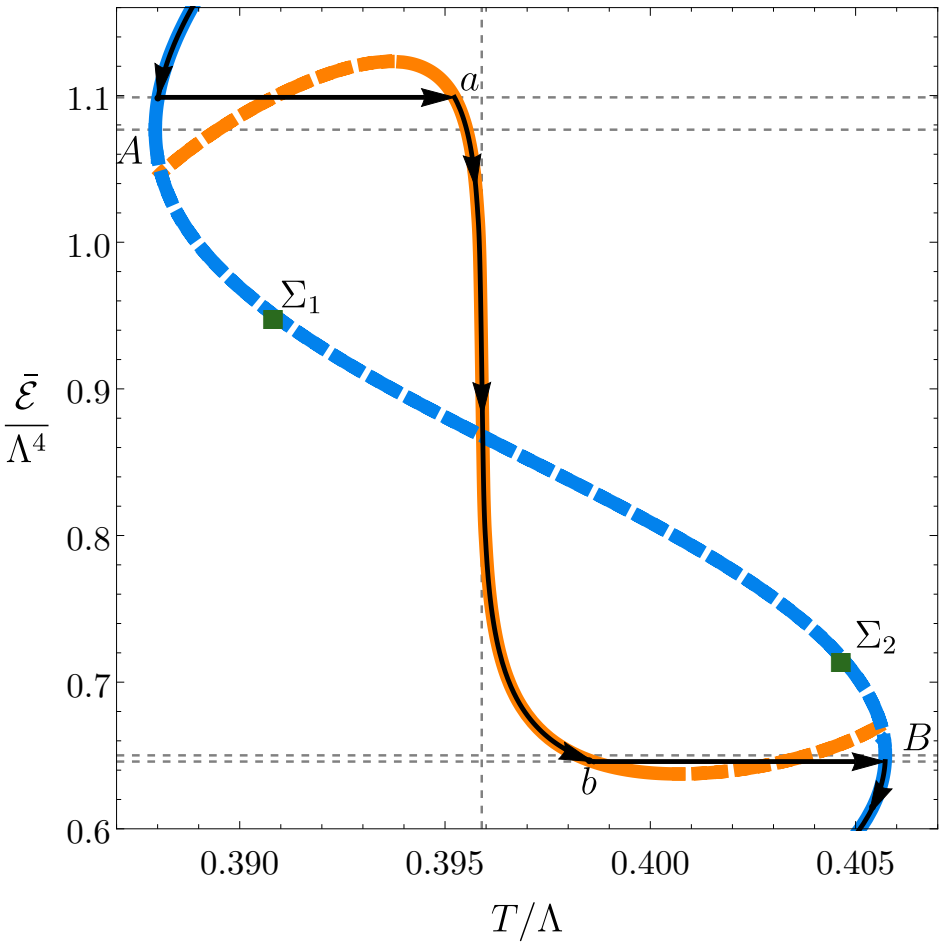

Figure 3.29: Phase diagram in the microcanonical ensemble for a length $\hat{L} \simeq 11.501849$ such that $\hat{L}_K < \hat{L}_{\Sigma_1} < \hat{L}_{\Sigma_2} < \hat{L}$. The blue and the orange curves correspond to homogeneous and inhomogeneous states, respectively. The orange curve is the same as the curve of orange circles in Fig. 3.11. Solid segments indicate locally dynamically stable states; dashed segments indicate unstable ones. The black curves with arrows indicate the sequence of globally preferred, maximum-entropy states as the average energy density decreases. The points a and b corrre-spond to those in Fig. 3.18. The first and fourth (from top to bottom) dashed horizontal lines indicate the energy densities at these points, whereas the second and third lines indicate the energy densities at the turning points A and B. The phase transitions between the homogeneous and the inhomogeneous branches, indicated by the horizontal arrows, are first-order.

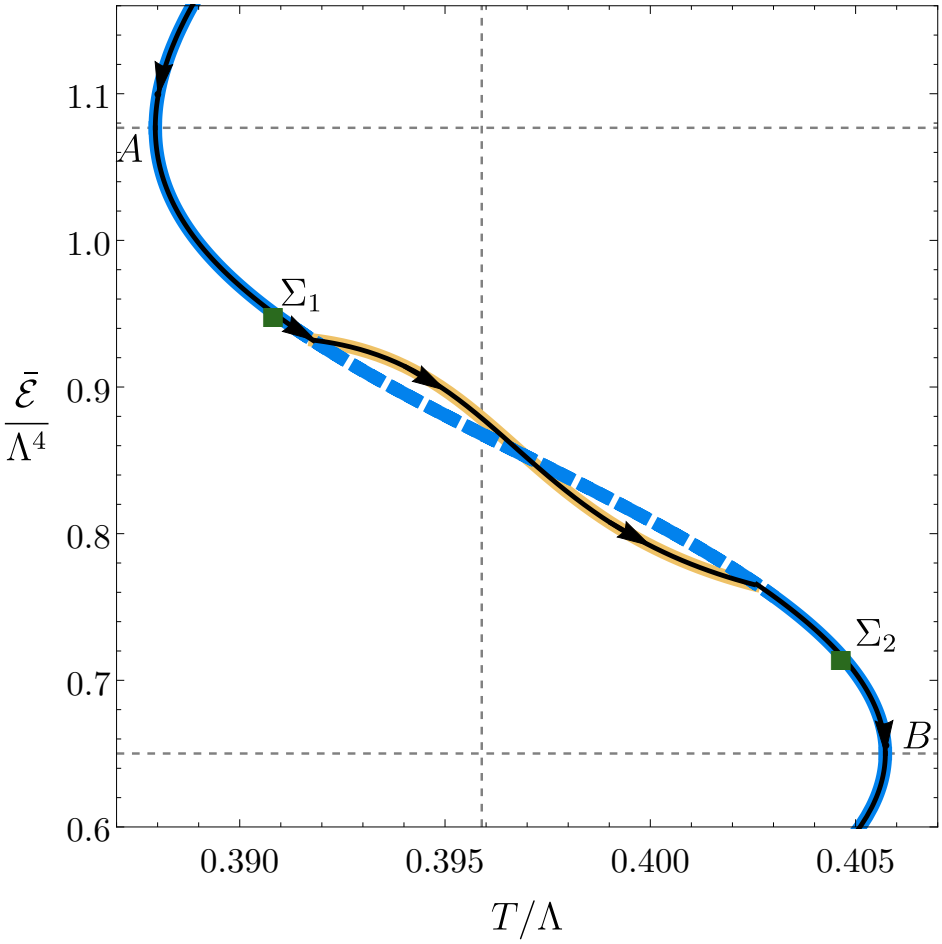

Figure 3.30: Phase diagram in the microcanonical ensemble for a length $\hat{L} \simeq 5.299674$ such that $\hat{L}_K < \hat{L} < \hat{L}_{\Sigma_1} < \hat{L}_{\Sigma_2}$. The blue and the beige curves correspond to homogeneous and inhomogeneous states, respectively. The beige curve is the same as the curve of beige inverted triangles in Fig. 3.11. Solid segments indicate locally dynamically stable states; dashed segments indicate unstable ones. The black curves with arrows indicate the sequence of globally preferred, maximum-entropy states as the average energy density decreases. The phase transitions between the homogeneous and the inhomogeneous branches take place at the points where these branches merge and they are second-order.

energy decreases from infinity to zero, as illustrated in Fig. 3.31.

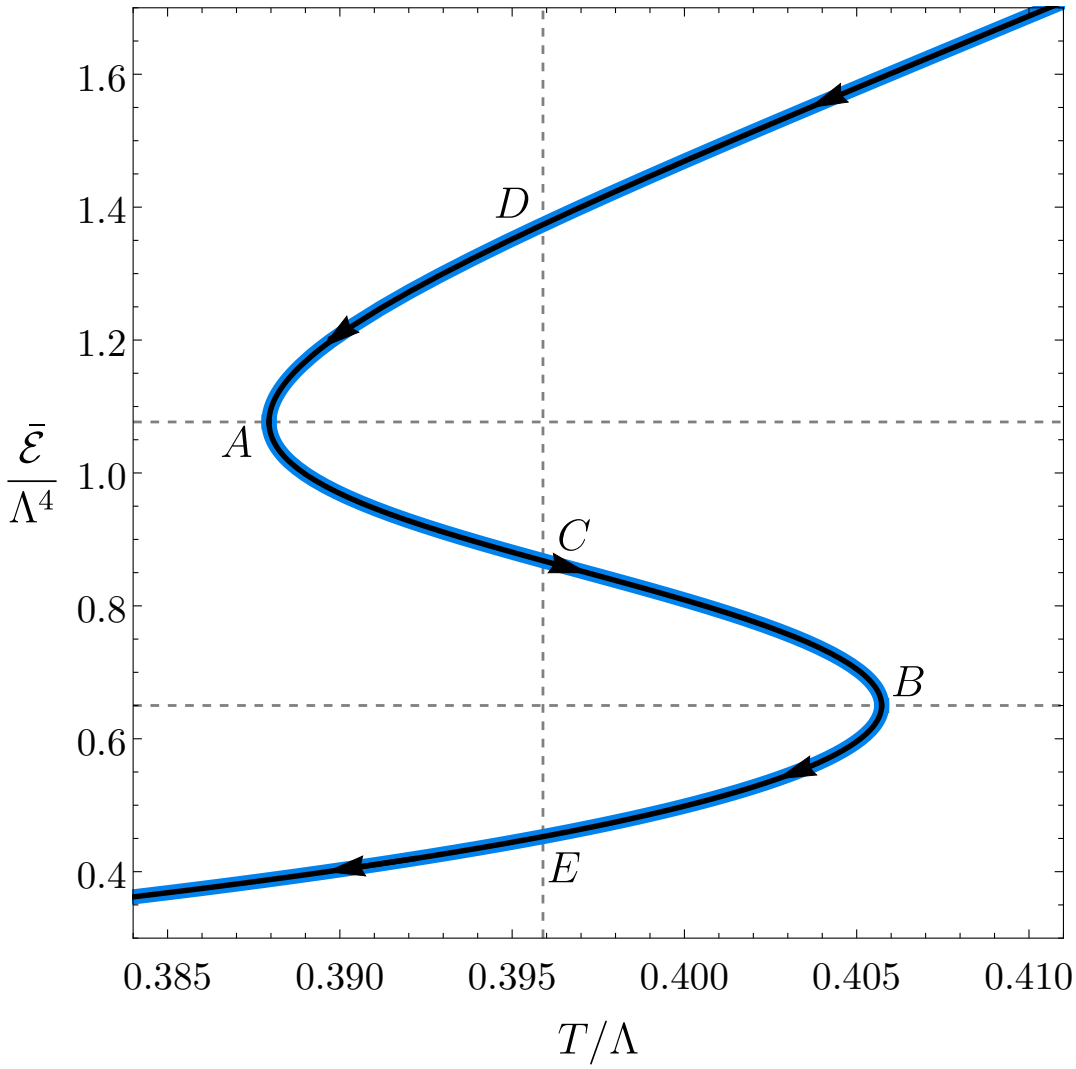

Figure 3.31: Phase diagram in the microcanonical ensemble for a length $\hat{L}$ such that $\hat{L} < \hat{L}_K < \hat{L}_{\Sigma_1} < \hat{L}_{\Sigma_2}$.

In the figures above we have used continuous and dashed segments to distinguish between locally dynamically stable and locally dynamically unstable states. In the case of homogeneous states these properties can be established via a perturbative analysis. In the case of inhomogeneous states we used a numerical code for time evolution to study the behaviour of small perturbations. The results are shown in Fig. 3.22 and can be succinctly summarised as follows: all states on the upper part of the curve, shown in blue, are stable, whereas those on the lower part, shown in red, are unstable (see also a relevant zoom in Fig. 3.27). Once an unstable state is slightly perturbed, its full time evolution and its end state depend on the perturbation. For example, the locally dynamically unstable state $\mathcal{X}_c$ in Fig. 3.22 and Fig. 3.27 can decay to either of the stable states $\mathcal{X}_d$ or $\mathcal{X}_e$. The corresponding time evolutions are shown in Figs. 3.28(left) and 3.28(right), respectively.

For completeness, note that, unlike in the microcanonical ensemble, at finite volume lumpy branes are never the dominant thermodynamic phase in the canonical ensemble, as illustrated by Fig. 3.19.

In our analysis we have benefited from two simplifying assumptions. The first one is that we imposed translational invariance along two of the three spatial directions of the box. Lifting this restriction will generically allow for inhomogeneities to develop in all three directions. It would be interesting to study this more general setup, in particular the possible interplays between different length scales in different directions. Hopefully, the "one-dimensional building blocks" that we have investigated will be useful to understand the three-dimensional case.

The second simplifying assumption is the fact that we have worked in the $N_{\rm c} \to \infty$ limit, which ensures that the system is in the thermodynamic limit despite the finite volume. In particular, it guarantees that true phase transitions may occur. At finite $N_{\rm c}$ these transitions will turn into cross-overs. However, the latter can be made arbitrarily rapid by making $N_{\rm c}$ sufficiently large. This means that our results should be a good approximation to the physics at finite but large $N_{\rm c}$.

Chapter 4

Domain Collisions

In the previous chapter we took a first look into the dynamical generation of inhomogeneous states in a theory with a first order thermal phase transition. The goal there was to obtain, as fast as possible, the desired inhomogeneous solution, thence the initial conditions were specifically designed. As a consequence, our time evolution lack rich physics that is uncovered when more generic initial conditions are considered.

Imagine placing the theory in an initial homogeneous state with an energy density in the unstable, spinodal region (see Fig. 4.1). If this state is perturbed, the system will evolve to a final state that will necessarily be inhomogeneous. The evolution consists of four generic stages [63] visible in Fig. 4.2: A first, linear stage in which the instability grows exponentially; a second, non-linear stage in which peaks and/or phase domains are formed; a third stage in which these structures collide and merge; and a fourth stage in which the system finally relaxes to a static, phase-separated configuration. In any given evolution of this type, the velocities of the different domains are a complicated function of the perturbation of the initial, homogeneous state. This makes it difficult to perform a systematic study of the physics of the collision as a function of the domain velocities. In this chapter we will overcome this difficulty by directly preparing initial states consisting of domains moving towards each other at a wide range of velocities.

On the gravity side the above dynamics translates into the physics of a time-dependent, inhomogeneous horizon. Understanding this physics provides one motivation for our work. For example, we will examine in detail how the area of the horizon changes as two domains merge. Another motivation comes from the possible relevance of the spinodal instability in experiments trying to observe the first order phase transition of QCD.

We emphasize from the start that the domains we consider here should not be confused with the bubbles created via a nucleation process in first-order phase transitions. The expansion of those bubbles is driven by a pressure difference between the inside and the outside of the bubble. Instead, in our case the domains move simply because they are created with some initial velocity. In fact, if a number of bubbles are nucleated in a large – but finite-size – box, and if the average energy density in the box is between $\mathcal{E}_{high}$ and $\mathcal{E}_{low}$, then the endpoint of the evolution will be a phase-separated state with two domains with energies $\mathcal{E}_{high}$ and $\mathcal{E}_{low}$.

4.1 The model

We will choose the same potential parameters for (2.3) as in the previous chapter, $\lambda_4 = -1/4$ and $\lambda_6 = 0.1$. The fact that this choice was giving us a model with all quantities of $\mathcal{O}(1)$ in units of Λ, in particular is highly convenient when numerically simulating the formation of a phase separation. The phase diagram of such model is shown in Fig. 4.1 and we recall that $T_{critical}/\Lambda = 0.3959$, $\mathcal{P}_{critical}/\Lambda^4 = 0.1124$, $\mathcal{E}_{high}/\Lambda^4 = 1.3739$ and $\mathcal{E}_{low}/\Lambda^4 = 0.4527$. For simplicity, we will allow for dynamics only along one of the three spatial directions of the gauge

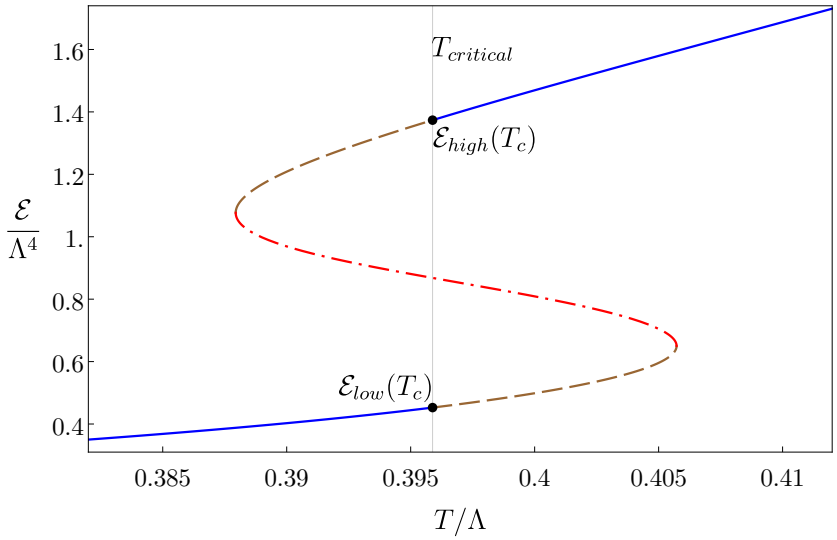

Figure 4.1: Energy as a function of temperature for the theory considered in this paper, with intrinsic scale Λ. Stable, metastable and unstable states are represented by solid, dashed and dot-dashed curves, respectively. The vertical grey line corresponds to the phase transition temperature.

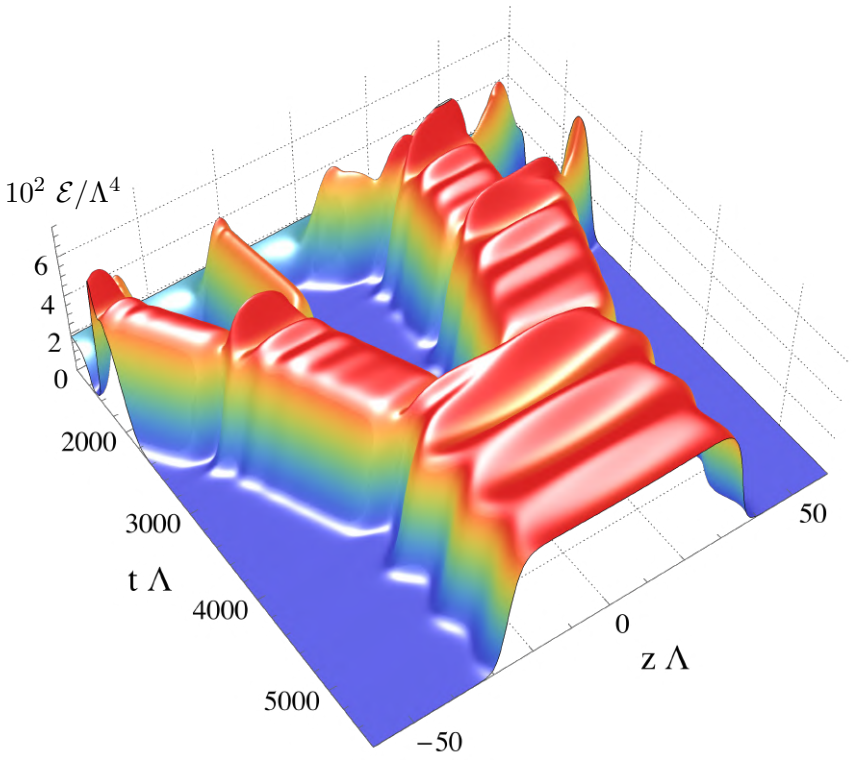

Figure 4.2: Evolution of the energy density as a function of time and space for an initial homogeneous state in the spinodal region that is slightly perturbed at $t = 0$. Figure taken from [63].

theory, which we call z. In other words, we impose translational symmetry along x, y. We will also refer to z as the longitudinal coordinate and to x, y as the transverse directions. We will

decompose the gauge theory stress tensor accordingly and work with the rescaled quantities

$$(\mathcal{E}, P_T, P_T, P_L, \mathcal{J}) = \frac{\kappa_5^2}{2\ell^3}(-T_t^t, T_x^x, T_y^y, T_z^z, T_z^t)\,, \tag{4.1}$$

where $\mathcal{E}$ is the energy density, P_L and P_T are the longitudinal and transverse pressures, and $\mathcal{J}$ is the momentum density in the z-direction. In addition, as we already did previously, we compactify the z-direction on a circle of length L. This infrared cut-off is technically convenient since it reduces the number of unstable modes of homogeneous states in the spinodal region to a finite number. In addition, compactifying the z-direction on a circle also brings about interesting new effects even for a single, boosted domain. We will start by analyzing this case in Sec. 4.2 and then we will move to collisions of two domains in Sec. 4.3. Note that we are slightly abusing the word "domain" in the following sense. At the end of the evolution in Fig. 4.2 there are two domains with energy densities $\mathcal{E}_{high}$ and $\mathcal{E}_{low}$. Nevertheless, we will often use the word "domain" to refer specifically to the high-density phase. In this sense, we will sometimes think of the end state of Fig. 4.2 as a domain surrounded by a low-density bath.

4.2 Domains in motion

In a domain collision, each of the participants is initially moving independently of the other, surrounded by a low-density bath. In this section we will study the dynamics of such a single domain. We will construct an initial, out-of-equilibrium state with a non-uniform fluid velocity in the z-direction and watch it evolve into a steady-state with uniform velocity. In addition to its intrinsic interest, this will also help us understand the construction of initial states in the case of domain collisions.

We start with a single, static domain obtained as the end-state of a simulation like that in Fig. 4.2. We then modify the near-boundary fall-offs of the metric functions on the initial time slice on the gravity side[1] so as to add a finite momentum density along the z-direction, $\mathcal{J}(z)$. We keep the total energy fixed as we inject this momentum; as we will see below this results in a decrease in the entropy of the system. The specific z-dependence is chosen to be

$$\mathcal{J}(z) = j\left(\mathcal{E}(z) - \mathcal{E}_{low}(T_c)\right), \tag{4.2}$$

where j is an appropriately chosen constant. At this initial step the momentum density has vanishing support on the low-density region. In order to be able to initialise our numerical code the initial value of j cannot be too large. However, choosing a small value, letting the system evolve for a few time steps, increasing the value of j, and iterating this procedure, allows us to eventually reach high velocities. The reason for the iterations is that, after each change in the near-boundary fall-offs, a few time steps of evolution allow the bulk functions to adapt to the new near-boundary fall-offs. In particular, this allows our code to find the new horizon within our numerical grid. We will define as the initial time, $t\Lambda = 0$, the time at the end of this iterative process. At each step in the iteration process a fraction of the total momentum gets transferred to the low-density bath. As a consequence, at the end of the process the bath will not be completely at rest, as illustrated by the blue curve in Fig. 4.3(top). Nevertheless, at this time most of the momentum density is still in the domain, where the fluid flow velocity is larger than in the bath. It is precisely this feature that tells us that the resulting state at $t\Lambda = 0$ is out of equilibrium.

After $t\Lambda = 0$ we do not inject any more momentum into the system. The subsequent evolution is characterized by a significant energy and momentum transfer between the domain and the bath. The initial state is so far from equilibrium that it splits into several fragments that eventually merge back to form a single domain, as illustrated in Fig. 4.4. The stationary

[1] Specifically the subleading terms, which determine the expectation values.

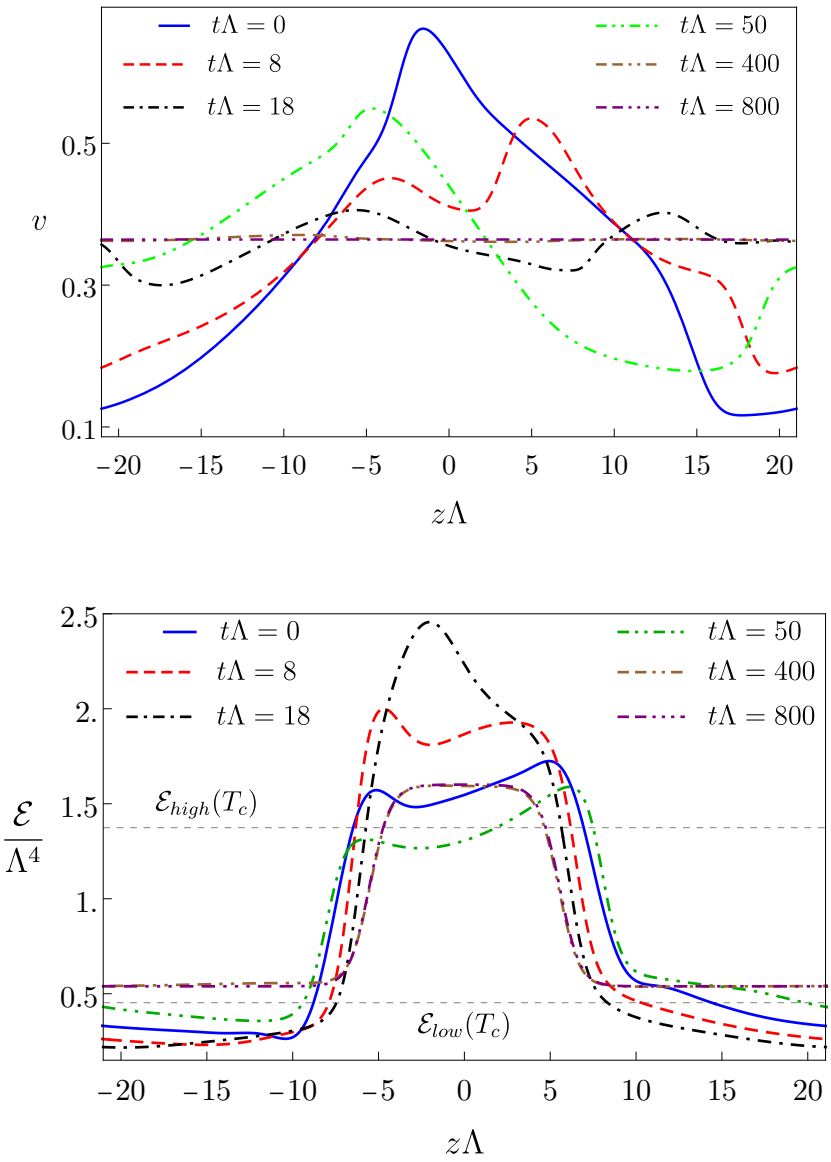

Figure 4.3: Time evolution of the fluid velocity (top) and of the energy density profile (bottom) for a domain in motion. To facilitate the comparison, each profile has been shifted by a constant amount to match the domain midpoint with $z\Lambda = 0$. The maximum of the fluid velocity at $t\Lambda = 0$ is $v_{max} = 0.66$.

state is reached around $t\Lambda \sim 400$. At this and at later times the fluid velocity field is constant along the z-direction with value $v = 0.364$, as seen in Fig. 4.3(top). In other words, the "system moves as a whole". This is illustrated in Fig. 4.5, where we see that the energy density profile remains constant in time once the steady state is reached to a precision better than 1%. This steady-state energy profile is narrower than that of the out-of-equilibrium state at $t\Lambda = 0$, as can be seen in Fig. 4.3(bottom), and it is also narrower than that of the static, equilibrium state with the same total energy, as illustrated in Fig. 4.6 for two different velocities.

We see in the figure that the domains become narrower as the velocity increases, and that the energy densities in the domain and in the bath are higher than $\mathcal{E}_{high}(T_c)$ and $\mathcal{E}_{low}(T_c)$, respectively. These features are consistent with the fact that, by construction, all these configurations have the same total energy.

In the steady state, a comoving observer traveling with velocity v sees a fluid configuration at

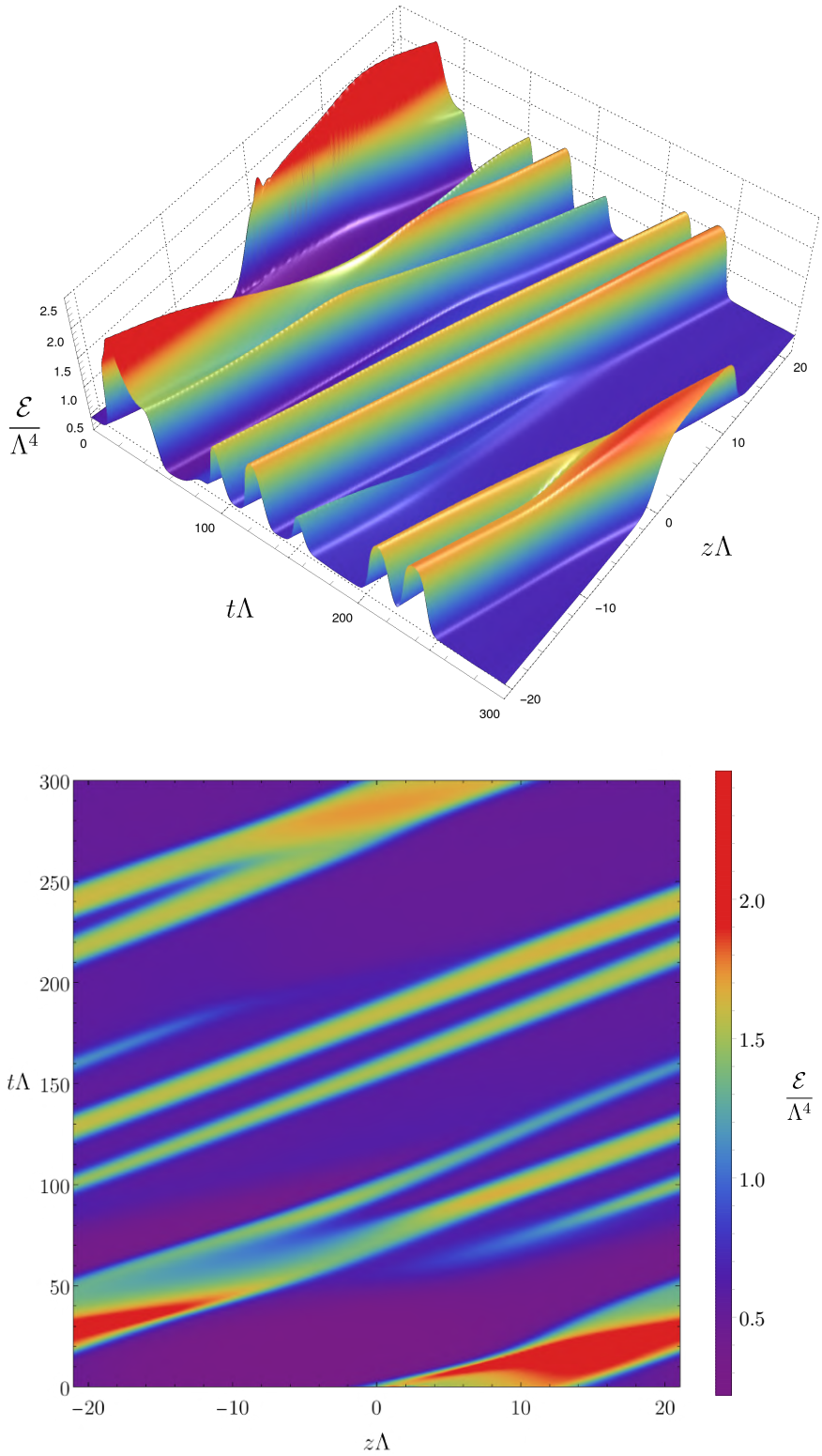

Figure 4.4: Plots of the energy density for the evolution of an initial, single-domain state that splits into several fragments that subsequently merge back into a single domain.

rest. This observer uses coordinates t', z' related to t, z through the usual Lorentz transformation

$$t' = \gamma(t - vz)\,, \qquad z' = \gamma(z - vt)\,, \qquad \gamma = (1 - v^2)^{-1/2}\,. \tag{4.3}$$

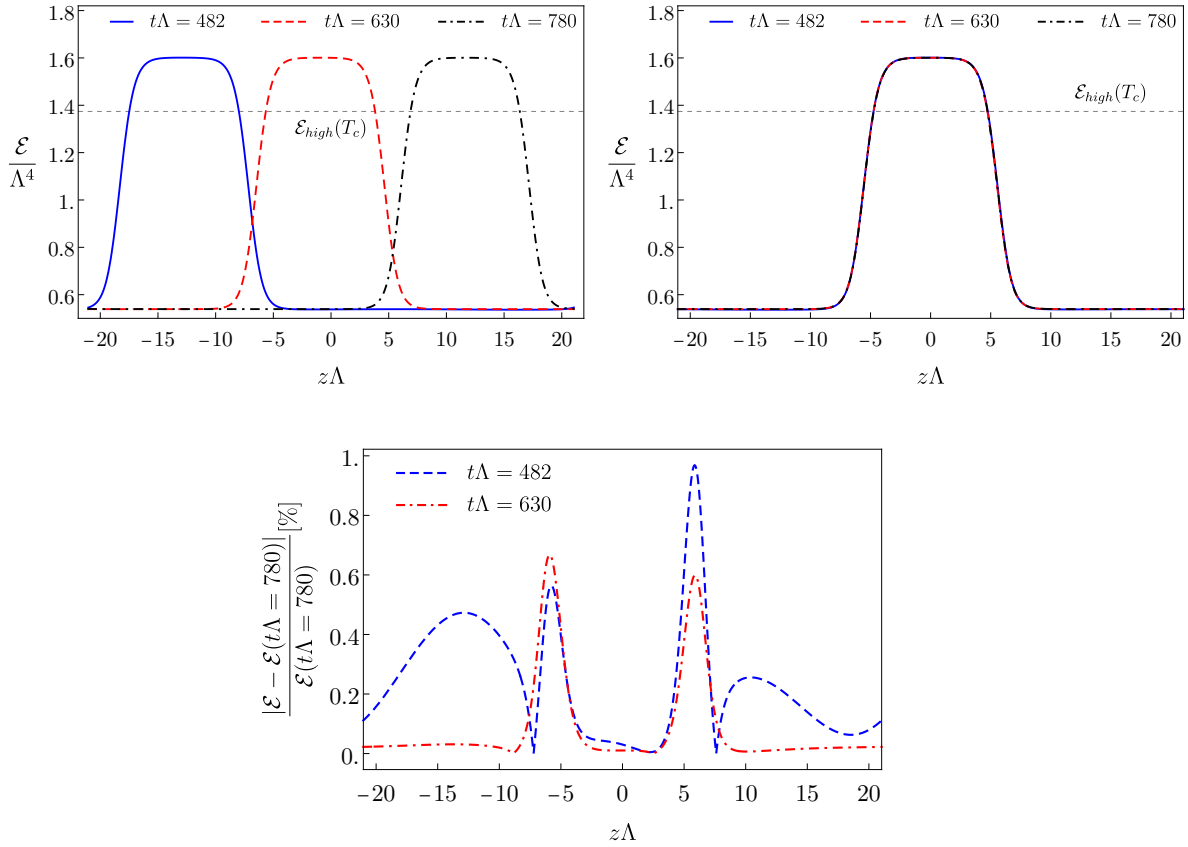

Figure 4.5: (Left) Snapshots of the energy density at late times for the same initial state as in Fig. 4.3. (Right) The same profiles shifted by an appropriate constant. (Bottom) Relative difference between the profiles.

The original identification $(t, z) \sim (t, z + L)$, translates into a non-trivial identification for the comoving observer

$$(t', z') \sim (t' - \gamma v L, z' + \gamma L)\,. \tag{4.4}$$

In other words, for the co-moving observer the identification is not purely along the spatial direction but it involves time as well. This imposes a non-trivial constraint on any physical configuration seen by this observer, since any such configuration must be invariant under (4.4). However, for configurations that are static with respect to the comoving observer this condition reduces to periodicity along the z'-direction with period $L' = \gamma L$. This is the case for the fluid configuration obtained by applying the Lorentz transformation (4.3) to the configurations of Fig. 4.6. In particular, the energy density in the comoving frame takes the form

$$\mathcal{E}' = \gamma^2 \left(\mathcal{E} + v^2 P_z - 2v\mathcal{J}\right)\,, \tag{4.5}$$

and the average energy in this frame is

$$\bar{\mathcal{E}}' = \bar{\mathcal{E}} - v\bar{\mathcal{J}}\,. \tag{4.6}$$

The result of applying (4.5) to the $v = 0.187$ case of Fig. 4.6 is shown by the dashed, red curve in Fig. 4.7. As expected, this matches the solid blue curve, corresponding to a profile obtained directly as an inhomogeneous, static configuration with average energy (4.6) in a box of size L'.

We see that, in the case of a single domain, we could have obtained the steady states of Fig. 4.6 by applying the inverse Lorentz transformation to the corresponding static configurations. In contrast, in the case of two domains moving towards each other that we will consider

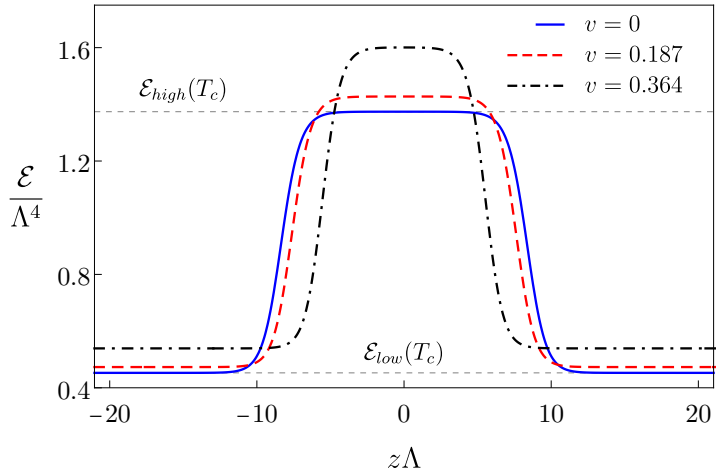

Figure 4.6: Steady-state energy profiles of domains with different velocities. The total energy in the box is the same in all cases. The average energy is $\bar{\mathcal{E}}/\Lambda^4 = 0.817$ and the box has size $L\Lambda = 42.0719$.

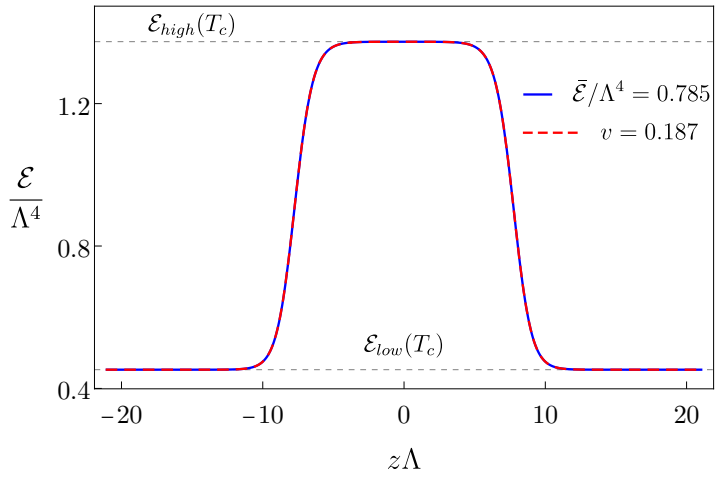

Figure 4.7: Comparison of the energy profile obtained by Lorentz-transforming the curve in Fig. 4.6 (dashed, red curve) with a configuration obtained directly as an inhomogeneous, static configuration with the same average energy (4.6) in a box of size $L' = \gamma L$ (solid, blue curve).

in the next section, it will be crucial to be able to construct the moving domains via the method described around (4.2), because in that case we will need to match two baths with opposite velocities.

4.3 Domain collisions

We now turn to the construction of initial states whose evolution will result in the collision of two domains. We start with a configuration consisting of two static domains separated by some distance from one another, like the one described by the dashed, red curve in Fig. 4.8(left). This can be constructed, for example, by gluing together two individual domains along the low-energy bath. We place the two domains at antipodal points of the z-circle, in which case the

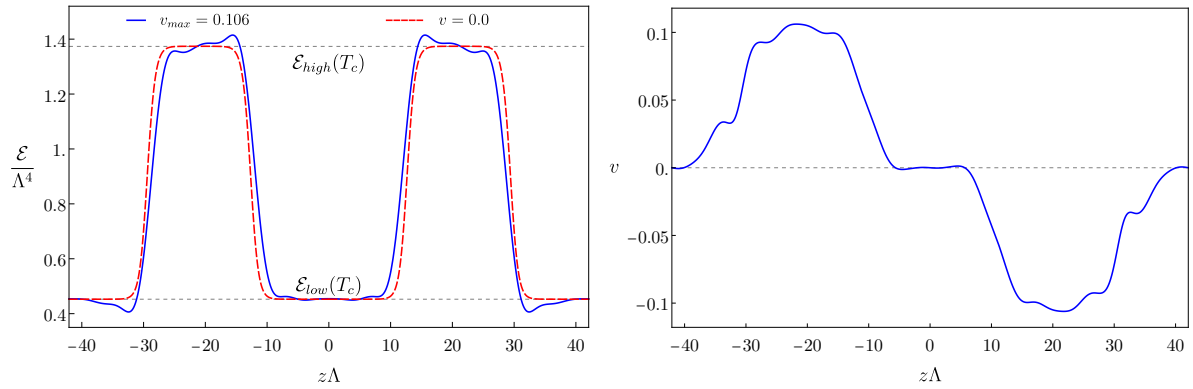

Figure 4.8: (Left) Initial configuration (dashed red) used to generate two domains in motion (solid blue) that will collide with each other. (Right) Fluid velocity for the domains in motion on the left.

resulting configuration is unstable but static [63]. If this configuration is slightly perturbed then, upon time evolution, the domains will approach each other and eventually collide. However, this collision will typically happen at low relative velocity [63]. Therefore, in order to explore the collision physics over a significant range of relative velocities, we will modify the initial configuration following the procedure described around (4.2). The crucial difference is that now we inject momentum densities of equal magnitudes but opposite signs in each domain. As in the case of a single domain, at the end of the iteration procedure some of the momentum is contained in the bath but most of it is in the domains, as illustrated in Fig. 4.8(right). Also, the shape of the domains, described by the solid, blue curve in Fig. 4.8(left), is modified with respect to the static situation. Note that, by symmetry, the fluid velocity must vanish at the two middle points in between the domains, i.e. at $z\Lambda = 0$ and $z\Lambda = L/2$. This is the reason why this initial state cannot be obtained by gluing together two individual steady states of the previous section moving towards each other, since at the middle points the baths would be moving with non-zero, opposite velocities, and hence the velocity field would be discontinuous. One may think that an alternative method would be to use superposition instead of gluing. Specifically, we recall that, in the characteristic formulation that we use on the gravity side (see [38] for details), the data on the initial time slice is free. We can therefore superpose the initial data corresponding to two individual domains moving towards each other. Although this procedure is conceptually sensible, it is technically challenging to find the apparent horizon in the resulting geometry. For this reason we followed the procedure described around (4.2).

We performed a series of identical simulations except for the fact that we varied the maximum velocity of the fluid in the initial state in the range $v_{\rm max} \in (0, 0.73)$. We use this velocity as one possible characterization of the initial state. In all cases we fixed the distance between the mid points of the domains to $d\Lambda \simeq 42$. We found three qualitatively different dynamical regimes. For low values $v_{\rm max} \lesssim v_1 \simeq 0.09$ the domains initially slow down, enter a quasi-static regime, and eventually collide and merge. For intermediate values $v_1 \lesssim v_{\rm max} \lesssim v_2 \simeq 0.2$ the quasi-static phase is absent. For high values $v_{\rm max} \gtrsim v_2$ the domains collide but do not merge. Instead they break apart and merge only in subsequent collisions.

We emphasize that there is no sharp transition between these regimes and hence the differences are qualitative in nature. For the specific simulations with the domains of Fig. 4.8 we found the quoted values $v_1 \simeq 0.09, v_2 \simeq 0.2$. Repeating these simulations for different initial domains we found that the values of v_1, v_2 depend on the choice of initial domains. However, the existence of three qualitatively different regimes persisted, suggesting that it is a robust property of the collision dynamics.

4.3.1 Low velocity

Fig. 4.9 shows the evolution of the energy density and the fluid velocity for a simulation with $v_{max} = 0.08$. We can distinguish several stages of the evolution: the initial slowing down of the domains, the quasi-static regime, the merging into a single domain and the subsequent relaxation to equilibrium.

In the first stage, $t\Lambda \lesssim 100$, the domains slow down as they transfer momentum to the low-energy bath in between them. This results in an increase of the energy density and of the longitudinal pressure at the center, as shown at early times in Fig. 4.10. We use the area density of the apparent horizon on the gravity side as a proxy for the entropy density of the system. As shown in Fig. 4.11, the dissipation in the initial phase causes a considerable increase in the entropy of the system, meaning that it is comparable to the entropy increase in the final merger.

In the period $100 \lesssim t\Lambda \lesssim 500$ the energy density (the pressure) at the centre increases (decreases) slowly. The quasi-static nature of this regime can be clearly seen in the entropy, which displays a plateau that extends up to $t\Lambda \sim 500$. Note that the entropy of the plateau coincides with that of the initial two-domain configuration (dashed, red curve in Fig. 4.8(left)), which is static. Presumably, this agreement is due to the fact that the velocity of the two domains in the quasi-static regime is extremely low, as can be seen in Fig. 4.9(bottom). This is consistent with the fact that the domains move as rigid bodies whose profiles are very well approximated by the equilibrium profile, as shown in Fig. 4.12(left). The right plot in this figure also shows that the dynamics is driven by a small pressure deficit in the region in between the domains.

The fact that the entropy of the system at times $t\Lambda \lesssim 100$ is lower than the entropy of two static domains means that the procedure by which we inject momentum into the system at constant total energy decreases the entropy. This can be easily understood on the gravity side, where this procedure increases the total momentum of the dual black brane while keeping its mass fixed. If one performs a Kaluza-Klain reduction along the z-direction, this corresponds to increasing the electric charge of the resulting, lower-dimensional black brane while keeping its mass fixed. Just in a Reissner-Nordström black hole, this procedure is expected to reduce the entropy.

The collision takes place around $t\Lambda \sim 500$. The two domains merge into a single, out-of-equilibrium, larger domain that will eventually reach equilibrium through damped oscillations. At sufficiently late times we expect to be able to describe the dynamics in terms of an equilibrium profile plus small deviations, $\delta\mathcal{E}/\mathcal{E} \ll 1$, so that we can apply a linear analysis. Following [63], we model the system at late times as two phases of energies $\mathcal{E}_{low}$ and $\mathcal{E}_{high}$ separated by two interfaces or walls that can move as a whole but whose shapes are rigid. Since the system is symmetric under $z \to -z$ we will often focus only on $z > 0$ and speak of "the" wall. We define the positions of the wall as the point at which the energy density is the average between $\mathcal{E}_{high}$ and $\mathcal{E}_{low}$, namely we require that $\mathcal{E}(t, z_{wall}) = (\mathcal{E}_{high} + \mathcal{E}_{low})/2$. The size of the high-energy phase is then $\ell_1 = 2z_{wall}$ and the size of the low-energy phase is $\ell_2 = L - \ell_1$. Rigidity implies that the perturbations of each phase must vanish at the wall, meaning that the only allowed perturbations are odd cosine harmonics of wavelength $\lambda_i = 2\ell_i$. In general there could also be sine harmonic of wavelength $\lambda_i = \ell_i$, but these are excluded in our particular case because of the reflection symmetry. As both subsystems are coupled and the wall is rigid we expect the two phases to oscillate in time as a whole, with identical frequencies. Since translation invariance is broken, all the modes in the Fourier decomposition of $\delta\mathcal{E} = \mathcal{E}(t, z) - \mathcal{E}_{eq}(z)$, with $\mathcal{E}_{eq}(z)$ the equilibrium profile at asymptotic times, will mix with one another. Thus, at late times they should all oscillate with the frequency of the longest-lived mode (as we saw in Fig. 3.25). We verified this for modes up to $n = 14$, i.e. for modes with momentum up to $k = 14 \times 2\pi/L$. Fig. 4.13 illustrates the result for the four lowest modes. This result motivates the following

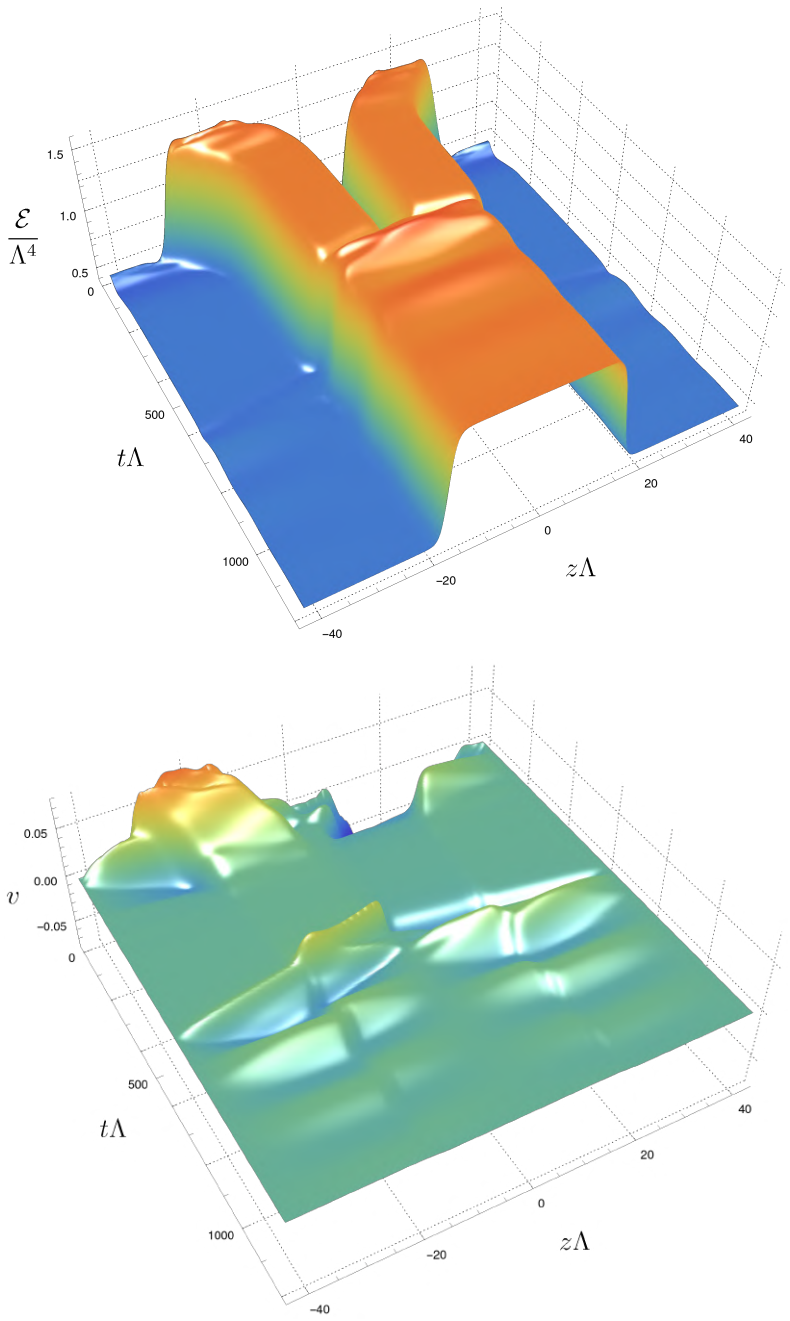

Figure 4.9: Evolution of the energy density (top) and of the fluid velocity (bottom) for a simulation with $v_{\max} = 0.08$.

ansatz for the perturbations of each phase at late times:

$$\delta\mathcal{E}_i(t,z) = \begin{cases} e^{\omega_1(t-t_0)} \sum_{n=0}^{\infty} a_n^i \cos\left[\omega_2(t-t_0) + \gamma_n^i\right] \cos\left[\frac{(2n+1)\pi}{\ell_i}\left(z - z_0^i\right)\right], & |z - z_0^i| \leq \frac{\ell_i}{2} \\ 0, \quad \text{otherwise}, \end{cases} \tag{4.7}$$

where the index i refers to each of the two phases and z_0^i refers to their midpoints. The form of the energy density at late times is then

$$\mathcal{E}(t,z) = \mathcal{E}_{eq}\left(z \mp \frac{\Delta\ell_1(t)}{2}\right) + \delta\mathcal{E}_{high}(t,z) + \delta\mathcal{E}_{low}(t,z), \tag{4.8}$$

where $\mp$ means that we use $-$ $(+)$ if $z > 0$ $(z < 0)$. The second and third terms on the right-

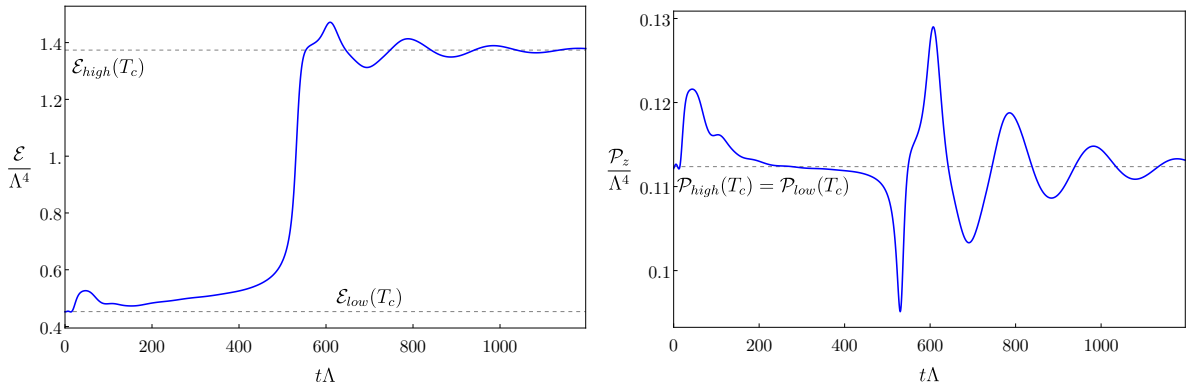

Figure 4.10: Energy density (left) and longitudinal pressure (right) as a function of time at $z\Lambda = 0$ for the collision of Fig. 4.9.

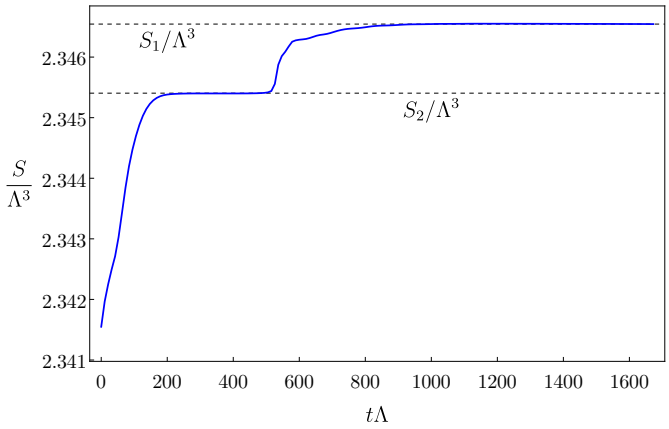

Figure 4.11: Time evolution of the total entropy (per unit transverse area) for the collision of Fig. 4.9. S_2 is the entropy of a static configuration with two domains (the dashed, red curve in Fig. 4.8). S_1 is the entropy of a static configuration with the same total energy but a single domain.

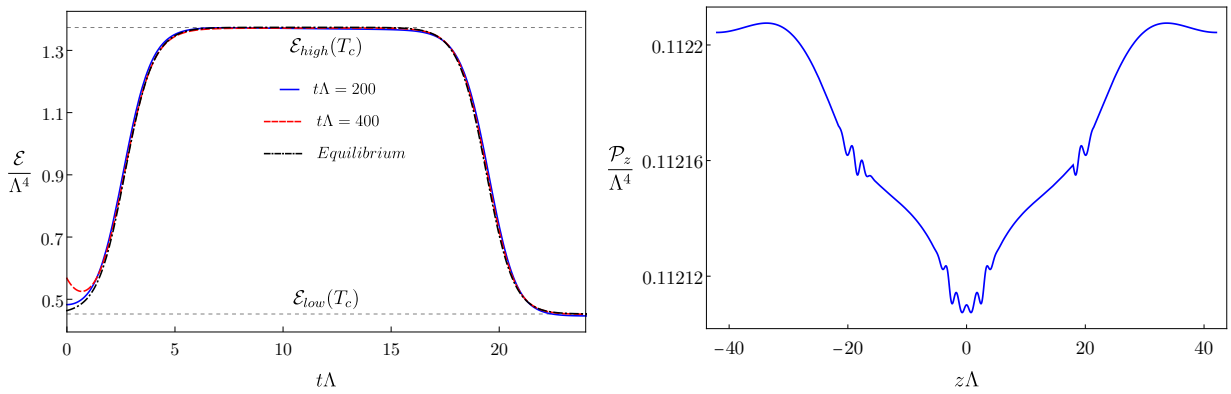

Figure 4.12: (Left) Energy profiles (shifted by an appropriate amount) of the domains during the quasi-static phase for the collision of Fig. 4.9. (Right) Snapshot of the longitudinal pressure distribution at $t\Lambda = 350$.

hand side describe the oscillation in time and space of the two phases. The first term is due to the rigid motion of the walls as the phase domains oscillate. If we call $\Delta\ell_1(t) = -\Delta\ell_2(t)$ the

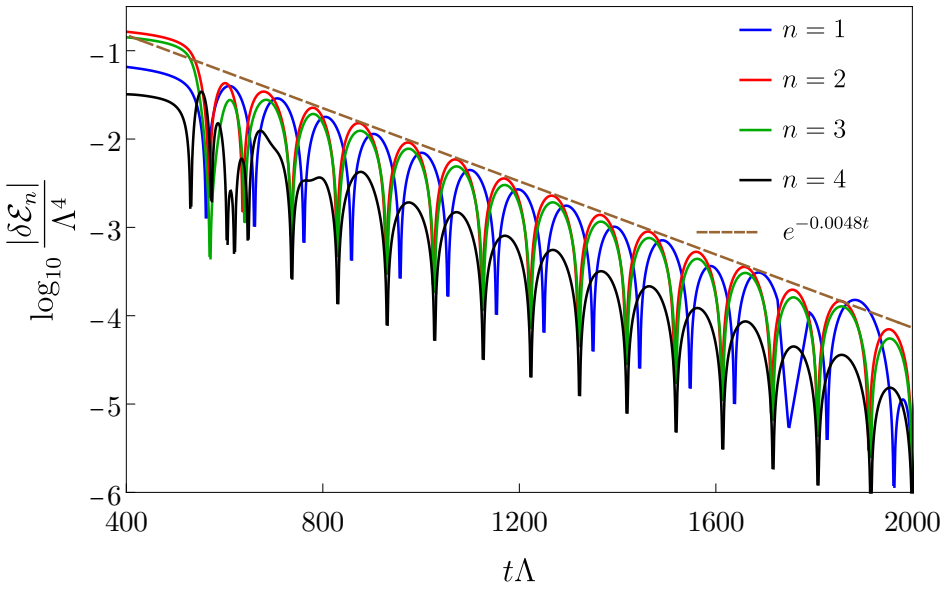

Figure 4.13: Time evolution of the spatial Fourier modes of $\delta\mathcal{E} = \mathcal{E}(t,z) - \mathcal{E}_{eq}(z)$ after the merging. All modes evolve as $\delta\mathcal{E}_n \sim \exp(\omega_1 t)\cos(\omega_2 t)$ with the same $(\omega_1, \omega_2) = (-0.012, 0.063)$.

changes in the sizes of the two phases caused by the motion of the walls, then mathematically this means that the oscillations happen on top of phases with sizes $\ell_i + \Delta\ell_i(t)$, whose energy density can be written approximately as the first term in (4.8). The form of this term is just a simple way of "stretching" (for positive $\Delta\ell_i$) or "compressing" (for negative $\Delta\ell_i$) the domain profile by "gluing in" or "cutting out" a small piece at the centre of each phase, taking advantage of the fact that the energy density is almost exactly constant there. In order to determine $\Delta\ell_1$ as a function of time, we simply impose conservation of energy, namely that the energy change associated to the rigid shift of the walls is exactly compensated by the energy change associated to the oscillations of the phases:

$$2\left(\mathcal{E}_{high} - \mathcal{E}_{low}\right)\Delta\ell_1(t) + \int_{-L/2}^{L/2} dz\Big[\delta\mathcal{E}_{high}(t,z) + \delta\mathcal{E}_{low}(t,z)\Big] = 0\,. \tag{4.9}$$

The approximation (4.8) becomes applicable soon after the merger, as illustrated by Fig. 4.14. To describe correctly the perturbations of the high-energy phase it is enough to truncate the series (4.7) at $n = 1$, whereas in order to obtain a good result for the low-energy phase we included the second mode, $n = 2$. The values that we found for the fit parameters in (4.7) are

$$\begin{array}{lll} \omega_1/\Lambda = -0.0048, & \omega_2/\Lambda = 0.032, & t_0\Lambda = 800, \\ L_{high}\Lambda = 33.33, & L_{low}\Lambda = 50.82, & L\Lambda = 84.14, \\ z_0^{high} = 0, & z_0^{low} = \pm L/2, & a_1^{high}/\Lambda^4 = 0.0375, \\ \gamma_1^{high} = 0.227, & a_1^{low}/\Lambda^4 = 0.0142, & \gamma_1^{low} = 2.346, \\ a_2^{low}/\Lambda^4 = -0.0022, & \gamma_2^{low} = -0.244. & \end{array} \tag{4.10}$$

4.3.2 Intermediate velocity

A simulation in this regime with $v_{max} = 0.11$ is shown in Fig. 4.15. In this case there is no quasi-static regime, as seen by the absence of an intermediate plateau in the entropy density in Fig. 4.16. The overall increase in the entropy is greater than in the low-velocity case, confirming

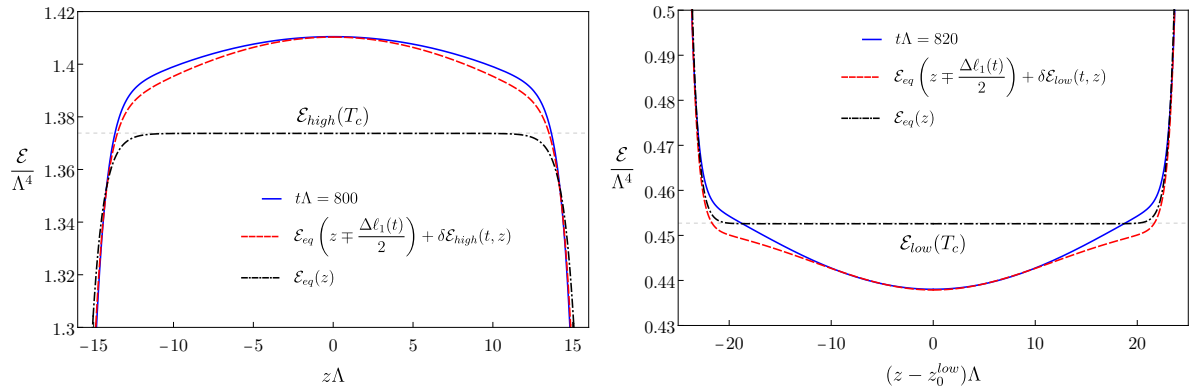

Figure 4.14: Oscillations of the high- and low-energy phases during the relaxation period after the merger.

the intuition that this is a more violent collision. The rest of the evolution is qualitatively similar to the low-velocity case: there is an initial excess of pressure between the domains that slows them down and they merge to form a domain that relaxes to equilibrium through the same kind of oscillations, see Fig. 4.17. Applying (4.8) leads to a good description of the oscillations at times soon after the collision, see Fig. 4.18. The parameters in this case are

$$\begin{array}{lll} \omega_1/\Lambda = -0.0047, & \omega_2/\Lambda = 0.032, & t_0\Lambda = 200, \\ L_{high}\Lambda = 33.33, & L_{low}\Lambda = 50.82, & L\Lambda = 84.14, \\ z_0^{high} = 0, & z_0^{low} = \pm L/2, & a_1^{high}/\Lambda^4 = 0.1065, \\ \gamma_1^{high} = 2.09, & a_1^{low}/\Lambda^4 = -0.0397, & \gamma_1^{low} = 1.306, \\ a_2^{low}/\Lambda^4 = -0.0082, & \gamma_2^{low} = 1.26\,. & \end{array} \tag{4.11}$$

Note that, up to fitting errors, the frequencies in this case and in the low-velocity case are the same. The reason is that the final equilibrium state is the same in both cases, and therefore the frequencies of the linear perturbations around it are identical. The only difference between the simulations is therefore in the amplitudes of the oscillations. The following table collects the ratios of the coefficients for the $n = 1, 2$ modes, a_2^i/a_1^i, for both phases for various simulations:

v_{max}	low	intermediate
low − energy phase	−0.158	0.2058
high − energy phase	−0.043	−0.044

(4.12)

We see that they are of the same order for different simulations, and that the ratio is smaller in the high-energy phase, consistently with our neglect of the $n = 2$ (and higher) modes in this phase.

4.3.3 High velocity

For velocities $v_{max} \geq v_2 = 0.2$ the domains collide but do not merge in the first collision. Instead, the excited state that results from the collision breaks apart into pieces that will subsequently collide again until they finally merge. Fig. 4.19 shows two illustrative cases. As shown by Fig. 4.20, the peak energy density right after the first collision increases significantly with v_{max}, meaning that the resulting configuration is a large deviation from an equilibrium domain. The maximum relative deformations are $\mathcal{E}_{peak}/\mathcal{E}_{high} \simeq 1.071, 1.096, 1.762, 3.966$, respectively, for the increasing velocities shown in Fig. 4.20. As a consequence, non-linear dynamics becomes

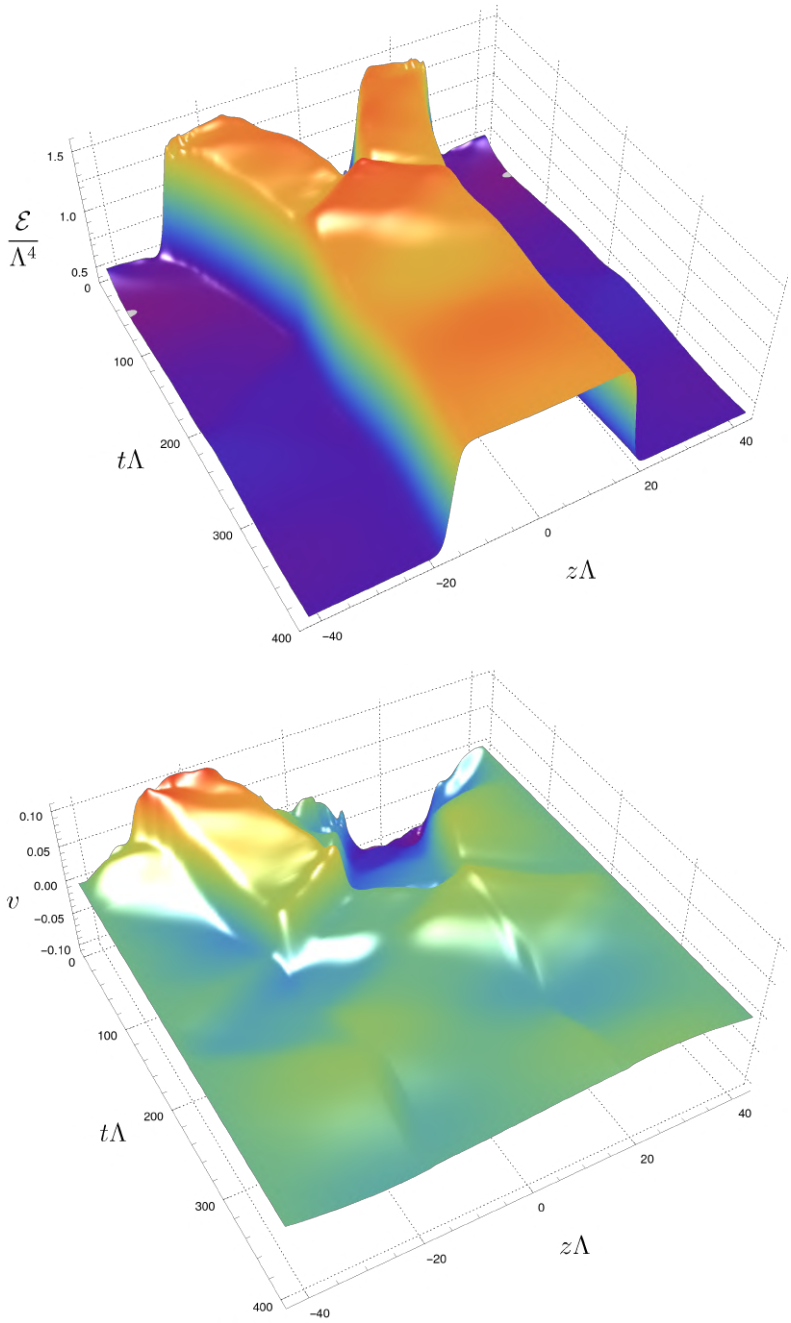

Figure 4.15: Evolution of the energy density (top) and of the fluid velocity (bottom) for a simulation with $v_{\max} = 0.11$.

important and the excited state breaks apart into smaller components rather than relaxing to a single equilibrium domain as in previous sections.

In both cases shown in Fig. 4.19, the initial excited state first "emits" perturbations that travel away from the central blob, and subsequently it splits into two fragments. The perturbations travel away from the central blob, colliding with each other on the other side of the box, at $z\Lambda \simeq 42$. We will refer to this as the second collision. This collision creates an excitation that quickly becomes a new domain smaller than the central fragments, as illustrated in Fig. 4.21. Note from the horizontal axis in this figure that the new domain is shown in the center of the figure and the central fragments on the sides of it. At later times the two central fragments reach the location of the new domain and a third collision, this time a three-body one, takes place. In cases with $v_{max} \gtrsim v_2$, such as the one in Fig. 4.19(top), this third collision results

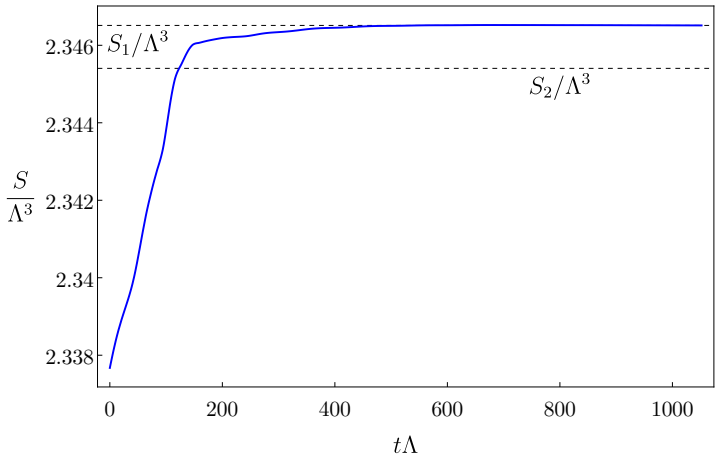

Figure 4.16: Time evolution of the total entropy (per unit transverse area) for the evolution in Fig. 4.15. S_2 is the entropy of a static configuration with two domains (the dashed, red curve in Fig. 4.8). S_1 is the entropy of a static configuration with the same total energy but a single domain.

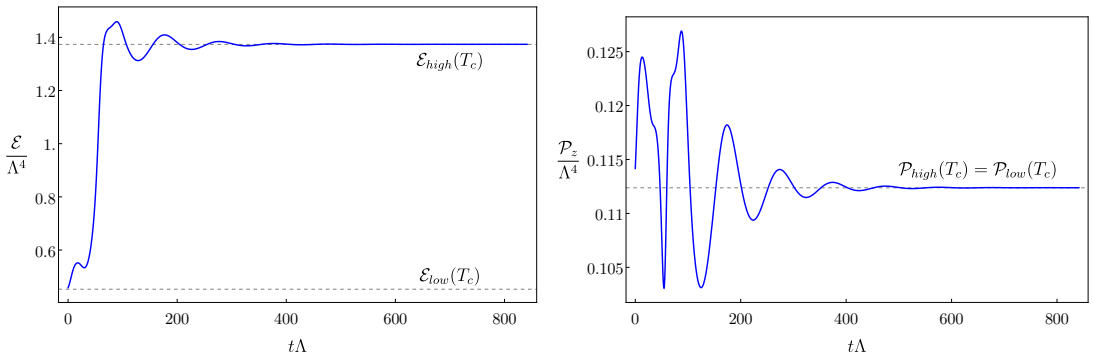

Figure 4.17: (Left) Energy density $\mathcal{E}/\Lambda^4$ and (Right) longitudinal pressure P_l/Λ^4 as a function of time for constant coordinate $z\Lambda = 0$ for the evolution in Fig. 4.15.

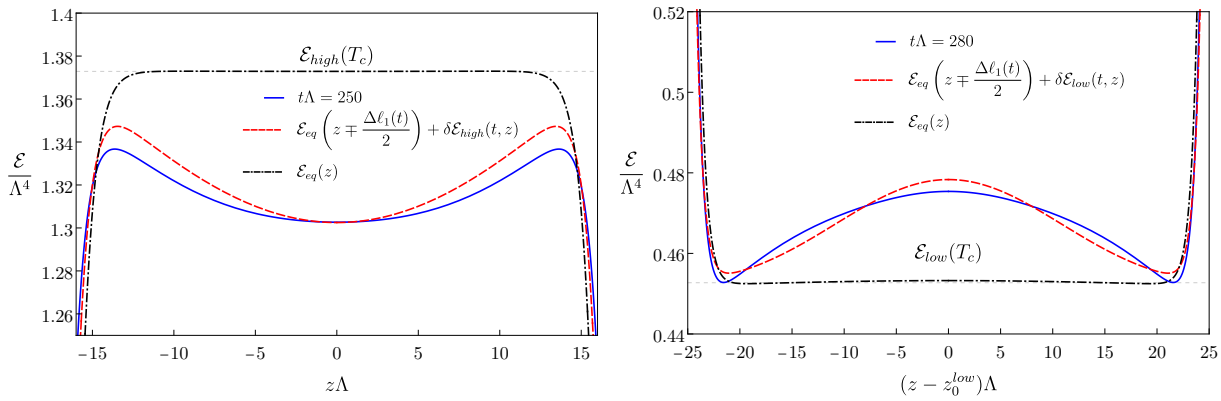

Figure 4.18: Oscillations of the high- and low-energy phases during the relaxation period after the merger for the evolution in Fig. 4.15.

in the formation of a single domain that then relaxes to equilibrium as described in previous sections.

In contrast, in cases with large enough v_{max}, such as the one of Fig. 4.19(bottom), the

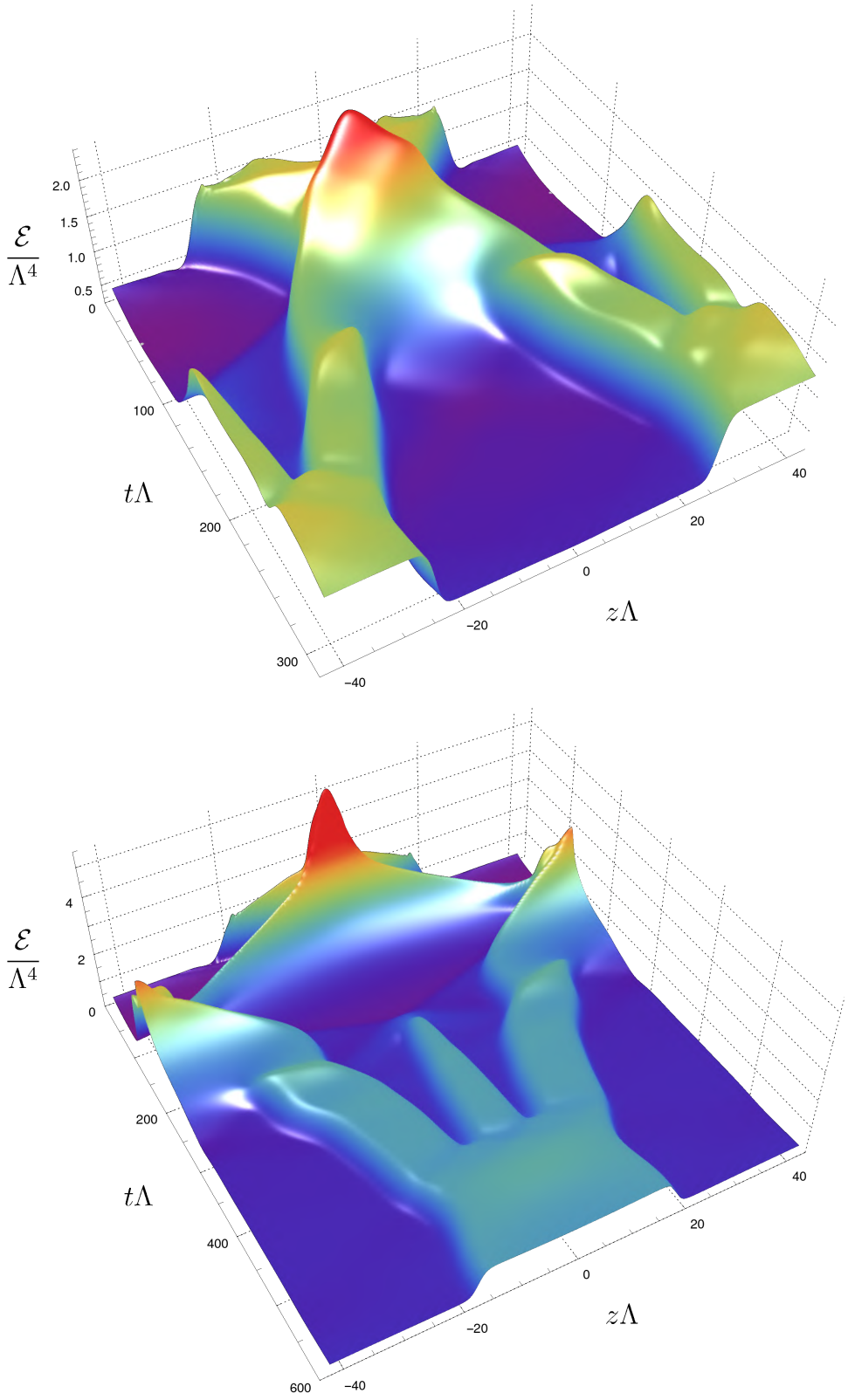

Figure 4.19: Evolution of the energy density for simulations with $v_{\max} = 0.25$ (top) and $v_{\max} = 0.73$ (bottom).

excitations emitted by the initial excited state, as well as the fragments to which it decays, travel faster to the opposite side of the box and do not have time to relax to domains, as shown

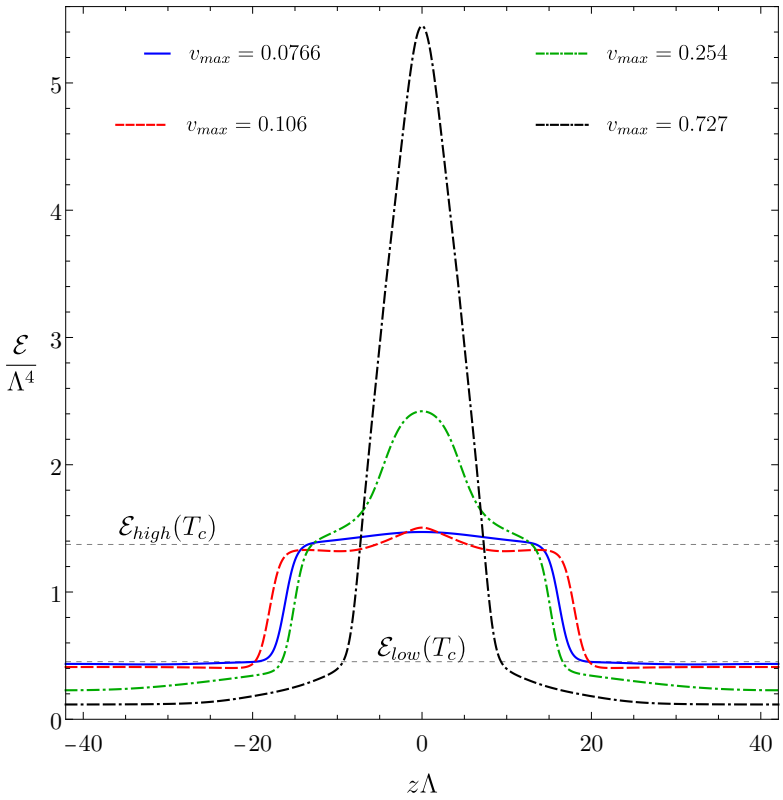

Figure 4.20: Snapshots of the energy density at the times at which the maximum energy is reached for collisions with different v_{max}.

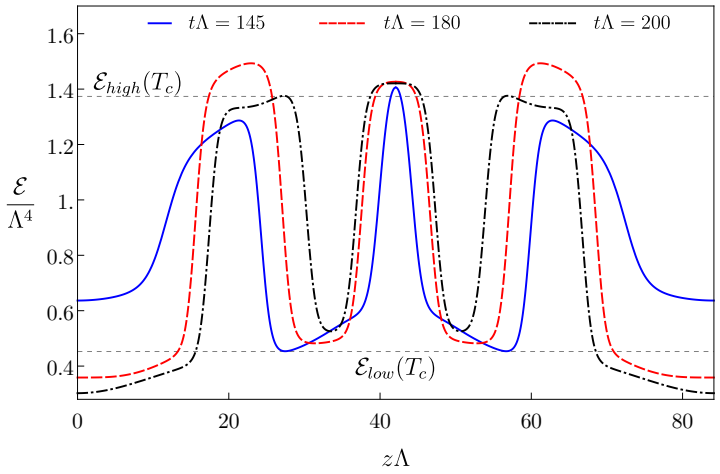

Figure 4.21: Snapshots of the energy density for the collision of Fig. 4.19(top) with $v_{max} = 0.25$. The blue curve corresponds to a time soon after the fragmentation of the excited state. Note that the horizontal axis in this figure has been shifted to show the new domain at the center of the figure and the central fragments on the sides of it.

in Fig. 4.22(top). As above, the perturbations collide in what we call the second collision. However, in this case the third collision, i.e. the collision between the resulting new structure and the fragments from the first excited state, is again a high-velocity collision. As a consequence, it results in the emission of new perturbations plus fragments that in this case travel from $z\Lambda \simeq 42$

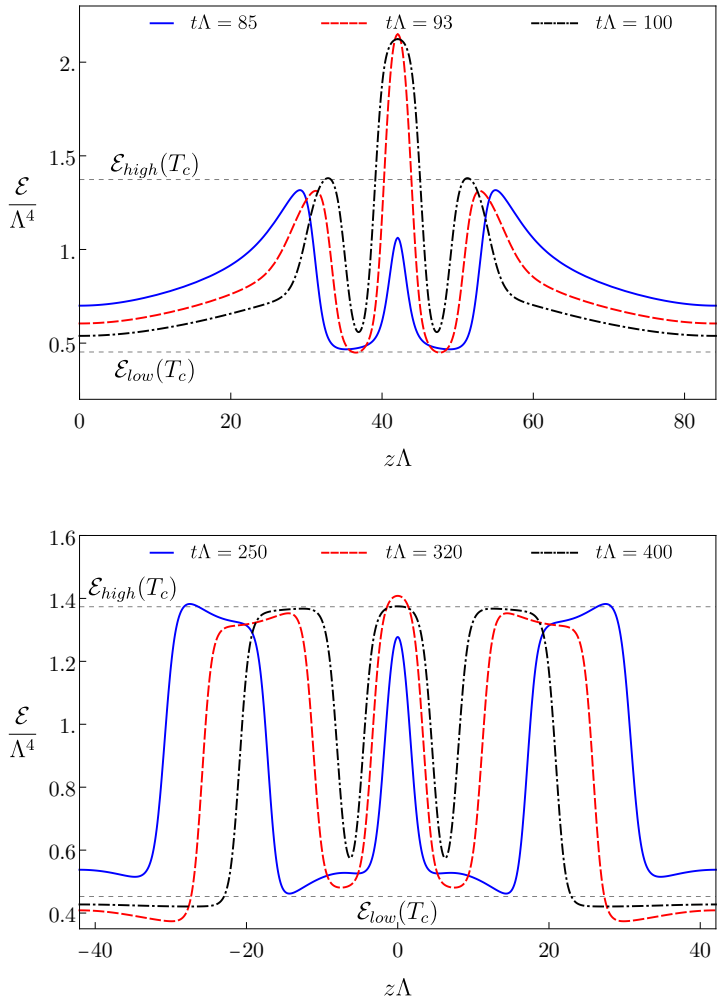

Figure 4.22: Snapshots of the energy density for the evolution in Fig. 4.19(bottom) with $v_{max} = 0.73$. The top (bottom) plot corresponds to a time shortly after the second (fourth) collision. The blue curve corresponds to a time soon after the fragmentation of the excited state.

towards $z\Lambda = 0$. These products now have time to relax to approximate domains, as illustrated in Fig. 4.22(bottom). The perturbations merge in a fourth collision at $z\Lambda = 0$, and finally a fifth collision occurs, again a three-body collision, which results in the formation of a single domain that relaxes to equilibrium as in previous sections.

The entropy production in Fig. 4.23 reflects the qualitative differences described above between the two evolutions of Fig. 4.19. On the left plot we can identify three different regimes corresponding to the three different collisions. In contrast, no such clear distinction is apparent on the right plot. In both cases, however, the relative amount of entropy increase is much larger than in the low- and intermediate-velocity collisions. For comparison, the relative entropy production in the evolutions with $v_{max} = 0.11$, $v_{max} = 0.25$ and $v_{max} = 0.73$ are 2, 9 and 45 times larger than in the $v_{max} = 0.08$ case, respectively.

4.4 Discussion

The time evolution of the spinodal instability in a theory with a first-order phase transition typically results in the creation of phase domains that subsequently collide with one another [63]. The velocities of the different domains are a complicated function of the perturbation of

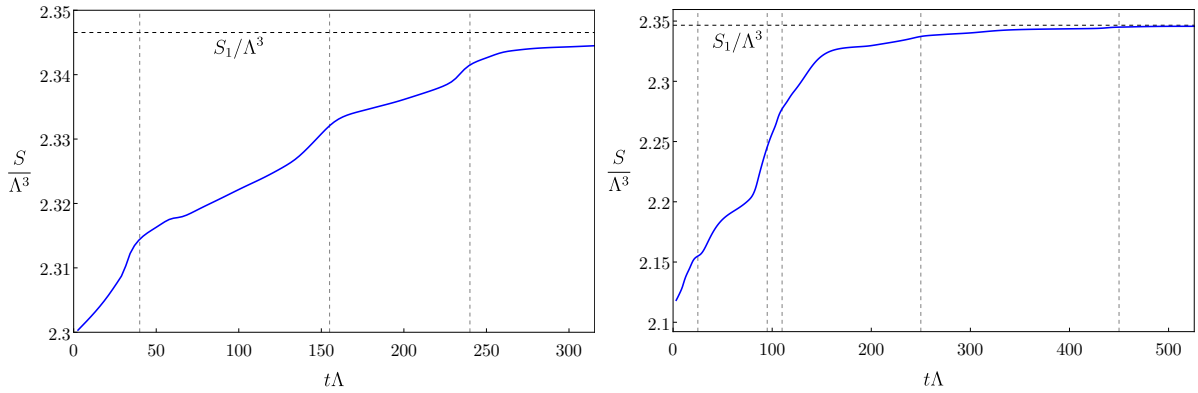

Figure 4.23: Time evolution of the total entropy (per unit transverse area) for the evolutions of Fig. 4.19 with $v_{max} = 0.25$ (left) and $v_{max} = 0.73$ (right). S_1 is the entropy of a static configuration with the same total energy but a single domain. The vertical dashed lines represent the approximate time of each collision.

the initial, homogeneous, unstable state. This makes it difficult to perform a systematic study of the physics of the collision as a function of the domain velocities. In this chapter we have overcome this difficulty by directly preparing initial states consisting of domains moving towards each other at velocities $0 \leq v_{max} \leq 0.73$, where v_{max} is the maximum fluid velocity in the initial state. Going to higher velocities becomes challenging due to numerical issues. Nevertheless, the above range sufficed to uncover three qualitatively different dynamical regimes.

For low velocities the domains initially slow down, enter a period of quasi-static evolution, and finally collide and merge into a single domain that then relaxes to equilibrium through damped oscillations. The quasi-static period is clearly visible as a plateau in the entropy of the system, which we computed from the area of the dual horizon on the gravity side. For intermediate velocities the evolution is qualitatively identical except for the fact that no quasi-static period is present. For high velocities the domains can collide several times before they eventually merge into a final, single domain that then relaxes to equilibrium. Our investigations suggest that, while the precise values of the velocities that distinguish these three regimes depend on the size of the domains in question, the existence of these regimes is a robust property of the collision dynamics.

Chapter 5

Bubbles: Expanding, Collapsing and Critical

Once studied the properties and formation dynamics of inhomogeneous solutions we will turn now to a very important aspect of first order phase transitions: bubble dynamics. As it was explained in Chapter 1, bubble nucleation, expansion and collision play a crucial role in the dynamical realization of a first order phase transition. Moreover, it is a source of stochastic emission of Gravitational Waves whose potential discovery requires and accurate understanding of bubble properties.

Although we will start studying the dynamics of planar bubbles, dynamics in 1+1 dimensions, where we will see that the stationary expansion state only depends on the nucleation temperature and we will observe a very interesting relation for the wall velocity. We will then use `Jecco` for the first time in this thesis, which extends the dynamics to one additional dimension. Thus, the effective dynamics will be 2+1 dimensional in the gauge theory and 3+1 dimensional on the gravity side. This will allow us to study cylindrical bubbles, which intuitively we can think of as circular bubbles in 2+1 dimensions in a theory with one extra spectator direction.

The extension from planar to circular bubbles brings about two new physical aspects. The first one is that the surface tension now plays a role. In particular, we will be able to identify a critical bubble in which the inward-pointing force due to the surface tension exactly balances the outward-pointing force coming from the pressure difference between the inside and the outside of the bubble. The second one is that the asymptotic, self-similar profile of an expanding bubble possesses a richer structure than in the planar case.

We will also compare the holographic result with the hydrodynamic approximation in both planar and cylindrical bubbles. As expected, we will find that hydrodynamics provides a good approximation everywhere except at the bubble wall.

5.1 Model and thermodynamics

For the first time in this work we will choose to work with a different choice of paramenters, namely $\lambda_4 = -0.346021$ while keeping $\lambda_6 = 0.1$ in (2.3). The reason behind the change to smaller values of λ_4 is that it corresponds to a model of greater pressure jump across the phase transition, leading to a sizeable bubble wall velocity as we will see in Sec. 5.4.2.

The thermodynamics of the gauge theory can be extracted from the homogeneous black brane solutions on the gravity side (see e.g. [114]). Figure 5.1 shows the result for the energy density as a function of temperature, where we see the usual multivaluedness associated to a first-order phase transition. At high and low temperatures there is only one phase available to the system. Each of these phases is represented by a solid, blue curve. At the critical

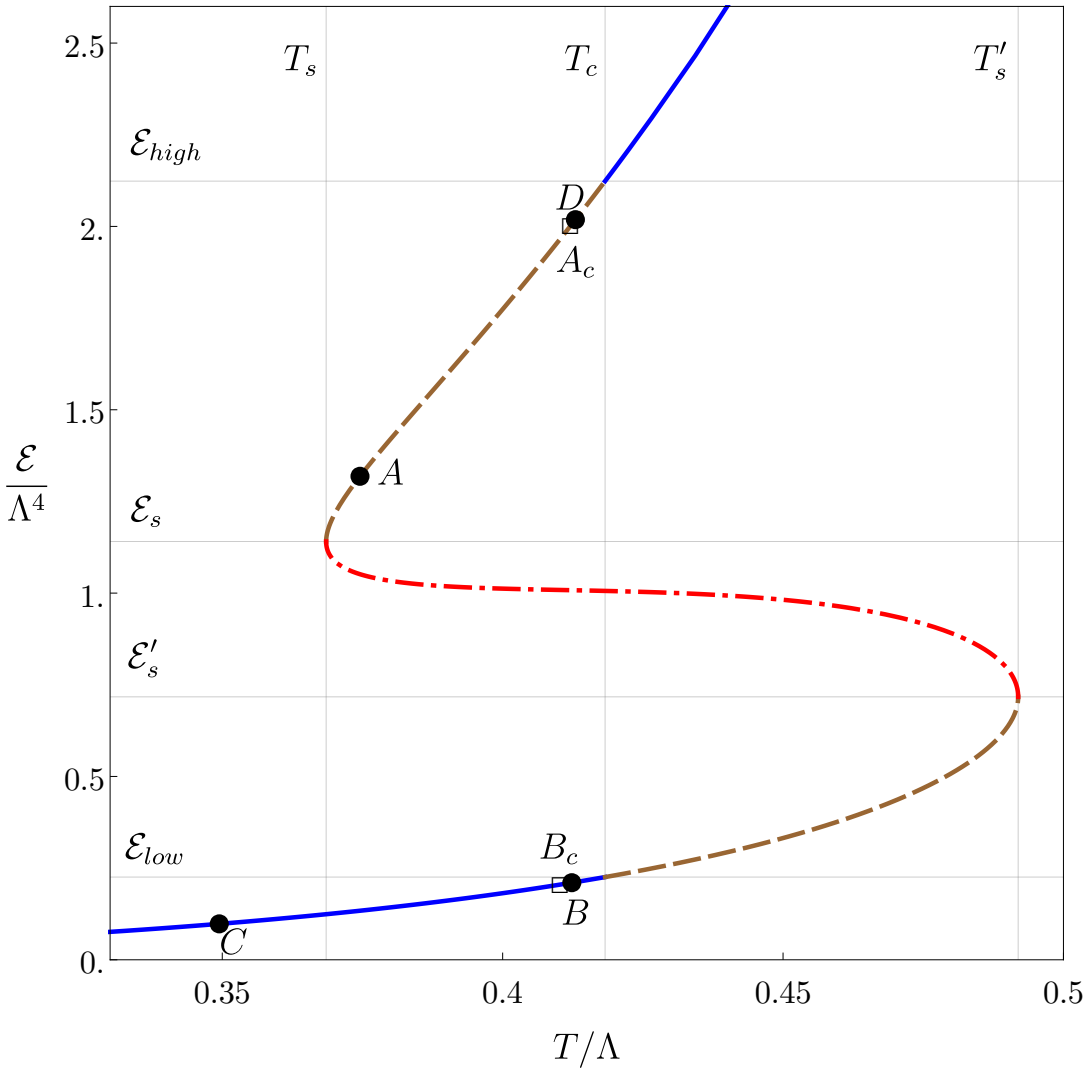

Figure 5.1: Energy density as a function of temperature for the gauge theory dual to the holographic model (2.1-2.3) with $\lambda_4 = -0.346021$ and $\lambda_6 = 0.1$. The squares B_c and A_c correspond, respectively, to the states inside and outside of the closest-to-critical bubble studied in Sec. 5.3. The dots B and C correspond to the initial states inside and outside the expanding bubble studied in Sec. 5.4.2, respectively. At late times, the state B inside the bubble evolves into C, and a heated region is created in front of the bubble that can be characterized in terms of the point D in the phase diagram.

temperature

$$T_c = 0.418\Lambda$$

the state that minimizes the free energy moves from one branch to the other. The first-order nature of the transition is encoded in the non-zero latent heat, namely in the discontinuous jump in the energy density given by

$$\mathcal{E}_{\text{latent}} = \mathcal{E}_{\text{high}} - \mathcal{E}_{\text{low}}\,, \qquad \mathcal{E}_{\text{low}} = 0.225\Lambda^4\,, \qquad \mathcal{E}_{\text{high}} = 2.123\Lambda^4\,. \tag{5.1}$$

Note that the phase transition is a transition between two deconfined, plasma phases, since both phases have energy densities of order N^2 and they are both represented by a black brane geometry with a horizon on the gravity side.

In a region

$$T_s = 0.3879\Lambda < T < T_s' = 0.4057\Lambda \tag{5.2}$$

around the critical temperature there are three different states available to the system for a given temperature. The thermodynamically preferred one is the state that minimizes the free energy, namely a state on one of the blue curves. The states on the dashed, brown curves are not globally preferred but they are locally thermodynamically stable, i.e. they are metastable. This follows from the fact that specific heat

$$c_v \equiv \frac{d\mathcal{E}}{dT} \tag{5.3}$$

is positive on this branches. At the temperatures T_s and T_s' the metastable curves meet the dotted-dashed, red curve, known as the "spinodal branch". States on this branch are locally unstable since their specific heat is negative and have energies comprised between

$$\mathcal{E}_s' = 0.717\Lambda^4\,, \qquad \mathcal{E}_s = 1.141\Lambda^4\,. \tag{5.4}$$

Note that the characteristic scale for all the quantities above is set by the microscopic scale in the gauge theory, Λ, given holographically by $\Lambda = \phi_0$ in terms of the leading term in the near-boundary fall-off of the scalar field in (2.13).

5.2 Initial data

As any other thermal system with a first order phase transition, the gauge theory can be overcooled past the critical temperature T_c. The homogeneous, overcooled state, represented by a point on the upper, brown branch in Fig. 5.1, is stable against small fluctuations, including thermal ones, but not against sufficiently large fluctuations. A particular class of large fluctuations are bubbles, namely inhomogeneous configurations in which the energy density of a certain region of space within the overcooled homogeneous phase is reduced. For sufficiently large bubbles, the energy density in the centre of this region lies in the stable branch of the phase diagram, represented by the lower, blue curve in Fig. 5.1, and the bubble smoothly interpolates between the stable and the metastable phases.

In a homogeneous and isotropic thermal system it is expected that the nucleated bubbles are spherical. However, given our symmetry restrictions we will study (almost) cylindrical bubbles. When we get to the planar bubble simulations the initial data is built in the analogous way, but all configurations we play with are inhomogeneous along only one of the gauge directions.

Our first task is to construct initial data corresponding to a bubble. By definition, this is a configuration consisting of a circular region filled with the stable phase (the inside of the bubble) connected to an asymptotic region filled with the metastable phase (the outside of the bubble) through an appropriate interface. The stable and metastable phases correspond to the points labeled B and A in Fig. 5.1, respectively, and both have $T < T_c$. As we will now explain,

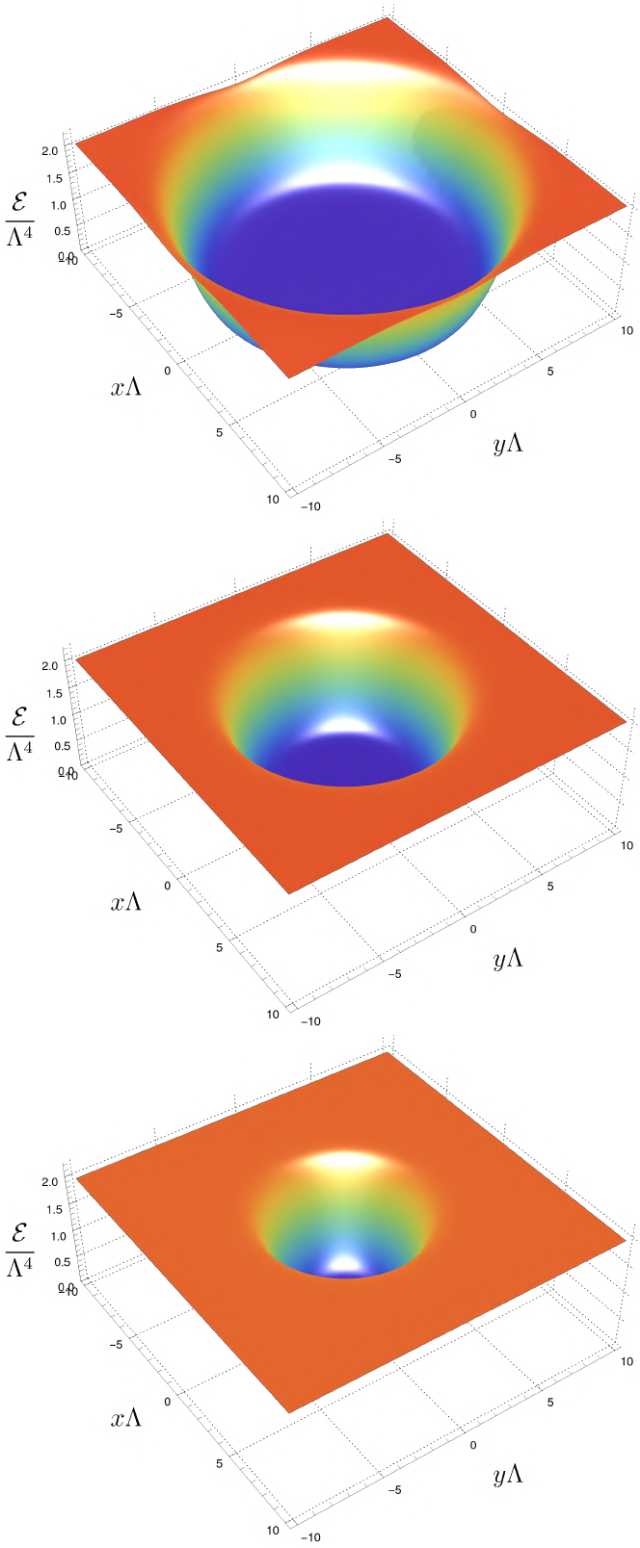

Figure 5.2: Phase-separated configurations in a box of size $L_x\Lambda = L_y\Lambda = 20$ with average energy densities $\bar{\mathcal{E}}/\Lambda^4 = 1.0$ (top), $\bar{\mathcal{E}}/\Lambda^4 = 1.6$ (middle) and $\bar{\mathcal{E}}/\Lambda^4 = 1.8$ (bottom).

our strategy to construct these bubbles will be to start with a phase-separated state, which has $T = T_c$, and to rescale it appropriately.

Phase-separated states are configurations in which the two homogeneous phases with energy densities $\mathcal{E}_{\rm high}$ and $\mathcal{E}_{\rm low}$ coexist in equilibrium at $T = T_c$. This is possible because at this temperature the free energy densities, and hence the pressures, are equal in the two phases. Three examples of such configurations in a box of constant size are shown in Fig. 5.2. The difference between the three cases is the relative fraction of the total volume occupied by each phase. For a box of fixed size, changing this relative fraction is equivalent to changing the average energy density in the box, $\bar{\mathcal{E}}$. The larger the average energy density, the larger the size of the high-energy region, and vice-versa. We will use this fact to our advantage when we search for the critical bubble below.

Strictly speaking, phase-separated states only exist in infinite volume, since only in that case the two coexisting phases become arbitrarily close to being homogeneous sufficiently far away from the interface. The middle and bottom panels of Fig. 5.2 correspond to states that are fairly close to this limit, but deviations can still be seen with the naked eye. For example, the energy density in the region outside the bubbles is slightly below $2\Lambda^4$, whereas the energy density in the high-energy phase at $T = T_c$ has $\mathcal{E}_{\rm high}$ above $2\Lambda^4$, as given in (6.4). The state in Fig. 5.2(top) is even more affected by finite box-size effects because the size of the low-energy region is comparable to the size of the box. In any case, these deviations this will have no implications for our purposes, since we are not interested in phase-separated states per se but only in using them to construct initial data for bubble configurations.

The value of $\bar{\mathcal{E}}$ in a box of fixed size is conserved upon time evolution. Therefore, phase-separated states with an average energy density in the region $\mathcal{E}_s' \leq \bar{\mathcal{E}} \leq \mathcal{E}_s$ can be generated by starting with a homogeneous state in the spinodal region of Fig. 5.1, perturbing it slightly, and letting evolve until it settles down to a phase-separated configuration, find examples in [63] and chapter 6. To initialize the code we specify some ϕ_2 that is not too far away from the value of the thermal state and generate a simple bulk profile for the scalar, $\phi(t = 0, u)$, given by the truncated series in (2.13h) to third order. This is not the geometry associated to the black brane of such energy density, but it would relax fast to the true static solution. The value for a_4 is obtained by using the energy expression in (2.18). On top of it we add a sinusoidal perturbation, so the final a_4 reads

$$a_4(t=0,x,y) = \bar{a}_4 \left[1 + \delta a_4 \left(\cos\left(\frac{2\pi}{L_x}(x - x_{\rm mid})\right) + \cos\left(\frac{2\pi}{L_y}(y - y_{\rm mid})\right)\right)\right], \tag{5.5}$$

where $\bar{a}_4$ is the value we obtained above, L_x and L_y are the lengths of the box, $x_{\rm mid}$ and $y_{\rm mid}$ correspond to the central point and δa_4 represents the amplitude of the perturbation, equal for both x- and y-directions. The fastest way to arrive at a phase-separated configuration is to assign the largest possible value to δa_4 compatible with keeping the apparent horizon within our grid. We have found that $\delta a_4 \sim 10^{-3}$ is a convenient choice. The state in Fig. 5.2(top) was generated following this method with $\phi_2 = 0.3\Lambda^3$. After a time $t\Lambda = 300$ the system has settled down to the configuration shown in the figure.

Phase-separated configurations with average energy densities in the regions

$$\mathcal{E}_s \leq \bar{\mathcal{E}} < \mathcal{E}_{\rm high} \qquad \text{and} \qquad \mathcal{E}_{\rm low} < \bar{\mathcal{E}} \leq \mathcal{E}_s' \tag{5.6}$$

also exist, but they cannot be found directly via time evolution of an initial state in the spinodal region. Instead, to obtain them we follow what we did in chapter 3. We take initial data corresponding to a phase-separated state with $\bar{\mathcal{E}}$ in the spinodal region, and we modify it by increasing or decreasing the value of $\bar{a}_4$ so that the new $\bar{\mathcal{E}}$ takes the desired value. We then let the system evolve. In a time around $t = 100/\Lambda$ the system relaxes to a new inhomogeneous, static configuration. The phase-separated configurations in the middle and bottom panels of Fig. 5.2 have $\mathcal{E}_s \leq \bar{\mathcal{E}} \leq \mathcal{E}_{\rm high}$ and were obtained with this procedure.

The phase-separated states interpolate between the energy densities $\mathcal{E}_{\rm low}$ and $\mathcal{E}_{\rm high}$. To construct initial data for bubble configurations that interpolate between two energy densities $\mathcal{E}_B$ and $\mathcal{E}_A$ we proceed as follows. Let $f_{\rm PS}$ be any of the functions specifying the initial data of a phase-separated state. This could be one of the metric components in the bulk or the scalar field, in which case $f_{\rm PS} = f_{\rm PS}(u,x,y)$, or one of the boundary functions such as a_4, in which case $f_{\rm PS} = f_{\rm PS}(x,y)$. We assume that the centre of the region with energy density $\mathcal{E}_{\rm low}$ is at $x = y = 0$, and that the point at the edge of the box $x = y = L/2$ lies in the region energy density $\mathcal{E}_{\rm high}$. Let f_A and f_B be the corresponding functions for the states A and B. Since these states are homogeneous, f_A and f_B depend on u for a bulk function and are just constants for a boundary function. We then define the corresponding initial data for a bubble through the rescaling

$$f_{\rm bubble}(u,x,y) = f_B(u) + \Big(f_A(u) - f_B(u)\Big)\left[\frac{f_{\rm PS}(u,x,y) - f_{\rm PS}(u,0,0)}{f_{\rm PS}(u,L/2,L/2) - f_{\rm PS}(u,0,0)}\right] . \tag{5.7}$$

If f is a boundary function then there the dependence on u is absent. At any fixed value of u, the term in square brackets interpolates smoothly between 0 at the centre of the low-energy region and 1 at the edge of the box. As a consequence, $f_{\rm bubble}(u,x,y)$ interpolates smoothly between f_B and f_A, as desired. A state generated with this procedure is shown in Fig. 5.3. If the subsequent time evolution leads to an expansion of the bubble, it is convenient to further enlarge the size of the box before starting the evolution, in order to prevent the bubble from reaching the boundary of the box before it has reached an asymptotic state. This can be done simply by "adding" more metastable bath outside the initial box.

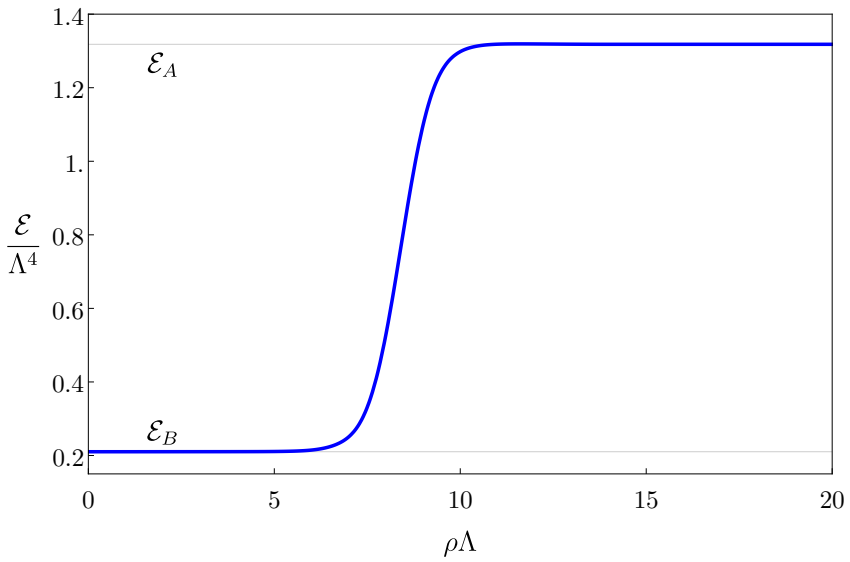

Figure 5.3: Initial energy density profile of a bubble.

Variations of an initial bubble state can be obtained in a simple way. For example, we can choose different states B for a fixed A. We could also multiply the bulk metric functions B_1 and B_2 in (2.8) by some factor, thus changing the pressure distribution (the anisotropy) along the wall but not the energy profile. We could further consider initial bubbles that are not perfectly cylindrically symmetric by starting with an initial phase-separated state whose low-energy region is comparable to the size of the box, as in Fig. 5.2(top).

5.3 Critical bubbles

It was argued in chapter 1 that the on-shell action of critical bubbles is directly connected to the nucleation probability and therefore to the avergae number density of bubbles during the dynamical realization of the phase transition in the early universe. Its importance is clear. In this section we will attempt to study such bubbles for one nucleation temperature.

Consider a circular bubble of radius ρ such that the states inside and outside the bubble correspond to the points marked as B_c and A_c in Fig. 5.1, respectively. The pressure difference between these states generates an outward-pointing force on the bubble wall. In turn, the surface tension of the bubble wall results in an inward-pointing force on the wall. A critical bubble is one for which these two forces exactly balance each other. Since these bubbles are static, they correspond to equilibrium states. As a consequence, the temperature must be constant across the entire system and, in particular, it must be equal to T_{A_c}. It follows that the state B_c is determined by A_c. If the radius of the bubble is large compared to the width of the interface between A_c and B_c, then the radius of the critical bubble takes the form

$$\rho_c = \frac{\gamma}{P_{B_c} - P_{A_c}} \,. \tag{5.8}$$

This follows from approximating the interface by a zero-width surface with free energy density γ, assigning a well defined pressure P_{B_c}, and hence a free energy density $-P_{B_c}$, to the interior of the bubble, and requiring that the critical bubble locally extremizes the free energy. The fact that this extremum is a maximum means that the critical bubble is in unstable equilibrium. This expression for the critical radius is only valid for large critical bubbles, which are realized when T_{A_c} is close to the phase transition temperature T_c, namely for $T_{A_c} \lesssim T_c$. This is the reason for our choice of the point A_c in Fig. 5.1. If the bubble is not large enough then the phase inside the bubble is not approximately homogeneous and it cannot be clearly separated from the interface. In this case one cannot assign a meaningful surface tension to the interface or a well defined pressure to the interior of the bubble. This situation is realized when T_{A_c} is sufficiently close to the turning point at $T = T_s$, namely when $T_s \lesssim T_{A_c}$. In this paper we will only discuss large critical bubbles; small bubbles will be analysed elsewhere.

The fact that critical bubbles are unstable means that supercritical bubbles expand, whereas undercritical bubbles collapse. Critical bubbles are therefore the static configurations that separate these two sets of large, inhomogeneous, circularly-symmetric fluctuations of the plasma. This is precisely the feature that will allow us to identify the critical bubbles with `Jecco`.

Following the procedure outlined in Sec. 5.2, we generate a family of initial circular bubbles with different radii and we numerically evolve them with `Jecco`. As expected from the discussion above, large bubbles expand and small bubbles collapse. This is illustrated in Fig. 5.4, where we plot the radius of each bubble, defined as the position of the inflection point of the energy density profile, as a function of time. We see that bubbles with initial radius $\Lambda\rho_c \geq 3.75$ eventually expand, whereas bubbles with radius $\Lambda\rho_c \leq 3.69$ eventually collapse. This means that the critical radius must be in between these two values. Substituting into (5.8) we then obtain an estimate for the surface tension γ. Thus,

$$3.69 < \Lambda\rho_c < 3.75 \,, \qquad 0.116 < \frac{\gamma}{\Lambda^3} < 0.118 \,.$$

As we approach the critical bubble, the dynamics becomes slower and slower. This feature can be seen in the contour plots of Fig. 5.5 and in the energy density snapshots of Fig. 5.6. In these figures the bubbles in the bottom row evolve more slowly than those in the top row because their initial radii are closer to ρ_c. By fine-tuning the radius of the initial bubble we can get closer and closer to the critical bubble. Fig. 5.7 shows that, as we approach this limit both from above and from below, the bubble profile converges to a single profile. In this figure we evaluate the profiles at $\Lambda t = 20$ so that the result is not contaminated by the fast-decaying, transient oscillations present around $\Lambda t = 0$ in Fig. 5.4.

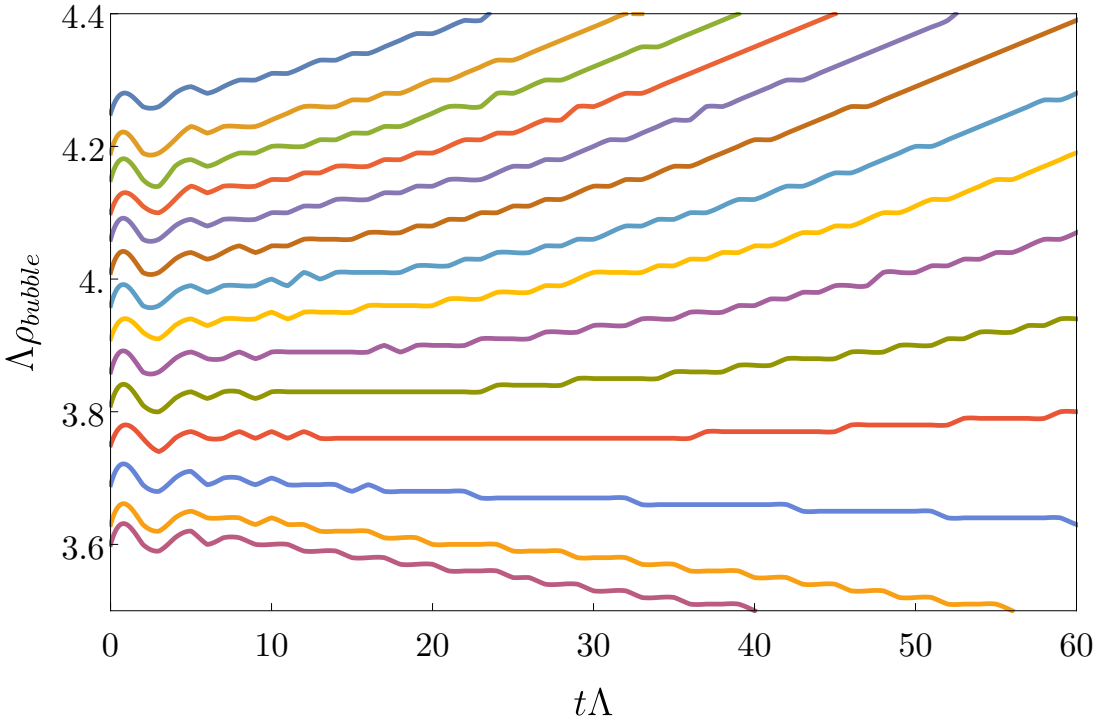

Figure 5.4: Time evolution of the wall position for several different initial bubbles. The critical bubble radius has to be $3.69 < \Lambda\rho_c < 3.75$.

The fact that we can approach the critical bubble by fine-tuning a single parameter is consistent with the fact that the critical bubble should possess a single unstable mode (see e.g. [115, 116]). Indeed, the latter property means that, in the infinite-dimensional space of configurations around the critical bubble, the hypersurface of stable perturbations has codimension one. As we change a single parameter in our initial data, we trace a curve in the space of configurations that will generically intersect this hypersurface. If we were to start the time evolution exactly on this hypersurface, we would remain within it and we would be attracted to the exact, static critical bubble solution. By tuning the radius of the bubble in our initial data we come close to this situation and therefore the dynamics becomes slower and slower.

Since the critical bubble is a static solution, an alternative method to determine it would be to solve an elliptic problem in two dimensions in AdS, along the lines of what was done in chapter 3.

5.4 Expanding bubbles

We now turn to the analysis of expanding bubbles, which play an important role in the dynamics of first order phase transitions. At sufficiently late times, the wall of these bubbles is expected to move with a constant velocity, which results from the balance between the friction that the plasma exerts on the wall and the pressure difference between the inside and the outside of the bubble. Moreover, the energy density profile should approach a characteristic and time-independent self similar behaviour. In this section we will use holography to determine both the bubble wall velocity and the asymptotic profile.

We will proceed in increasing difficulty level. We will start by studying bubbles with `SWEC` in 1+1 dynamical dimensions, i.e. planar wall bubbles, and we will then use `Jecco` to study bubbles in 2+1 dynamical directions, which are cylindrical. In the second scenario we will see

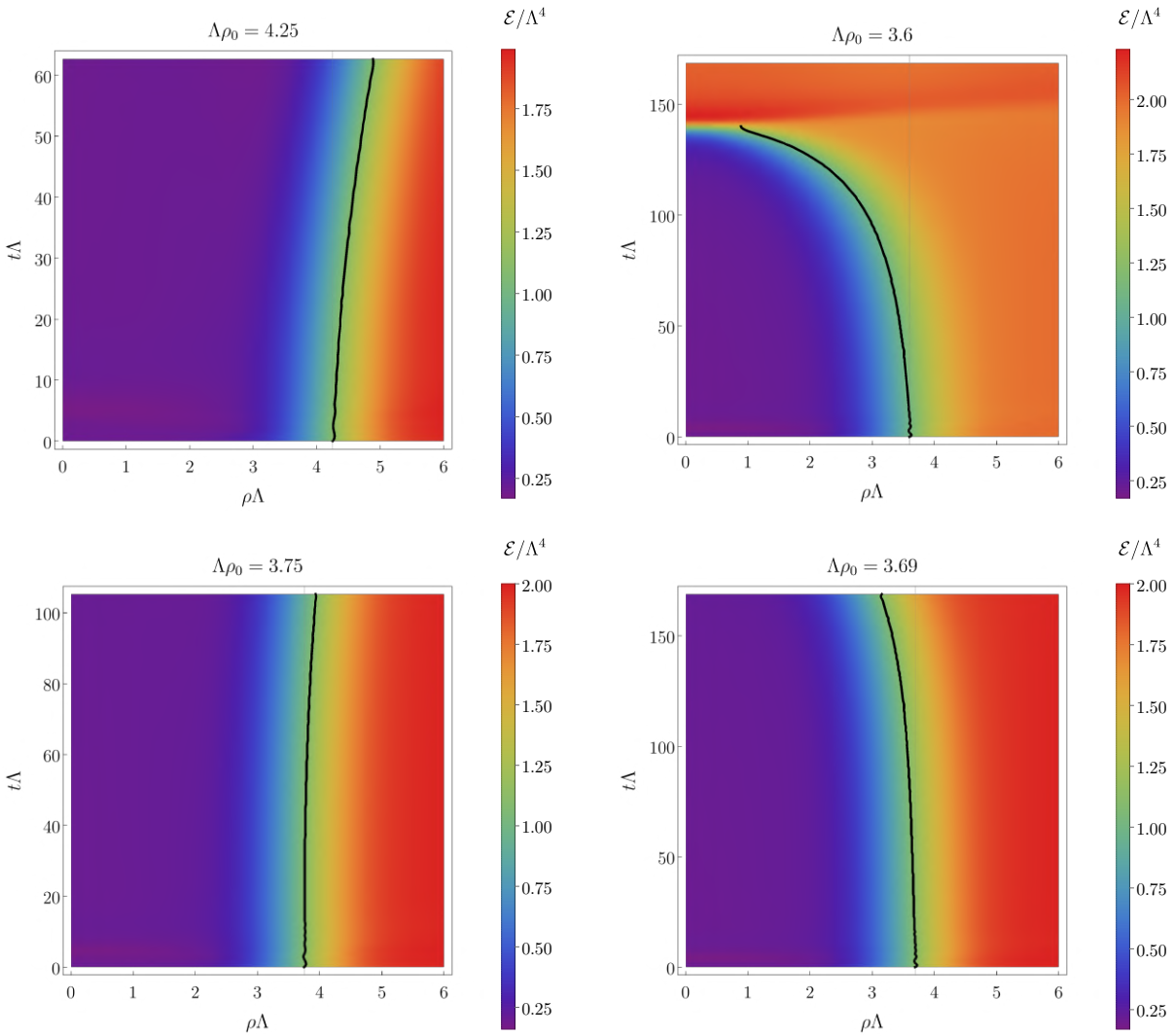

Figure 5.5: Time evolution of bubbles with different initial radii. The black curves represent the position of the wall, defined as the inflection point in the energy density profile. The radius of the critical bubble lies in the interval $3.69 < \Lambda\rho_c < 3.75$. The bubbles on the left column are supercritical and they expand. The bubbles on the right column are subcritical and they collapse. The bubbles in the bottom row are closer to the critical bubble than those on the top row and hence they evolve more slowly. Videos of each of the evolutions can be found at https://youtube.com/playlist?list=PL6eUQq2UUQ4JJTD_pRfJt-ShPGKxGBRW9

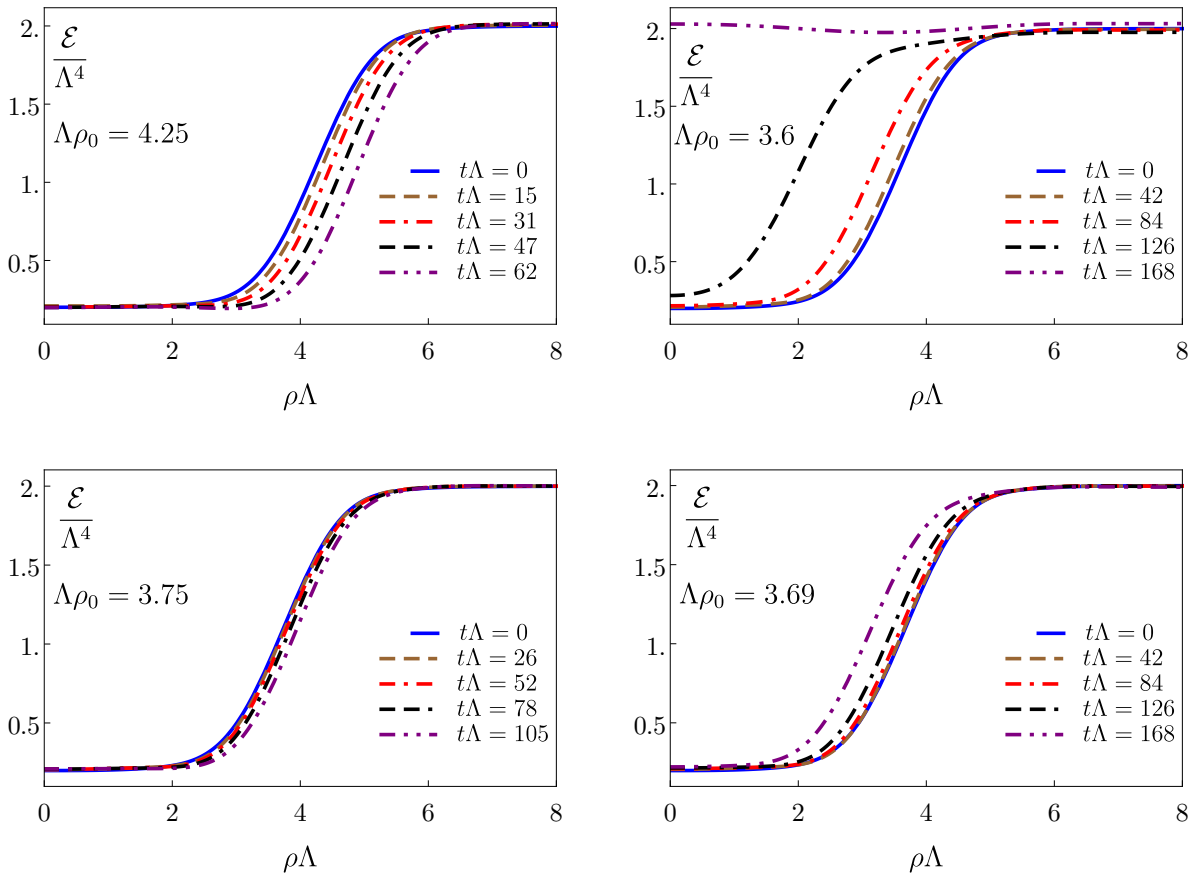

Figure 5.6: Snapshots of the energy density profile of bubbles with different initial radii. The radius of the critical bubble lies in the interval $3.69 < \Lambda\rho_c < 3.75$. The bubbles on the left column are supercritical and they expand. The bubbles on the right column are subcritical and they collapse. The bubbles in the bottom row are closer to the critical bubble than those on the top row and hence they evolve more slowly.

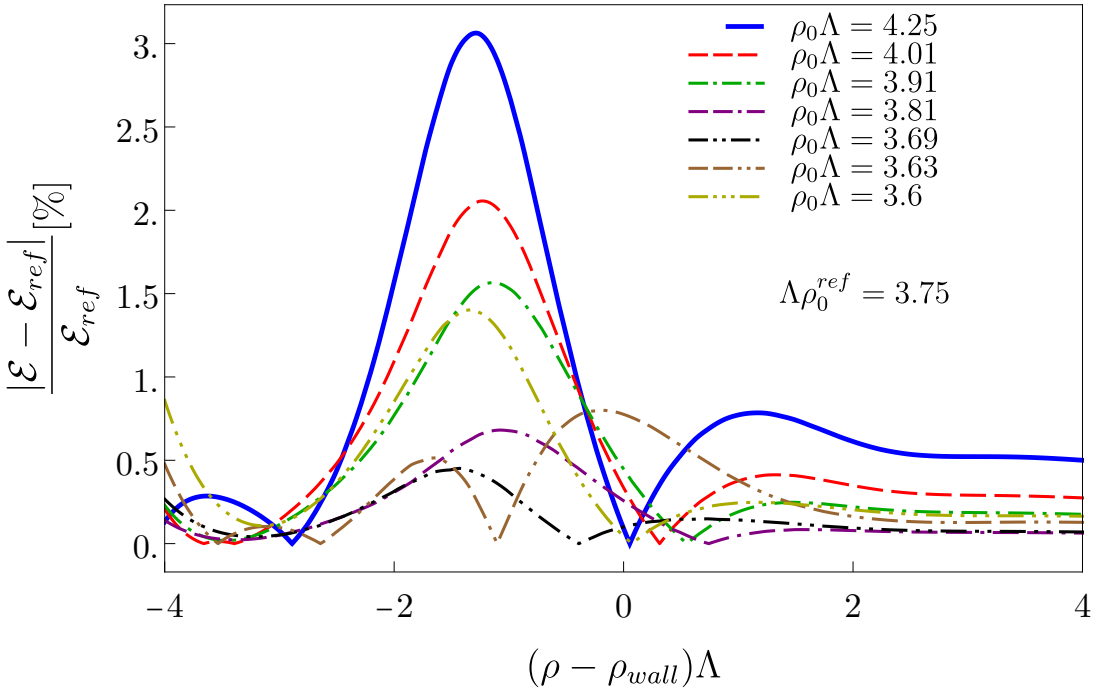

Figure 5.7: Relative difference between the energy density profiles at $t\Lambda \sim 20$ of bubbles with different initial radii. We take as a reference the profile for a bubble with initial radius $\Lambda\rho = 3.75$, which is close to the critical radius. We see that, as this value is approached both from above and from below, the profiles converge to a single profile.

how the self similar profile is richer in structure.

5.4.1 Planar bubbles

For clearness we show again the phase diagram for the theory in question in Fig. 5.8 with those states that are relevant for this subsection.

We now imagine that the system has been supercooled to some state A on the upper metastable branch, and that at this point a bubble corresponding to some state B on the lower stable branch is nucleated. The nucleation temperature is therefore $T_N = T_A$. On general grounds we expect a non-zero probability to nucleate bubbles with different initial wall profiles and with different initial sizes. We will therefore vary these parameters and determine their effect on the subsequent post-nucleation dynamics. We will also vary the initial state B inside the bubble. Although this is often assumed to have the same temperature as A, the initial-value problem with $T_B \neq T_A$ is perfectly well-defined on the gravity side. These parameters do not completely determine the initial quantum state of the bubble. On the gauge theory side they only specify the one-point function of the stress-tensor in the initial state, for example the profile of the energy density. On the gravity side they only specify the fall-off of the metric near the asymptotic AdS boundary. A complete determination of the initial quantum state requires knowledge of all the higher correlation functions in the gauge theory or, equivalently, the complete metric on the gravity side. Therefore we will also scan over different metrics in the initial data.

We begin with a bubble of size $14\Lambda^{-1}$ and a state B inside the bubble with temperature $T_B = T_A = 0.374\Lambda$, as indicated in Fig. 5.8. The initial energy profile, shown as a dashed blue curve in Fig. 5.9, is arbitrarily chosen except for the fact that it must interpolate between the

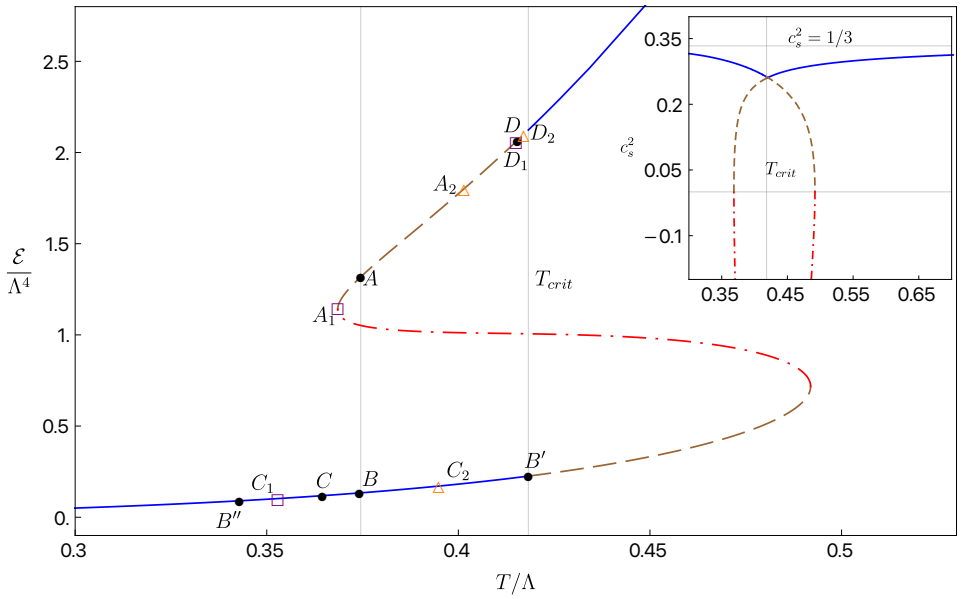

Figure 5.8: Energy density as a function of temperature and (inset) speed of sound for $\lambda_6 = 0.1, \lambda_4 = -0.346021$. The grey vertical line on the right indicates the critical temperature at which the PT takes place. The grey vertical line on the left indicates that A and B have the same temperature. Stable states are shown in solid blue, metastable ones in dashed brown, and unstable ones in dotted-dashed red.

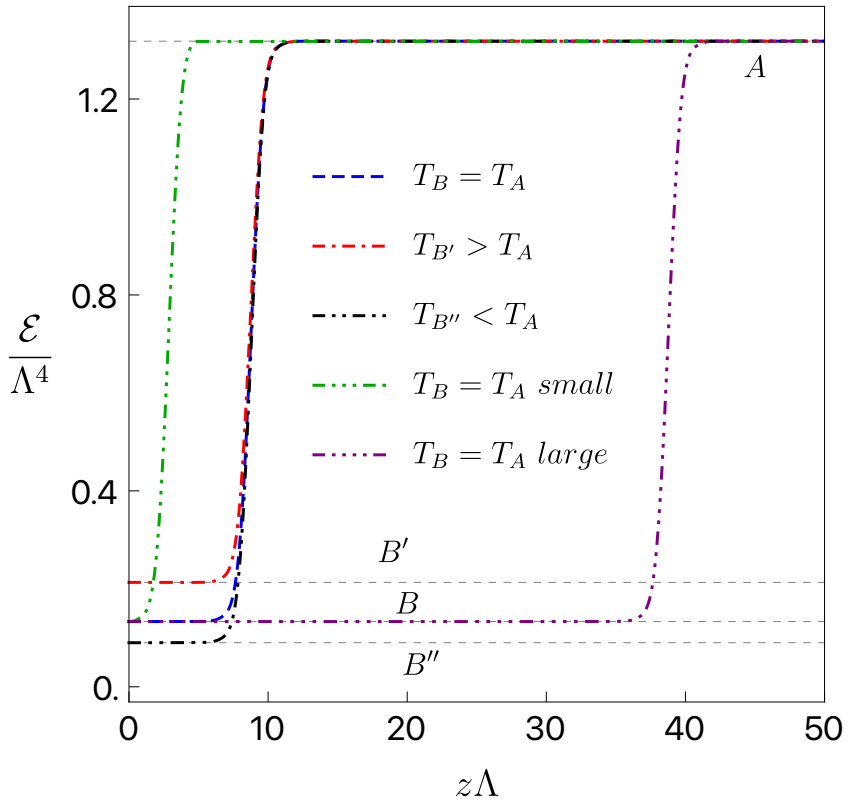

Figure 5.9: Different initial energy profiles for the same nucleation temperature T_A. In this and in subsequent plots we only show positive values of z because we only consider states invariant under $z \to -z$.

energy $\mathcal{E}_B$ inside the bubble and the energy $\mathcal{E}_A$ outside the bubble.

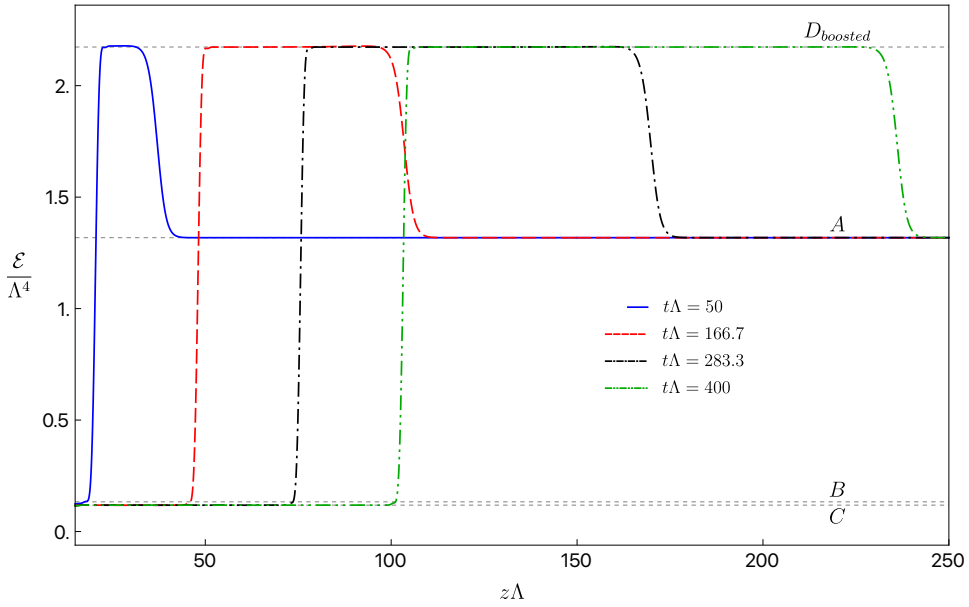

Figure 5.10: Snapshots of the energy density profile at different times for the initial state with $T_B = T_A$ shown as a dashed blue curve in Fig. 5.9.

Since the pressure in B is higher than in A, the initial wall is accelerated towards the right. Fig. 5.10 shows several snapshots of the resulting energy density at different times. The wall starts at rest and reaches a terminal velocity $v^A_{wall} \simeq 0.24$ in a time of order $\Delta t \sim 50\Lambda^{-1}$. As illustrated by the solid blue curve in Fig. 5.10, in this time the wall profile relaxes to a preferred shape. This shape remains constant at subsequent times, as shown by Fig. 5.11. In addition, in this time the energy density inside the wall evolves to that of the state marked as C in Fig. 5.8. As time progresses, energy conservation implies that an intermediate "hot" region develops in between the wall and the asymptotic A-region. We have dubbed this region $D_{boosted}$ in Fig. 5.10. The reason is that the fluid velocity in this intermediate region is constant and given by $v_D \simeq 0.22$, so $D_{boosted}$ is the state D in Fig. 5.8 boosted to the right with velocity v_D. The interface between the $D_{boosted}$- and the A-regions moves at constant velocity $v_{int} \simeq 0.57$. This means that the size of $D_{boosted}$ grows linearly with time. The width of the interface also grows, but more slowly than linearly. As a consequence, if we plot the energy profile in terms of $\xi = z/t$ for different fixed times, the interface between $D_{boosted}$ and A approaches a discontinuity at late times, as illustrated in Fig. 5.12. In this limit the profile becomes a function of ξ alone, as it is commonly assumed.

The features of the late-time state such as the wall profile, the wall velocity, and the C- and D-states, are determined dynamically and are independent of the bubble initial conditions. We illustrate this for the wall profile in Fig. 5.13. To obtain this plot we take the set of initial conditions above and vary one initial condition at a time to obtain a new set of wall profiles. Specifically, we change the initial state B inside the bubble to the states B' and B'' in Fig. 5.8, whose corresponding energy profiles are shown in Fig. 5.9. We also vary the initial size of the bubble to the larger and smaller values shown by the corresponding curves in Fig. 5.9. In addition, the wall profile for the smaller bubble is different from that of the original bubble. Finally, we change the initial bulk metric so as to increase or decrease the initial pressure anisotropy between the longitudinal and the transverse directions by an order of magnitude. As we see in Fig. 5.13, all these changes result in the same late-time wall profile.

We now turn to the dependence on the nucleation temperature. The states C and D and

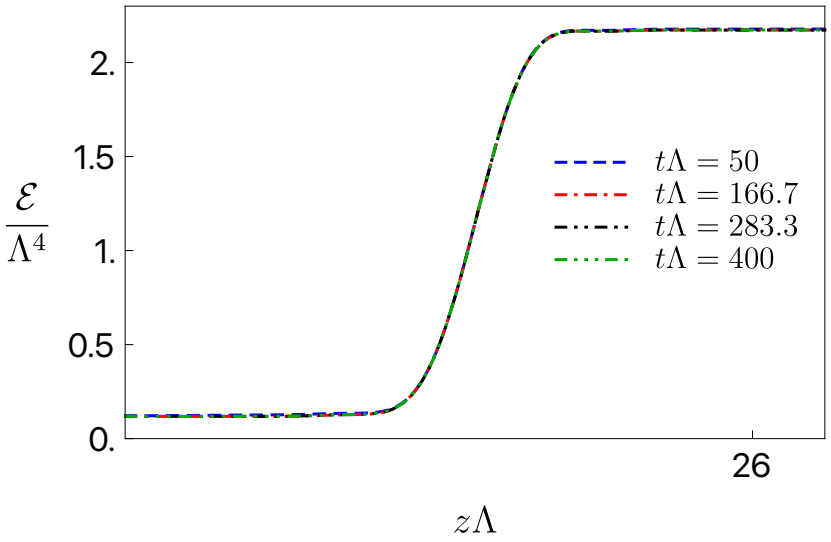

Figure 5.11: Same wall profiles as in Fig. 5.10, each shifted in z by a different amount, to show that the wall profile remains constant in time.

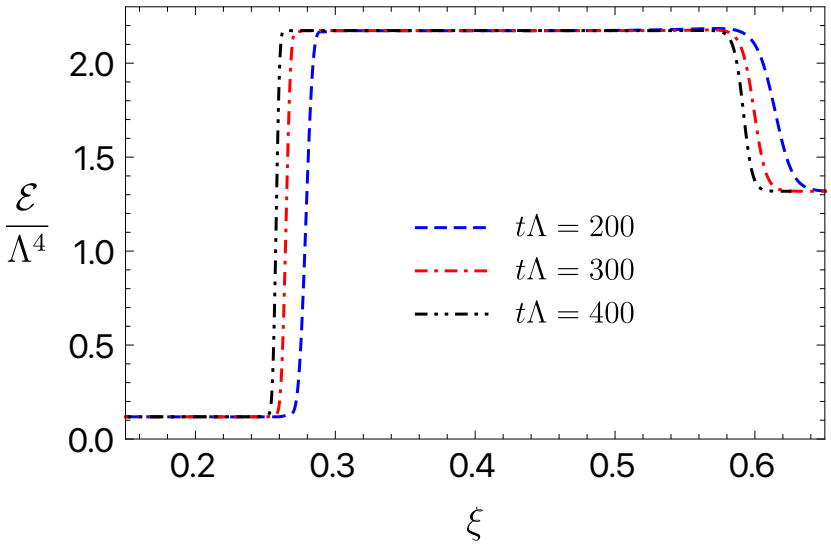

Figure 5.12: Energy profile at as a function of $\xi = z/t$ for different values of t.

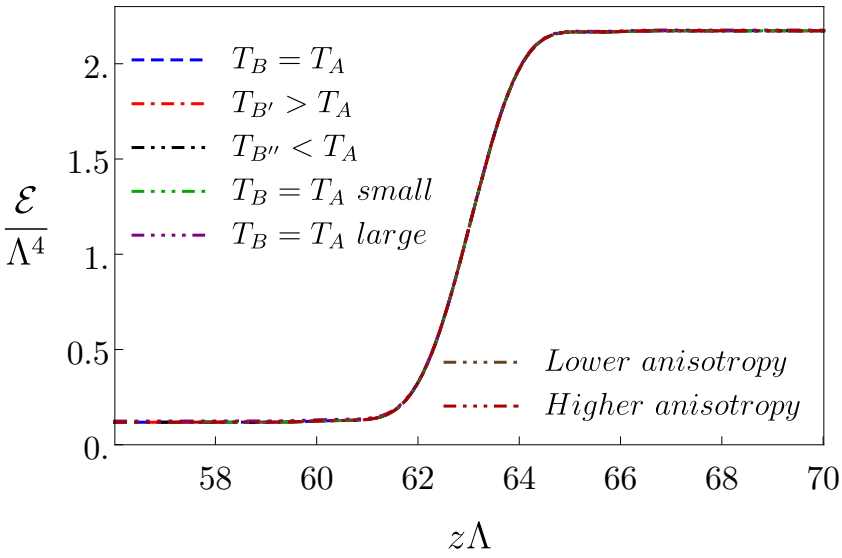

Figure 5.13: Wall profiles for the same nucleation temperature $T_N = T_A$ but different initial conditions, each shifted in z by a different amount to show that the wall profile is independent of the initial conditions.

the wall velocity vary monotonically with T_N. Indeed, as T_N approaches T_{crit} from the left the states C and D approach the vertical line at $T = T_{crit}$, the wall velocity goes to zero and the system approaches a static, phase-separated configuration in which the states inside and outside the bubble coexist at the critical temperature [63]. In the opposite limit, as T_N decreases from T_{crit} towards the end of the metastable branch, labelled as A_1 in Fig. 5.8, the states C and D move to the left and approach C_1 and D_1, respectively. Similarly, the wall velocity increases monotonically from zero to a maximum value $v_{wall}^{A_1} \simeq 0.29$.

We have explored the dependence of v_{wall} on different properties of the state A. The most suggestive result is shown in Fig. 5.14, which seems to imply a linear dependence on the ratio between the pressure difference inside and outside the bubble and the energy density outside the bubble. Heuristically, this relation seems plausible given that the force trying to accelerate the bubble increases with the pressure difference, whereas the resisting force grows with the energy density outside the bubble.

Changing the nucleation temperature also changes the wall profile. However, we empirically observe that, up to a rescaling, the latter is well approximated by the interface of a phase-separated configuration at $T = T_{crit}$ [63]. Specifically, the wall profile for any T_N is given by

$$\mathcal{E}(z) = \mathcal{E}_C + (\mathcal{E}_D - \mathcal{E}_C) f(\Lambda z)\,, \tag{5.9}$$

where the energies of the C- and D-states depend on T_N but f is a T_N-independent, universal function that only depends on the theory. In particular, taking $T_C = T_D = T_{crit}$, this formula gives the profile of the phase-separated configuration. The latter is shown in Fig. 5.15, where we also compare the exact wall profiles for several nucleation temperatures with those predicted by Eq. (5.9).

Hydrodynamics

As the bubble expands the gradients away from the wall get diluted. Therefore the late-time state is expected to be well described by ideal hydrodynamics everywhere except in the region near the wall. This is confirmed by Fig. 5.16, where we compare the exact result for the

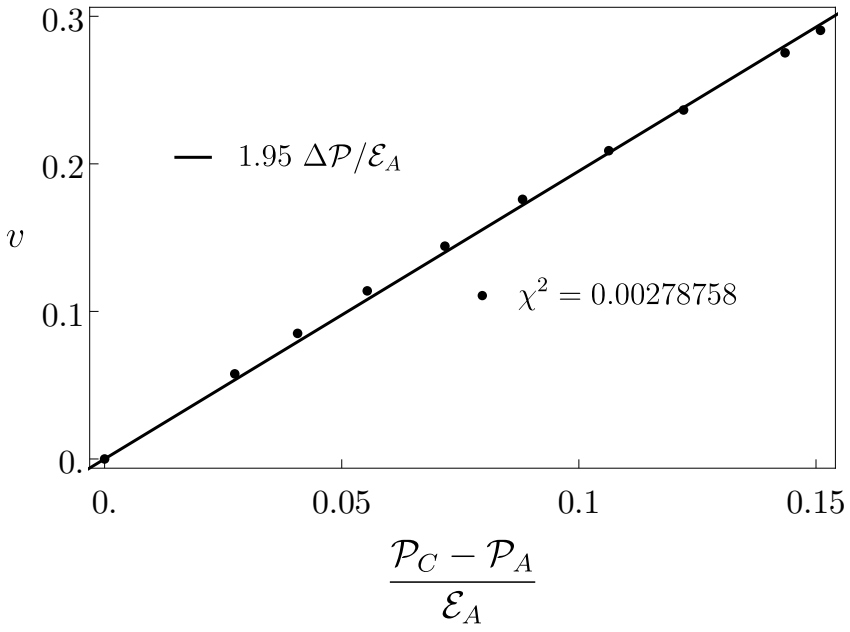

Figure 5.14: The points show the wall velocity for different nucleation temperatures. The line is a fit as a function of the ratio between the pressure difference inside and outside the bubble and the energy density outside the bubble.

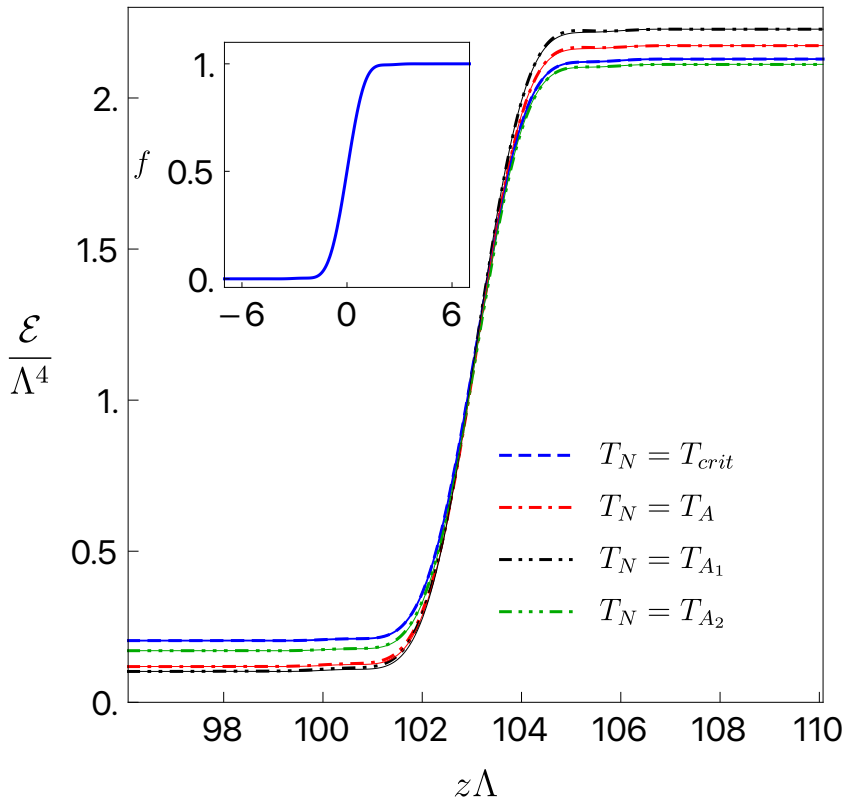

Figure 5.15: Comparison between the exact wall profiles for several nucleation temperatures with the results of applying Eq. (5.9). The case $T_N = T_{crit}$ corresponds to a static, phase-separated configuration. The universal function f is shown in the inset.

longitudinal pressure with the prediction of both ideal and first-order viscous hydrodynamics at late times. We see that none of the hydrodynamic curves describe the wall region correctly.

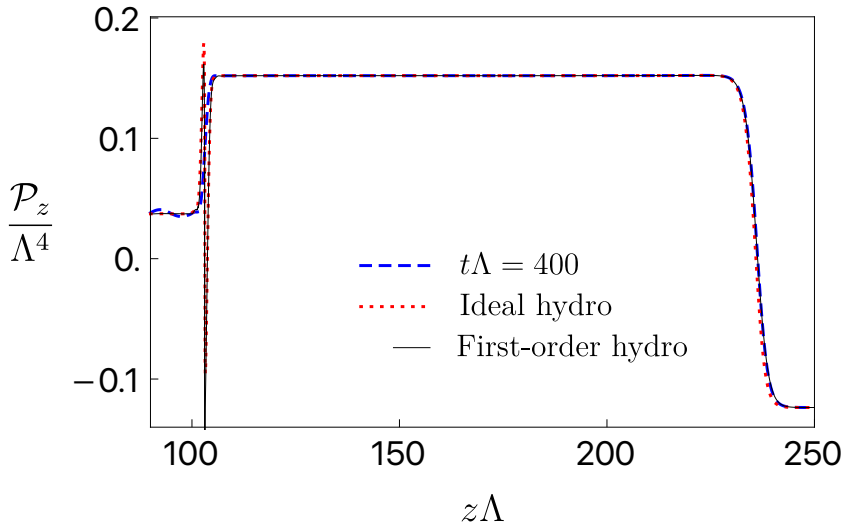

Figure 5.16: Comparison between the holographic longitudinal pressure at late times and the ideal and the first-order hydrodynamic predictions.

Nevertheless, at asymptotically late times the size of the wall becomes negligible and we can use ideal hydrodynamics to constraint the properties of the bubble. At those times we can treat both the wall and the interface between the $D_{boosted}$- and A-regions as discontinuities and assume that the physics only depends on ξ. Requiring that the energy and momentum fluxes are the same on both sides of these discontinuities leads to a set of matching conditions (see e.g. [117]). In combination with the hydrodynamic equations away from the wall, these conditions determine the C- and D-states, the fluid velocity in D, and the velocity of the interface in terms of the nucleation temperature and the wall velocity. This means that, for a given nucleation temperature, the entire system is controlled by the wall velocity.

5.4.2 Cylindrical bubbles

We will now study a single case of a expanding cylindrical bubble thanks to `Jecco`.

Wall profile, wall velocity and hydrodynamics

For computational reasons, it is easier to identify the late-time limit for bubbles that expand at high velocity, since for these configurations the evolution is faster and we need to run our code for a shorter time to reach the late-time, asymptotic limit. Based on the mechanical picture we described above we expect that, as the pressure difference between the inside and the outside of the bubble grows, the wall velocity will grow too. Therefore, we will focus on bubbles formed in the large overcooling limit, when the metastable phase is close to the limit of local stability and the pressure difference between the inside and outside of the bubble is the largest. For this reason we will choose the state A outside the bubble as indicated in Fig. 5.1, whereas for the state inside we choose the one indicated as B. Following Sec. 5.2, we then construct a bubble that interpolates monotonically between the states B inside and A outside, as in Fig. 5.3. This is our initial state at $t = 0$.

In Fig. 5.17(top) we show snapshots of the subsequent evolution of the energy density of the bubble and in https://youtu.be/wFLpOFSeO8Q we show a video of the full time evolution. As time progresses, the energy density in the interior of the bubble evolves until it reaches the

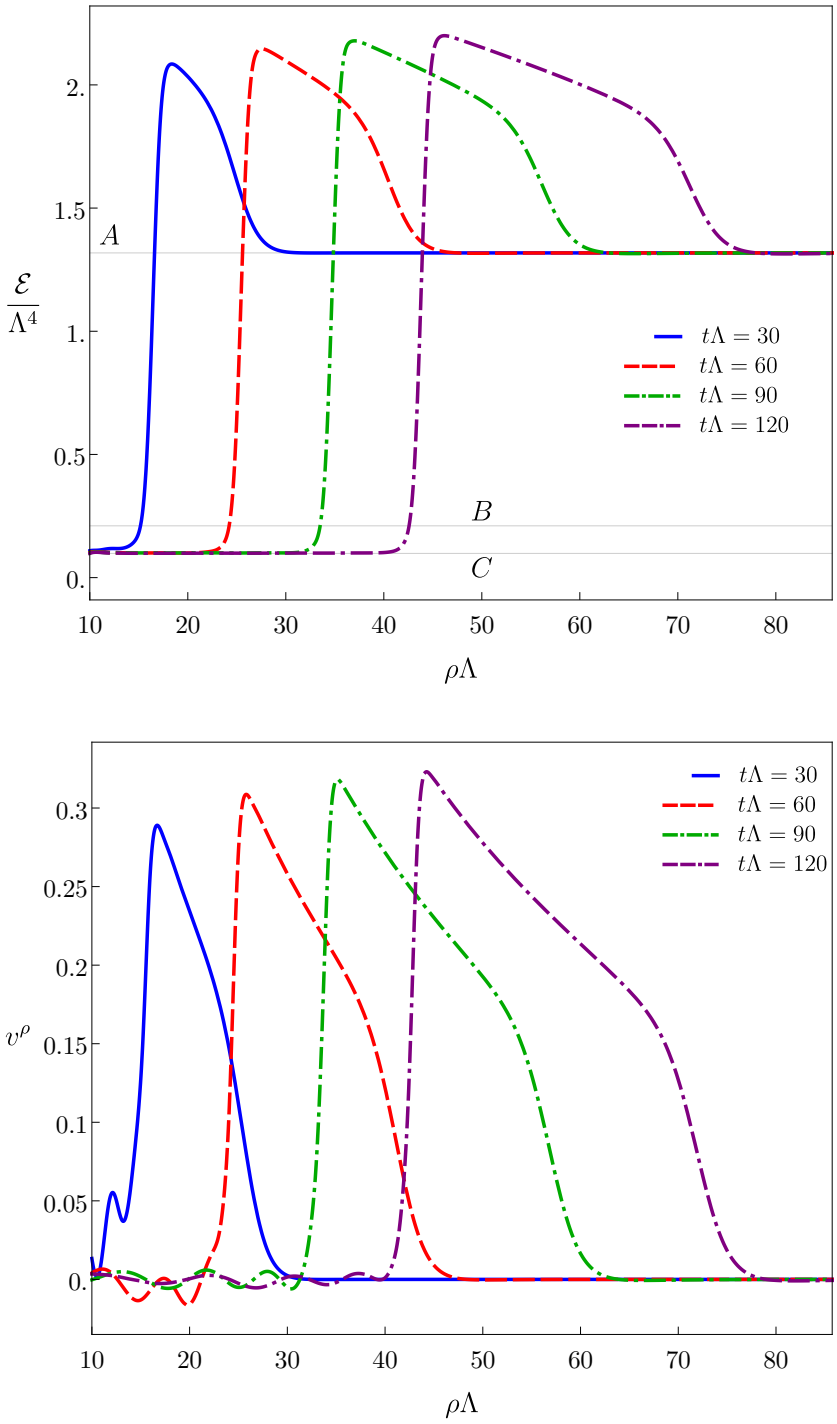

Figure 5.17: (Top) Snapshots of the energy density profile (top) and of the fluid velocity (bottom) for an expanding bubble. The bubble at $t = 0$ interpolates monotonically between the states B inside and A outside, as in Fig. 5.3. At late times the state inside the bubble evolves dynamically to C. The states A, B and C are indicated by black dots in Fig. 5.1. A full time evolution video of the energy density can be found at https://youtu.be/wFLp0FSeO8Q

value corresponding to the state C in Fig. 5.1. This means that, as in the planar case, this state is dynamically determined.

While the initial configuration at $\Lambda t = 0$ interpolates monotonically between the stable and meta-stable branches of the phase diagram, the expanding bubbles quickly develop a non-monotonic energy density profile. As illustrated in Fig. 5.17, the propagation of the bubble leads to an overheating of the region in front of the bubble that gradually decreases back to $\mathcal{E}_A$ sufficiently far away from the bubble front. This overheated region possesses non-vanishing energy and momentum fluxes, which allows us to define a flow velocity via the Landau matching condition,

$$T^{\nu\mu}u_\mu = -\mathcal{E}_{\rm loc}u^\nu\,, \tag{5.10}$$

with $\mathcal{E}_{\rm loc}$ the energy density of the fluid in the local rest frame. The flow velocity $v = u^\rho/u^0$, with u^ρ the radial component of the flow field, for this configuration is shown in Fig. 5.17(bottom). As we can see in these figures, the region between the bubble wall and the asymptotic metastable state grows linearly with time as the bubble expands. As a consequence, we expect that, at late times, the gradients of the bubble profile decrease and most of the dynamics is captured by hydrodynamics. We can test this expectation by checking the validity of the hydrodynamic constitutive relations for the stress tensor in the Landau frame. After extracting the rest frame energy density and the fluid velocity from the holographic stress tensor, we can predict the rest of the components of the stress tensor via the constitutive relations with or without viscous corrections. The result of this comparison at $\Lambda t = 110$ is shown in Fig. 5.18. We see that hydrodynamics becomes a very good approximation for the dynamics of the entire system except for the bubble wall, where the failure of hydrodynamics is expected on general grounds.

Despite its non-hydrodynamic nature, the dynamics of the bubble wall becomes remarkably simple at sufficiently late times: it moves almost rigidly at constant velocity. The velocity $v \simeq 0.31$ can be extracted from Fig. 5.17 via a linear fit to the wall position of the form

$$\rho_{\rm wall}(t) = \rho_{\rm wall,0} + v_{\rm wall}t\,. \tag{5.11}$$

To illustrate the rigidity, in Fig. 5.19 we compare the bubble wall profiles at several different times. To facilitate the comparison, we shift the position of each curve such that the inflexion point of the different walls at different times coincide with one another. We see that the way that the wall deviates from the inner region C is identical for all sufficiently late times. In contrast, the maximum value of the energy density at the end of the wall grows slowly with time. As we will explain in the next section, this growth indicates that, in the times covered by our simulation, the bubble has not yet reached the asymptotic late-time form. Despite this, Fig. 5.19 shows that the wall has a fixed size set by the microscopic scale of the theory, Λ. In particular, the size of the wall does not grow with time, in contrast with the overheated region in front of the bubble wall.

In the case of planar bubbles, we showed that the late-time wall profile only depends on the asymptotic metastable state A. In other words, the profile is independent of the initial conditions used to generate the bubble in the first place, as long as they lead to an expanding bubble. We expect the same conclusion to hold for the circular bubbles considered here, but it would be interesting to verify it explicitly. Assuming this, it is interesting to check how the wall profile of an expanding bubble compares to those of (almost) static walls. For this purpose, in Fig. 5.20 we compare the profile of the expanding wall of Fig. 5.17 with that of the critical bubble of Sec. 5.3 and with the walls of phase-separated planar and circular configurations. Following analogous steps to the planar bubble case, to facilitate the comparison we shift and rescale each profile appropriately so that it interpolates between 0 on the left of the wall and 1 on the right. We achieve this by plotting not just the energy density $\mathcal{E}(\rho)$ but the combination $(\mathcal{E}(\rho) - \mathcal{E}_L)/(\mathcal{E}_R - \mathcal{E}_L)$, with $\mathcal{E}_L$ and $\mathcal{E}_R$ the values of the energy density on the left and on the right of the wall, respectively. In the case of the expanding bubble, we define $\mathcal{E}_R$ as the value

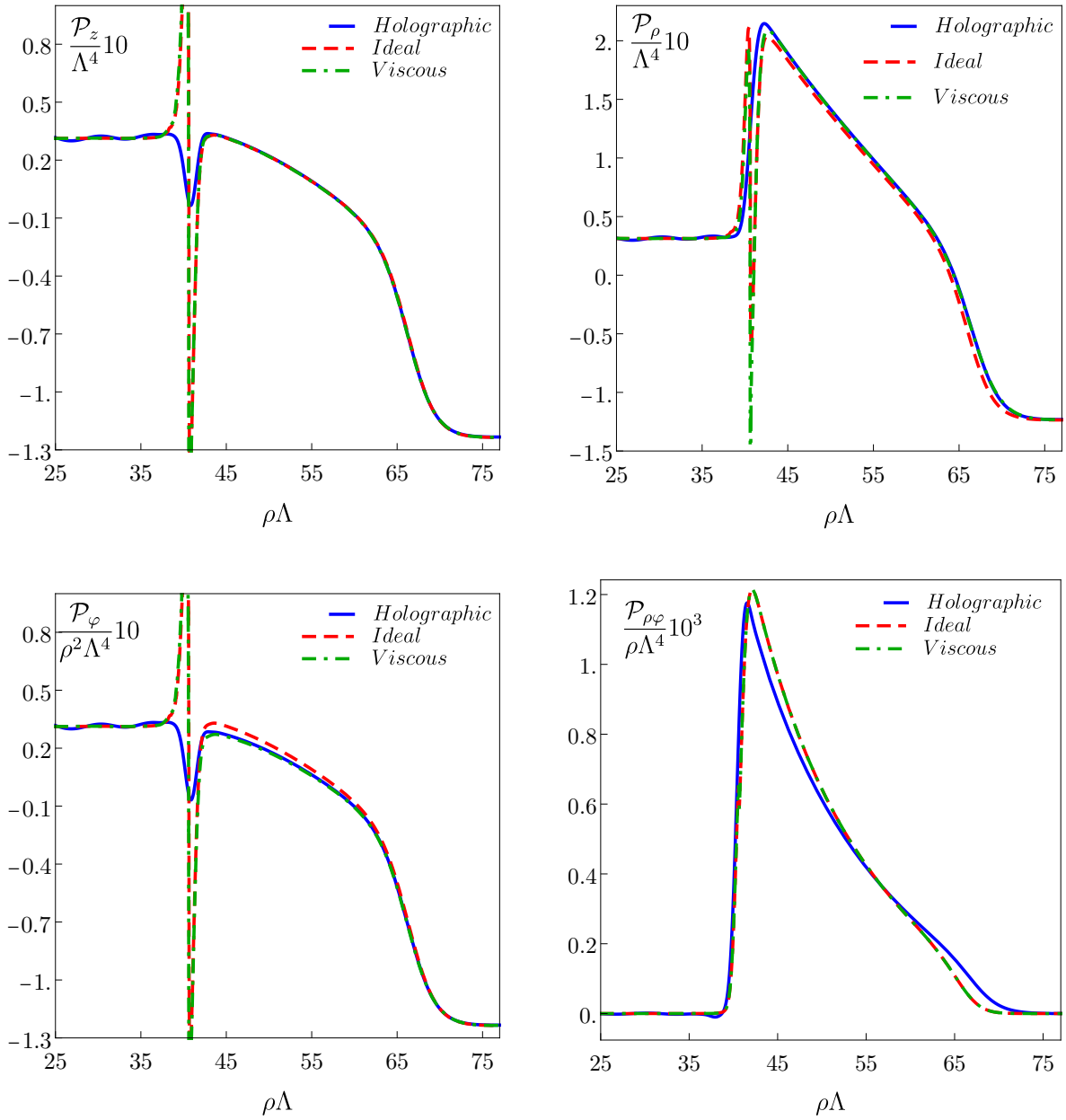

Figure 5.18: Comparison of the holographic stress tensor with the ideal and viscous hydrodynamic approximations based on the constitutive relations at a time $\Lambda t = 110$ at which the bubble wall is located at $\Lambda\rho = 40.7$. $\mathcal{P}_z, \mathcal{P}_\rho, \mathcal{P}_\varphi$ and $\mathcal{P}_{\rho\varphi}$ are the stress tensor components in the $zz-, \rho\rho-, \varphi\varphi-$ and $\rho\varphi-$directions, respectively.

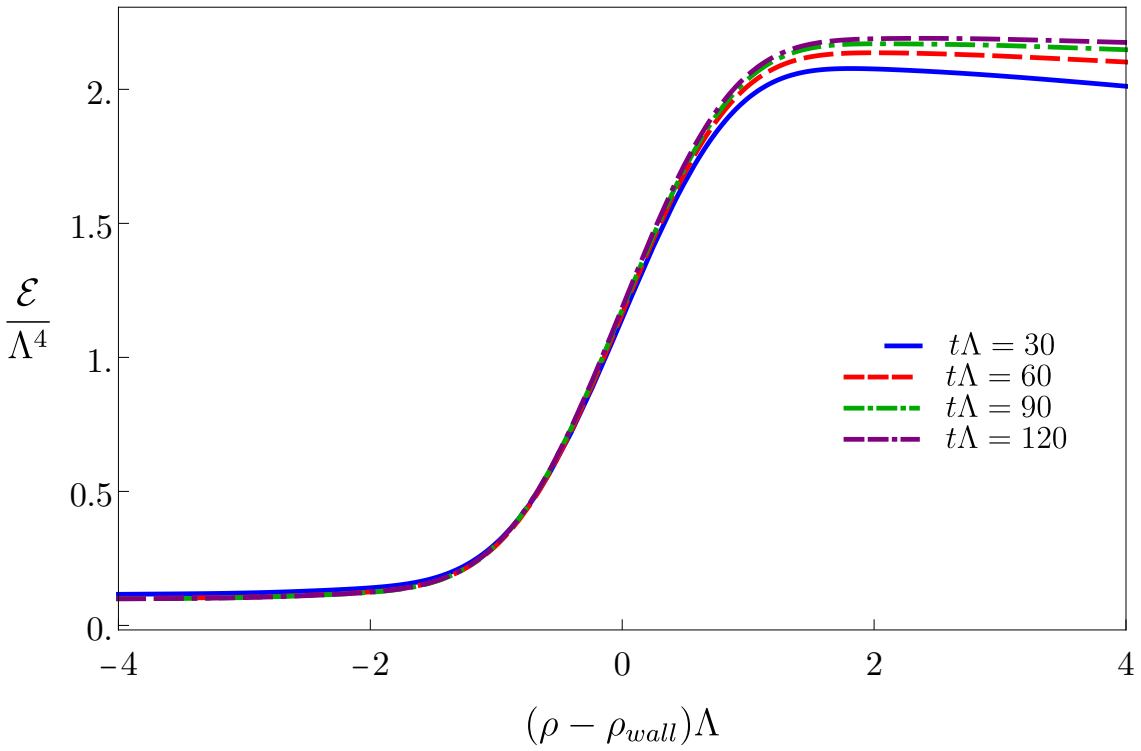

Figure 5.19: Comparison of the bubble wall profiles at several different times for the expanding bubble of Fig. 5.17. To facilitate the comparison, we shift the position of each curve such that the inflexion point of the different walls at different times coincide with one another.

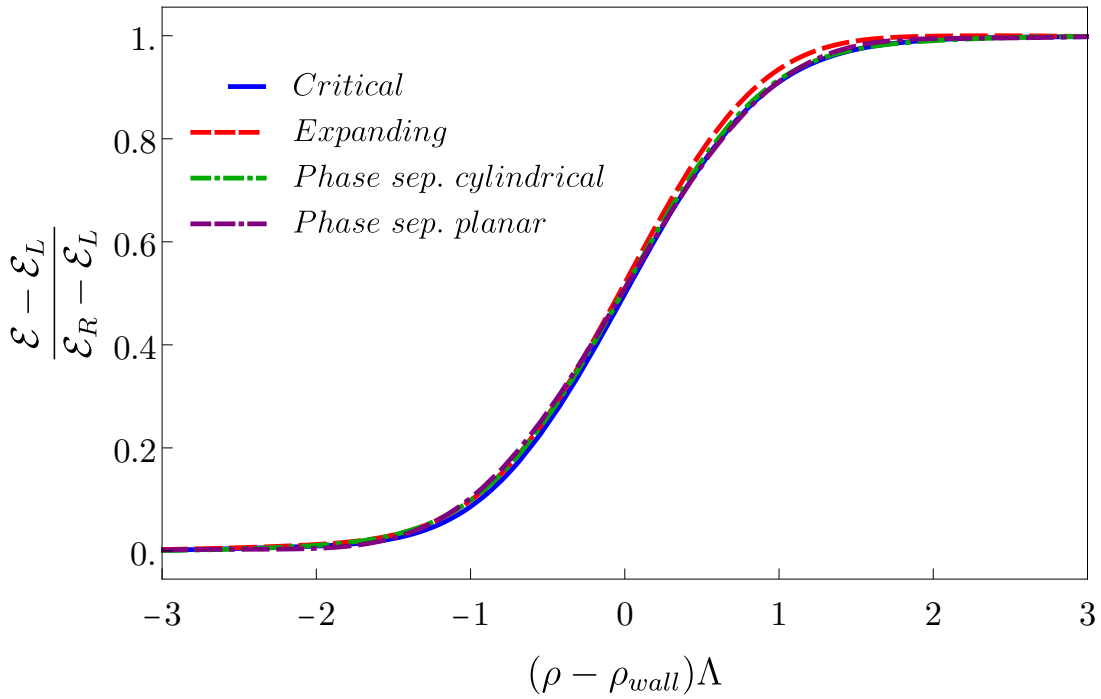

Figure 5.20: Comparison of wall profiles for several configurations. "Critical" refers to the bubble of Fig. 5.5 with $\Lambda\rho_0 = 3.75$. "Expanding" refers to the bubble of Fig. 5.17. "Phase sep." refers to phase-separated configurations, be they planar or circular. Each profile has been shifted and rescaled so that it interpolates between 0 on the left of the wall and 1 on the right. In the case of the expanding bubble, we define $\mathcal{E}_R$ as the value of the energy density at the maximum located right in front of the wall.

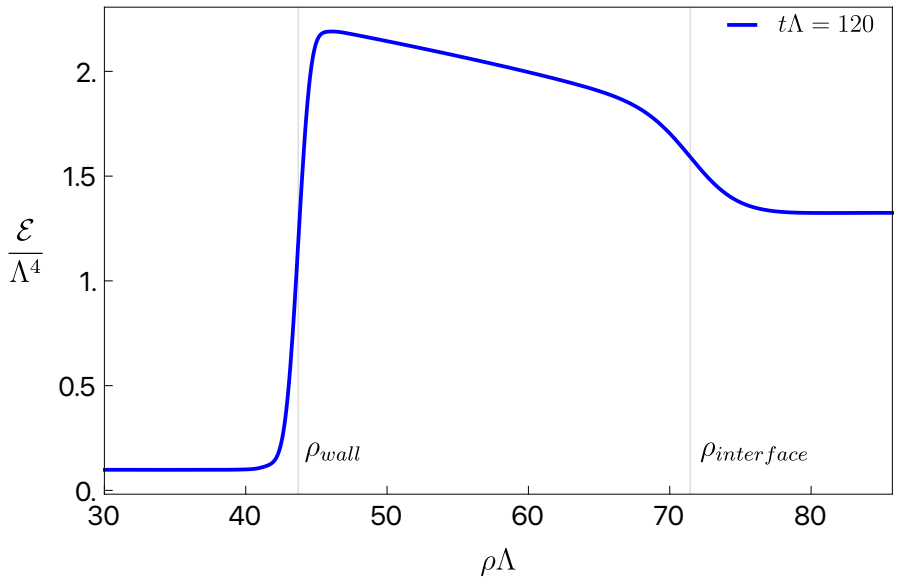

Figure 5.21: Expanding bubble profile at late times and inflection points, marked with vertical grey lines, used to define the size of the overheated region.

of the energy density at the maximum located right in front of the wall. We see from the figure that, while all profiles are fairly similar, differences can be seen with the naked eye. These are more pronounced in the regions where the second derivative is larger, where they are of the order of 9%.

Late-time self-similar solution

As we have seen, for sufficiently late time the bubble wall becomes rigid and moves at a constant velocity $v_{\rm wall}$. This implies that the radius of the region inside the bubble grows linearly with time. Since the energy density in this region is lower than that in the asymptotic, metastable phase, this linear growth of the bubble radius must be compensated by a linear growth in the size of the overheated region in front of the bubble. At very late times, when all the microscopic scales become irrelevant, this behaviour leads to a self-similar solution for the bubble that only depends on the ratio ρ/t, as described in e.g. [117]. In this section we study how our numerical solutions approach this late-time self-similar solution. For this purpose, we shift the time and radial coordinates by appropriate amounts $t_{\rm shift}$ and $\rho_{\rm shift}$ that we will define below. In other words, we define

$$\xi = \frac{\rho - \rho_{\rm shift}}{t - t_{\rm shift}} \,. \tag{5.12}$$

These shifts are motivated by the fact that our initial configuration has a finite size, and that it takes a certain amount of time for the configuration to become sufficiently close to the late-time asymptotic solution. While at asymptotic times these shifts become irrelevant, we find that this procedure accelerates the convergence to the self-similar regime in our finite-time simulations.

The shifts in question are defined as follows. Consider the overheated region in front of the bubble wall. This region is connected with the asymptotic region A by an interface. We begin by locating the inflection point on this interface, indicated by a vertical line at $\rho = \rho_{\rm interface}$ in Fig. 5.21. We then consider sufficiently late times such that both the wall and the interface positions move with constant velocity. In this regime $\rho_{\rm wall}(t)$ is given by (5.11) and

$$\rho_{\rm interface}(t) = \rho_{\rm interface,0} + v_{\rm interface} t \,. \tag{5.13}$$

We then impose that, as soon as this regime starts, the values of ξ at the positions of the wall and of the interface immediately agree their late-time limits. In other words, we adjust the two parameters $t_{\rm shift}$ and $\rho_{\rm shift}$ so that the following two conditions are satisfied:

$$\xi_{\rm wall} = v_{\rm wall}\,, \qquad \xi_{\rm interface} = v_{\rm interface}\,. \tag{5.14}$$

In Fig. 5.22 we show the energy density and fluid velocity profiles for different simulation times as a function of ξ. In both plots we see two regions of fast change that separate three smooth regions. The first region of fast change occurs around $\xi = v_{\rm wall}$ and connects the state C in the interior of the bubble, at rest and with a fixed energy density, with the overheated boosted region in front of the bubble. This abrupt behaviour is associated to the presence of the bubble wall. Since the size of the wall remains approximately constant in time, its width in the ξ-coordinate decreases with time. As a consequence, the wall becomes a discontinuity at asymptotically late times. The shape of the overheated region in front of the wall is not constant in time. In particular, its slope in the ρ-coordinate decreases with time. However, going to the ξ-coordinate enhances this slope, since at late times $d\mathcal{E}/d\xi \sim t\, d\mathcal{E}/d\rho$. The curves in Fig. 5.22 indicate that these two effects exactly cancel each other at asymptotically late times, resulting in a constant, non-zero value of the slope in the ξ-coordinate in this limit. The second abrupt region occurs at $\xi \simeq 0.52$ and corresponds to the interface between the overheated region and the asymptotic metastable region A. In the times covered by our simulations, the width of this interface grows with time, but this growth is slower than linear. However, it is possible that, at sufficiently late times, the width of this interface approaches a constant value. It would be interesting to verify this in the future through longer simulations. In any case, this interface also approaches a discontinuity in the ξ-coordinate at late times. Despite this, both the interface and the overheated region are well described by hydrodynamics at late times, as we saw in Fig. 5.18.

This discussion suggests that, at asymptotically late times, the bubble profile should consist of a static inner region C and an outer static region A connected through discontinuities with an intermediate overheated region with non-zero fluid velocity. This behaviour agrees with hydrodynamic analysis of large bubbles, as performed for example in [117]. At very late times, when the bubble profile depends only on the scaling variable ξ, the ideal hydrodynamic equations lead to the following equation for the energy density and the velocity field of a circular bubble

$$\gamma^2\Big[1-\xi\, v(\xi)\Big]\Big[c_s^2\mu^2-1\Big]v'(\xi) - \frac{v(\xi)}{\xi} = 0\,, \tag{5.15}$$

$$\frac{c_s^2}{\mathcal{W}}\Big[1-\xi v(\xi)\Big]\mathcal{E}'_{\rm loc}(\xi) - \gamma^2\Big[\xi - v(\xi)\Big]v'(\xi) = 0\,, \tag{5.16}$$

where $\gamma = 1/\sqrt{1-v^2}$ is the Lorentz factor, c_s is the speed of sound, $\mathcal{E}_{\rm loc}$ is the energy density in the local rest frame of the fluid,

$$\mathcal{W} = \mathcal{E}_{\rm loc} + \mathcal{P}_{\rm eq}(\mathcal{E}_{\rm loc}) \tag{5.17}$$

is the enthalpy density, and

$$\mu = \frac{\xi - v}{1-\xi v}\,. \tag{5.18}$$

It is well known that the ideal hydrodynamic equation (5.15) for the fluid velocity does not posses non-trivial continuous solutions with zero velocity in the interior and exterior of the bubble. Therefore, in this approximation the description of an expanding bubble requires the introduction of discontinuities in the hydrodynamic fields. These discontinuities are constrained by energy-momentum conservation: although the local energy density or the fluid velocity may be discontinuous, the energy-momentum flux across the discontinuity must be continuous. For each value of the wall velocity, these "junction conditions" at the discontinuities, together with

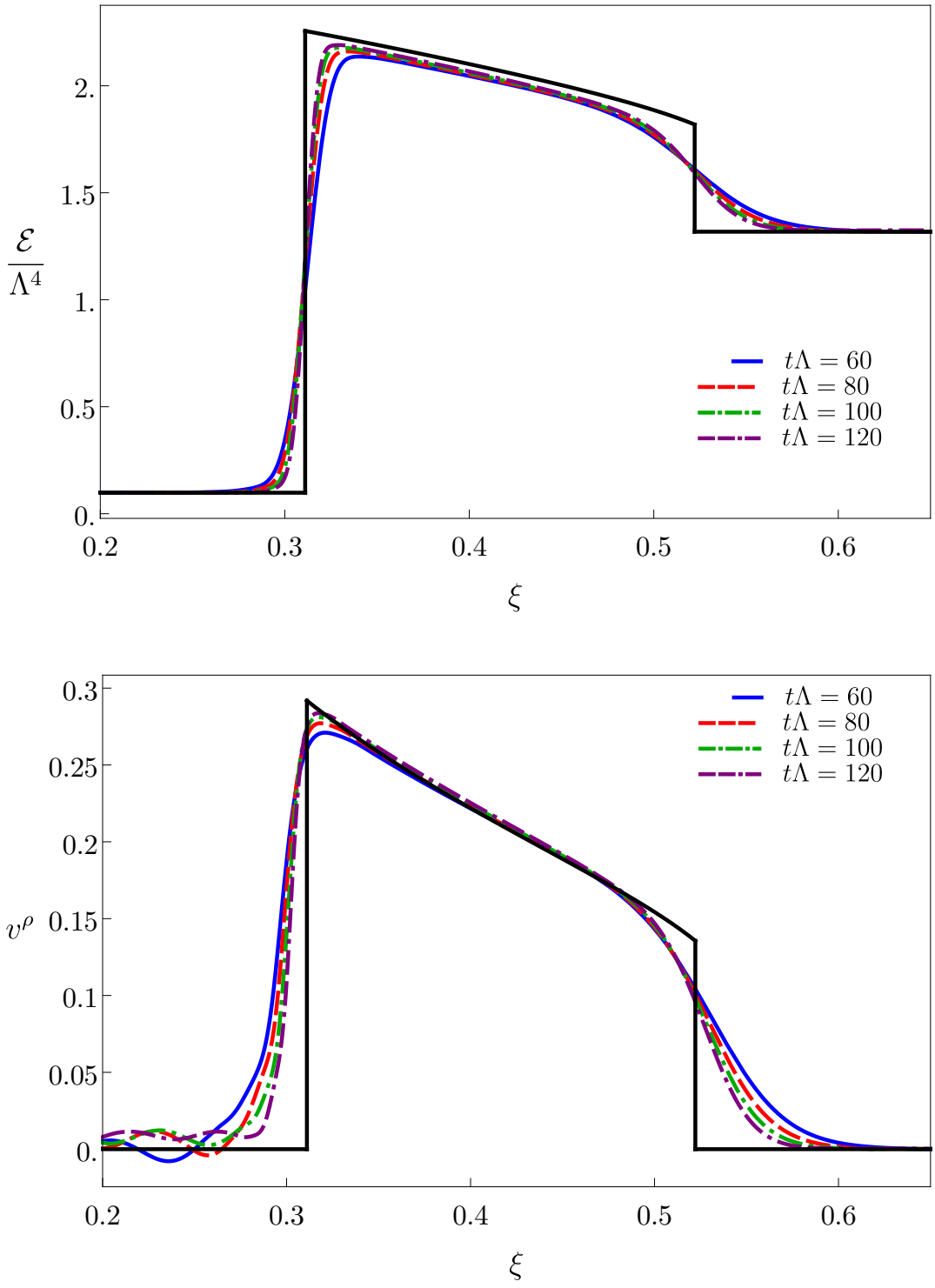

Figure 5.22: Energy density (top) and fluid velocity (bottom) profiles for different simulation times as a function of the scaling variable (5.12). The black solid curves correspond to the ideal hydrodynamic prediction.

the hydrodynamic equations elsewhere, determine the entire bubble profile in terms of the energy density in A. This is the reason why a microscopic model is needed in order to determine the wall velocity. In our case, this model is provided by holography. Using the holographic prediction for $v_{\rm wall}$ as an input, we have solved the hydrodynamic equations plus the junction conditions and we have determined the profiles represented by the black solid lines in Fig. 5.22. The result is consistent with the holographic profiles at late times in the sense that the holographic curves approach the black curves more and more as time progresses.

Incidentally, these results allow us to define an analogue of "the state in front of the bubble wall" for planar bubbles. In the planar case the entire overheated region in front of the bubble has constant energy density and moves with constant fluid velocity v_D. Using this velocity one can boost the overheated region to its rest frame and thus define a state in the phase diagram of Fig. 5.1. This state was dubbed D, and the state in the overheated region was dubbed $D_{\rm boosted}$. The difference between A and D gives an intuitive idea of the intensity of the overheating in front of the wall, since in the absence of it we would have $A = D$. In the circular case we can obtain a similar idea by defining the state $D_{\rm boosted}$ in terms of the maximum values of the black solid curves in Fig. 5.22 as we approach the bubble wall discontinuity from the right. The values we obtain are

$$\mathcal{E}_{D_{\rm boosted}} = 2.26\Lambda^4\,, \qquad v_D = 0.292\,, \qquad \mathcal{E}_D = 2.06\Lambda^4\,. \tag{5.19}$$

The state D is represented by a black dot in Fig. 5.1.

5.5 Discussion

In this chapter we have presented a study of the dynamics of both planar and cylindrical bubbles in a strongly-coupled four-dimensional gauge theory. We have shown that our numerical code allows us to construct configurations that are arbitrarily close to this critical bubble. The fact that we can do this with a time evolution code by fine-tuning a single parameter (which we chose to be the radius of the bubble) is compatible with the fact that the space of perturbations of a critical bubble has only one unstable direction. Nevertheless, since the critical bubble is static, it would be interesting to find it by solving an elliptic 2D problem in AdS along the lines of Chapter 3. This would allow for an efficient exploration of the bubble properties for the entire range of temperatures on the metastable branch.

We have seen how both planar and cylindrical bubbles tend to a self similar profile at asymptotically late times, just as expected, veryfying that the cylindrical self similar profile possesses a richer structure than in the planar case. We have verified this by plotting our holographic result for the gauge theory stress tensor at late times as a function of the appropriate scaling variable. We have also compared the holographic result with the hydrodynamic approximation. As expected, we have found that hydrodynamics provides a good approximation everywhere except at the bubble wall.

For the planar case we have observed two very interesting features. The wall looks unique for a given theory up to trivial rescaling and the wall velocity depends linearly on the pressure jump across the bubble divided by the energy density asymptotically far. The latter quantity can be interpreted as the force leading the expansion divided by the resistance. As a future work it would be very interesting to check these features for cylindrical bubbles and try to conclude its possible generality in any number of dimensions.

Chapter 6

A new mechanism for Gravitational Wave production

In this last chapter we will explore in detail the possibility of the universe not undergoing the first order phase transition via the usual bubble nucleation, expansion and collision. On the contrary, we will argue that under certain conditions the universe will overcool all the way until it enters the spinodal, locally unstable region of the phase diagram. This will completely change the subsequent dynamical evolution, now dominated by the local instability, and, as a consequence, the Gravitational Wave spectrum that one would expect to detect by next generation interferometers.

6.1 The theory

6.1.1 Gauge theory thermodynamics

For this chapter we turn back to our original choice of parameters for the gravity scalar potential (2.3): $\lambda_4 = -1/4$ and $\lambda_6 = 0.1$. We have already derived all the thermodynamics previously, but we will nevertheless summarize the main results in what follows, giving emphasis to the features that will be relevant for the rest of the chapter.

In the gauge theory we use Cartesian coordinates $\{t, x_i\} = \{t, x, y, z\}$ and work with energy density $\mathcal{E}$ and pressures $\mathcal{P}_i$ obtained by rescaling the stress tensor according to

$$\mathcal{E} = -\frac{\kappa_5^2}{2\ell^3}\langle T_t^t\rangle\,, \qquad \mathcal{P}_i = \frac{\kappa_5^2}{2\ell^3}\langle T_i^i\rangle\,, \tag{6.1}$$

with no sum over i on the right-hand side. In thermal equilibrium all pressures are equal, $\mathcal{P}_i = \mathcal{P}$, and the free energy density is $\mathcal{F} = -\mathcal{P}$. The stress tensor and the expectation of the scalar operator are related through the Ward identity

$$\langle T_\mu^\mu\rangle = -\Lambda\langle\mathcal{O}\rangle\,. \tag{6.2}$$

In treatments of the Electroweak transition it is common to separate the scalar degree of freedom associated to the expectation value of the Higgs field from the plasma degrees of freedom. In our treatment this is neither necessary nor natural, since the holographic stress tensor that we will determine in Sec. 6.3 includes the contribution of all degrees of freedom in the theory.

The thermodynamics of the gauge theory can be extracted from the homogeneous black brane solutions on the gravity side (see e.g. [114]). Fig. 6.1 shows the results for the free energy density (top) and the energy density (bottom) as a function of temperature. In Fig. 6.1(top) we see the familiar swallow-tail behaviour characteristic of the free energy for a first-order phase transition. In Fig. 6.1(bottom) this leads to the usual multivaluedness of the energy density as a function of temperature. At high and low temperatures there is only one phase available to

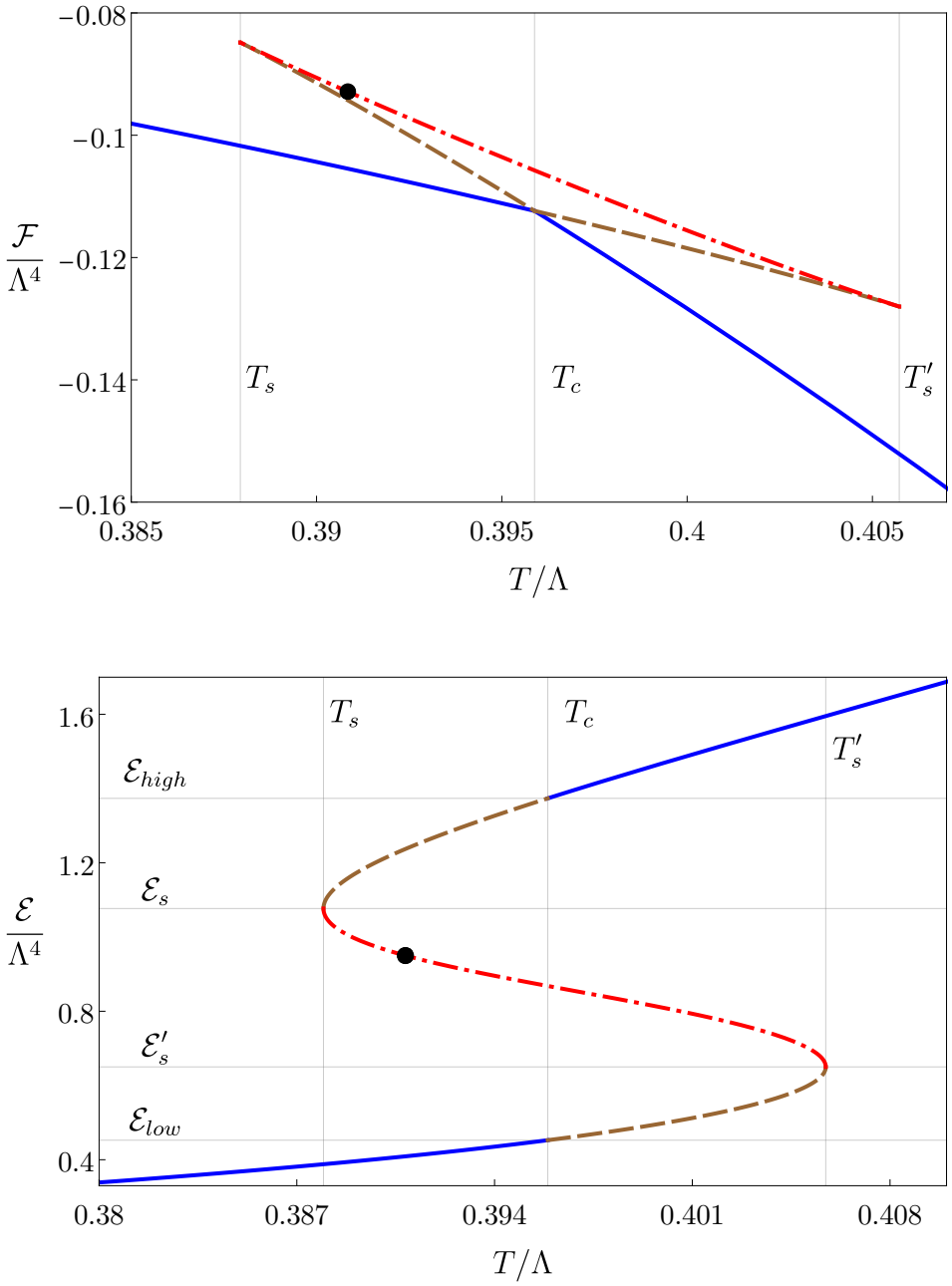

Figure 6.1: Free energy density (top) and energy density (bottom) of the four-dimensional gauge theory dual to (2.1-2.4). States on the solid, blue curves are thermodynamically stable. States on the dashed, brown curves are metastable. States on the dashed-dotted, red curve are unstable. The black circle with $T = 0.3908\Lambda$ indicates the initial state on which we will focus in this paper.

the system. Each of these phases is represented by a solid, blue curve. In Fig. 6.1(top) these two curves cross at a critical temperature

$$T_c = 0.396\Lambda\,. \tag{6.3}$$

At this point the state that minimizes the free energy moves from one branch to the other. The first-order nature of the transition is encoded in the non-zero latent heat, namely in the discontinuous jump in the energy density in Fig. 6.1(bottom) given by

$$\mathcal{E}_{\rm latent} = \mathcal{E}_{\rm high} - \mathcal{E}_{\rm low} = 0.92\,\Lambda^4\,. \tag{6.4}$$

Note that the phase transition is a transition between two deconfined, plasma phases, since both phases have energy densities of order N^2 and they are both represented by a black brane geometry with a horizon on the gravity side.

In a region

$$T_s = 0.3879\Lambda < T < T_s' = 0.4057\Lambda \tag{6.5}$$

around the critical temperature there are three different states available to the system for a given temperature. The thermodynamically preferred one is the state that minimizes the free energy, namely a state on one of the blue curves. The states on the dashed, brown curves are not globally preferred but they are locally thermodynamically stable, i.e. they are metastable. This follows from the convexity of the free energy, which indicates a positive specific heat

$$c_v \equiv \frac{d\mathcal{E}}{dT}\,. \tag{6.6}$$

This can be more clearly seen from the positive slope of the dashed, brown curves in Fig. 6.1(bottom). At the temperatures T_s and T_s' the metastable curves meet the dotted-dashed, red curve. States on the latter are locally unstable since their specific heat is negative. This region is known as the spinodal region.

In terms of an effective potential for the expectation value of the scalar operator, $\langle\mathcal{O}\rangle$, the region outside the range (T_s, T_s') corresponds to temperatures for which the potential has only one minimum and therefore there is a unique available state. In contrast, for temperatures within the range (T_s, T_s') the effective potential has two minima and one maximum. The global minimum corresponds to a stable state on a blue curve, the local but not global minimum corresponds to a metastable state on a brown curve, and the maximum corresponds to an unstable state on the red curve.

As anticipated, we see that the phase diagram in Fig. 6.1 is generic in the sense that there are no large ratios of energy densities, in contrast to e.g. [61, 63], where $\mathcal{E}_{\rm high}$ and $\mathcal{E}_{\rm low}$ differed by more than two orders of magnitude.

6.1.2 Spinodal instability

States on the dashed-dotted red curves of Fig. 6.1 are locally thermodynamically unstable since the specific heat is negative, $c_v < 0$. These states are also dynamically unstable. The connection with the dynamic instability was pointed out in an analogous context in [90] and it arises as follows. The speed of sound is related to the specific heat c_v and the entropy density s through

$$c_s^2 \equiv \frac{d\mathcal{P}}{d\mathcal{E}} = \left(\frac{d\mathcal{P}}{dT}\right)\left(\frac{d\mathcal{E}}{dT}\right)^{-1} = \frac{s}{c_v}\,. \tag{6.7}$$

Since the entropy density is positive everywhere, c_s^2 is negative on the dashed-dotted, red curves of Fig. 6.1, as shown in Fig. 6.2(top), and consequently c_s is purely imaginary. The amplitude of long-wave length, small-amplitude sound modes behaves as

$$\mathcal{A} \sim e^{-i\omega(k)t}\,, \tag{6.8}$$

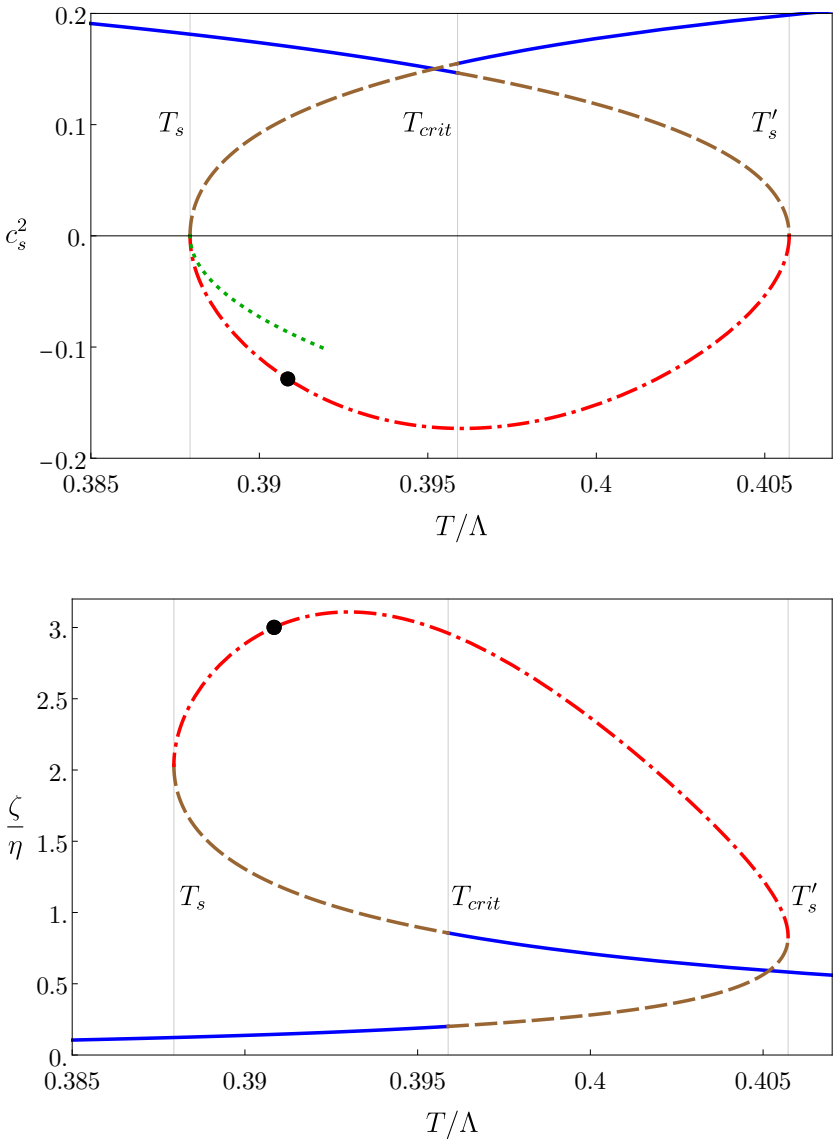

Figure 6.2: Speed of sound squared (top) and ratio of the bulk viscosity over the shear viscosity (bottom) versus temperature for the gauge theory dual to (2.1-2.4). The color coding is as in Fig. 6.1. The dotted, green curve in the top figure corresponds to the approximation (6.19).

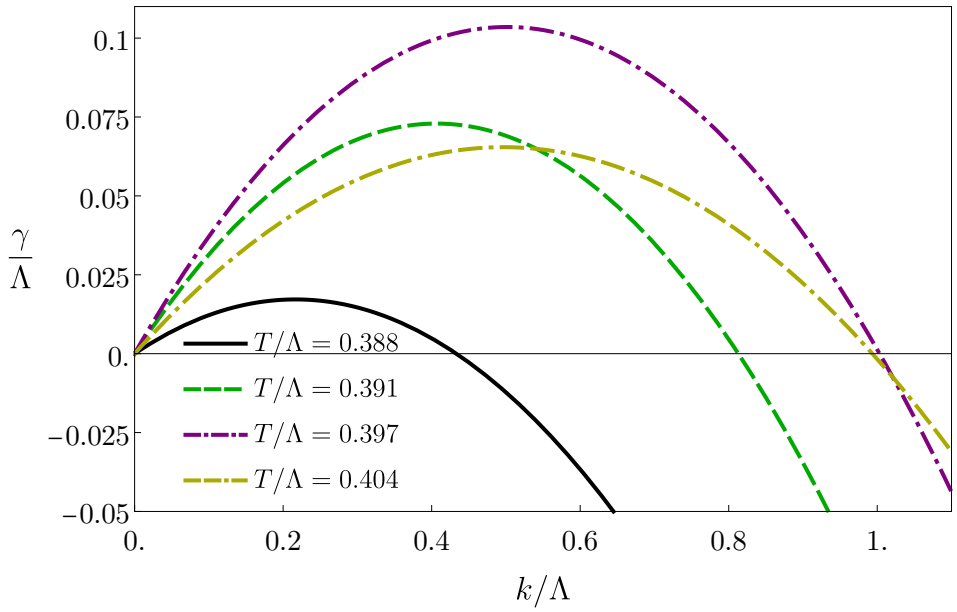

Figure 6.3: Hydrodynamic approximation to the growth rates $\gamma(k)$ for different states on the spinodal region of Fig. 6.1.

with a dispersion relation given by (see e.g. Appendix A of [63] for the derivation)

$$\omega_{\pm}(k) = \pm\, c_s k - \frac{i}{2}\Gamma k^2 + O(k^3)\,. \tag{6.9}$$

We emphasize that, as indicated, this expression is an expansion valid at low momentum. In other words, it is a hydrodynamic approximation to the exact dispersion relation; we will come back to this point in Sec. 6.3. The plus sign corresponds to an unstable mode, while the minus sign leads to a stable mode. In this expression

$$\Gamma = \frac{1}{T}\left(\frac{4}{3}\frac{\eta}{s} + \frac{\zeta}{s}\right) \tag{6.10}$$

is the sound attenuation constant, and η and ζ are the shear and bulk viscosities, respectively. In our model $\eta/s = 1/4\pi$ [118]. We compute ζ numerically following [119] and we show the result in Fig. 6.2(bottom).

An imaginary value of c_s leads to a purely real value of the growth rate

$$\gamma(k) \equiv -i\omega(k)\,. \tag{6.11}$$

For small momenta (6.9) yields for the unstable mode

$$\gamma(k) = |c_s|\, k - \frac{1}{2}\Gamma k^2 + O(k^3)\,. \tag{6.12}$$

We see that, in this hydrodynamic approximation, the dispersion relation gives rise to the familiar parabolas displayed in Fig. 6.3. As illustrated by this figure, these curves depend on the energy density $\mathcal{E}$ of the state under consideration because both c_s and Γ depend on $\mathcal{E}$. Working to order k^2 we see that the growth rate is positive for momenta in the range $0 < k < k_*$ with

$$k_*^{\rm hyd} \simeq \frac{2\,|c_s|}{\Gamma}\,, \tag{6.13}$$

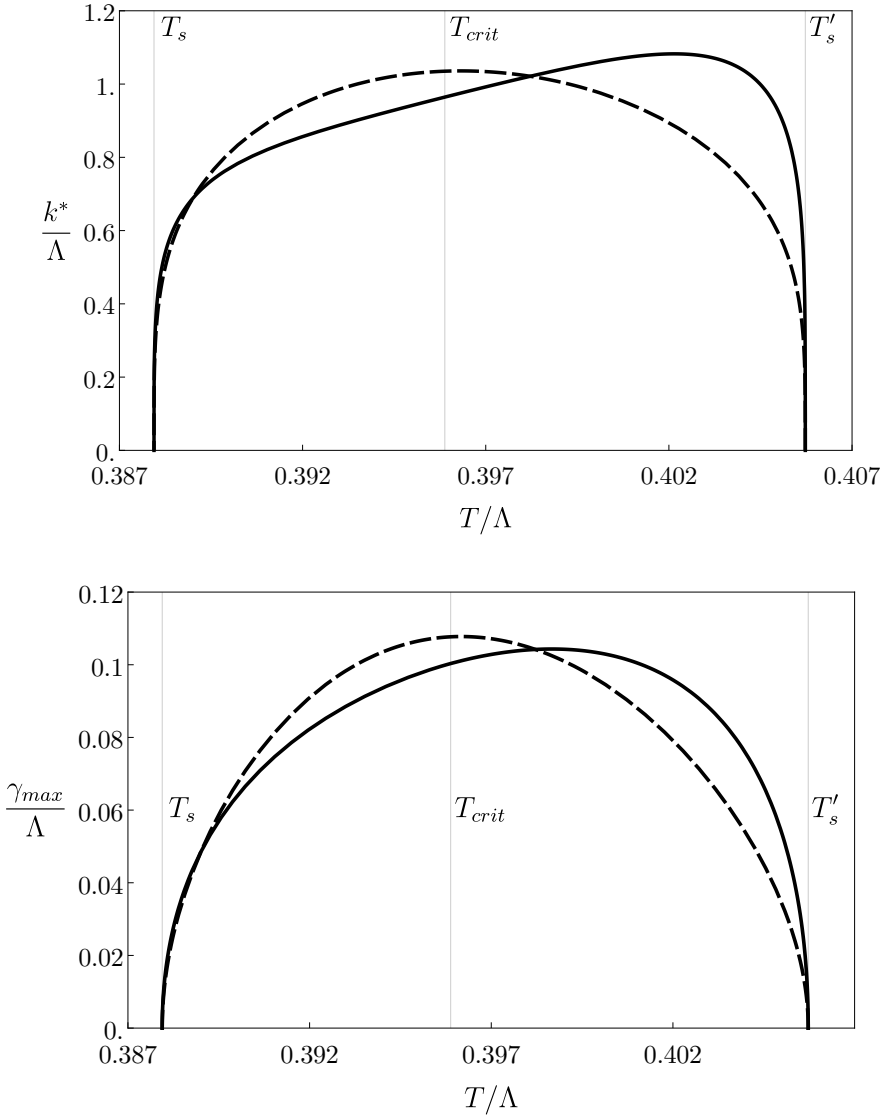

Figure 6.4: Comparison between the hydrodynamic values of k_* (top) and $\gamma_{\max}$ (bottom) given by (6.12) (solid curves) and the ball-park estimates (6.16) (dashed curves).

where the superscript is to emphasize that this is the hydrodynamic approximation to the exact value. We see that the spinodal instability is an infrared instability, since only modes with momentum below a certain threshold are unstable. The most unstable mode, namely the mode with the largest growth rate, has momentum and growth rate given by

$$k_{\max}^{\rm hyd} \simeq \frac{|c_s|}{\Gamma}\,, \qquad \gamma_{\max}^{\rm hyd} \simeq \frac{|c_s|^2}{2\Gamma}\,. \tag{6.14}$$

A ballpark estimate for these quantities can be obtained by using $\eta/s = 1/4\pi$ and approximating $\zeta/\eta \sim 2$ in the spinodal region, which implies

$$\Gamma \sim \frac{1}{\pi T}\,. \tag{6.15}$$

Under these conditions

$$k_*^{\rm hyd} \sim 2\,|c_s|\,\pi T\,, \qquad k_{\max}^{\rm hyd} \sim |c_s|\,\pi T\,, \qquad \gamma_{\max}^{\rm hyd} \sim \frac{1}{2}\,|c_s|^2\,\pi T\,. \tag{6.16}$$

Note that

$$\gamma_{\rm max}^{\rm hyd} = \frac{1}{2}\,|c_s|\,k_{\rm max}^{\rm hyd}\,. \tag{6.17}$$

As mentioned above, these quantities depend on the energy density $\mathcal{E}$ of the state under consideration. In particular, they all go to zero as the state on the spinodal branch approaches one of the turning points at $T = T_s, T_s'$, since at those points $c_s = 0$. As the state moves away from these points towards the interior of the spinodal region these quantities increase and reach a maximum. This is illustrated in Fig. 6.4, where we compare the values of k_* and $\gamma_{\rm max}$ given by (6.12) with those given by the estimates (6.16). We see that the latter provide a reasonable approximation in the entire range, and that this is better close to the turning points, which will be a particularly important region below. The maxima of, and the points where, the curves in Fig. 6.3 cross the horizontal axis are consistent with the values of k_* and $\gamma_{\rm max}$ in Fig. 6.4. Rotating Fig. 6.1 ninety degrees we see that, close to the turning point at T_s, the temperature has a minimum as a function of the energy density. This means that, close to this point,

$$T - T_s \sim (\mathcal{E} - \mathcal{E}_s)^2\,. \tag{6.18}$$

Inverting this relation, computing the specific heat (6.6), and substituting in (6.7) we find that, close to T_s,

$$c_s^2 \simeq \frac{1}{\sqrt{T_s}}\sqrt{T - T_s} + \cdots\,, \tag{6.19}$$

where we have estimated the prefactor based on dimensional analysis. This approximation to the function $c_s^2(T)$ is shown as a green, dashed curve in Fig. 6.2(top).

We emphasize again that the analysis in this section is based on a hydrodynamic approximation to the dispersion relation. In Sec. 6.3 we will determine the exact dispersion relation and, in particular, the exact values of $k_*, k_{\rm max}$ and $\gamma_{\rm max}$. For concreteness, in several places in the paper we will use the hydrodynamic dispersion relation $\gamma(k)$ since it has the advantage that it is analytically known. Nevertheless, most final results will only depend on $k_*^{\rm hyd}, k_{\rm max}^{\rm hyd}, \gamma_{\rm max}^{\rm hyd}$ and $|c_s|$. In these cases one can obtain the exact result by simply replacing

$$k_*^{\rm hyd} \to k_*\,, \qquad k_{\rm max}^{\rm hyd} \to k_{\rm max}\,, \qquad \gamma_{\rm max}^{\rm hyd} \to \gamma_{\rm max}\,, \qquad |c_s| \to \frac{2\gamma_{\rm max}}{k_{\rm max}}\,. \tag{6.20}$$

To summarize this section, states on the dashed, red curves of Fig. 6.1 are afflicted by a dynamical instability, known as spinodal instability, whereby long-wave length, small-amplitude perturbations in the sound channel grow exponentially in time. The growth rate of the unstable modes is zero at the turning points and increases as the state moves deeper into the spinodal region.

6.2 Dynamics of a first-order phase transition

We will now discuss the conditions for the phase transition to take place via the spinodal instability. An important observation is that the expansion of the Universe may not be driven by the same sector that undergoes the phase transition. In particular, the temperatures in these two sectors may be vastly different. This may happen if the phase transition takes place in a hidden sector. If the hidden sector couples weakly to the inflaton, then the energy density injected into this sector at the end of reheating, and hence its temperature, may be vastly smaller than in the visible, SM sector. Therefore in the following we will distinguish between the temperature T of the sector undergoing the phase transition and the radiation temperature $T_{\rm rad}$ driving the expansion of the Universe. If the phase transition takes place in the sector driving the expansion then these two temperatures coincide, otherwise they may differ.

6.2.1 Suppressed bubble nucleation

We imagine that the sector where the phase transition will take place starts off in the high-temperature, stable branch represented by the upper blue, solid curve in Fig. 6.1(bottom). As the Universe cools down the temperature falls below T_c and we enter the metastable branch. Bubbles of the stable phase represented by the lower blue, solid curve in Fig. 6.1(bottom) can then begin to nucleate. This process requires thermal fluctuations large enough to decrease the energy density from the metastable phase to the stable phase in a finite region of space with a volume equal to that of the critical bubble. The larger the number of degrees of freedom that participate in the transition the more unlikely these fluctuations are, the more suppressed the bubble nucleation rate becomes, and the closer to T_s bubbles begin to be effectively nucleated. Under these circumstances there are two crucial aspects that are often overlooked in usual treatments. First, the nucleated bubbles are very small both in size and in amplitude and hence they need time to grow to the point where the energy density in their interior reaches that of the stable phase. Second, there is a finite available time for the transition. Under these conditions the arguments usually employed to compute the duration of the transition are misleading. We will therefore repeat the standard calculation paying attention to these two aspects. In order to be concrete about the large number of degrees of freedom involved in the transition we will assume that the theory in question is a large-N gauge theory. We will see that if N is sufficiently large then the transition cannot be completed via bubble nucleation. Instead, the temperature eventually reaches T_s and the Universe enters the spinodal region. Recent analyses of bubble dynamics in large-N gauge theories include [120, 121].

We follow the discussion in Sec. 7.1 of [11]. The starting point is the expression for the fraction of the volume of the Universe that remains in the metastable phase of the sector undergoing the phase transition. Let t_c the time at which the temperature of this sector crosses T_c. Then at a time $t > t_c$ this fraction is

$$h(t) = e^{-I(t)} \,, \tag{6.21}$$

with

$$I(t) = \int_{t_c}^{t} dt' \, \frac{4\pi}{3} v^3 (t - t')^3 \, \frac{\Gamma(t')}{V} \,. \tag{6.22}$$

In this expression v is the bubble wall terminal velocity. The integrand is the volume of a bubble nucleated at time $t' < t$ multiplied by the bubble nucleation rate per unit volume, which takes the form

$$\frac{\Gamma(T)}{V} \sim T^4 \, e^{-S(T)} \,. \tag{6.23}$$

Here $S(T)$ is the action of the instanton that mediates the transition, namely the critical bubble, and $\Gamma(T)$ should not be confused with the sound attenuation constant (6.10). Eqn. (6.22) assumes that the interior of a nucleated bubble is instantaneously in the stable phase, and that the bubble wall instantaneously begins to move with the corresponding terminal velocity v. We will come back to this below.

Let t_s be the time at which the temperature in the sector undergoing the phase transition reaches T_s. Below we will be interested in evaluating the fraction $h(t)$ at the latest possible time, namely at $t = t_s$. A crucial point is that the instanton action must vanish at the turning point, since there the barrier to nucleate bubbles disappears. Therefore, close to this point we have

$$S(T) \sim N^2 \left(\frac{T - T_s}{T_s} \right)^x \,, \tag{6.24}$$

where x is a constant with typical values $x \sim 3/2$ [122] and we have explicitly displayed the N^2 scaling of the action expected for a large-N gauge theory. Unless T is very close to T_s this scaling makes the instanton action very large, which in turn makes Γ and I exponentially close

to zero, which makes h exponentially close to one. Let us define the nucleation temperature, T_n, as the temperature at which this suppression disappears, namely the temperature at which

$$S(T_n) \sim 1\,. \tag{6.25}$$

This is given by

$$T_n = T_s + \frac{T_s}{N^{2/x}}\,. \tag{6.26}$$

Up to logarithmic corrections, this is also the temperature at which one bubble per Hubble time per Hubble volume is nucleated, namely the temperature such that

$$\frac{\Gamma(T_n)}{V} \sim H^4\,. \tag{6.27}$$

As the Universe cools down, the temperature drops below T_c, but the phase transition does not start until the time $\theta_{(n)}$ at which the temperature reaches $T_n < T_c$. The remaining available time for the phase transition to take place is therefore

$$\Delta t \,=\, t_{\rm s} - \theta_{(n)} = \frac{1}{HT_s}\,(T_n - T_s) \sim \frac{1}{HN^{2/x}}\,, \tag{6.28}$$

where we have used the usual relation to translate between time and temperature

$$\frac{dt}{dT} = -\frac{1}{TH}\,. \tag{6.29}$$

Note that the Hubble rate H is controlled by $T_{\rm rad}$ through the Friedmann equation

$$H^2 \sim G T_{\rm rad}^4 \sim \frac{T_{\rm rad}^4}{M_p^2}\,, \tag{6.30}$$

where G is the four-dimensional Newton's constant and M_p is the (reduced) Planck mass. Recall that $T_{\rm rad}$ may or may not coincide with T.

The key point is that, because T_n is parametrically close to T_s, the bubbles that get nucleated are small bubbles that do not have the stable phase at their center. On the contrary, as T_n approaches T_s, the energy density at the centre of the nucleated bubbles approaches the energy density of the metastable phase [122]. These bubbles need a certain time to grow in size and in amplitude until the energy density at their centre reaches that of the stable phase. If this time is too long compared to the available time (6.28) then no volume will be occupied by the stable phase when the system reaches the spinodal region. Since the critical bubbles are unstable, we expect their growth to be of the form $\exp(\gamma t)$. A natural estimate for the growth rate is $\gamma \sim T_s \sim T_c$, since we expect this to be set by a microscopic scale. Comparing the growth time γ^{-1} to Δt we see that the condition that the transition does not take place, $\gamma^{-1} \gtrsim \Delta t$, translates into

$$N^{2/x} \gtrsim \frac{T_c}{H} \sim \frac{T_c\, M_p}{T_{\rm rad}^2}\,, \tag{6.31}$$

where in the second equation we have used (6.30).

Before we analyse the condition (6.31), we note that, if it is not satisfied, then the transition does take place via bubble nucleation. In this case the growth time of the bubbles is short compared to Δt and we can neglect it. We can also neglect the time it takes the bubbles to accelerate to their terminal velocity v, since presumably this time is also of order $1/T_c$. We can then evaluate what fraction of the volume has been converted to the stable phase between the times $\theta_{(n)}$ and $t_{\rm s}$. For this purpose we use (6.23) and (6.24) in (6.22) and we change the integration variable from time to temperature according to

$$t_{\rm s} - t' = \frac{1}{HT_s}\,(T' - T_s)\,. \tag{6.32}$$

The result is

$$I(T_s) = \left(\frac{4\pi}{3}v^3\right)\left(\frac{T_s}{H}\right)^4 \int_{T_s}^{T_n} \frac{dT'}{T_s}\left(\frac{T'-T_s}{T_s}\right)^3 \exp\left[-N^2\left(\frac{T'-T_s}{T_s}\right)^x\right] . \tag{6.33}$$

Because of the exponential suppression we can extend the integral to $T_n \to \infty$. Changing variables through

$$y = \frac{T'-T_s}{T_s} \tag{6.34}$$

we then get

$$I(T_s) = \left(\frac{4\pi}{3}v^3\right)\left(\frac{T_s}{H}\right)^4 \int_0^\infty dy\, y^3 \exp\left(-N^2 y^x\right) . \tag{6.35}$$

The integral can be performed explicitly and we arrive at

$$I(T_s) = \left(\frac{4\pi}{3}v^3\right)\left(\frac{T_s}{H}\right)^4 \frac{1}{N^{8/x}}\frac{\Gamma(4/x)}{x} . \tag{6.36}$$

Focussing on the parametric dependence we see that the condition for $I(T_s) \lesssim 1$ is the same as (6.31).

Eqn. (6.31) shows that the transition via bubble nucleation can always be prevented if N is sufficiently large. This is simply a consequence of the fact that the time available for the transition decreases parametrically with N and that the nucleated bubbles near T_s need a finite amount of time to grow to the stable phase. To estimate the value of N we must distinguish two cases. If the expansion of the Universe is driven by the same sector undergoing the phase transition then $T_{\rm rad} = T_c$. This results in a fairly large value of N unless $T_{\rm rad}$ is close to M_p. For example, for a phase transition at a GUT scale this ratio is $M_p/T_c \sim 10^2$, which gives $N \gtrsim 7$, whereas for a transition at the electroweak scale we have $M_p/T_c \sim 10^{16}$, resulting in $N \gtrsim 10^6$. Suppose instead that the transition takes place in a hidden sector at a temperature $T_c < T_{\rm rad}$, as would be the case if this sector couples to the inflaton more weakly than the SM degrees of freedom. In this case the condition to suppress bubble nucleation results in mild constraints on the parameters of the hidden sector for two reasons. First, large values of N are natural, since string theory compactifications can give rise to gauge-group ranks as large as $O(10^5)$ [123–126]. Second, even if N is of order unity the condition (6.31) only requires $T_c \lesssim T_{\rm rad}^2/M_p$, which still results in a huge range of possible values for T_c.

6.2.2 Thermal inflation

When the Universe enters the metastable branch it is initially undergoing decelerated expansion, since it is radiation-dominated. We have seen that if N is large enough then the Universe will supercool along the metastable branch until it enters the spinodal branch. Along this process the Universe may or may not enter a period of thermal inflation [127, 128], namely a period of accelerated expansion. Although in our model (2.1)-(2.2) with the choice of parameters (2.4) this does not happen, we will now show that it would happen for other choices of the parameters.

Whether thermal inflation takes place depends on the equation state of the model, specifically on the sign of the combination $\mathcal{E} + 3\mathcal{P}$. If this becomes negative along the metastable branch then the acceleration of the Universe becomes positive and we enter a period of inflation. This can be equivalently characterized in terms of the ratio $w = \mathcal{P}/\mathcal{E}$. If $w < -1/3$ then the Universe inflates. Further, if $w = -1$ then the Universe inflates exponentially.

The combination $\mathcal{E}+3\mathcal{P}$ for the model (2.1-2.2) with the choice of parameters (2.4) is shown in Fig. 6.5. We see that it is positive everywhere and hence there is no period of thermal inflation. Nevertheless, this same model can lead to thermal inflation for other choices of the parameters. In other words, by varying these parameters we can continuously interpolate between models with and without thermal inflation. To see this let us keep $\lambda_6 = 0.1$ fixed and vary λ_4, as in

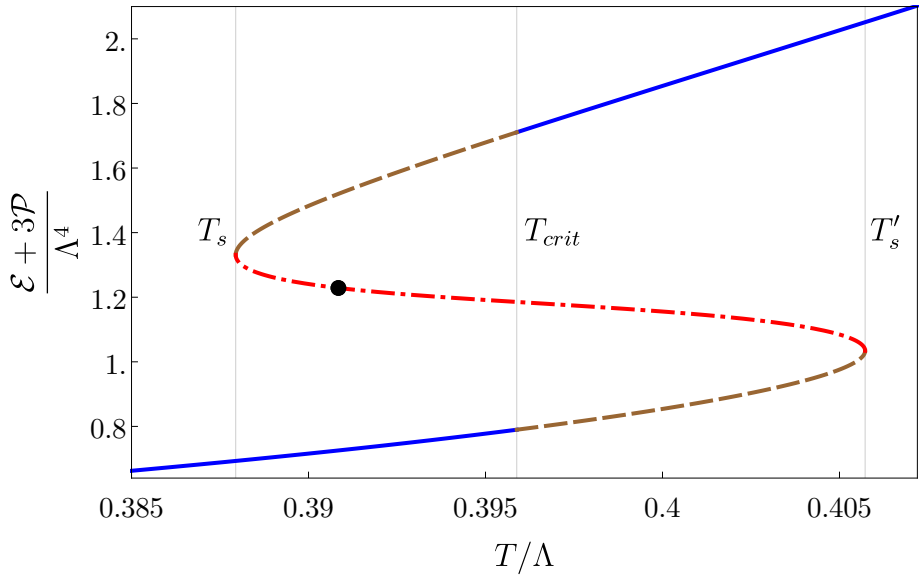

Figure 6.5: Energy density plus three times the pressure for the four-dimensional gauge theory dual to (2.1-2.2) with the choice of parameters (2.4).

[58]. The results for $\lambda_4 = -0.39$, $\lambda_4 = -0.61$ and $\lambda_4 = -0.74$ are illustrated in Figs. 6.6, 6.7 and 6.8, respectively.

In Fig. 6.6 we see that $\mathcal{E} + 3\mathcal{P}$ attains a smaller value than in the case $\lambda_4 = -0.25$, but it remains positive. Similarly, w remains above $-1/3$. In contrast, Fig. 6.7 shows that $\mathcal{E} + 3\mathcal{P}$ becomes negative in the lowest part of the upper metastable branch, which would lead to a period of thermal inflation. In fact, at the end of the metastable branch w comes close to the value that would lead to exponential inflation. Finally, in Fig. 6.8 the metastable branch extends all the way down to $T = 0$. This indicates that this theory possesses two vacua, a stable one with zero energy and a metastable one with non-zero energy. Since both are Lorentz-invariant, the pressure at the metastable one is exactly $\mathcal{P} = -\mathcal{E} \neq 0$ and therefore $w = -1$. The appearance of this metastable vacuum in the gauge theory is due to the appearance of an additional minimum in the scalar potential (2.3) on the gravity side [58].

The spinodal regions in Figs. 6.7 and 6.8 are slightly peculiar in that the specific heat becomes positive in the central region (the red, dotted part). This may seem to indicate that this region is locally stable. However, analysis of the quasi-normal modes on the gravity side reveals that this region is actually dynamically unstable [129], along the lines of [130]. In any case, this peculiar feature could be removed by considering a more general potential with more parameters while still interpolating between models with and without thermal inflation.

The two main messages from this section are as follows. First, supercooling does not necessarily lead to a period of thermal inflation. The former requires that bubble nucleation be sufficiently suppressed, whereas the latter requires that the metastable branch extend sufficiently close to $T = 0$. Our model illustrates this distinction clearly. Since it corresponds to a large-N gauge theory supercooling is always present, but whether thermal inflation takes place depends on the choice of parameters. Second, irrespectively of whether thermal inflation does or does not take place, the phase transition can still be completed, since the Universe can eventually enter the spinodal branch, whose dynamics we describe in the following section.

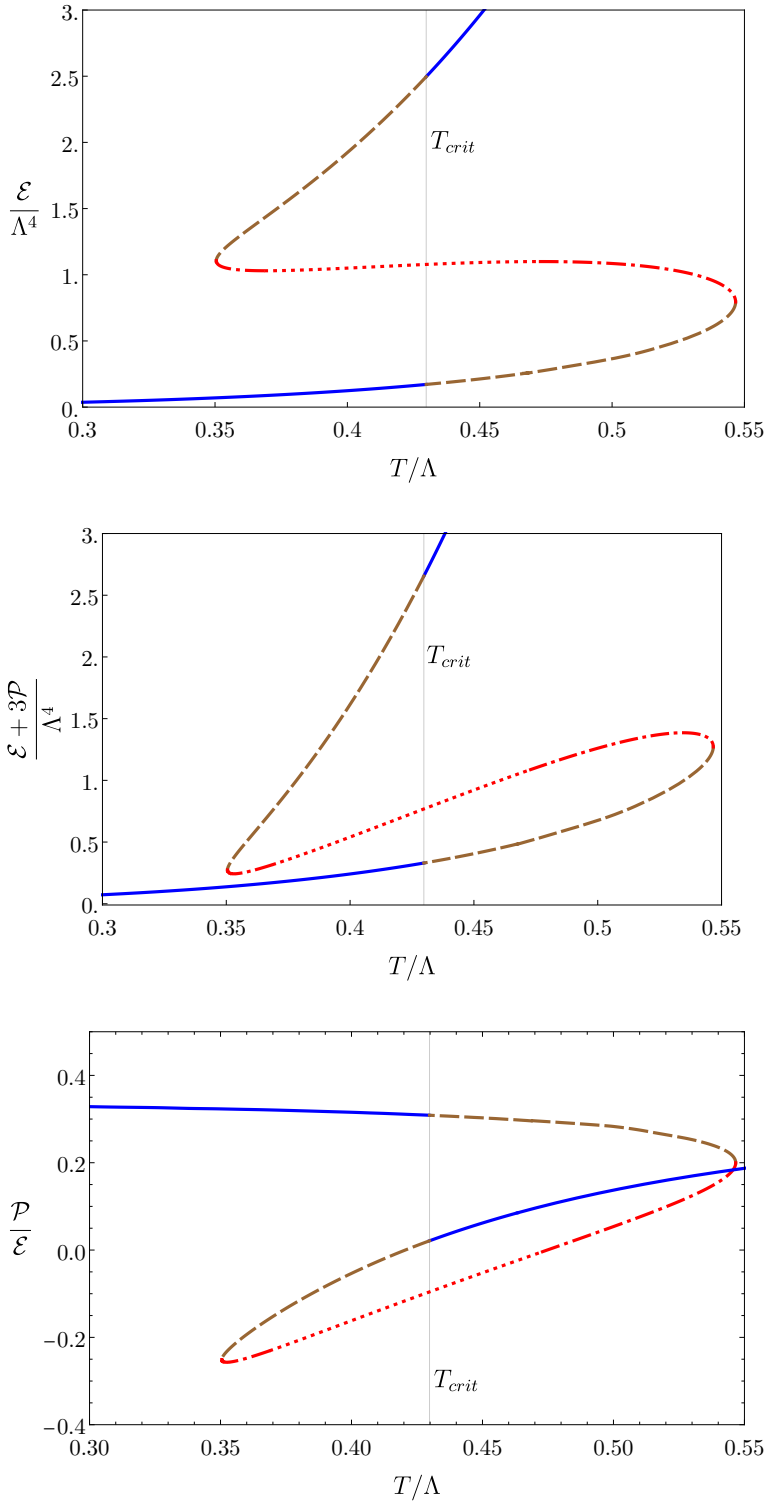

Figure 6.6: $\mathcal{E}$ (top), $\mathcal{E}+3\mathcal{P}$ (middle) and $\mathcal{P}/\mathcal{E}$ (bottom) for the four-dimensional gauge theory dual to (2.1-2.2) with the choice of parameters $\lambda_4 = -0.39, \lambda_6 = 0.1$ (Plots reproduced from [58].)

6.3 Initial state and time evolution

We have argued above that, if the bubble nucleation rate is sufficiently suppressed, then the Universe will roll down the metastable branch and enter the spinodal region. Slightly past this

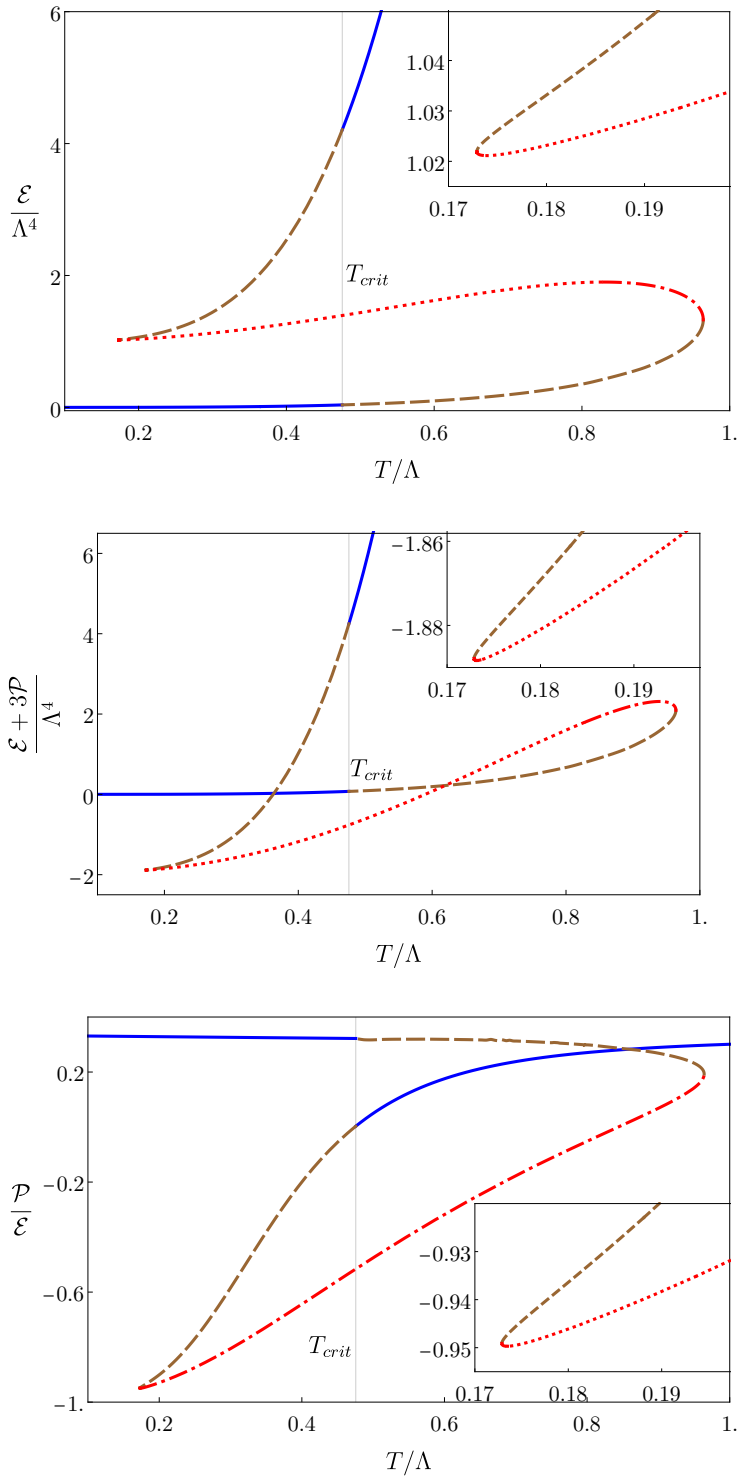

Figure 6.7: $\mathcal{E}$ (top), $\mathcal{E}+3\mathcal{P}$ (middle) and $\mathcal{P}/\mathcal{E}$ (bottom) for the four-dimensional gauge theory dual to (2.1-2.2) with the choice of parameters $\lambda_4 = -0.61, \lambda_6 = 0.1$ Note that the region close to T_s is smooth, not a cusp, as shown by the insets. (Plots reproduced from [58].)

point unstable modes can begin to grow. However, their growth rate, which is bounded from above by $\gamma_{\max}$, is initially very small compared to the expansion rate of the Universe, since precisely at $T = T_s$ we have $c_s = 0$ and hence $\gamma_{\max} = 0$ – see Fig. 6.4. Thus, the growth

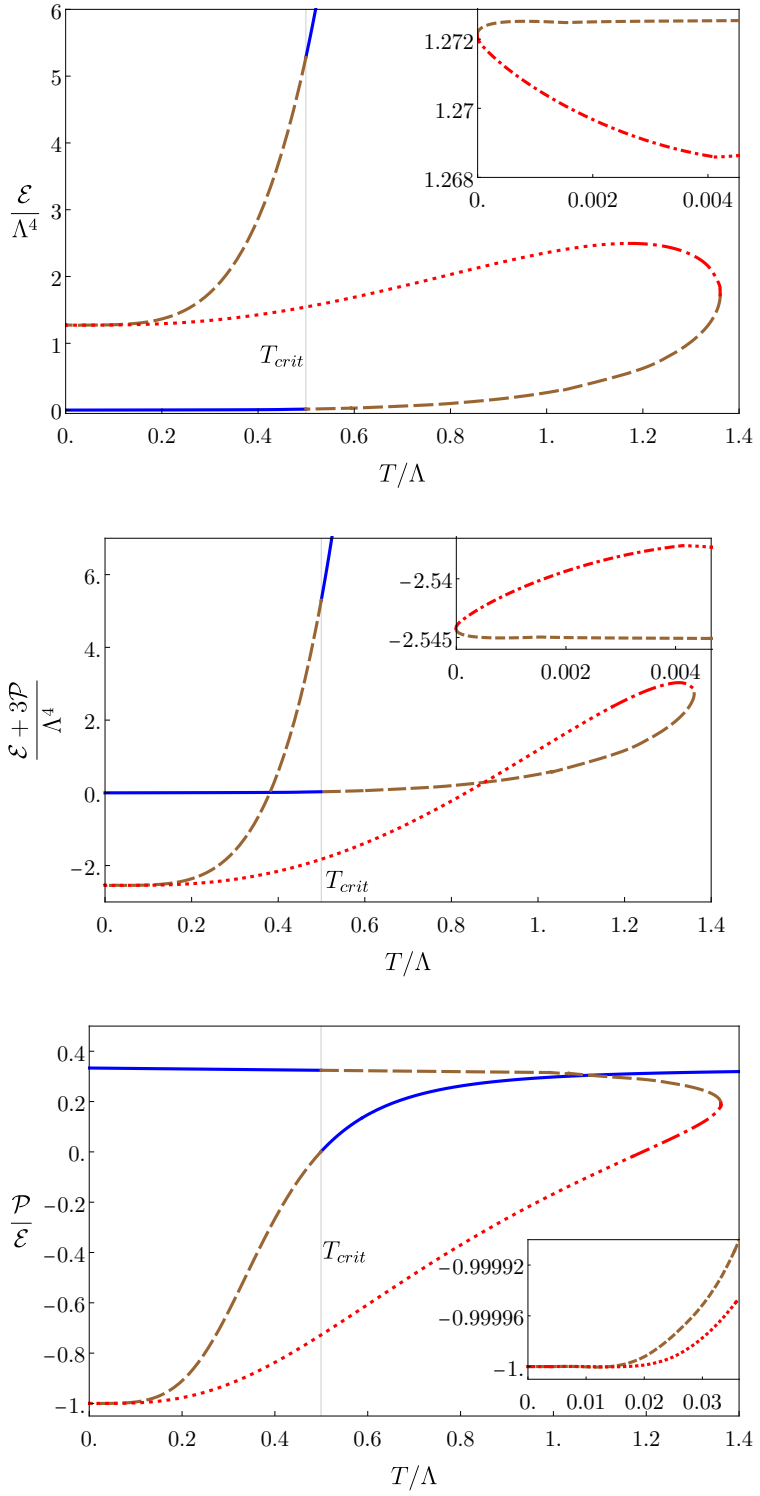

Figure 6.8: $\mathcal{E}$ (top), $\mathcal{E}+3\mathcal{P}$ (middle) and $\mathcal{P}/\mathcal{E}$ (bottom) for the four-dimensional gauge theory dual to (2.1-2.2) with the choice of parameters $\lambda_4 = -0.74, \lambda_6 = 0.1$ (Plots reproduced from [58].)

becomes important when the Universe has moved far enough along the spinodal branch so that $\gamma_{\max} \sim H$. Let T_g be the "growth temperature" at which this happens. Since in the next few paragraphs we are only interested in parametric estimates we will not distinguish between the exact $\gamma_{\max}, k_{\max}$, etc and their hydrodynamic approximations. Using the parametric dependence

(6.16) we then have that T_g is determined by the condition

$$\gamma_{\rm max}(T_g) \sim |c_s(T_g)|^2 \, T_g \sim H \,. \tag{6.37}$$

In order to proceed we must distinguish three cases depending on the hierarchy between T_g and H. We recall again that T_g refers to the temperature in the sector undergoing the phase transition, which may or may not coincide with the temperature in the sector driving the expansion, $T_{\rm rad}$.

If $H \gg T_g$ then the unstable modes do not have time to grow unless $|c_s|^2$ is parametrically large. This means that the Universe can traverse the spinodal region without the instability having a significant effect, so we will not consider this case further.

If $T_g \sim H$ then we must have $|c_s(T_g)| \sim 1$ and the modes that will dominate the exponential growth will have momenta $k_{\rm max}$ that, by virtue of (6.16), is given by

$$k_{\rm max} \sim T_c \sim H \,, \tag{6.38}$$

where on the right-hand side we have approximated $T_g \sim T_c$. A necessary condition for this case to occur is that the transition takes place in a hidden sector with $T_c \sim H \ll T_{\rm rad}$.

If the transition takes place in the sector driving the expansion then $T_g \sim T_{\rm rad}$ and $H \ll T_g$. In this case $|c_s(T_g)|^2 \ll 1$ and we can use in (6.37) the approximation for the speed of sound (6.19) to obtain

$$T_g - T_s \simeq \frac{H^2}{T_s} \,. \tag{6.39}$$

The time it takes for this change in temperature is parametrically small, since using (6.29) we can translate (6.39) into

$$t_g - t_{\rm s} \simeq \frac{H}{T_s^2} \,. \tag{6.40}$$

Using again the parametric dependence (6.16) we see that in this case the modes that will dominate the exponential growth will have momenta

$$k_{\rm max} \simeq \sqrt{\frac{H}{T_c}}\, T_c \,, \tag{6.41}$$

which satisfies

$$H \ll k_{\rm max} \ll T_c \,. \tag{6.42}$$

where on the right-hand side of the last two equations we have approximated $T_g \sim T_c$.

In order to simulate the evolution numerically we need to choose a specific value of T_g. As we will discuss below, we expect the results to be qualitatively similar for any choice. We will choose the value $T_g = 0.3908\Lambda$, which differs from T_s by about 1%. In other words, we choose the initial state to be the one indicated by the black circle in Fig. 6.1. For this state the hydrodynamic values of the key quantities introduced in Sec. 6.1.2 are

$$k_*^{\rm hyd} = 0.81\Lambda \,, \qquad k_{\rm max}^{\rm hyd} = 0.41\Lambda \,, \qquad \gamma_{\rm max}^{\rm hyd} = 0.073\Lambda \,. \tag{6.43}$$

We then imagine that small thermal fluctuations on top of this homogeneous state trigger the instability. Since the dynamics is dominated by the unstable modes, and since their typical momentum is $k \lesssim T$ according to (6.38) and (6.42), we will ignore the Boltzmann factor $\exp(-k/T)$ and assume that fluctuations with any k are equally likely in the initial state. For simplicity, in this paper we will assume that all initial fluctuations start off with the same small amplitude $\delta\mathcal{E}/\mathcal{E} = 10^{-4}$. We will come back to this point in Sec. 6.5.

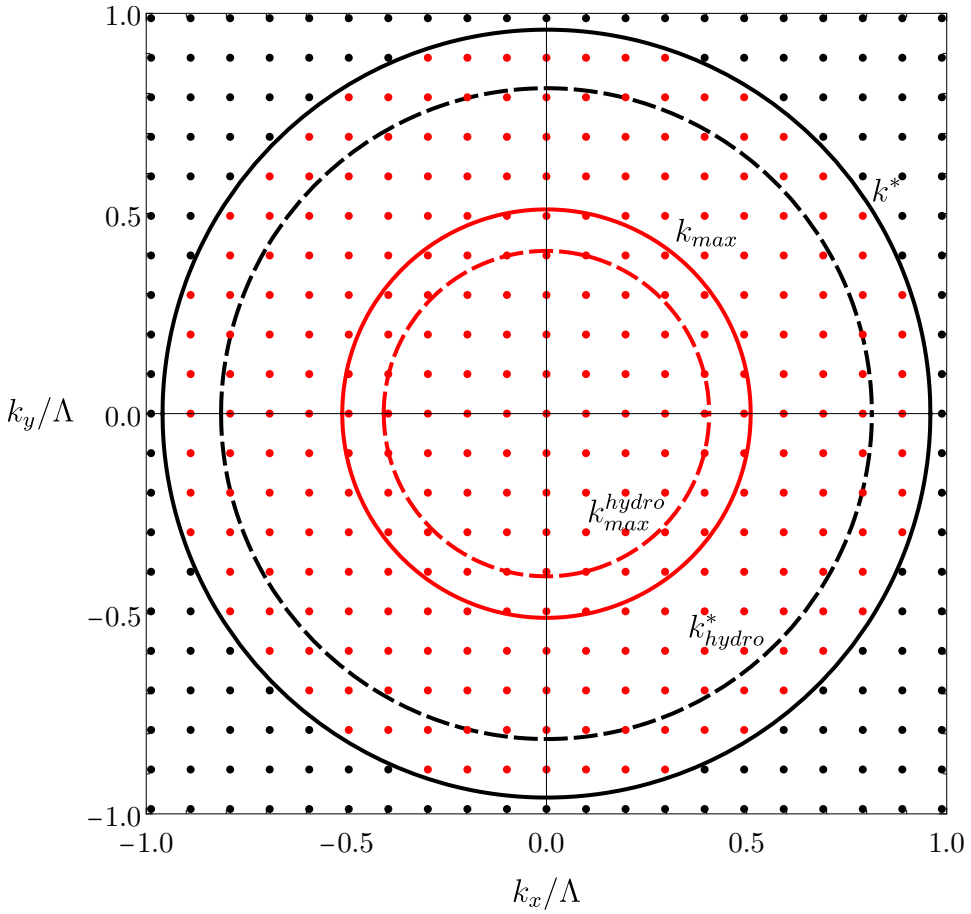

Figure 6.9: Allowed momenta in the (k_x, k_y)-plane. The solid curves indicate the exact values of k_* (black) and $k_{\rm max}$ (red) for the initial state under consideration, given in (6.47). The dashed curves indicate the hydrodynamic approximations to these quantities, $k_*^{\rm hyd}$ and $k_{\rm max}^{\rm hyd} = 0$, given in (6.43). Modes inside the black, solid circle are unstable. Within these, those with the largest growth rate are those on the solid, red circle.

We will allow for dynamics only along two of the three spatial directions of the gauge theory, which we call x, y. In other words, we impose translational symmetry along z. In addition, we compactify the x- and the y-directions on circles of equal lengths

$$L = 63.6\Lambda^{-1}\,, \tag{6.44}$$

namely we impose periodic boundary conditions on these coordinates. This infrared cut-off is technically convenient because it reduces the number of unstable sound modes to a finite number, since excitations along the x- and y-directions must have quantized momenta

$$(k_x, k_y) = \frac{2\pi}{L}\,(n_x, n_y)\,, \tag{6.45}$$

with n_x, n_y integer numbers. This means that the allowed momenta lie on a two-dimensional grid in the (k_x, k_y)-plane, as shown in Fig. 6.9, where the circles indicate the values k_* and $k_{\rm max}$ for the initial state under consideration. Although only modes with $n \leq 10$ are shown in the figure, we have included modes with up to $n = 50$ in the fluctuations of the initial state, all of them with amplitude $\delta\mathcal{E}/\mathcal{E} = 10^{-4}$. We have determined the corresponding time evolution by numerically evolving the Einstein-plus-scalar equations that follow from (2.1-2.4) using our new code [131].

From the near-boundary fall-off of the bulk fields we have extracted the boundary stress tensor. Snapshots of the resulting energy density are shown in Fig. 6.10. The interested reader can also find a video of this evolution at https://www.youtube.com/watch?v=qIhbpchr3gE.

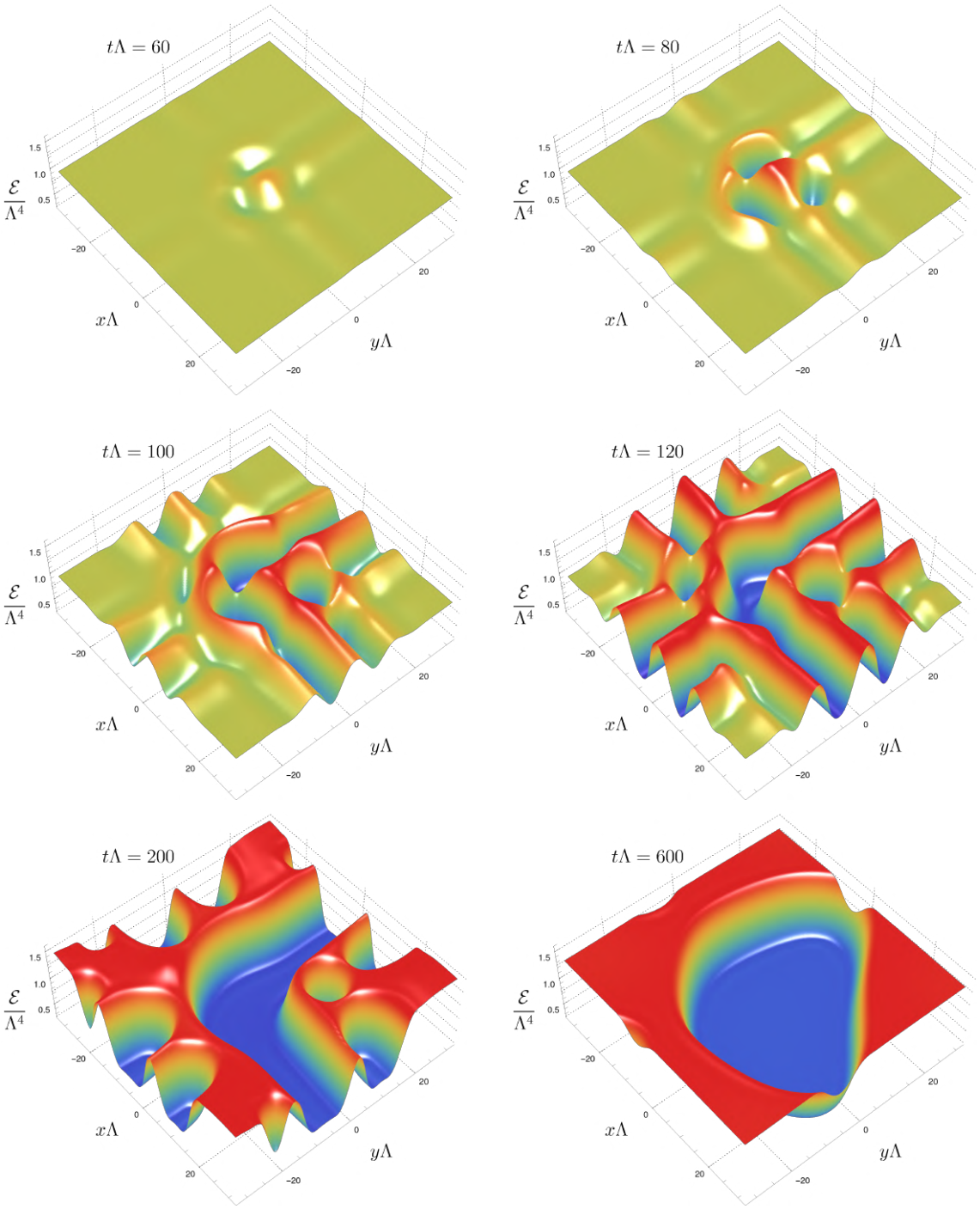

Figure 6.10: Spacetime evolution of the energy density for the initial homogeneous state in the spinodal region indicated by a black circle in Fig. 6.1, perturbed with small fluctuations. A video of the evolution can be found at https://www.youtube.com/watch?v=qIhbpchr3gE.

As explained above, the initial state includes high-momentum fluctuations with momenta up to

$$|k| = 50 \times \frac{2\pi}{L} \simeq 5k_* \,. \tag{6.46}$$

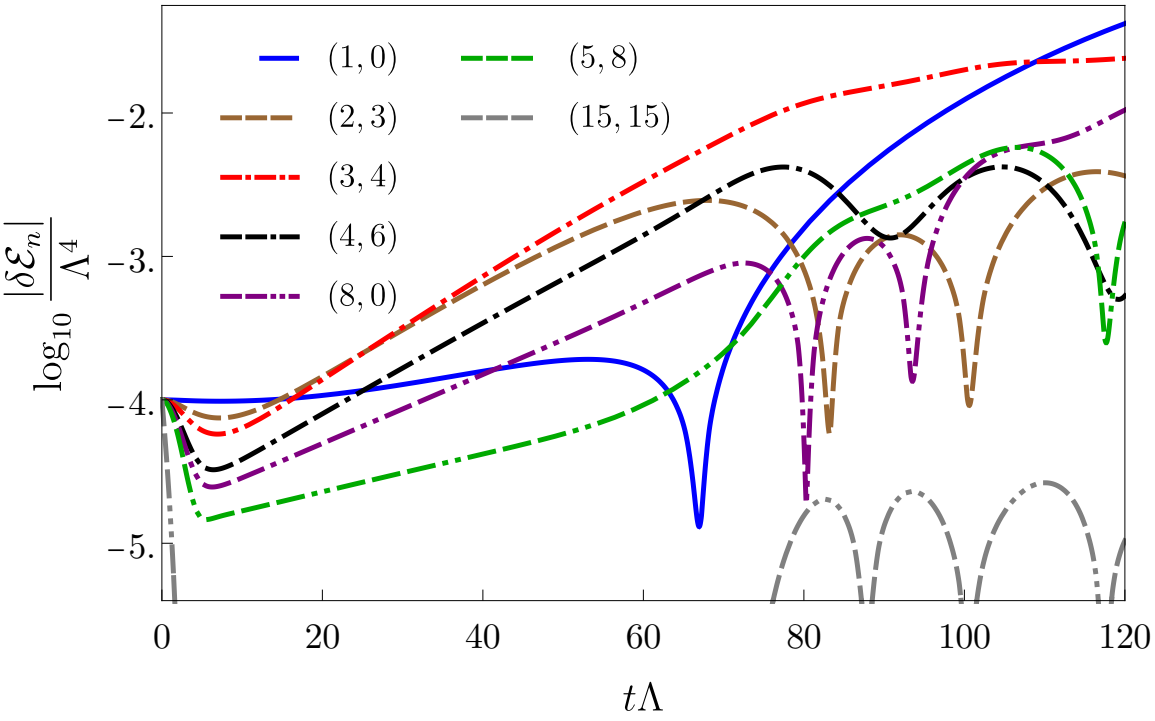

Figure 6.11: Time evolution of the amplitudes of several Fourier modes corresponding to the run in Fig. 6.10. The different momenta are labelled by integers (n_x, n_y) as in (6.45).

Most of these modes are outside the black, solid circle in Fig. 6.9, i.e. they are stable. Since the initial perturbation is small, the first stage of the evolution is well described by a linear analysis around the initial homogeneous state. According to this, the stable modes decay exponentially fast as soon as the simulation begins, on a time scale of order $T_s^{-1} \sim \Lambda^{-1}$. For the unstable modes, linear theory predicts a behavior which is the sum of two exponentials, precisely the two solutions of the sound mode (6.9). In the spinodal region, one of these modes decays with time while the other one grows. After some time the latter dominates. This physics can be seen in Fig. 6.11, which shows the time evolution of the amplitudes of several Fourier modes corresponding to the run in Fig. 6.10. The straight lines at early times correspond to the regime of exponential growth. At late times some of these slopes can change due to resonant behaviour, namely to the coupling between different modes [63].

In Fig. 6.12 we compare the growth rates predicted by the hydrodynamic approximation with those extracted from a fit to the slopes of the straight lines in Figs. 6.11 at early times. We see that the hydrodynamic approximation captures the correct qualitative shape everywhere, and that it provides a good approximation at the quantitative level at low k, as expected. The exact values of the key parameters,

$$k_* = 0.96\Lambda\,, \qquad k_{\rm max} = 0.51\Lambda\,, \qquad \gamma_{\rm max} = 0.086\Lambda\,, \tag{6.47}$$

are slightly larger than their hydrodynamic counterparts.

Once the amplitudes of some modes grow large enough, the evolution enters a non-linear regime. The dynamics here is rich and involves several phases. The interested reader can find a thorough discussion in [63]. In a nutshell, the initial exponential growth gives rise to peaks and valleys. These are initially separated from each other by a distance of order $k_{\rm max}^{-1}$, but they eventually merge with one another until the system reaches a maximum-entropy state which,

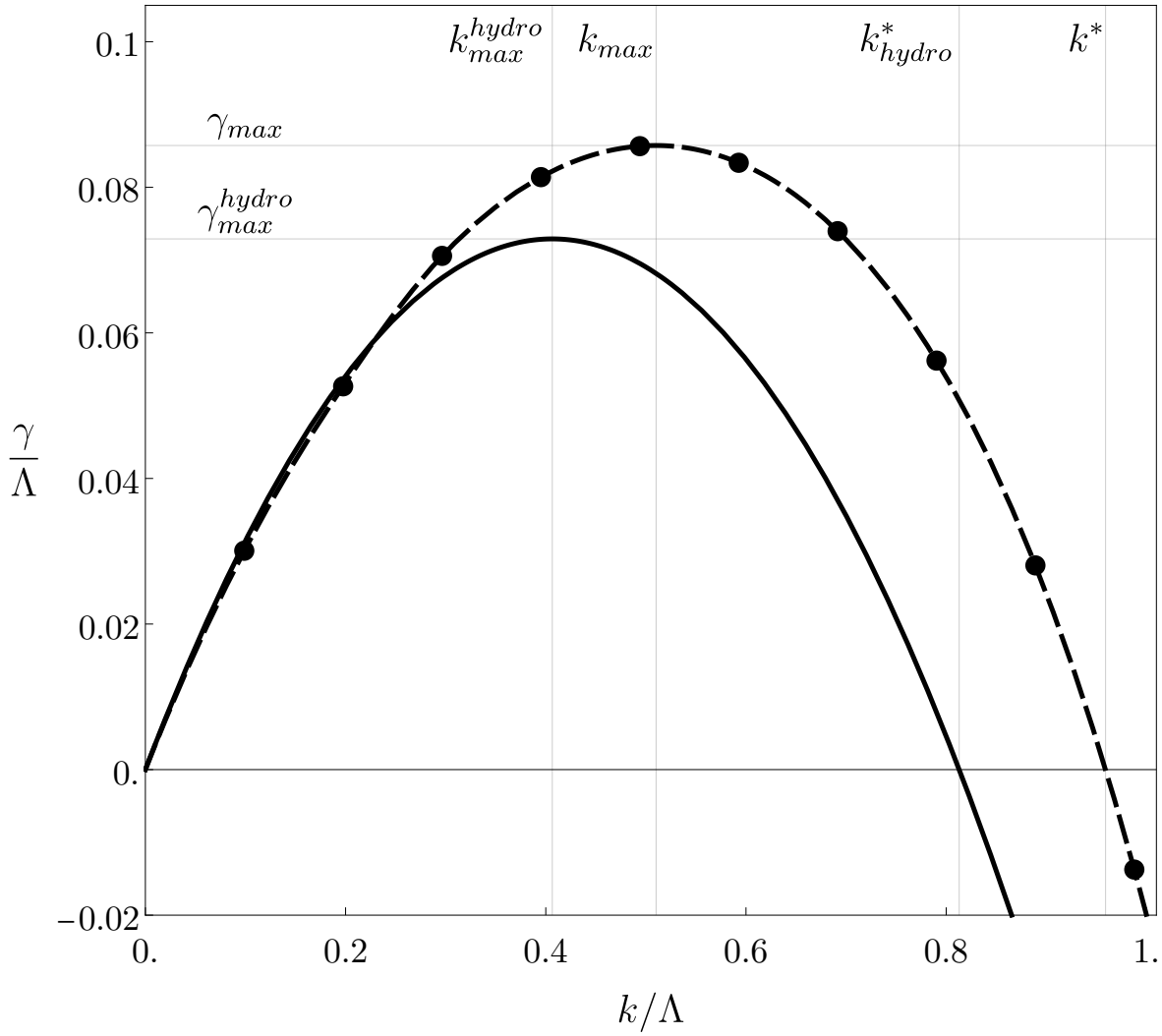

Figure 6.12: Comparison between dispersion relations. The continuous black curve shows the growth rates predicted by the hydrodynamic approximation (6.12) for the state under consideration. The black dots show the growth rates extracted from a fit to the early-time slopes in Fig. 6.11. The dashed black curve is an interpolation of these points.

in large enough a box, is a phase-separated state at a constant, homogeneous temperature $T = T_c$. This dynamics can be observed by following the different snapshots in Fig. 6.10. In particular, the bottom-right plot shows a configuration that is close to a phase-separated state, in which the total volume is divided in two regions with energies precisely equal to $\mathcal{E}_{\rm high}$ and $\mathcal{E}_{\rm low}$, respectively, separated by an interface of thickness $\sim T_c^{-1} \sim \Lambda^{-1}$.

Note that in our simulations we have ignored the expansion of the Universe. We will come back to this point in Sec. 6.5.

6.4 Gravitational wave spectrum

We will consider GWs as metric perturbations around flat space, which ignores the expansion of the Universe. We will come back to this approximation in Sec. 6.5. A GW in flat space is

described by a metric perturbation h of the form

$$ds^2 = -dt^2 + (\delta_{ij} + h_{ij})\, dx^i dx^j \,. \tag{6.48}$$

Indices on h_{ij} are raised and lowered with δ_{ij}. In the purely transverse traceless (TT) gauge, its evolution is governed by the perturbed Einstein equations

$$\ddot{h}_{ij}(t, \boldsymbol{x}) - \nabla^2 h_{ij}(t, \boldsymbol{x}) = 16\pi G\, \Pi_{ij}(t, \boldsymbol{x}) \,, \tag{6.49}$$

where Π_{ij} is the TT part of the stress tensor. In momentum space (along the spatial directions) the equation of motion becomes

$$\ddot{h}_{ij}(t, \boldsymbol{k}) + k^2 h_{ij}(t, \boldsymbol{k}) = 16\pi G\, \Pi_{ij}(t, \boldsymbol{k}) \,. \tag{6.50}$$

The fact that Π_{ij} is TT guarantees that it only sources the GW components of h, namely the spin-two, tensor component. Given the stress tensor, its TT part is given by

$$\Pi_{ij}(\boldsymbol{k}) = \Lambda_{ij}^{mn}(\hat{\boldsymbol{k}})\, T_{mn}(\boldsymbol{k}) \,, \tag{6.51}$$

where

$$\Lambda_{ij}^{mn}(\hat{\boldsymbol{k}}) = P_i^m(\hat{\boldsymbol{k}}) P_j^n(\hat{\boldsymbol{k}}) - \frac{1}{2} P_{ij}(\hat{\boldsymbol{k}}) P^{mn}(\hat{\boldsymbol{k}}) \tag{6.52}$$

and

$$P_{ij}(\hat{\boldsymbol{k}}) = \delta_{ij} - \hat{k}_i \hat{k}_j \,. \tag{6.53}$$

We have imposed translation invariance along the z-direction, so $\Pi_{ij}(t, \boldsymbol{k})$ vanishes when $\boldsymbol{k}$ points along this direction. Through (6.50) this means that we cannot produce GWs along this direction. Therefore, let us consider GWs propagating along a direction in the xy-plane at an angle θ with the x-axis. In this case

$$\boldsymbol{k} = (k_x, k_y, 0) \tag{6.54}$$

and therefore the projector takes the form

$$P_{ij} = \begin{pmatrix} M & 0 \\ 0 & 1 \end{pmatrix} , \qquad M = \frac{1}{k^2} \begin{pmatrix} k_y^2 & k_x k_y \\ k_x k_y & k_x^2 \end{pmatrix} . \tag{6.55}$$

In our case the stress tensor is

$$T_{ij} = \begin{pmatrix} T_{xx} & T_{xy} & 0 \\ T_{xy} & T_{yy} & 0 \\ 0 & 0 & T_{zz} \end{pmatrix} . \tag{6.56}$$

Projecting with P we obtain

$$\Pi_{ij} = A \times \begin{pmatrix} M & 0 \\ 0 & -1 \end{pmatrix} , \tag{6.57}$$

where

$$A = \frac{1}{2k^2} \Big(k_y^2\, T_{xx} + 2 k_x k_y\, T_{xy} + k_x^2\, T_{yy} - k^2 T_{zz} \Big) . \tag{6.58}$$

The tensor Π_{ij} will source the GW components h_{xx}, h_{xy}, h_{yy} and h_{zz}. These will only propagate in the xy-plane, namely their dependence will be of the form $e^{ik_x x + k_y y}$.

Once h has been found, the GW energy density is given by

$$\rho_{\rm GW} = \frac{1}{32\pi G L^3} \int d^3x\, \dot{h}^{ij}(t, \boldsymbol{x})\, \dot{h}_{ij}(t, \boldsymbol{x}) \,, \tag{6.59}$$

where L^3 is the volume over which the energy is averaged. Integrating in z and Fourier-trasforming in x, y we get

$$\rho_{\rm GW} = \int dk_x\, dk_y\, \frac{d\rho_{\rm GW}}{dk_x dk_y}\,, \tag{6.60}$$

where the energy density per unit two-momentum is

$$\frac{d\rho_{\rm GW}}{dk_x dk_y} = \frac{1}{32\pi G L^2}\frac{1}{(2\pi)^2}\,\dot{h}^{ij}(t,k_x,k_y)\,\dot{h}^*_{ij}(t,k_x,k_y)\,. \tag{6.61}$$

Changing to polar coordinates (k,φ), we define the differential energy density per unit logarithmic momentum as

$$\frac{d\rho_{\rm GW}}{d\log k} = k\frac{d\rho_{\rm GW}}{dk} = \frac{1}{32\pi G L^2}\frac{k^2}{(2\pi)^2}\int_0^{2\pi} d\varphi\,\dot{h}^{ij}(t,k,\varphi)\,\dot{h}^*_{ij}(t,k,\varphi)\,. \tag{6.62}$$

It is often convenient (see e.g. [132]) to make use of the fact that the relation between Π_{ij} and T_{ij}, as well as the equation of motion for h_{ij}, are both linear. This means that, instead of evolving (6.50) for the variable h, we can evolve the following equation of motion

$$\ddot{u}_{ij}(t,\boldsymbol{k}) + k^2 u_{ij}(t,\boldsymbol{k}) = 16\pi G\, T_{ij}(t,\boldsymbol{k}) \tag{6.63}$$

for the auxiliary variable u, which is nothing but (6.50) but sourced by the full stress tensor instead of by its TT part. This is useful because projecting requires going to Fourier space, which is time-consuming. Then we can obtain the GW metric at any desired time by applying the projector to the solution,

$$h_{ij}(\boldsymbol{k}) = \Lambda_{ij}^{mn}(\hat{\boldsymbol{k}})\,u_{mn}(\boldsymbol{k})\,, \tag{6.64}$$

and the differential energy density takes the form

$$\frac{d\rho_{\rm GW}}{d\log k} = \frac{1}{32\pi G L^2}\frac{k^2}{(2\pi)^2}\int_0^{2\pi} d\varphi\,\dot{u}^{ij}(t,k,\varphi)\,\Lambda_{ij}^{mn}(\hat{\boldsymbol{k}})\,\dot{u}^*_{mn}(t,k,\varphi)\,. \tag{6.65}$$

6.4.1 Sound waves

Since the modes that drive the spinodal instability are sound modes, we expect that the evolution at early times may be well described by hydrodynamics. In the next section we will perform a quantitative analysis of the GW production in the hydrodynamic approximation. In order to develop some intuition, in this section we will analyse the production when only two isolated sound waves collide.

Consider a small perturbation around a system in thermal equilibrium. Assume that the perturbation can be described within the hydrodynamic approximation, namely that it is controlled by fluctuations δT and δv^i of the hydrodynamic variables. In the case of the velocity field we have $\delta v^i = v^i$ since the velocity is zero in static equilibrium. Then the fluctuation in the (spatial part) of the stress tensor takes the form

$$\delta T^{ij} = \delta^{ij}\, c_s^2 c_v\, \delta T + \omega_0\, v^i v^j\,, \tag{6.66}$$

where $\omega_0 = \mathcal{E}_0 + \mathcal{P}_0$ is the enthalpy of the unperturbed state, c_v is the specific heat (6.6), and c_s is the speed of sound (6.7). In writing (6.66) we have worked only to second order in the fluctuations, in particular in velocities. This means that, in addition to the hydrodynamic expansion in gradients, we are further expanding in the amplitude of the fluctuations. We expect this to be justified at sufficiently early times.

The first term in (6.66) is a pure trace and therefore it does not contribute to the TT part of the stress tensor. This can be seen explicitly in (6.57), since in this case

$$T_{xx} = T_{yy} = T_{zz}\,, \qquad T_{xy} = 0\,, \tag{6.67}$$

and therefore the prefactor in this equation vanishes. Thus only the second term in (6.66) can contribute to the production of GWs at leading order. The velocities can be extracted from the T^{0i} components, since at leading order

$$\delta T^{0i} = \omega_0 v^i \,. \tag{6.68}$$

The fluctuations in the velocity field decompose into two decoupled channels. The longitudinal or sound channel is the one for which the momentum of the perturbation is aligned with the velocity field, namely $\boldsymbol{k}$ is parallel to $\boldsymbol{v}$. The transverse or shear channel is the one in which the momentum of the perturbation is orthogonal to the velocity field. We will focus on the sound mode because this is the one that is unstable in the spinodal region. Before we proceed note that we need a superposition of at least two sound waves in different directions in order to produce GWs. Indeed, suppose we have a single sound wave with momentum $\boldsymbol{q}$. Without loss of generality we can assume that it propagates along the x-direction. Then

$$\boldsymbol{v} = (v^x, 0, 0)\,, \qquad \boldsymbol{q} = (q_x, 0, 0)\,. \tag{6.69}$$

This means that the only non-zero component of the second term in (6.66) is δT^{xx}. Moreover, the momentum of the resulting gravitational wave is $\boldsymbol{k} = 2\boldsymbol{q}$, which also points along the x-direction. Therefore in (6.54) we have $k_y = 0$. Substituting this in (6.58) we see that $A = 0$. Physically, the reason for this is that a sound wave has spin zero and hence it only induces fluctuations in the pressure along its direction of propagation, whereas a GW is transverse and therefore it is only sourced by fluctuations in the transverse components of the pressure.

Consider therefore a superposition of two sound waves with momenta $\boldsymbol{p}$ and $\boldsymbol{q}$, and with velocities $\boldsymbol{u}_p$ and $\boldsymbol{u}_q$ parallel to the respective momenta. Then the velocity field takes the form

$$\boldsymbol{v}(t, \boldsymbol{x}) = \boldsymbol{u}_p\, e^{\gamma_p t}\, e^{i\boldsymbol{p}\cdot\boldsymbol{x}} + \boldsymbol{u}_q\, e^{\gamma_q t}\, e^{i\boldsymbol{q}\cdot\boldsymbol{x}}\,, \tag{6.70}$$

where we have assumed that the time dependence is the one dictated by the spinodal instability with the corresponding growth rates $\gamma_p = \gamma(p)$ and $\gamma_q = \gamma(q)$. This velocity field can source a GW with momentum along $\boldsymbol{k} = \boldsymbol{p} + \boldsymbol{q}$. Without loss of generality, let us assume that $\boldsymbol{p}$ points along the x-direction and that θ is the angle in the xy-plane between $\boldsymbol{p}$ and $\boldsymbol{q}$. Then

$$\begin{aligned}
\boldsymbol{p} &= (p, 0, 0)\,, && (6.71)\\
\boldsymbol{u}_p &= (u_p, 0, 0)\,, && (6.72)\\
\boldsymbol{q} &= q(\cos\theta, \sin\theta, 0)\,, && (6.73)\\
\boldsymbol{u}_q &= u_q(\cos\theta, \sin\theta, 0)\,, && (6.74)\\
\boldsymbol{k} &= (p + q\cos\theta, q\sin\theta, 0)\,. && (6.75)
\end{aligned}$$

The second term in (6.66) has three contributions proportional to $\boldsymbol{u}_p^2$, to $\boldsymbol{u}_q^2$ and to the crossed term $\boldsymbol{u}_p\boldsymbol{u}_q$. The first two terms do not produce GWs for the same reason as with a single wave. Only the third one contributes. The corresponding non-zero components of the stress tensor become

$$\begin{aligned}
\delta T_{xx} &= \omega_0\, e^{(\gamma_p+\gamma_q)t} e^{i\boldsymbol{k}\cdot\boldsymbol{x}}\, u_p u_q\, \cos\theta\,, && (6.76)\\
\delta T_{xy} &= \omega_0\, e^{(\gamma_p+\gamma_q)t} e^{i\boldsymbol{k}\cdot\boldsymbol{x}}\, u_p u_q\, \sin\theta\,. && (6.77)
\end{aligned}$$

The prefactor in (6.57) is then

$$A = \frac{1}{2}\,\omega_0\, e^{(\gamma_p+\gamma_q)t} e^{i\boldsymbol{k}\cdot\boldsymbol{x}}\, u_p u_q\, f(r,\theta)\,, \tag{6.78}$$

where $r = q/p$ and

$$f(r,\theta) = \frac{r\sin^2\theta(2 + 3r\cos\theta)}{1 + r^2 + 2r\cos\theta}\,. \tag{6.79}$$

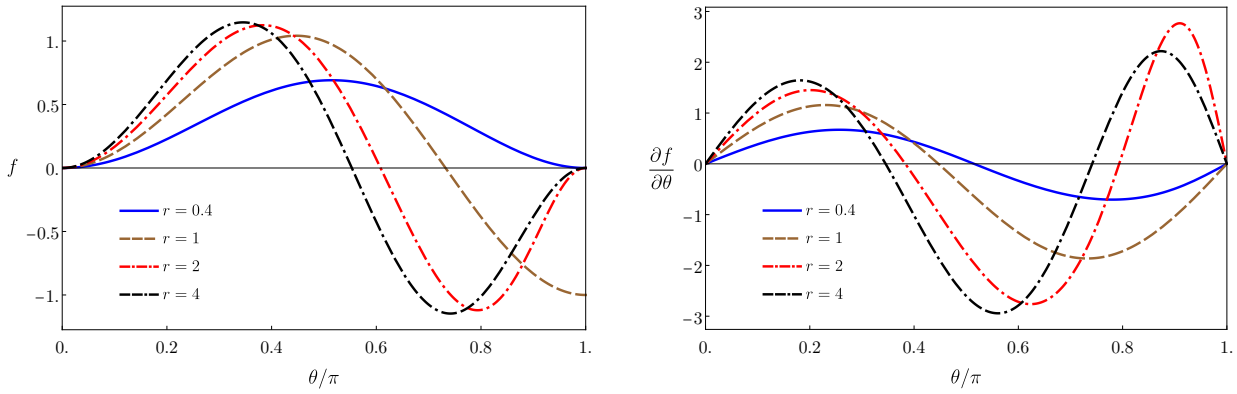

Figure 6.13: The function $f(r,\theta)$ (left) and its derivative $df/d\theta$ (right).

The function $f(r,\theta)$ and its derivative $df/d\theta$ are shown in Fig. 6.13. We see that f vanishes at $\theta = 0$ regardless of the value of r. This is expected since in this case $\boldsymbol{p}$ and $\boldsymbol{q}$ are collinear. If $r \neq 1$ then f also vanishes at $\theta = \pi$. However, if $r = 1$ then $f \to -1$ as $\theta \to \pi$. This case corresponds to the limit $k \to 0$, which is approached as $\boldsymbol{p}$ and $\boldsymbol{q}$ become antiparallel.

(6.78) contains a crucial insight about the spectrum of GWs in the early-time part of the evolution. The key point is that the time dependence at a given GW momentum $\boldsymbol{k}$ is controlled by the exponent $\gamma_p + \gamma_q$. The largest possible value of this exponent is $2\gamma_{\rm max}$, with $\gamma_{\rm max}$ the maximum growth rate in Fig. 6.12. This maximum value can only be realised by composing two sound-wave momenta $\boldsymbol{p}$ and $\boldsymbol{q}$ such that their moduli satisfy $p = q = k_{\rm max}$. In other words, $\boldsymbol{p}$ and $\boldsymbol{q}$ must lie on the red, solid circle in Fig. 6.9. By adding two such momenta one can only obtain momenta $\boldsymbol{k}$ with modulus in the range

$$0 \leq k \leq 2k_{\rm max}\,. \tag{6.80}$$

As a result, the GW spectrum (6.62) will be exponentially suppressed for $k \geq 2k_{\rm max}$. The fact that f does not vanish in the opposite limit, $\boldsymbol{k} \to 0$, means that the TT part of the stress tensor is not suppressed in this limit. Therefore we expect that the only suppression of the differential energy density $d\rho_{\rm GW}/d\log k$ in the limit $k \to 0$ will be due to the k^2 factor in (6.62).

6.4.2 Hydrodynamics

We will now provide a more detailed analysis of the GW production in the early-time part of the evolution based on hydrodynamics. In this approximation, the part of the perturbed stress tensor that gives rise to the TT component is the second term in (6.66), namely

$$\delta T_{ij}(t,\boldsymbol{x}) = \omega_0\, v_i(t,\boldsymbol{x}) v_j(t,\boldsymbol{x})\,. \tag{6.81}$$

In Fourier space, this leads to

$$\delta T_{ij}(t,\boldsymbol{k}) = \omega_0 \int \frac{d^2q}{(2\pi)^2}\, v_i(t,\boldsymbol{k}-\theta)\, v_j(t,\theta)\,. \tag{6.82}$$

Note that, in this and in some subsequent equations, boldface symbols such as $\boldsymbol{x}, \boldsymbol{k}, \ldots$ refer to two-dimensional vectors.

Since the excitations of interest are sound waves, the velocity is longitudinal, which means that

$$\boldsymbol{v}(t,\theta) = v(t,\theta)\,\hat{\theta}\,. \tag{6.83}$$

Using the hydrodynamic equations of motion, we can relate the modulus of the velocity field to the time derivative of the energy density fluctuation:

$$v(t,\theta) = \frac{i}{q\,\omega_0}\,\partial_t\,\delta\mathcal{E}(t,\theta)\,. \tag{6.84}$$

In our simulation the initial velocity at $t = 0$ vanishes, and the amplitude of the energy density perturbation is a small number ϵ_θ. This initial value arises as a combination of the growing and the decaying sound modes. Imposing the condition $\boldsymbol{v}(t,\theta) = 0$ fixes the relative coefficient in such a way that

$$\delta\mathcal{E}(t,q) = \frac{\epsilon_\theta}{2}\left[\left(1+\frac{\tilde{q}}{2}\right)e^{\gamma_q t} + \left(1-\frac{\tilde{q}}{2}\right)e^{-\tilde{\gamma}_q t}\right]\,, \tag{6.85}$$

where γ_q and $\tilde{\gamma}_q$ are the growth rates of the unstable and stable modes, respectively, and

$$\tilde{q} = \frac{q}{k_{\rm max}}\,. \tag{6.86}$$

Note that both $\delta\mathcal{E}(t,q)$ and ϵ_θ have dimensions of $(\text{mass})^2$ because of the Fourier transform. In hydrodynamics the growth rates are given by

$$\gamma_q = \frac{|c_s|}{2}\,\tilde{q}(2-\tilde{q})\,k_{\rm max}\,, \qquad \tilde{\gamma}_q = \frac{|c_s|}{2}\,\tilde{q}(2+\tilde{q})\,k_{\rm max}\,. \tag{6.87}$$

Hereafter we will only consider the unstable mode, since it dominates as soon as the stable mode has decayed. With this approximation we can write

$$\delta T_{ij}(t,\boldsymbol{k}) = -\frac{|c_s|^2}{4\omega_0}\int\frac{q\,dq\,d\theta}{(2\pi)^2}\,\epsilon_\theta\epsilon_{\theta'}\left(1-\frac{\tilde{q}^2}{4}\right)\left(1-\frac{\tilde{q}'^2}{4}\right)\frac{q_i}{q}\,\frac{q'_j}{q'}\,e^{(\gamma_q+\gamma_{q'})t}\,, \tag{6.88}$$

where θ is the angle between $\boldsymbol{k}$ and θ and

$$\theta' = \boldsymbol{k} - \theta\,, \qquad q' = \sqrt{k^2+q^2-2kqx}\,, \qquad x = \cos\theta\,, \qquad \tilde{q}' = \frac{q'}{k_{\rm max}}\,. \tag{6.89}$$

Without loss of generality we assume that $\boldsymbol{k}$ points along the x-direction. The exponent controlling the time growth in the integrand of (6.88) takes the form

$$t\gamma_{\rm tot}(k,q,x) = t\,(\gamma_q+\gamma_{q'}) = t\,k_{\rm max}\,\frac{|c_s|}{2}\Big[\tilde{q}(2-\tilde{q}) + \tilde{q}'(2-\tilde{q}')\Big]\,. \tag{6.90}$$

If

$$k \le 2k_{\rm max} \tag{6.91}$$

then, for fixed k, this exponent has a maximum at

$$\tilde{q}_M = 1\,, \qquad x_M = \frac{\tilde{k}}{2}\,, \tag{6.92}$$

and at this point we have

$$\tilde{q}'_M = 1\,, \qquad \gamma_{{\rm tot},M} = 2\gamma_{\rm max}\,. \tag{6.93}$$

These equations mean that, for momenta $\boldsymbol{k}$ in the range (6.80), the exponent achieves its largest possible value $2t\gamma_{\rm max}$ and the integral is dominated by sound waves with momenta of equal moduli,

$$q = q' = k_{\rm max}\,, \tag{6.94}$$

lying at angles θ_M and $-\theta_M$ with respect to $\boldsymbol{k}$. This reproduces the conclusion anticipated in the paragraph of (6.80). In this range we can evaluate the integral via a saddle-point approximation.

For this purpose, we expand the exponent to quadratic order around its maximum. The Hessian in variables

$$\Delta q = q - q_M \,, \qquad \Delta x = x - x_M \tag{6.95}$$

is not diagonal. Therefore, to facilitate the Gaussian integration we introduce the variables (α, β) defined through

$$\Delta q = k_{\rm max}\left(\alpha\cos\Psi + \beta\sin\Psi\right) \,, \qquad \Delta x = -\alpha\sin\Psi + \beta\cos\Psi \,, \tag{6.96}$$

with

$$\tan 2\Psi = \frac{4\tilde{k}(2-\tilde{k}^2)}{(8-8\tilde{k}^2+\tilde{k}^4)} \,. \tag{6.97}$$

With these variables we can write the exponent up to quadratic order as

$$t\gamma_{\rm tot}(k,\alpha,\beta) \;\simeq\; t|c_s|k_{\rm max} - \frac{\alpha^2}{2\sigma_\alpha^2} - \frac{\beta^2}{2\sigma_\beta^2} \,, \tag{6.98}$$

with

$$\sigma_\alpha^2 \;=\; \frac{1}{t|c_s|k_{\rm max}\left(1+\frac{\tilde{k}^4}{8}+\sqrt{1-\tilde{k}^2+\frac{\tilde{k}^4}{4}+\frac{\tilde{k}^8}{64}}\right)} \,, \tag{6.99}$$

$$\sigma_\beta^2 \;=\; \frac{1}{t|c_s|k_{\rm max}\left(1+\frac{\tilde{k}^4}{8}-\sqrt{1-\tilde{k}^2+\frac{\tilde{k}^4}{4}+\frac{\tilde{k}^8}{64}}\right)} \,. \tag{6.100}$$

For generic values of $\tilde{k}$ these widths become arbitrary narrow as time increases and therefore we can replace their exponentials by δ-functions with appropriate normalizations. However, for small $\tilde{k}$ the width of the β-variable scales as

$$\sigma_\beta^2 \sim \frac{1}{t|c_s|k_{\rm max}\,\tilde{k}^2} \,. \tag{6.101}$$

Therefore, the δ-function approximation is only valid for

$$k_{\rm low} \ll k < 2k_{\rm max} \,, \tag{6.102}$$

where

$$k_{\rm low} \equiv \sqrt{\frac{k_{\rm max}}{|c_s|t}} \tag{6.103}$$

and the upper bound comes from the condition (6.91) for the existence of the saddle. Under these conditions, we can write the stress tensor as

$$\delta T_{ij} = -\frac{9}{64\pi}\,\epsilon_{\theta_M}\epsilon_{\theta'_M}\,\frac{|c_s|}{\omega_0\,t}\,\frac{k_{\rm max}}{\tilde{k}\sqrt{4-\tilde{k}^2}}\;\tilde{q}_{M\,i}\,\tilde{q}'_{M\,j}\,e^{2\gamma_{\rm max}t} \qquad \left[k_{\rm low} \ll k \leq 2k_{\rm max}\right] , \tag{6.104}$$

where

$$\tilde{q}_{M\,i} = \left(\frac{\tilde{k}}{2}, \sqrt{1-\frac{\tilde{k}^2}{4}}, 0\right) \,, \qquad \tilde{q}'_{M\,j} = \left(\frac{\tilde{k}}{2}, -\sqrt{1-\frac{\tilde{k}^2}{4}}, 0\right) \,, \qquad \tilde{k} = \frac{k}{k_{\rm max}} \,, \tag{6.105}$$

and we recall that we have assumed that $\boldsymbol{k}$ points along the x-direction.

For sufficiently small k we see from (6.97) that $\Psi \to 0$ and hence $\Delta q \simeq k_{\rm max}\alpha$ and $\Delta x \simeq \beta$. In this limit we can still perform the Gaussian approximation for the integral over k. This

localises the integrand at $q = q' = k_{\rm max}$. Assuming that $\epsilon_\theta, \epsilon_{\theta'}$ are θ-independent, the only θ dependence in the integrand is in the vectors

$$q_i/q = (\cos\theta, \sin\theta, 0)\,, \qquad q'_j/q = (-\cos\theta, -\sin\theta, 0)\,. \tag{6.106}$$

Integrating over θ we then find that, at leading order in k in the limit $k \to 0$, the stress tensor approaches a finite, k-independent value

$$\delta T_{ij} = -\frac{9}{256\pi^{3/2}}\,\epsilon_{\theta_M}\epsilon_{\theta'_M}\,\frac{|c_s|^{3/2}}{\omega_0}\,\frac{k_{\rm max}^{3/2}}{\sqrt{t}}\,q'_{M\,i}\,q_{M\,j}\,e^{2\gamma_{\rm max}t} \qquad \Big[k \to 0\Big]\,, \tag{6.107}$$

where

$$\tilde{q}_{M\,i}\,\tilde{q}'_{M\,j} = -{\rm diag}(\pi, \pi, 0)\,. \tag{6.108}$$

We emphasize again that, as the vector $\boldsymbol{k}$ approaches zero, it does so along the x-direction.

For $k > 2k_{\rm max}$ the exponent in (6.88) must be smaller than $2\gamma_{\rm max}$ since k cannot be obtained by adding two vectors of modulus $k_{\rm max}$. The fact that the growth rate $\gamma(k)$ is a concave function of k, meaning that $\gamma''(k) < 0$, implies that the maximum value of $\gamma_{\rm tot}$ is obtained by taking θ and θ' to be almost parallel to each other and to k and to have equal moduli $q = q' = k/2$. They cannot be exactly parallel because then the TT component of te resulting stress tensor would vanish identically, but they can be exponentially close to being parallel. In this case the growth rate is given by

$$\gamma_{\rm tot} \simeq 2\,\gamma\left(\frac{k}{2}\right) < 2\gamma_{\rm max}\,. \tag{6.109}$$

Therefore, for $k > 2k_{\rm max}$, we expect the GW production to be exponentially suppressed with respect to the case $k < 2k_{\rm max}$ by a factor

$$\frac{\rho_{\rm GW}(k > 2k_{\rm max})}{\rho_{\rm GW}(k < 2k_{\rm max})} \simeq \exp\Big\{-4t\Big(\gamma_{\rm max} - \gamma\,(k/2)\Big)\Big\}\,. \tag{6.110}$$

Using the stress tensors above we can compute the spectrum of GWs. For concreteness let us focus on the case (6.104). Substituting this in (6.63) we find that, neglecting subleading terms in $1/t$, the solution is

$$u_{ij}(t, \boldsymbol{k}) = -\frac{9}{4}\,\epsilon_{\theta_M}\epsilon_{\theta'_M}\,\frac{1}{\tilde{k}\sqrt{4-\tilde{k}^2}}\,\frac{1}{|c_s^2| + \tilde{k}^2}\,\frac{G|c_s|}{\omega\,k_{\rm max}^3 t}\,\tilde{q}_{M\,i}\,\tilde{q}'_{M\,j}\,e^{2\gamma_{\rm max}t}\,. \tag{6.111}$$

We now need to compute the contraction associated to the projector Λ_{ij}^{mn} in (6.65). If we assume that $\epsilon_{\theta_M}, \epsilon_{\theta'_M}$ are independent of the angle then $u_{ij}(t, \boldsymbol{k})$ only depends on k and we can assume that $\boldsymbol{k}$ points along the x-direction. In this case the projector (6.53) becomes

$$P_{ij} = {\rm diag}\,(0, 1, 1)\,. \tag{6.112}$$

Since $u^*_{ij}(t, \boldsymbol{k}) = u_{ij}(t, -\boldsymbol{k})$ we obtain

$$\tilde{q}^i_M(\boldsymbol{k})\,\tilde{q}'^j_M(\boldsymbol{k})\,\Lambda_{ij}^{mn}(\hat{\boldsymbol{k}})\,\tilde{q}_{M\,m}(-\boldsymbol{k})\,\tilde{q}'_{M\,n}(-\boldsymbol{k}) = \frac{1}{4}\sqrt{4-\tilde{k}^2}\,. \tag{6.113}$$

Substituting in (6.65) we finally arrive at

$$\frac{d\rho_{\rm GW}}{d\log k} = \frac{G}{32\pi^2 L^2}\left(\frac{9}{16}\right)^2 \epsilon_{\theta_M}\epsilon_{\theta'_M}\epsilon_{-\theta_M}\epsilon_{-\theta'_M}\,\frac{1-\frac{\tilde{k}^2}{4}}{\Big(|c_s|^2 + \tilde{k}^2\Big)^2}\,\frac{|c_s|^4 k_{\rm max}^2}{\omega_0^2\,t^2}\,e^{4\gamma_{\rm max}t}\,, \tag{6.114}$$

where we have made use of the fact that

$$\theta_M(-\boldsymbol{k}) = \theta'_M(\boldsymbol{k})\,. \tag{6.115}$$

Recall that (6.114) is only valid in the range (6.102). To obtain an estimate for the total energy we proceed as follows. First, we note that, in an statistical ensamble characterised by a white noise, we expect that

$$\left\langle \epsilon_{\theta_M} \epsilon_{\theta'_M} \epsilon_{-\theta_M} \epsilon_{-\theta'_M} \right\rangle = \langle \epsilon_{\theta_M} \epsilon_{-\theta_M} \rangle^2 = \kappa \, (k_{\rm max})^2 \,, \tag{6.116}$$

where $\kappa(q)$ is the strength of the noise and we have made use of (6.94). Second, the relevant integral is given by

$$\int d\tilde{k} \, \frac{1}{\tilde{k}} \, \frac{1 - \frac{\tilde{k}^2}{4}}{\left(|c_s|^2 + \tilde{k}^2\right)^2} = \frac{1}{8|c_s|^4} \left(\frac{|c_s|^2 (4 + |c_s|^2)}{|c_s|^2 + \tilde{k}^2} + 4 \log \frac{\tilde{k}^2}{c_s|^2 + \tilde{k}^2} \right) . \tag{6.117}$$

Assuming that

$$|c_s|^2 \ll \sqrt{\frac{1}{|c_s| k_{\rm max} t}} \ll 2 \tag{6.118}$$

we can expand the integral for small $|c_s|$. In this case the integral is dominated by the lower cut-off, and to leading order in the cut-off we get

$$\int_{\sqrt{1/(|c_s| k_{\rm max} t)}}^{4} d\tilde{k} \, \frac{1}{\tilde{k}} \, \frac{1 - \frac{\tilde{k}^2}{4}}{\left(|c_s|^2 + \tilde{k}^2\right)^2} \simeq \frac{1}{4} \Big(|c_s| k_{\rm max} t \Big)^2 . \tag{6.119}$$

The energy density is thus given by

$$\rho_{\rm GW} = \frac{G}{32 \pi^2 L^2} \left(\frac{9}{32} \right)^2 \epsilon_\theta^4 \, \frac{|c_s|^6 k_{\rm max}^4}{\omega_0^2} \, e^{4 \gamma_{\rm max} t} \,. \tag{6.120}$$

The end of the exponential regime is determined by the condition that the amplitudes of the growing modes become of the same order as the latent heat (6.4) [63]. Thus

$$\epsilon_\theta \, e^{\gamma_{\rm max} t} \sim \frac{\mathcal{E}_{\rm latent}}{k_{\rm max}^2} \,. \tag{6.121}$$

Substituting into the expression for the energy we arrive at

$$\rho_{\rm GW} = \frac{G}{32 \pi^2 L^2} \left(\frac{9}{32} \right)^2 \frac{\mathcal{E}_{\rm latent}^4 \, |c_s|^6}{\omega_0^2 \, k_{\rm max}^4} \,. \tag{6.122}$$

The parametric dependence of this equation can be understood as follows. Conservation of the stress tensor implies that, at the end of exponential evolution, the velocity field is

$$v(x) \sim |c_s| \frac{\mathcal{E}_{\rm latent}}{\omega_0} \,, \tag{6.123}$$

where we have used the fact that $\partial_t \sim |c_s| k_{\rm max}$. The relevant part of the stress tensor is then

$$T_{ij}(x) \sim \omega_0 \, v(x)^2 \sim \frac{\mathcal{E}_{\rm latent}^2}{\omega_0} \, |c_s|^2 \,. \tag{6.124}$$

It follows that the metric fluctuation scales as

$$h_{ij}(x) \sim \frac{G}{k_{\rm max}^2} \, \frac{\mathcal{E}_{\rm latent}^2}{\omega_0} \, |c_s|^2 \,, \tag{6.125}$$

where we have used that the charateristic size of T_{ij} is $1/k_{\rm max}$. Therefore

$$\dot{h}(x)_{ij}^2 \sim \frac{G^2}{k_{\rm max}^2} \, \frac{\mathcal{E}_{\rm latent}^4}{\omega_0^2} \, |c_s|^6 \,. \tag{6.126}$$

Since the characteristic size of $\dot{h}$ is also $1/k_{\rm max}$, integrating over space and dividing by GL^2 we get

$$\rho_{\rm GW} \sim \frac{G}{L^2 \, k_{\rm max}^4} \, \frac{\mathcal{E}_{\rm latent}^4}{\omega_0^2} \, |c_s|^6 \,, \tag{6.127}$$

as in (6.122).

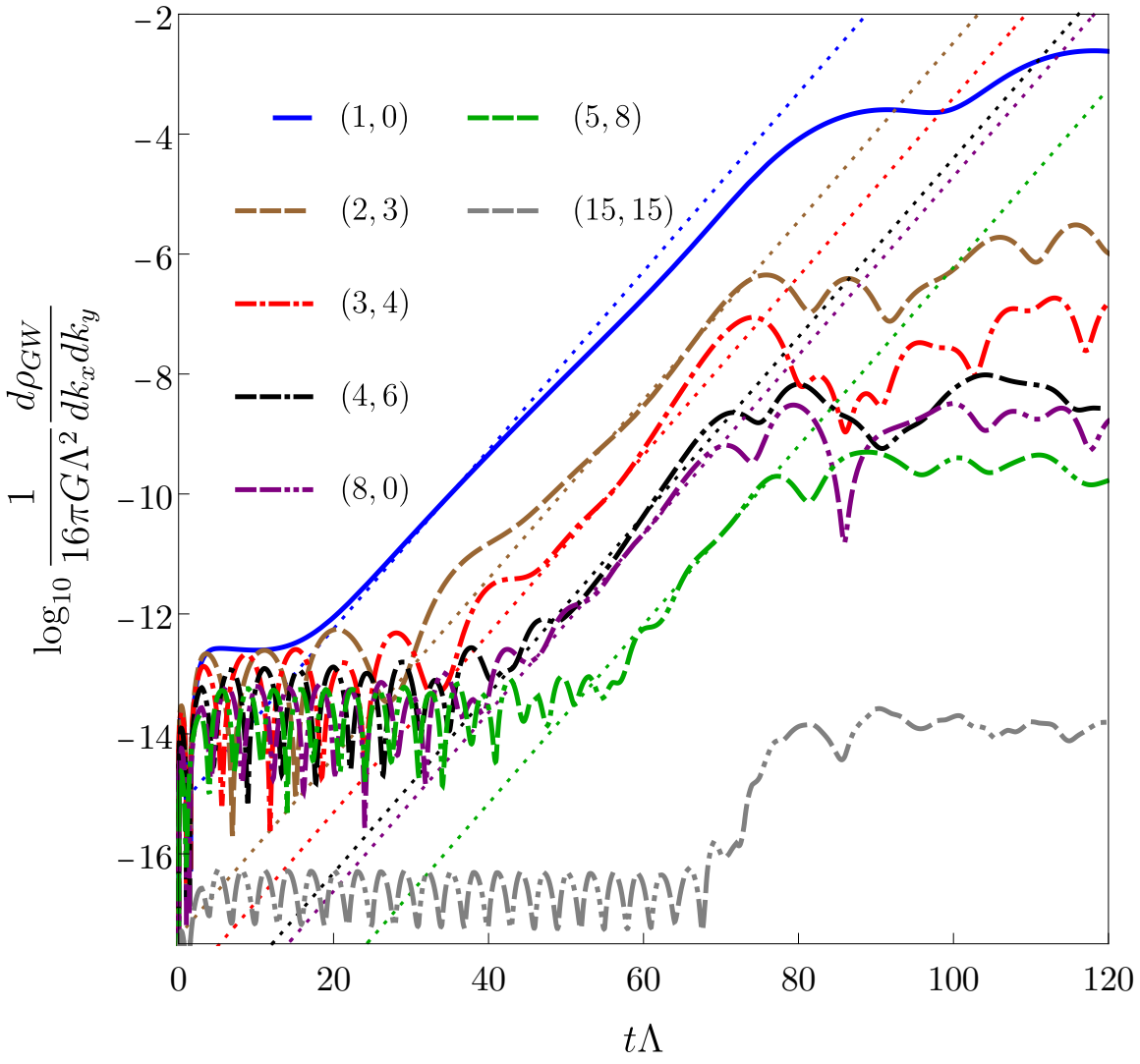

Figure 6.14: GW energy density per unit two-momentum (6.61) at early times. The different momenta are labelled by integers (n_x, n_y) as in (6.45). Except for the mode with $n_x = n_y = 15$, all the other modes shown have $k < 2k_{\max}$ and therefore at early times they grow approximately as $e^{4\gamma_{\max} t}$, as indicated by the dotted, diagonal lines.

6.4.3 Full result

In the previous section we estimated the GW emission in the regime of exponential growth. Once some modes become large enough this regime ends and the non-linear evolution begins [63]. In this section we will present the exact results for the GW production for both the linear and the non-linear regimes.

The behaviour of the differential energy density per unit two-momentum at early times is shown in Fig. 6.14. We see that the energy density in modes with $k < 2k_{\max}$ grows at early times approximately as $e^{4\gamma_{\max} t}$, as predicted by (6.114). The deviations from this behaviour, which begin around $60 \lesssim t\Lambda \lesssim 80$, indicate the end of the linear regime.

The differential energy density per unit logarithmic momentum is shown in Figs. 6.15 and 6.16. In Fig. 6.15 we have marked the two values corresponding to the range (6.102). In Fig. 6.16 we zoom into this range. At each time we show with a dotted curve in the same color

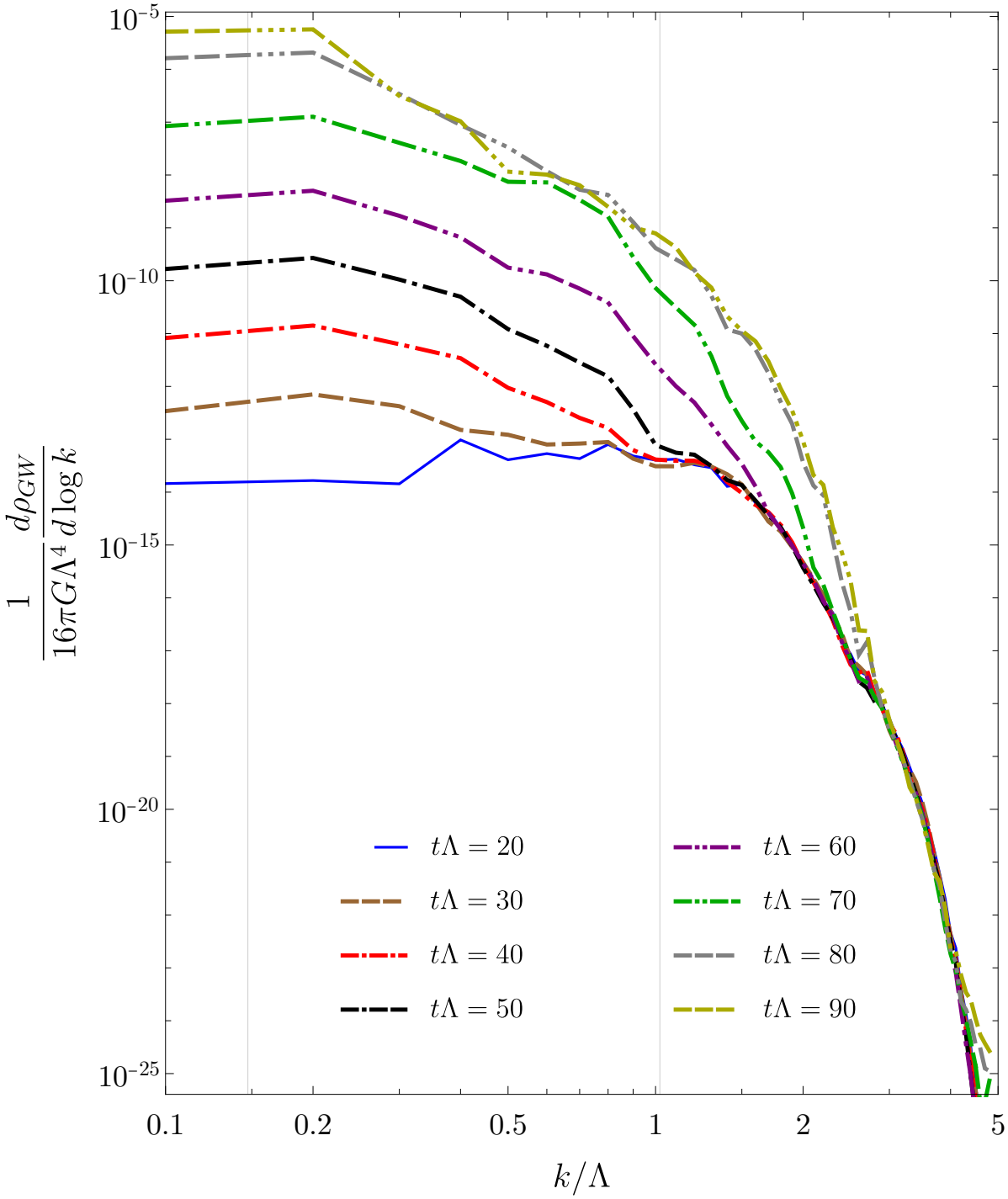

Figure 6.15: GW differential energy density per unit logarithmic momentum at early times. From left to right, the grey, vertical lines lie at $k_{\rm low} \simeq 0.15\Lambda$ (computed according to (6.103) with $\Lambda t = 70$) and $2k_{\rm max}$.

the k-dependence predicted by (6.114), except for an overall factor that we fix by requiring agreement at $k/\Lambda = 0.2$. The need to fix this factor comes from the fact that the real evolution includes effects that were not included in the derivation of (6.114), such as initial excitations of quasi-normal modes or the decaying exponential in (6.85). Once this factor is fixed, we see that (6.114) agrees fairly well with the exact result for intermediate values of k at the times around the end of the linear regime, namely for $40 \lesssim \Lambda t \lesssim 70$. For values $k > 2k_{\rm max}$ we see in

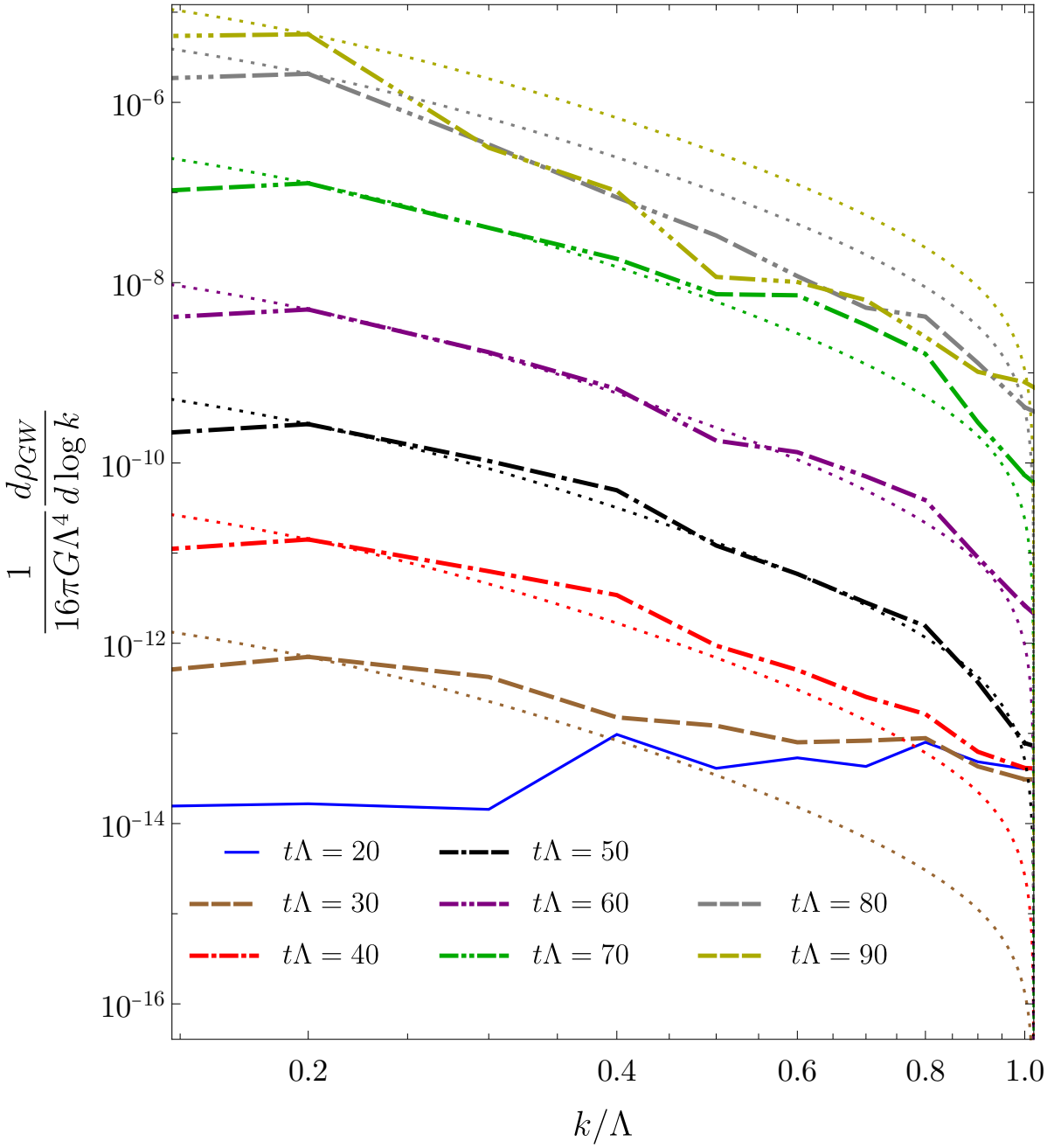

Figure 6.16: GW differential energy density per unit logarithmic momentum at early times for momenta approximately in the range (6.102). For each color, the dotted curve corresponds to the k-dependence predicted by (6.114), except for an overall factor that we fix by requiring agreement at $k/\Lambda = 0.2$.

Fig. 6.15 that the energy density decreases exponentially in k, as expected. We will comment on the behaviour at $k < k_{\rm low}$ in Sec. 6.5.

Performing the integral over k in (6.61) or (6.62) we obtain the total energy density radiated into GWs. The result at early times is shown in Fig. 6.17. We see that the exponential growth of the individual modes with $k < 2k_{\rm max}$ results in an analogous growth of the total energy, as indicated by the dashed line.

The exponential growth ceases when the non-linear regime begins at around $t\Lambda \sim 70$. Fig. 6.18 shows the differential energy density for the entire evolution. We see that the energy density keeps increasing in the non-linear phase until it saturates at late times. Fig. 6.19

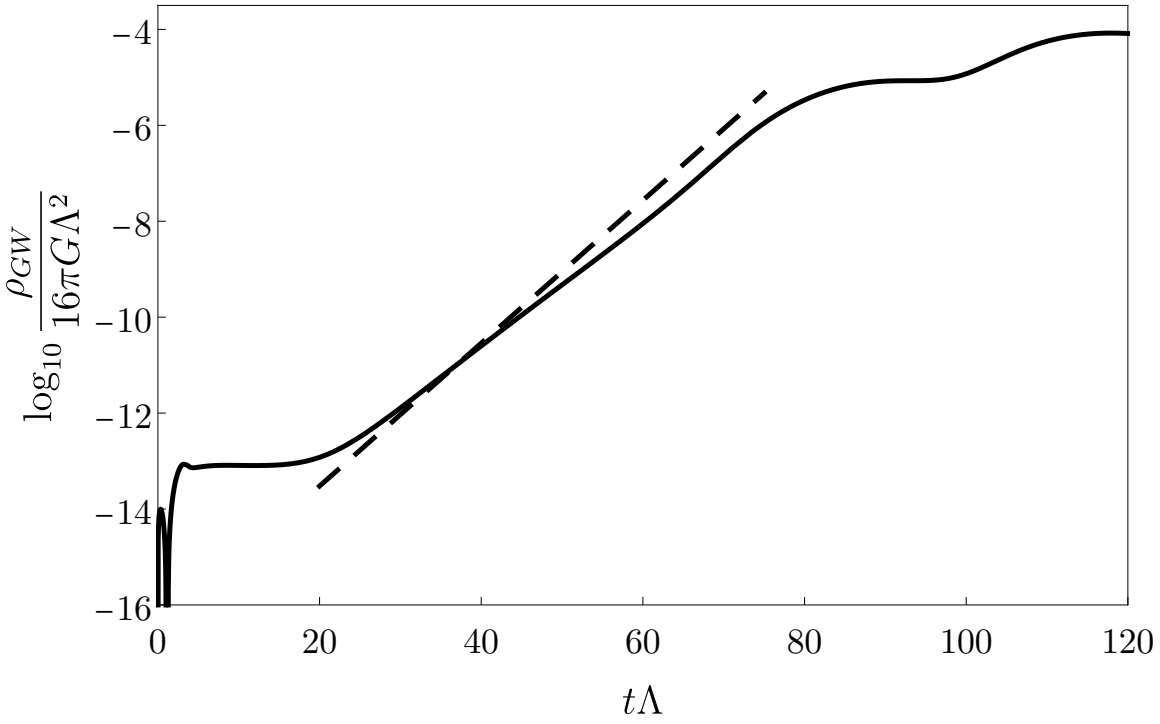

Figure 6.17: Total energy density radiated into GWs at early times. The black, dashed line corresponds to $\rho_{\rm GW} \propto e^{4\gamma_{\rm max} t}$.

shows the corresponding total energy density on a linear scale. In this figure we can see the oscillations in the late time behaviour expected for the energy density of a wave. We also note that most of the energy is radiated in the short reshaping period [63] that takes place right after the linear regime, around $100 \lesssim \Lambda t \lesssim 150$. In this period the energy density increases from about 0.1 to about 0.7 on the scale of the plot. We will come back to this point in Sec. 6.5.

6.5 Discussion

Cosmological, first-order, thermal phase transitions are usually assumed to take place via the nucleation of bubbles of the stable phase inside the metastable phase. However, if the nucleation rate is sufficiently suppressed, then the Universe can cool down all the way to the end of the metastable phase and enter the spinodal region. Under these circumstances the transition proceeds via the exponential growth of unstable modes and the subsequent formation, merging and relaxation of phase domains. We have performed the first calculation of the GW spectrum produced by this mechanism.

The conditions for the nucleation rate to be sufficiently suppressed depend on whether the transition takes place in the sector driving the expansion of the Universe or in a hidden sector that couples weakly, in some cases only gravitationally, to the former. The crucial point is that, as a result of the different amounts of energy injected into each sector by the reheating process, the temperature of the hidden sector may be parametrically smaller than that in the sector driving the expansion. For concreteness we have assumed that both sectors ar described by a non-Abelian gauge theory. Under these circumstances, we have shown that the constraint on the rank of the gauge group is fairly stringent if the transition takes place in the sector driving the expansion of the Universe, whereas it is fairly weak if it takes place in a hidden sector.

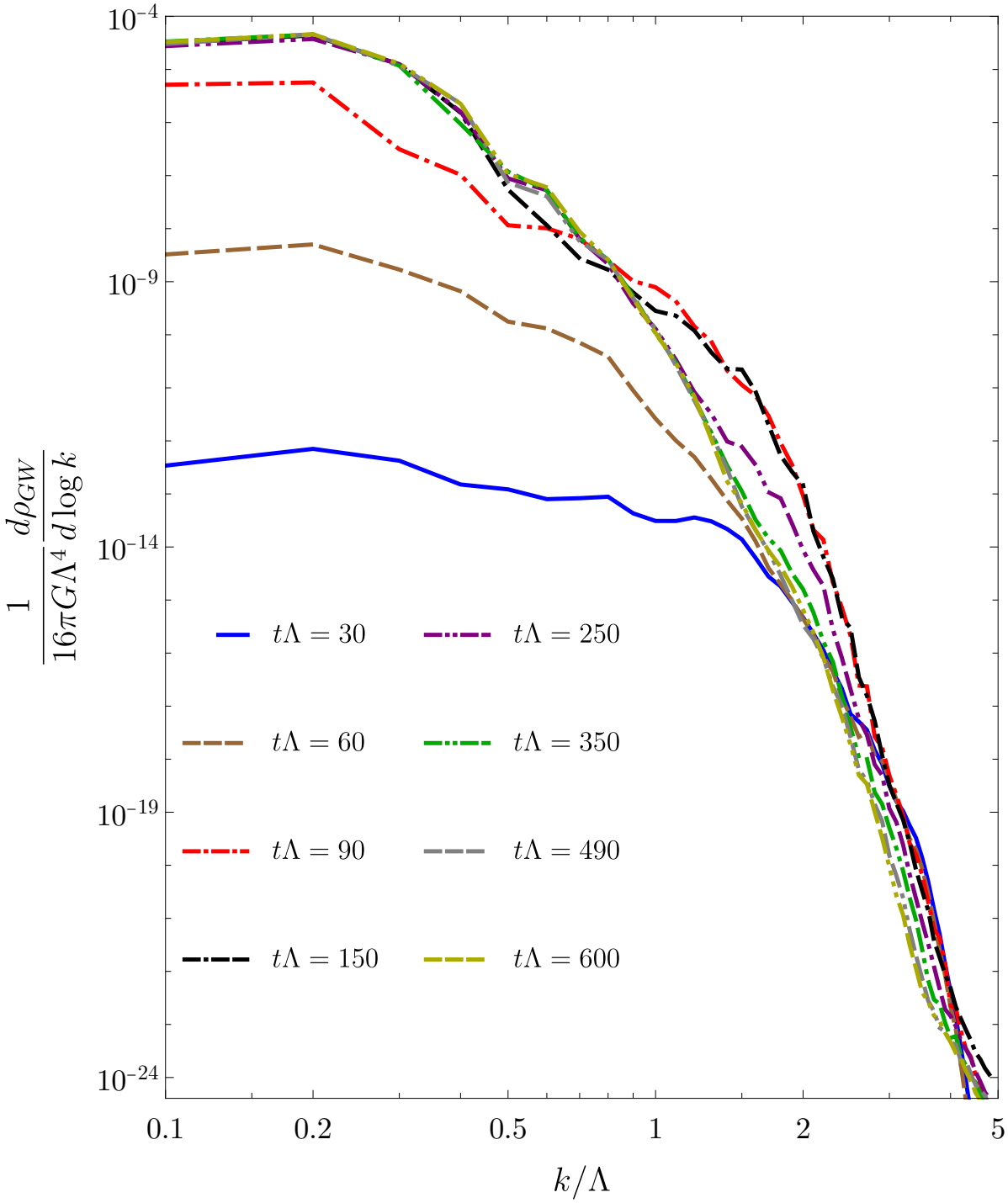

Figure 6.18: GW differential energy density per unit logarithmic momentum over the entire evolution.

Once the system enters the spinodal region, the physics at early times can be understood via a linear analysis around the unstable state. This makes two characteristic predictions. First, an exponential growth in time of the energy radiated into GWs, as illustrated by Fig. 6.17. Second, as shown by Figs. 6.15 and 6.16, a specific spectrum for the differential energy density per unit logarithmic momentum, $d\rho_{\rm GW}/d\log k$. The fact that this is qualitatively different from the spectrum in transitions mediated by bubble nucleation opens the exciting possibility of distinguishing them experimentally. Note from (6.3) that, up to a factor of order unity, the

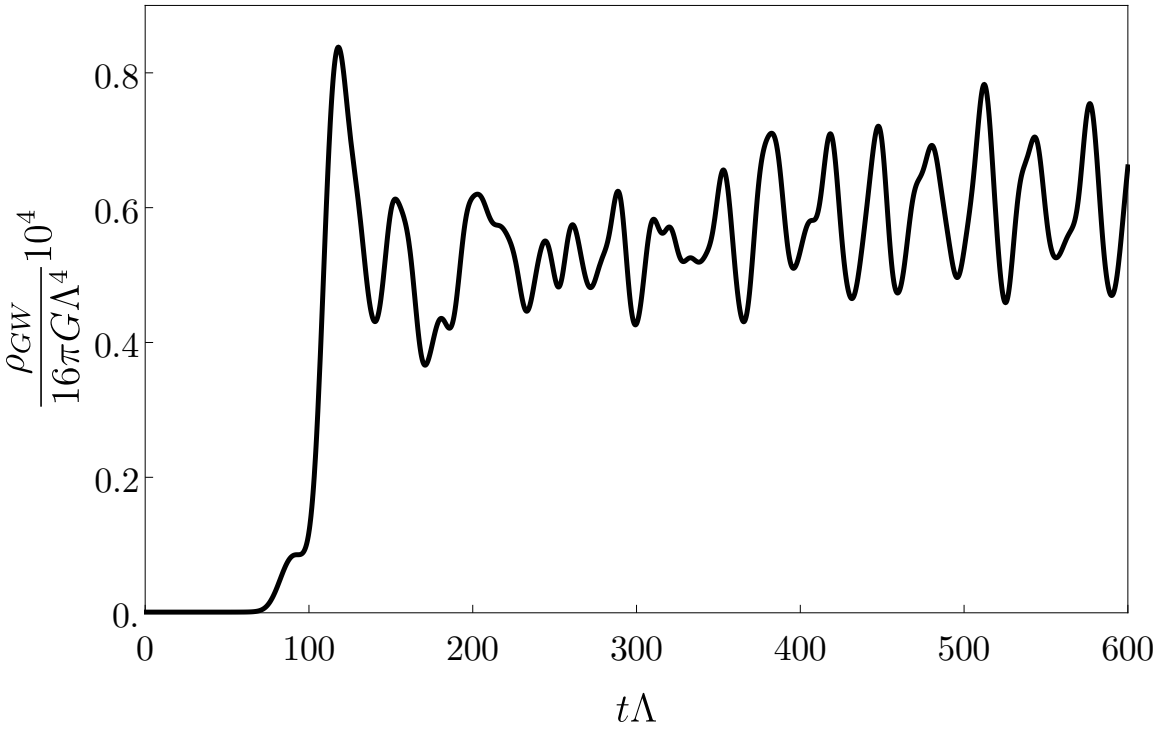

Figure 6.19: GW total energy density over the entire evolution.

scale Λ in this and other figures coincides with the critical temperature of the phase transition, T_c.

Interestingly, most of the radiated energy is produced in the short reshaping period that takes place right after the linear regime, as illustrated by Fig. 6.19. Presumably, the intuition for this is as follows. When a lump of energy is accelerated, the amount of GW radiation that is emitted increases both with the amount of energy in the lump and with the acceleration. During most of the linear regime the acceleration is large because of the exponential dependence in time, but the amount of energy being displaced is small since the initial state is homogeneous. During this regime peaks and valleys of increasing height and depth, respectively, get formed. The end of the linear regime takes place precisely when these peaks and valleys are close to their maximum values. At this point the accelerations involved in reshaping these structures are still large. This is the phase in which most of the GW emission takes place. At later times the energies being displaced are still large but the acceleration decreases as the system approaches the final, equilibrium state.

We are currently improving the simulation presented in this paper in two ways. First, we are running simulations on bigger boxes. This is important in order to be able to explore the low-k behaviour. Since the TT stress tensor attains a non-zero limit as $k \to 0$, we expect that in this limit

$$\frac{d\rho_{\rm GW}}{d\log k} \sim k^2 \,. \tag{6.128}$$

At the moment our infrared cutoff is $2\pi/L \simeq 0.1\Lambda$, which is not sufficiently smaller than $k_{\rm low}$ to verify this expected behaviour. Second, in our simulation we assumed that all modes have equal amplitudes at $t = 0$. In order to simulate a stochastic background, we are running several simulations in which the amplitudes of these fluctuations follow a normal distribution. This Gaussianity is justified by the fact that, in a large-N gauge theory, n-point connected

correlators with $n > 2$ are $1/N$-suppressed. In addition, since the second central moment of the random distribution is also $1/N$-suppressed with respect to the square of the mean energy density, the variance of the Gaussian distribution is also small in the large-N limit. This motivated our choice of a small $\delta\mathcal{E}/\mathcal{E} = 10^{-4}$ in the simulation presented here. Our preliminary results indicate that the stochasticity does not change our conclusions at the qualitative level.

In our time evolution we assumed that the boundary geometry where the gauge theory lives is flat space. In other words, we ignored the expansion of the Universe. The growth rate of the unstable modes in the linear regime is comparable to the Hubble rate, see (6.37), and the subsequent non-linear dynamics is slower, but not parametrically slower. Therefore, while it is reasonable to expect that neglecting the expansion of the Universe may provide a good approximation at the qualitative level, it would nevertheless be interesting to perform more sophisticated simulations including the expansion of the Universe. If the phase transition takes place in a hidden sector that is reacting to, but not affecting the, expansion of the Universe, then this would amount to fixing the boundary metric to be time-dependent but not dynamical, as in e.g. [133–140]. If the transition takes place in the sector driving the expansion of the Universe, then a more rigorous calculation should include the backreaction of the degrees of freedom undergoing the transition on the spacetime metric, along the lines of [141]. In both cases we expect that the behaviour of the system at sufficiently late times will be modified. The reason is that, in flat space, the system will tend at late times to a phase-separated state in which two phases with energy densities $\mathcal{E}_{\text{high}}$ and $\mathcal{E}_{\text{low}}$ coexist. In this way the spinodal instability leads to a redistribution of the total energy in a given volume from a homogeneous state with energy density $\mathcal{E} \simeq \mathcal{E}_s$ to two approximately homogeneous regions with smaller volumes and with energy densities $\mathcal{E}_{\text{low}} < \mathcal{E}_s < \mathcal{E}_{\text{high}}$. In an expanding Universe the energy density will keep decreasing everywhere, so the region with energy density $\mathcal{E}_{\text{high}}$ will cool down and eventually enter the spinodal phase again, leading to a repetition of the dynamics that we have discussed here. The volume of the region with energy density $\mathcal{E}_{\text{high}}$ decreases with each repetition. When this volume reaches a scale $\sim \Lambda^{-3}$ the spinodal instability no longer leads to a phase-separated configuration [63] and the process stops, leading to the completion of the phase transition.

Chapter 7

Final remarks

In this thesis we have explored the features and consequences of first order phase transitions in strongly coupled gauge theories with the help of holography. In order to capture the physics of phase transitions we used a bottom-up model consisting of Hilbert-Einstein gravity plus a self interacting scalar field in a 4+1 asymptotically AdS spacetime. The scalar field potential is a simple polynomial with two free parameters whose tuning give rise to a family of non-conformal boundary theories characterized by a unique energy scale Λ and its associated dimension three scalar operator.

Chapter 2 presented the techniques used to perform the numerical time evolution of Einstein's equations. We use the characteristic formulation, whose despite its potential problems it has proven to be very convenient to simulate infinitely extended black brane dynamics. The outcome is a freely accessible numerical code, named `Jecco`, written in the Julia programming language.

Chapters 3 and 4 will study setups whose dynamics is 1+1 dimensional. For them we will use `Jecco`'s predecesor, `SWEC`, already developed at the time this thesis started. The only modification required was the gravitational model change. In chapter 5 and 6 we moved on to using `Jecco`.

In chapter 3 we studied the set of inhomogeneous solutions present in a large-N_c theory with a first order thermal phase transition. Analogous families are expected to be present in generic first order phase transitions due to the spinodal instability. We obtained the thermodynamic properties of the states at finite size L and observed inhomogeneous-inhomogeneous together with inhomogeneous-homogeneous phase transitions of first and second order. As $L \to \infty$ the thermodynamically preferred set of solution tends to the well known phase separated configurations. Non-uniform states are dual to horizons that break the translational invariance along one of the boundary directions.

In chapter 4 we investigated the collision dynamics of phase domains, which are part of the familiy of non-uniform states found in the previous chapter for large enough L. This collisions were found in the past as an intermediate during the full time evolution of the spinodal instability.

We scanned over initial domain speeds while fixing the rest of the parameters of the problem. We uncovered three regimes of collision dynamics. For low velocities, the domains initially slow down and enter a quasistatic regime in which they move towards each other slowly. Eventually the merge takes place and the result is a excited phase domain whose small perturbations oscillate as said by linear theory until equilibrium is reached. Intermediate domain speeds result in a similar merge but with no initial quasistatic regime. For high speeds the dynamics becomes much richer. The collision turns into a highly excited blob that breaks down into two small pieces that travel away in opposite directions. Due to the periodic boundary conditions, the fragments merge again on the other side of the system. The dissipaive nature of the system implies that at each merge domains move slower until it falls into the category of intermediate

or low speed merger.

We then moved to understand a crucial part in the dynamical realization of first order phase transitions, bubble dynamics. Chapter 5 shows the results found for expanding planar bubbles first (`SWEC`) and for cylindrical ones after (`Jecco`). We found that there is a unique late time bubble for each nucleation temperature, including the value of its wall velocity. As it is assumed in the literature the profile is self similar, being richer for cylindrical ones, and ideal hydrodynamics is applicable everywhere except at the wall. For planar bubbles the wall seems unique only dependent on the theory, but this is not the case for cylindrical bubbles. Moreover, we observed a plausible linear relation between the wall speed and the pressure jump across the bubble compared to the energy of the metastable state. More research might be required, including its validity for cylindrical bubbles, but this could be a very powerful tool to sensibly estimate the wall speed from the equilibrium properties of a theory.

Additionally, we studied the critical bubble for a unique nucleation temperature. Its importance resides in its direct connection with the bubble nucleation rate, which affects the subsequent expected bubble number density in the early universe. By tuning the initial conditions we managed to obtain bubbles close to the critical, bounding its radius within a 2% range. Further study of the critical bubble would be interesting. By using similar techniques to the ones employed in 3, a more systematic study could be conducted.

Finally, in chapter 6, we analyzed the possibility of the early universe avoiding the bubble nucleation, expansion and collision. We concluded that, for theories that have sufficient degrees of freedom (N_c) or for hidden sectors (where the its temperature is decoupled from the one driving the expansion) with a moderate number of degrees of freedom this is the case. In this scenario the universe would cool down all the way out of the metastable branch, into the spinodal, locally unstable one. Due to the instability, the slightlest thermal fluctuations will be exponentially enhanced.

We numerically followed the full, non-linear, time evolution of the instabilit. We computed the gravitational wave spectrum along the way by using the holographic stress tensor directly as a source for the linearized Einstein's Equations. The main conclusion is that one can also identify a linear regime in the gravitational wave emission with the same growth rate for a wide range of frequencies and exponentially suppress for high frequencies. Although the emission rate is fastest during the linear regime, the biggest amount of radiation is produced right after the linear regime. The frequency dependence of the emitted energy is manifestly different to a broken power law, the one arising in bubble collisions, which opens the exciting possibility of distinguishing them in next generation experiments.

7.1 Future directions

In what follows we expose some of the relevant projects we are pursuing at the moment and that represent an extension of this thesis.

First, it would be interesting to start by doing a deeper exploration of the cylindrical bubble expansion. More precisely we want to explore the dependence of different features of the bubbles as a function of the nucleation temperature, as it was done for planar bubbles; where there is particular interest on checking the validity of the linear relation found for the wall speed of planar bubbles. Additionally, so far we have only obtained bubble wall velocities up to $v \sim 0.3$, which is lower than the speed of sound of the fluid ahead of the wall. This is referred to as a deflagrations, while those in which the velocity is greater thatn the speed of sound is a detonation. The features predicted by hydrodynamics for detonations are substantially different, so an extension of our study to such case is of great interest.

Going further into a systematic way of studying the bubble properties, junction conditions could be the answer. At late times the bubble profile consists of multiple, in local equilibrium regions of size much bigger than the connecting surfaces, the wall and the interface. The dual

to this picture is that of different geometries joined by presumably thin walls. In this kind of setups one has to impose certain conditions on the separating hypersurfaces so that properties transition consistently from one side to the other. This conditions are expected to restrict the velocity wall to a unique value, given the geometries under consideration. In other words, the holographic direction is the microscopic information we require to link the velocity to the nucleation temperature. Such an approach is considerably more efficient when wanting to scan over several theories and nucleation temperatures.

Regarding the collision of bubbles, its direct simulation is of great interest. In a similar fashion to what was done in chapter 6, we will follow the full time evolution of the collision of bubbles and use the read off boundary energy-stress tensor as a source for gravitational waves. In this study not only the direct computation of the emission and the applicability of hydrodynamics is of great interest. We would like to identify the relevance of the emission coming from turbulence, how does it compared to the emission from sound waves and to what extent the estimations done in the literature are justified.

In another order of things, we are making steps towards the extension of previous Heavy Ion Collisions to non-conformal theories at finite baryonic charge. In the literature we find simulations in either non-conformal theories or conformal ones at finite charge density. The proposed setup would get holographic collisions one step closer to the experiments. We will explore the behavior of the plasma near the hypothesized critical point and obtain important lessons to have in mind in next generation experiments. Additionally, `Jecco`, being a code with dynamics along 2+1 directions, will allow us to study collisions other than head on, where the effect of angular momentum on the phase transition can be investigated.

Finally, a longer term project is to deep ourselves into the gravitational wave emission from neutron stars. Holography provides us with many possible strongly coupled theories whose equation of state and transport coefficients can be extracted and used for neutron star collision simulation. Thanks to the possibility of playing with many holographic models, numerous different simulations can be performed, from where we can infer the implications in the gravitational wave signal and the imprint left by the QCD transport properties.

Over the years holography has shown to be a powerful approach to treating strongly coupled QFTs and/or out-of-equilibrium physics. This thesis represents yet another step into the understanding of the physics involved in two of the most exciting experiments of our era. With the development of the new code, `Jecco`, we sure expect this to be the beginning of a period of novel results.

Appendix A

Nested Scheme of ODEs

We list the radial equations obtained from ansatz (2.8). It is useful to introduce the following variables,

$$\begin{aligned}
f' &= \partial_r f\,, \\
\dot{f} &= \left(\partial_t + \frac{A}{2}\partial_r\right) f\,, \\
\tilde{f} &= \left(\partial_x - F_x\partial_r\right) f\,, \\
\hat{f} &= \left(\partial_y - F_y\partial_r\right) f\,, \\
\bar{f} &= \left(\partial_x^2 - 2F_x\partial_r\partial_x + F_x^2\partial_r^2\right) f\,, \\
f^\star &= \left(\partial_y^2 - 2F_y\partial_r\partial_y + F_y^2\partial_r^2\right) f\,, \\
f^\times &= \left(\partial_x\partial_y - F_x\partial_r\partial_y - F_y\partial_r\partial_x + F_xF_y\partial_r^2\right) f\,.
\end{aligned} \tag{A.1}$$

The full set of equations is:

$$6S'' + S\left(\cosh^2(G)\left(B_1'\right)^2 + 3\left(B_2'\right)^2 + \left(G'\right)^2 + \left(\phi'\right)^2\right) = 0 \tag{A.2}$$

$$\begin{aligned}
&2e^{B_1}S^2F_x'' + e^{B_1}\left(S^2\left(-2\left(\cosh^2(G)\left(\tilde{B}_1{}' - B_1'F_x'\right) + B_2'\left(3\tilde{B}_2 - F_x'\right) + \tilde{G}\left(B_1'\sinh(2G) + G'\right) + \tilde{B}_2{}'\right.\right.\right. \\
&\left.\left.\left.+4\tilde{\phi}\phi'\right) - 2\tilde{B}_1B_1'\cosh^2(G)\right) + S\left(-6\tilde{S}\left(B_1'\cosh^2(G) + B_2'\right) - 8\tilde{S}' + 2S'F_x'\right) + 8\tilde{S}S'\right) \\
&+ S^2\left(-2G'\left(\hat{B}_1 + F_y'\right) + \sinh(2G)\left(\hat{B}_1{}' - B_1'\left(\hat{B}_1 + F_y'\right)\right) + 2\hat{G}B_1'\cosh(2G) + 2\hat{G}'\right) \\
&+ 3\hat{S}S\left(B_1'\sinh(2G) + 2G'\right) = 0
\end{aligned}$$

$$\begin{aligned}
&2S^2F_y'' + e^{B_1}\left(S^2\left(2\left(G'\left(\tilde{B}_1 - F_x'\right) + \tilde{G}'\right) - \sinh(2G)\left(B_1'\left(\tilde{B}_1 - F_x'\right) + \tilde{B}_1{}'\right) - 2\tilde{G}B_1'\cosh(2G)\right)\right. \\
&\left.-3S\tilde{S}\left(B_1'\sinh(2G) - 2G'\right)\right) + 2S^2\left(\cosh^2(G)\left(\hat{B}_1{}' - B_1'F_y'\right) + B_2'\left(F_y' - 3\hat{B}_2\right)\right. \\
&\left.+\hat{G}\left(B_1'\sinh(2G) - G'\right) - \hat{B}_1B_1'\cosh^2(G) - \hat{B}_2{}' - 4\hat{\phi}\phi'\right) + S\left(6\hat{S}\left(B_1'\cosh^2(G) - B_2'\right)\right. \\
&\left.+2S'F_y' - 8\hat{S}'\right) + 8\hat{S}S' = 0
\end{aligned} \tag{A.3}$$

$$
\begin{aligned}
&12e^{B_1}S^3\dot{S}' + e^{B_1+B_2}\left(S^2\left(2\cosh(G)\left(-\hat{G}\left(\tilde{B}_1+\tilde{B}_2-F_x'\right)+\tilde{G}\left(\hat{B}_1-\hat{B}_2+F_y'\right)+G'\left(\tilde{F}_y+\hat{F}_x\right)\right.\right.\right.\\
&\left.-2G^{\times}\right)+2\sinh(G)\left(B_2'\left(\tilde{F}_y+\hat{F}_x\right)+F_y'\left(\tilde{B}_2-F_x'\right)+\hat{B}_2\left(F_x'-4\tilde{B}_2\right)-2{B_2}^{\times}+{\tilde{F}_y}'\right.\\
&\left.-2\hat{G}\tilde{G}-4\hat{\phi}\tilde{\phi}+{\hat{F}_x}'\right)\Big)+S\left(2\sinh(G)\left(\hat{S}\left(F_x'-4\tilde{B}_2\right)+\tilde{S}\left(F_y'-4\hat{B}_2\right)\right.\right.\\
&\left.+4S'\left(\tilde{F}_y+\hat{F}_x\right)-8S^{\times}\right)-8\cosh(G)\left(\hat{S}\tilde{G}+\hat{G}\tilde{S}\right)\Big)+8\hat{S}\tilde{S}\sinh(G)\Big)+e^{2B_1+B_2}\left(S^2\right.\\
&\left(2\sinh(G)\left(\tilde{G}\left(2\tilde{B}_1+\tilde{B}_2-F_x'\right)-G'\tilde{F}_x+\bar{G}\right)+\cosh(G)\left(2\left(-\left(B_1'+B_2'\right)\tilde{F}_x\right.\right.\right.\\
&\left.+\bar{B}_1+\bar{B}_2-{\tilde{F}_x}'+\tilde{G}^2+2\tilde{\phi}^2\right)-2\left(\tilde{B}_1+\tilde{B}_2\right)F_x'+2\left({\tilde{B}_1}^2+\tilde{B}_2\tilde{B}_1+2{\tilde{B}_2}^2\right)+\left(F_x'\right)^2\Big)\Big)\\
&+S\left(2\cosh(G)\left(\tilde{S}\left(4\left(\tilde{B}_1+\tilde{B}_2\right)-F_x'\right)+4\left(\bar{S}-S'\tilde{F}_x\right)\right)+8\tilde{G}\tilde{S}\sinh(G)\right)\\
&-4\tilde{S}^2\cosh(G)\Big)+e^{B_2}\left(S^2\left(2\sinh(G)\left(\hat{G}\left(-2\hat{B}_1+\hat{B}_2-F_y'\right)-\hat{F}_yG'+G^{\star}\right)\right.\right.\\
&+\cosh(G)\left(2\left(\left(B_1'-B_2'\right)\hat{F}_y-B_1^{\star}+B_2^{\star}-{\hat{F}_y}'+\hat{G}^2+2\hat{\phi}^2\right)+2\left(\hat{B}_1-\hat{B}_2\right)F_y'\right.\\
&\left.+2\left({\hat{B}_1}^2-\hat{B}_2\hat{B}_1+2{\hat{B}_2}^2\right)+\left(F_y'\right)^2\right)\Big)+S\left(8\hat{G}\hat{S}\sinh(G)-2\cosh(G)\right.\\
&\left.\left(\hat{S}\left(4\hat{B}_1-4\hat{B}_2+F_y'\right)+4\hat{F}_yS'-4S^{\star}\right)\right)-4\hat{S}^2\cosh(G)\Big)+e^{B_1}\left(8S^4V(\phi)+24\dot{S}S^2S'\right)\\
&=0
\end{aligned}
\tag{A.4}
$$

$$
\begin{aligned}
&12e^{B_1}S^4\dot{B}_1'+e^{B_1+B_2}\left(6S^2\mathrm{sech}(G)\left(\hat{G}\left(F_x'-\tilde{B}_2\right)+\tilde{G}\left(\hat{B}_2-F_y'\right)+G'\left(\tilde{F}_y-\hat{F}_x\right)\right)+6S\mathrm{sech}(G)\right.\\
&\left(\hat{S}\tilde{G}-\hat{G}\tilde{S}\right)\Big)+e^{2B_1+B_2}\left(-3S^2\mathrm{sech}(G)\left(-2B_2'\tilde{F}_x-2\tilde{B}_2F_x'+4{\tilde{B}_2}^2+2\bar{B}_2-2{\tilde{F}_x}'+4\tilde{\phi}^2\right.\right.\\
&\left.+\left(F_x'\right)^2\right)-6S\mathrm{sech}(G)\left(\tilde{S}\left(\tilde{B}_2+2F_x'\right)-S'\tilde{F}_x+\bar{S}\right)+12\tilde{S}^2\mathrm{sech}(G)\Big)+e^{B_2}\\
&\left(3S^2\mathrm{sech}(G)\left(-2B_2'\hat{F}_y-2\hat{B}_2F_y'+4{\hat{B}_2}^2+2B_2^{\star}+\left(F_y'\right)^2-2{\hat{F}_y}'+4\hat{\phi}^2\right)+6S\mathrm{sech}(G)\right.\\
&\left(\hat{S}\left(\hat{B}_2+2F_y'\right)-\hat{F}_yS'+S^{\star}\right)-12\hat{S}^2\mathrm{sech}(G)\Big)+e^{B_1}\left(12S^4\tanh(G)\left(\dot{B}_1G'+\dot{G}B_1'\right)\right.\\
&\left.+18S^3\left(\dot{B}_1S'+\dot{S}B_1'\right)\right)=0
\end{aligned}
$$

$$
\begin{aligned}
&12e^{B_1}S^4\dot{G}'+e^{B_1+B_2}\left(6S^2\cosh(G)\left(B_1'\left(\hat{F}_x-\tilde{F}_y\right)-B_2'\left(\tilde{F}_y+\hat{F}_x\right)+\left(\hat{B}_1-F_y'\right)\left(\tilde{B}_2-F_x'\right)-\hat{B}_2\right.\right.\\
&\left(\tilde{B}_1-4\tilde{B}_2+F_x'\right)+\tilde{B}_1F_y'+2B_2^{\times}-{\tilde{F}_y}'+4\hat{\phi}\tilde{\phi}-{\hat{F}_x}'\Big)+6S\cosh(G)\left(\hat{S}\left(-\tilde{B}_1+\tilde{B}_2+2F_x'\right)\right.\\
&\left.+\tilde{S}\left(\hat{B}_1+\hat{B}_2+2F_y'\right)-S'\left(\tilde{F}_y+\hat{F}_x\right)+2S^{\times}\right)-24\hat{S}\tilde{S}\cosh(G)\Big)+e^{2B_1+B_2}\left(-3S^2\sinh(G)\right.\\
&\left(-2B_2'\tilde{F}_x-2\tilde{B}_2F_x'+4{\tilde{B}_2}^2+2\bar{B}_2-2{\tilde{F}_x}'+4\tilde{\phi}^2+\left(F_x'\right)^2\right)-6S\sinh(G)\left(\tilde{S}\left(\tilde{B}_2+2F_x'\right)\right.\\
&\left.-S'\tilde{F}_x+\bar{S}\right)+12\tilde{S}^2\sinh(G)\Big)+e^{B_2}\left(-3S^2\sinh(G)\left(-2B_2'\hat{F}_y-2\hat{B}_2F_y'+4{\hat{B}_2}^2+2B_2^{\star}+\left(F_y'\right)^2\right.\right.\\
&\left.-2{\hat{F}_y}'+4\hat{\phi}^2\right)-6S\sinh(G)\left(\hat{S}\left(\hat{B}_2+2F_y'\right)-\hat{F}_yS'+S^{\star}\right)+12\hat{S}^2\sinh(G)\Big)+e^{B_1}\left(18S^3\right.\\
&\left.\left(\dot{S}G'+\dot{G}S'\right)-6\dot{B}_1S^4B_1'\sinh(2G)\right)=0
\end{aligned}
\tag{A.5}
$$

$$
\begin{aligned}
&12e^{B_1}S^4\dot{B}_2{}' + e^{B_1+B_2}\Big(S^2\Big(2\cosh(G)\Big(\hat{G}\Big(\tilde{B}_1 - 2\tilde{B}_2 - F_x'\Big) - \tilde{G}\Big(\hat{B}_1 + 2\hat{B}_2 + F_y'\Big) - G'\Big(\tilde{F}_y + \hat{F}_x\Big)\\
&+2G^{\times}\Big) + 2\sinh(G)\Big(2B_2'\Big(\tilde{F}_y + \hat{F}_x\Big) + F_y'\Big(2\tilde{B}_2 + F_x'\Big) + 2\hat{B}_2\Big(F_x' - \tilde{B}_2\Big) - 4B_2^{\times} - \tilde{F}_y{}' + 2\hat{G}\tilde{G}\\
&+4\hat{\phi}\tilde{\phi} - \hat{F}_x{}'\Big)\Big) + S\Big(2\sinh(G)\Big(2\Big(\hat{S}\Big(F_x' - \tilde{B}_2\Big) + \tilde{S}\Big(F_y' - \hat{B}_2\Big) + S^{\times}\Big) - S'\Big(\tilde{F}_y + \hat{F}_x\Big)\Big)\\
&+2\cosh(G)\Big(\hat{S}\tilde{G} + \hat{G}\tilde{S}\Big)\Big) - 8\hat{S}\tilde{S}\sinh(G)\Big) + e^{2B_1+B_2}\Big(S^2\Big(2\sinh(G)\Big(\tilde{G}\Big(-2\tilde{B}_1 + 2\tilde{B}_2 + F_x'\Big)\\
&+G'\tilde{F}_x - \bar{G}\Big) - \cosh(G)\Big(2\Big(-\left(B_1' - 2B_2'\right)\tilde{F}_x + \bar{B}_1 - 2\bar{B}_2 - \tilde{F}_x{}' + \tilde{G}^2 + 2\tilde{\phi}^2\Big) - 2\Big(\tilde{B}_1 - 2\tilde{B}_2\Big)F_x'\\
&+2\Big(\tilde{B}_1{}^2 - 2\tilde{B}_2\tilde{B}_1 - \tilde{B}_2{}^2\Big) + \left(F_x'\right)^2\Big)\Big) + S\Big(-2\cosh(G)\Big(\tilde{S}\Big(\tilde{B}_1 - 2\tilde{B}_2 + 2F_x'\Big) - S'\tilde{F}_x + \bar{S}\Big)\\
&-2\tilde{G}\tilde{S}\sinh(G)\Big) + 4\tilde{S}^2\cosh(G)\Big) + e^{B_2}\Big(S^2\Big(2\sinh(G)\Big(\hat{G}\Big(2\Big(\hat{B}_1 + \hat{B}_2\Big) + F_y'\Big) + \hat{F}_yG' - G^{\star}\Big)\\
&-\cosh(G)\Big(2\Big(\left(B_1' + 2B_2'\right)\hat{F}_y - B_1^{\star} - 2B_2^{\star} - \hat{F}_y{}' + \hat{G}^2 + 2\hat{\phi}^2\Big) + 2\Big(\hat{B}_1 + 2\hat{B}_2\Big)F_y'\\
&+2\Big(\hat{B}_1{}^2 + 2\hat{B}_2\hat{B}_1 - \hat{B}_2{}^2\Big) + \Big(F_y'\Big)^2\Big)\Big) + S\Big(2\cosh(G)\Big(\hat{S}\Big(\hat{B}_1 + 2\hat{B}_2 - 2F_y'\Big) + \hat{F}_yS' - S^{\star}\Big)\\
&-2\hat{G}\hat{S}\sinh(G)\Big) + 4\hat{S}^2\cosh(G)\Big) + 18e^{B_1}S^3\Big(\dot{B}_2S' + \dot{S}B_2'\Big) = 0
\end{aligned}
\tag{A.6}
$$

$$
\begin{aligned}
&8e^{B_1}S^3\dot{\phi}' + e^{B_1+B_2}\Big(S\Big(4\sinh(G)\Big(\hat{\phi}\Big(F_x' - \tilde{B}_2\Big) + \tilde{\phi}\Big(F_y' - \hat{B}_2\Big) + \phi'\Big(\tilde{F}_y + \hat{F}_x\Big) - 2\phi^{\times}\Big) - 4\cosh(G)\\
&\Big(\hat{\phi}\tilde{G} + \hat{G}\tilde{\phi}\Big)\Big) - 4\sinh(G)\Big(\hat{\phi}\tilde{S} + \hat{S}\tilde{\phi}\Big)\Big) + e^{2B_1+B_2}\Big(4S\Big(\cosh(G)\Big(\tilde{\phi}\Big(\tilde{B}_1 + \tilde{B}_2 - F_x'\Big)\\
&-\phi'\tilde{F}_x + \bar{\phi}\Big) + \tilde{G}\tilde{\phi}\sinh(G)\Big) + 4\tilde{S}\tilde{\phi}\cosh(G)\Big) + e^{B_2}\Big(S\Big(4\hat{G}\hat{\phi}\sinh(G) - 4\cosh(G)\\
&\Big(\hat{\phi}\Big(\hat{B}_1 - \hat{B}_2 + F_y'\Big) + \hat{F}_y\phi' - \phi^{\star}\Big)\Big) + 4\hat{S}\hat{\phi}\cosh(G)\Big) + e^{B_1}\Big(12S^2\Big(\dot{\phi}S' + \dot{S}\phi'\Big)\\
&-4S^3V'(\phi)\Big) = 0
\end{aligned}
\tag{A.7}
$$

$$
\begin{aligned}
&6e^{B_1}S^4A'' + e^{B_1+B_2}\Big(S^2\Big(6\cosh(G)\Big(\Big(\hat{B}_2 - \hat{B}_1\Big)\tilde{G} + \hat{G}\Big(\tilde{B}_1 + \tilde{B}_2\Big) - G'\Big(\tilde{F}_y + \hat{F}_x\Big) + 2G^{\times}\Big)\\
&+6\sinh(G)\Big(-B_2'\Big(\tilde{F}_y + \hat{F}_x\Big) + 2B_2^{\times} + 4\hat{B}_2\tilde{B}_2 + 2\hat{G}\tilde{G} + 4\hat{\phi}\tilde{\phi} - F_x'F_y'\Big)\Big) + 24S\left(\sinh(G)\right.\\
&\Big(\hat{B}_2\tilde{S} + \hat{S}\tilde{B}_2 - S'\Big(\tilde{F}_y + \hat{F}_x\Big) + 2S^{\times}\Big) + \cosh(G)\Big(\hat{S}\tilde{G} + \hat{G}\tilde{S}\Big)\Big) - 24\hat{S}\tilde{S}\sinh(G)\Big)\\
&+ e^{2B_1+B_2}\Big(S^2\Big(3\cosh(G)\Big(\left(F_x'\right)^2 - 2\Big(-\left(B_1' + B_2'\right)\tilde{F}_x + \tilde{B}_1{}^2 + 2\tilde{B}_2{}^2 + \bar{B}_1 + \bar{B}_2 + \tilde{B}_1\tilde{B}_2\\
&+\tilde{G}^2 + 2\tilde{\phi}^2\Big)\Big) - 6\sinh(G)\Big(\Big(2\tilde{B}_1 + \tilde{B}_2\Big)\tilde{G} - G'\tilde{F}_x + \bar{G}\Big)\Big) + S\left(-24\cosh(G)\right.\\
&\Big(\Big(\tilde{B}_1 + \tilde{B}_2\Big)\tilde{S} - S'\tilde{F}_x + \bar{S}\Big) - 24\tilde{G}\tilde{S}\sinh(G)\Big) + 12\tilde{S}^2\cosh(G)\Big)\\
&+ e^{B_2}\Big(S^2\Big(6\sinh(G)\Big(\Big(2\hat{B}_1 - \hat{B}_2\Big)\hat{G} + \hat{F}_yG' - G^{\star}\Big) + 3\cosh(G)\\
&\Big(\Big(F_y'\Big)^2 - 2\Big(\left(B_1' - B_2'\right)\hat{F}_y + \hat{B}_1{}^2 + 2\hat{B}_2{}^2 - B_1^{\star} + B_2^{\star} - \hat{B}_1\hat{B}_2 + \hat{G}^2 + 2\hat{\phi}^2\Big)\Big)\Big)\\
&+S\Big(24\cosh(G)\Big(\Big(\hat{B}_1 - \hat{B}_2\Big)\hat{S} + \hat{F}_yS' - S^{\star}\Big) - 24\hat{G}\hat{S}\sinh(G)\Big) + 12\hat{S}^2\cosh(G)\Big)\\
&+ e^{B_1}\Big(S^4\Big(6\Big(\dot{B}_1B_1'\cosh^2(G) + 3\dot{B}_2B_2' + \dot{G}G' + 4\dot{\phi}\phi' + 4\Big) - 2(4V(\phi) + 12)\Big) - 72S^2\dot{S}S'\Big)\\
&= 0
\end{aligned}
\tag{A.8}
$$

$$
\begin{aligned}
&6e^{B_1}\ddot{S}S^3 + e^{B_1+B_2}\left(S^2\left(\sinh(G)\left(-A'\left(\tilde{F}_y+\hat{F}_x\right)+\hat{B}_2\left(\tilde{A}+2\dot{F}_x\right)+\tilde{B}_2\left(\hat{A}+2\dot{F}_y\right)+2A^{\times}+2\tilde{\dot{F}}_y\right.\right.\right.\\
&\left.\left.+2\hat{\dot{F}}_x\right)+\cosh(G)\left(\hat{G}\left(\tilde{A}+2\dot{F}_x\right)+\tilde{G}\left(\hat{A}+2\dot{F}_y\right)\right)\right)+S\sinh(G)\left(\hat{S}\left(\tilde{A}+2\dot{F}_x\right)\right.\\
&\left.\left.+\tilde{S}\left(\hat{A}+2\dot{F}_y\right)\right)\right)+e^{2B_1+B_2}\left(S^2\left(\tilde{G}\sinh(G)\left(-\left(\tilde{A}+2\dot{F}_x\right)\right)-\cosh(G)\left(-A'\tilde{F}_x\right.\right.\right.\\
&\left.\left.\left.+\left(\tilde{B}_1+\tilde{B}_2\right)\left(\tilde{A}+2\dot{F}_x\right)+\bar{A}+2\tilde{\dot{F}}_x\right)\right)-S\tilde{S}\cosh(G)\left(\tilde{A}+2\dot{F}_x\right)\right)-e^{B_1+2B_2}\left(\hat{F}_x-\tilde{F}_y\right)^2\\
&+e^{B_2}\left(S^2\left(\cosh(G)\left(A'\hat{F}_y+\left(\hat{B}_1-\hat{B}_2\right)\left(\hat{A}+2\dot{F}_y\right)-A^{\star}-2\hat{\dot{F}}_y\right)-\hat{G}\sinh(G)\left(\hat{A}+2\dot{F}_y\right)\right)\right.\\
&\left.-S\hat{S}\cosh(G)\left(\hat{A}+2\dot{F}_y\right)\right)+e^{B_1}\left(S^4\left(\dot{B_1}^2\cosh^2(G)+3\dot{B_2}^2+\dot{G}^2+4\dot{\phi}^2\right)-3S^3\dot{S}A'\right)=0
\end{aligned}
\tag{A.9}
$$

$$
\begin{aligned}
&4e^{B_1}S^3\dot{F_x}'+e^{B_1}\left(2S^3\left(\left(\tilde{A}+2\dot{F}_x\right)\left(B_1'\cosh^2(G)+B_2'\right)+2\tilde{A}'+2\tilde{\dot{B}}_1\cosh^2(G)\right.\right.\\
&\left.+2\dot{B}_1\left(\tilde{B}_1\cosh^2(G)+\tilde{G}\sinh(2G)\right)+2\tilde{\dot{B}}_2+6\dot{B}_2\tilde{B}_2+2\dot{G}\tilde{G}+8\dot{\phi}\tilde{\phi}-A'F_x'\right)+4S^2\\
&\left(-S'\left(\tilde{A}+2\dot{F}_x\right)+3\tilde{S}\left(\dot{B}_1\cosh^2(G)+\dot{B}_2\right)+4\tilde{\dot{S}}+3\dot{S}F_x'\right)-16\dot{S}S\tilde{S}\Big)+e^{B_1+B_2}\\
&\left(4S\sinh(G)\left(\hat{F}_x\left(F_x'-2\tilde{B}_2\right)+2\tilde{B}_2\tilde{F}_y-\tilde{F}_xF_y'-F_x^{\times}+\bar{F}_y\right)+4\tilde{S}\sinh(G)\left(\hat{F}_x-\tilde{F}_y\right)\right)\\
&+e^{B_2}\left(4S\cosh(G)\left(2\hat{B}_2\left(\hat{F}_x-\tilde{F}_y\right)+\tilde{F}_yF_y'-F_y^{\times}-\hat{F}_yF_x'+F_x^{\star}\right)+4\hat{S}\cosh(G)\left(\tilde{F}_y-\hat{F}_x\right)\right)\\
&+S^3\left(-\left(\hat{A}+2\dot{F}_y\right)\left(B_1'\sinh(2G)+2G'\right)+4\hat{B}_1\dot{G}-2\hat{\dot{B}}_1\sinh(2G)+2\dot{B}_1\left(\hat{B}_1\sinh(2G)\right.\right.\\
&\left.\left.-2\hat{G}\cosh(2G)\right)-4\hat{\dot{G}}\right)-6\hat{S}S^2\left(\dot{B}_1\sinh(2G)+2\dot{G}\right)=0\\
&4S^3\dot{F_y}'+e^{B_1}\left(S^3\left(\left(\tilde{A}+2\dot{F}_x\right)\left(B_1'\sinh(2G)-2G'\right)-4\dot{G}\tilde{B}_1+2\tilde{\dot{B}}_1\sinh(2G)+2\dot{B}_1\left(\tilde{B}_1\sinh(2G)\right.\right.\right.\\
&\left.\left.+2\tilde{G}\cosh(2G)\right)-4\tilde{\dot{G}}\right)+6S^2\tilde{S}\left(\dot{B}_1\sinh(2G)-2\dot{G}\right)\Big)+e^{B_2}\left(4S\sinh(G)\left(2\hat{B}_2\left(\hat{F}_x-\tilde{F}_y\right)\right.\right.\\
&\left.+\tilde{F}_yF_y'-F_y^{\times}-\hat{F}_yF_x'+F_x^{\star}\right)+4\hat{S}\sinh(G)\left(\tilde{F}_y-\hat{F}_x\right)\Big)+e^{B_1+B_2}\left(4S\cosh(G)\left(\hat{F}_x\left(F_x'-2\tilde{B}_2\right)\right.\right.\\
&\left.+2\tilde{B}_2\tilde{F}_y-\tilde{F}_xF_y'-F_x^{\times}+\bar{F}_y\right)+4\tilde{S}\cosh(G)\left(\hat{F}_x-\tilde{F}_y\right)\Big)+2S^3\left(-A'F_y'-\left(\hat{A}+2\dot{F}_y\right)\right.\\
&\left(B_1'\cosh^2(G)-B_2'\right)+2\hat{A}'-2\hat{\dot{B}}_1\cosh^2(G)+2\dot{B}_1\left(\hat{B}_1\cosh^2(G)-\hat{G}\sinh(2G)\right)+2\hat{\dot{B}}_2+6\dot{B}_2\hat{B}_2\\
&\left.+2\dot{G}\hat{G}+8\dot{\phi}\hat{\phi}\right)+4S^2\left(-S'\left(\hat{A}+2\dot{F}_y\right)+3\hat{S}\left(\dot{B}_2-\dot{B}_1\cosh^2(G)\right)+3\dot{S}F_y'+4\hat{\dot{S}}\right)-16\dot{S}\hat{S}S\\
&=0
\end{aligned}
\tag{A.10}
$$

Appendix B

Tracking the Apparent Horizon

We find the Apparent Horizon by imposing that the outgoing null-ray congruence has vanishing expansion while the ingoing one has negative. In other words, we find the marginally trapped surface . We can construct the tangent vector to such outgoing congruence using the ingoing null rays, n, together with the form perpendicular to the AH, s,

$$\begin{aligned} &= N_s \left(-\partial_t\sigma dt - \partial_y\sigma dy - \partial_y\sigma dy + dr\right), \\ &= -N_n \partial_r, \end{aligned} \tag{B.1}$$

The normalisation factors, N_s and N_n, can be computed by imposing $s^2 = 1$ and $s \cdot n = -1/\sqrt{2}$. Outgoing light ray tangent vector is then,

$$l^\mu = \sqrt{2} s^\mu + n^\mu, \tag{B.2}$$

with normalization, $l \cdot n = -1$. The expansion then follows,

$$\theta_l = h^{\mu\nu} \nabla_\mu l_\nu, \tag{B.3}$$

where

$$h_{\mu\nu} = g_{\mu\nu} + l_\mu n_\nu + l_\nu n_\mu \tag{B.4}$$

is the induced metric over hypersurfaces normal to both in- and out-going null rays. The AH should be the surface $\sigma(t, x, y)$ such that it vanishes the expansion $r = \theta_l$,

$$\begin{aligned} &2e^{B_2}\left(F_y + \partial_y\sigma\right)\Big(S\left(e^{B_1}\cosh(G)\left(\tilde{G} + G'\left(F_x + \partial_x\sigma\right)\right) + e^{B_1}\sinh(G)\left(\tilde{B}_2 + B_2'\left(F_x + \partial_x\sigma\right)\right)\right. \\ &\left. + \cosh(G)\left(B_1'\left(F_y + \partial_y\sigma\right) + \hat{B}_1\right) - \cosh(G)\left(B_2'\left(F_y + \partial_y\sigma\right) + \hat{B}_2\right) - \sinh(G)\left(G'\left(F_y + \partial_y\sigma\right) + \hat{G}\right)\right) \\ &+ e^{B_1}\sinh(G)\left(\tilde{S} - 2S'\left(F_x + \partial_x\sigma\right)\right) - \cosh(G)\left(S'\left(F_y + \partial_y\sigma\right) + \hat{S}\right)\Big) - 2e^{B_1+B_2}\left(F_x + \partial_x\sigma\right) \\ &\Big(S\left(e^{B_1}\left(\cosh(G)\left(\tilde{B}_1 + B_1'\left(F_x + \partial_x\sigma\right)\right) + \cosh(G)\left(\tilde{B}_2 + B_2'\left(F_x + \partial_x\sigma\right)\right)\right.\right. \\ &\left.\left. + \sinh(G)\left(\tilde{G} + G'\left(F_x + \partial_x\sigma\right)\right)\right) - \sinh(G)\left(B_2'\left(F_y + \partial_y\sigma\right) + \hat{B}_2\right) - \cosh(G)\left(G'\left(F_y + \partial_y\sigma\right) + \hat{G}\right)\right) \\ &+ e^{B_1}\cosh(G)\left(\tilde{S} + S'\left(F_x + \partial_x\sigma\right)\right) - \sinh(G)\left(S'\left(F_y + \partial_y\sigma\right) + \hat{S}\right)\Big) + S\Big(e^{B_1}\Big(2e^{B_2}\sinh(G) \\ &\left(\tilde{F}_y + F_y'\left(F_x + \partial_x\sigma\right) + \partial_{xy}\sigma\right) - 2e^{B_1+B_2}\cosh(G)\left(\tilde{F}_x + F_x'\left(F_x + \partial_x\sigma\right) + \partial_{xx}\sigma\right) + 6S\dot{S}\Big) \\ &+ 2e^{B_1+B_2}\sinh(G)\left(F_x'\left(F_y + \partial_y\sigma\right) + \hat{F}_x + \partial_{xy}\sigma\right) - 2e^{B_2}\cosh(G)\left(F_y'\left(F_y + \partial_y\sigma\right) + \hat{F}_y + \partial_{yy}\sigma\right)\Big) \\ &+ 3e^{2B_1+B_2}\cosh(G)S'\left(F_x + \partial_x\sigma\right)^2 + 3e^{B_2}\cosh(G)S'\left(F_y + \partial_y\sigma\right)^2 = 0, \end{aligned} \tag{B.5}$$

where every function is evaluated at the $r = \sigma(x, y)$. If, on the contrary, we want to impose zero expansion at constant coordinate r we simply do $\sigma(t, x, y) = r = \text{constant}$,

$$\begin{aligned}\Theta = &-2e^{B_1+B_2}F_x\Big(S\Big(e^{B_1}\Big(\cosh(G)\Big(\tilde{B}_1+B_1'F_x\Big)+\cosh(G)\Big(\tilde{B}_2+B_2'F_x\Big)+\sinh(G)\Big(\tilde{G}+F_xG'\Big)\Big)\\ &-\sinh(G)\Big(B_2'F_y+\hat{B}_2\Big)-\cosh(G)\Big(F_yG'+\hat{G}\Big)\Big)+e^{B_1}\cosh(G)\Big(\tilde{S}+F_xS'\Big)-\sinh(G)\Big(F_yS'+\hat{S}\Big)\Big)\\ &+2e^{B_2}F_y\Big(S\Big(e^{B_1}\cosh(G)\Big(\tilde{G}+F_xG'\Big)+e^{B_1}\sinh(G)\Big(\tilde{B}_2+B_2'F_x\Big)+\cosh(G)\Big(B_1'F_y+\hat{B}_1\Big)\\ &-\cosh(G)\Big(B_2'F_y+\hat{B}_2\Big)-\sinh(G)\Big(F_yG'+\hat{G}\Big)\Big)+e^{B_1}\sinh(G)\Big(\tilde{S}-2F_xS'\Big)-\cosh(G)\Big(F_yS'+\hat{S}\Big)\Big)\\ &+S\Big(e^{B_1}\Big(2e^{B_2}\sinh(G)\Big(\tilde{F}_y+F_xF_y'\Big)-2e^{B_1+B_2}\cosh(G)\Big(\tilde{F}_x+F_xF_x'\Big)+6S\dot{S}\Big)\\ &+2e^{B_1+B_2}\sinh(G)\Big(F_yF_x'+\hat{F}_x\Big)-2e^{B_2}\cosh(G)\Big(F_yF_y'+\hat{F}_y\Big)\Big)+3e^{2B_1+B_2}F_x^2\cosh(G)S'\\ &+3e^{B_2}F_y^2\cosh(G)S'\end{aligned} \tag{B.6}$$

This new expansion is the one involved in (2.16).

Solving the differential equation (B.5) for the AH location means solving a non-linear PDE of the form,

$$\begin{aligned}\mathcal{L}\left(\sigma,\partial\sigma,\partial^2\sigma\right) = &\,\alpha_{xx}(t,\sigma,x,y)\partial_{xx}\sigma+\alpha_{xy}(t,\sigma,x,y)\partial_{xy}\sigma+\alpha_{yy}(t,\sigma,x,y)\partial_{yy}\sigma\\ &+\beta_{xx}(t,\sigma,x,y)\left(\partial_x\sigma\right)^2+\beta_{xy}(t,\sigma,x,y)\partial_x\sigma\partial_y\sigma+\beta_{yy}(t,\sigma,x,y)\left(\partial_y\sigma\right)^2\\ &+\gamma_x(t,\sigma,x,y)\partial_x\sigma+\gamma_y(t,\sigma,x,y)\partial_y\sigma+\delta(t,\sigma,x,y)=0,\end{aligned} \tag{B.7}$$

where

$$\begin{aligned}\alpha_{xx} &= -e^{B_1+B_2}S\cosh(G),\\ \alpha_{xy} &= 2e^{B_2}S\sinh(G),\\ \alpha_{yy} &= -e^{B_2-B_1}S\cosh(G),\\ \beta_{xx} &= \frac{1}{2}e^{B_1+B_2}\left(\cosh(G)S'-2S\left(B_1'\cosh(G)+B_2'\cosh(G)+G'\sinh(G)\right)\right),\\ \beta_{xy} &= e^{B_2}\left(2S\left(B_2'\sinh(G)+G'\cosh(G)\right)-\sinh(G)S'\right),\\ \beta_{yy} &= \frac{1}{2}e^{B_2-B_1}\left(2S\left(B_1'\cosh(G)-B_2'\cosh(G)+G'(-\sinh(G))\right)+\cosh(G)S'\right),\\ \gamma_x &= e^{B_2}\Big(S\Big(-e^{B_1}\tilde{G}\sinh(G)-e^{B_1}\tilde{B}_1\cosh(G)-e^{B_1}\tilde{B}_2\cosh(G)-2e^{B_1}F_xG'\sinh(G)\\ &\quad -2e^{B_1}B_1'F_x\cosh(G)-2e^{B_1}B_2'F_x\cosh(G)-e^{B_1}\cosh(G)F_x'+2B_2'F_y\sinh(G)+\hat{B}_2\sinh(G)\\ &\quad +2F_yG'\cosh(G)+\sinh(G)F_y'+\hat{G}\cosh(G)\Big)-e^{B_1}\tilde{S}\cosh(G)+e^{B_1}F_x\cosh(G)S'\\ &\quad -F_y\sinh(G)S'+\hat{S}\sinh(G)\Big),\\ \gamma_y &= e^{B_2-B_1}\Big(S\Big(e^{B_1}\tilde{B}_2\sinh(G)+e^{B_1}\tilde{G}\cosh(G)+2e^{B_1}F_xG'\cosh(G)+2e^{B_1}B_2'F_x\sinh(G)\\ &\quad +e^{B_1}\sinh(G)F_x'+2B_1'F_y\cosh(G)-2B_2'F_y\cosh(G)+\hat{B}_1\cosh(G)-\hat{B}_2\cosh(G)\\ &\quad -2F_yG'\sinh(G)-\cosh(G)F_y'-\hat{G}\sinh(G)\Big)+e^{B_1}\tilde{S}\sinh(G)-e^{B_1}F_x\sinh(G)S'\\ &\quad +F_y\cosh(G)S'+\hat{S}(-\cosh(G))\Big),\\ \delta &= -e^{B_2-B_1}S\Big(-F_y\Big(e^{B_1}\tilde{B}_2\sinh(G)+e^{B_1}\tilde{G}\cosh(G)+2e^{B_1}F_xG'\cosh(G)+2e^{B_1}B_2'F_x\sinh(G)\\ &\quad +e^{B_1}\sinh(G)F_x'+\hat{B}_1\cosh(G)-\hat{B}_2\cosh(G)-\cosh(G)F_y'-\hat{G}\sinh(G)\Big)+e^{B_1}F_x\Big(e^{B_1}\tilde{G}\sinh(G)\\ &\quad +e^{B_1}\tilde{B}_1\cosh(G)+e^{B_1}\tilde{B}_2\cosh(G)+e^{B_1}\cosh(G)F_x'-\hat{B}_2\sinh(G)-\sinh(G)F_y'-\hat{G}\cosh(G)\Big)\end{aligned}$$

$$
\begin{aligned}
&+e^{2B_1}\cosh(G)\tilde{F}_x - e^{B_1}\sinh(G)\tilde{F}_y + e^{2B_1}F_x^2\left(B_1'\cosh(G)+B_2'\cosh(G)+G'\sinh(G)\right)\\
&+F_y^2\left(-B_1'\cosh(G)+B_2'\cosh(G)+G'\sinh(G)\right) - e^{B_1}\hat{F}_x\sinh(G)+\hat{F}_y\cosh(G)\Big)\\
&+\frac{1}{2}e^{B_2-B_1}\left(-2F_y\left(\hat{S}\cosh(G)-e^{B_1}\sinh(G)\left(\tilde{S}-F_xS'\right)\right)+e^{B_1}F_x\left(2\hat{S}\sinh(G)\right.\right.\\
&\left.\left.-e^{B_1}\cosh(G)\left(2\tilde{S}-F_xS'\right)\right)+F_y^2\cosh(G)S'\right)+3\dot{S}S^2,
\end{aligned}
$$

We solve it by using relaxation methods. We linearize the equation around a guess, solve it and iterate until we converge to the solution. Expanding the operator $\mathcal{L}$ around $\sigma_0(t,x,y)$,

$$
\begin{aligned}
\mathcal{L}\left(\sigma,\partial\sigma,\partial^2\sigma\right) = \Bigg(&\mathcal{L}+\frac{\partial\mathcal{L}}{\partial\sigma}+\frac{\partial\mathcal{L}}{\partial(\partial_x\sigma)}\partial_x+\frac{\partial\mathcal{L}}{\partial(\partial_y\sigma)}\partial_y+\frac{\partial\mathcal{L}}{\partial(\partial_{xx}\sigma)}\partial_{xx}+\frac{\partial\mathcal{L}}{\partial(\partial_{xy}\sigma)}\partial_{xy}\\
&+\frac{\partial\mathcal{L}}{\partial(\partial_{yy}\sigma)}\partial_{yy}\Bigg)_{\sigma=\sigma_0}\delta\sigma+\mathcal{O}\left(\delta\sigma^2\right)=0,
\end{aligned}
\tag{B.8}
$$

where $\delta\sigma=\sigma(x,y)-\sigma_0(x,y)$. The associated linear problem for the correction $\delta\sigma$ is,

$$
\begin{aligned}
&\left[\alpha_{xx}(\sigma_0)\partial_{xx}+\alpha_{xy}(\sigma_0)\partial_{xy}+\alpha_{yy}(\sigma_0)\partial_{yy}+\left(\gamma_x(\sigma_0)+2\beta_{xx}(\sigma_0)\partial_x\sigma_0+\beta_{xy}(\sigma_0)\partial_y\sigma_0\right)\partial_x\right.\\
&\left.+\left(\gamma_y(\sigma_0)+2\beta_{yy}(\sigma_0)\partial_y\sigma_0+\beta_{xy}(\sigma_0)\partial_x\sigma_0\right)\partial_y+\partial_\sigma\mathcal{L}(\sigma_0)\right]\delta\sigma=-\mathcal{L}(\sigma_0,\partial\sigma_0,\partial^2\sigma_0),
\end{aligned}
\tag{B.9}
$$

which is a linear PDE already described how to solve during the thesis.

Bibliography

[1] Georges Aad et al. "Observation of a new particle in the search for the Standard Model Higgs boson with the ATLAS detector at the LHC". In: *Phys. Lett. B* 716 (2012), pp. 1–29. DOI: 10.1016/j.physletb.2012.08.020. arXiv: 1207.7214 [hep-ex].

[2] Alex Keshavarzi, Kim Siang Khaw, and Tamaki Yoshioka. "Muon $g-2$: A review". In: *Nuclear Physics B* 975 (2022), p. 115675. ISSN: 0550-3213. DOI: 10.1016/j.nuclphysb.2022.115675. URL: http://dx.doi.org/10.1016/j.nuclphysb.2022.115675.

[3] C. N. Yang and R. L. Mills. "Conservation of Isotopic Spin and Isotopic Gauge Invariance". In: *Phys. Rev.* 96 (1 1954), pp. 191–195. DOI: 10.1103/PhysRev.96.191. URL: https://link.aps.org/doi/10.1103/PhysRev.96.191.

[4] Jana N. Guenther. *Overview of the QCD phase diagram – Recent progress from the lattice*. 2021. arXiv: 2010.15503 [hep-lat].

[5] Misha A. Stephanov, K. Rajagopal, and Edward V. Shuryak. "Signatures of the tricritical point in QCD". In: *Phys. Rev. Lett.* 81 (1998), pp. 4816–4819. DOI: 10.1103/PhysRevLett.81.4816. arXiv: hep-ph/9806219.

[6] Misha A. Stephanov, K. Rajagopal, and Edward V. Shuryak. "Event-by-event fluctuations in heavy ion collisions and the QCD critical point". In: *Phys. Rev. D* 60 (1999), p. 114028. DOI: 10.1103/PhysRevD.60.114028. arXiv: hep-ph/9903292.

[7] M. Stephanov and Y. Yin. "Hydrodynamics with parametric slowing down and fluctuations near the critical point". In: *Phys. Rev. D* 98.3 (2018), p. 036006. DOI: 10.1103/PhysRevD.98.036006. arXiv: 1712.10305 [nucl-th].

[8] B. P. Abbott et al. "Observation of Gravitational Waves from a Binary Black Hole Merger". In: *Phys. Rev. Lett.* 116 (6 2016), p. 061102. DOI: 10.1103/PhysRevLett.116.061102. URL: https://link.aps.org/doi/10.1103/PhysRevLett.116.061102.

[9] B. P. Abbott et al. "GW170817: Observation of Gravitational Waves from a Binary Neutron Star Inspiral". In: *Phys. Rev. Lett.* 119 (16 2017), p. 161101. DOI: 10.1103/PhysRevLett.119.161101. URL: https://link.aps.org/doi/10.1103/PhysRevLett.119.161101.

[10] R. Abbott et al. "Observation of Gravitational Waves from Two Neutron Star–Black Hole Coalescences". In: *The Astrophysical Journal Letters* 915.1 (2021), p. L5. DOI: 10.3847/2041-8213/ac082e. URL: https://doi.org/10.3847/2041-8213/ac082e.

[11] Mark B. Hindmarsh et al. "Phase transitions in the early universe". In: *SciPost Phys. Lect. Notes* 24 (2021), p. 1. DOI: 10.21468/SciPostPhysLectNotes.24. arXiv: 2008.09136 [astro-ph.CO].

[12] Daniel Cutting, Mark Hindmarsh, and David J. Weir. "Vorticity, Kinetic Energy, and Suppressed Gravitational-Wave Production in Strong First-Order Phase Transitions". In: *Physical Review Letters* 125.2 (2020). ISSN: 1079-7114. DOI: 10.1103/physrevlett.125.021302. URL: http://dx.doi.org/10.1103/PhysRevLett.125.021302.

[13] Guy D. Moore and Tomislav Prokopec. "Bubble wall velocity in a first order electroweak phase transition". In: *Phys. Rev. Lett.* 75 (1995), pp. 777–780. DOI: 10.1103/PhysRevLett.75.777. arXiv: hep-ph/9503296.

[14] Dietrich Bodeker and Guy D. Moore. "Electroweak Bubble Wall Speed Limit". In: *JCAP* 05 (2017), p. 025. DOI: 10.1088/1475-7516/2017/05/025. arXiv: 1703.08215 [hep-ph].

[15] Stefan Höche et al. "Towards an all-orders calculation of the electroweak bubble wall velocity". In: *Journal of Cosmology and Astroparticle Physics* 2021.03 (2021), p. 009. ISSN: 1475-7516. DOI: 10.1088/1475-7516/2021/03/009. URL: http://dx.doi.org/10.1088/1475-7516/2021/03/009.

[16] Mark Hindmarsh. "Sound Shell Model for Acoustic Gravitational Wave Production at a First-Order Phase Transition in the Early Universe". In: *Physical Review Letters* 120.7 (2018). ISSN: 1079-7114. DOI: 10.1103/physrevlett.120.071301. URL: http://dx.doi.org/10.1103/PhysRevLett.120.071301.

[17] Mark Hindmarsh and Mulham Hijazi. "Gravitational waves from first order cosmological phase transitions in the Sound Shell Model". In: *Journal of Cosmology and Astroparticle Physics* 2019.12 (2019), 062–062. ISSN: 1475-7516. DOI: 10.1088/1475-7516/2019/12/062. URL: http://dx.doi.org/10.1088/1475-7516/2019/12/062.

[18] Chiara Caprini et al. "Detecting gravitational waves from cosmological phase transitions with LISA: an update". In: *JCAP* 03 (2020), p. 024. DOI: 10.1088/1475-7516/2020/03/024. arXiv: 1910.13125 [astro-ph.CO].

[19] Marcela Carena, M. Quiros, and C. E. M. Wagner. "Opening the window for electroweak baryogenesis". In: *Phys. Lett. B* 380 (1996), pp. 81–91. DOI: 10.1016/0370-2693(96)00475-3. arXiv: hep-ph/9603420.

[20] D. Delepine et al. "A Light stop and electroweak baryogenesis". In: *Phys. Lett. B* 386 (1996), pp. 183–188. DOI: 10.1016/0370-2693(96)00921-5. arXiv: hep-ph/9604440.

[21] M. Laine and K. Rummukainen. "The MSSM electroweak phase transition on the lattice". In: *Nucl. Phys. B* 535 (1998), pp. 423–457. DOI: 10.1016/S0550-3213(98)00530-6. arXiv: hep-lat/9804019.

[22] S. J. Huber and M. G. Schmidt. "Electroweak baryogenesis: Concrete in a SUSY model with a gauge singlet". In: *Nucl. Phys. B* 606 (2001), pp. 183–230. DOI: 10.1016/S0550-3213(01)00250-4. arXiv: hep-ph/0003122.

[23] Christophe Grojean, Geraldine Servant, and James D. Wells. "First-order electroweak phase transition in the standard model with a low cutoff". In: *Phys. Rev. D* 71 (2005), p. 036001. DOI: 10.1103/PhysRevD.71.036001. arXiv: hep-ph/0407019.

[24] Stephan J. Huber et al. "Baryogenesis in the MSSM, nMSSM and NMSSM". In: *Nucl. Phys. A* 785 (2007). Ed. by F. Karsch, D. Kharzeev, and R. Venugopalan, pp. 206–209. DOI: 10.1016/j.nuclphysa.2006.11.154. arXiv: hep-ph/0608017.

[25] Stefano Profumo, Michael J. Ramsey-Musolf, and Gabe Shaughnessy. "Singlet Higgs phenomenology and the electroweak phase transition". In: *JHEP* 08 (2007), p. 010. DOI: 10.1088/1126-6708/2007/08/010. arXiv: 0705.2425 [hep-ph].

[26] Vernon Barger et al. "LHC Phenomenology of an Extended Standard Model with a Real Scalar Singlet". In: *Phys. Rev. D* 77 (2008), p. 035005. DOI: 10.1103/PhysRevD.77.035005. arXiv: 0706.4311 [hep-ph].

[27] M. Laine, G. Nardini, and K. Rummukainen. "Lattice study of an electroweak phase transition at $m_h \backsimeq 126$ GeV". In: *JCAP* 01 (2013), p. 011. DOI: 10.1088/1475-7516/2013/01/011. arXiv: 1211.7344 [hep-ph].

[28] G. C. Dorsch, S. J. Huber, and J. M. No. "A strong electroweak phase transition in the 2HDM after LHC8". In: *JHEP* 10 (2013), p. 029. DOI: 10.1007/JHEP10(2013)029. arXiv: 1305.6610 [hep-ph].

[29] P. H. Damgaard et al. "Effective Field Theory and Electroweak Baryogenesis in the Singlet-Extended Standard Model". In: *JHEP* 02 (2016), p. 107. DOI: 10.1007/JHEP02(2016)107. arXiv: 1512.01963 [hep-ph].

[30] Pedro Schwaller. "Gravitational Waves from a Dark Phase Transition". In: *Phys. Rev. Lett.* 115.18 (2015), p. 181101. DOI: 10.1103/PhysRevLett.115.181101. arXiv: 1504.07263 [hep-ph].

[31] Isabel Garcia Garcia, Sven Krippendorf, and John March-Russell. "The String Soundscape at Gravitational Wave Detectors". In: *Phys. Lett. B* 779 (2018), pp. 348–352. DOI: 10.1016/j.physletb.2018.02.028. arXiv: 1607.06813 [hep-ph].

[32] Wei-Chih Huang et al. "Testing the Dark Confined Landscape: From Lattice to Gravitational Waves". In: (Dec. 2020). arXiv: 2012.11614 [hep-ph].

[33] James Halverson et al. "Gravitational waves from dark Yang-Mills sectors". In: *JHEP* 05 (2021), p. 154. DOI: 10.1007/JHEP05(2021)154. arXiv: 2012.04071 [hep-ph].

[34] Nancy Aggarwal et al. "Challenges and opportunities of gravitational-wave searches at MHz to GHz frequencies". In: *Living Rev. Rel.* 24.1 (2021), p. 4. DOI: 10.1007/s41114-021-00032-5. arXiv: 2011.12414 [gr-qc].

[35] Juan Martin Maldacena. "The Large N limit of superconformal field theories and supergravity". In: *Adv. Theor. Math. Phys.* 2 (1998), pp. 231–252. DOI: 10.1023/A:1026654312961. arXiv: hep-th/9711200.

[36] Maximilian Attems et al. "Holographic Collisions across a Phase Transition". In: *Phys. Rev. Lett.* 121.26 (2018), p. 261601. DOI: 10.1103/PhysRevLett.121.261601. arXiv: 1807.05175 [hep-th].

[37] Jorge Casalderrey-Solana et al. "Holographic heavy ion collisions with baryon charge". In: *JHEP* 09 (2016), p. 108. DOI: 10.1007/JHEP09(2016)108. arXiv: 1607.05273 [hep-th].

[38] Maximilian Attems et al. "Paths to equilibrium in non-conformal collisions". In: *JHEP* 06 (2017), p. 154. DOI: 10.1007/JHEP06(2017)154. arXiv: 1703.09681 [hep-th].

[39] Paul M. Chesler and Laurence G. Yaffe. "Holography and colliding gravitational shock waves in asymptotically AdS5 spacetime". In: *Phys.Rev.Lett.* 106 (2011), p. 021601. DOI: 10.1103/PhysRevLett.106.021601. arXiv: 1011.3562 [hep-th].

[40] Jorge Casalderrey-Solana et al. "From full stopping to transparency in a holographic model of heavy ion collisions". In: *Phys. Rev. Lett.* 111 (2013), p. 181601. DOI: 10.1103/PhysRevLett.111.181601. arXiv: 1305.4919 [hep-th].

[41] Jorge Casalderrey-Solana et al. "Longitudinal Coherence in a Holographic Model of Asymmetric Collisions". In: *Phys. Rev. Lett.* 112.22 (2014), p. 221602. DOI: 10.1103/PhysRevLett.112.221602. arXiv: 1312.2956 [hep-th].

[42] Paul M. Chesler and Laurence G. Yaffe. "Holography and off-center collisions of localized shock waves". In: *JHEP* 10 (2015), p. 070. DOI: 10.1007/JHEP10(2015)070. arXiv: 1501.04644 [hep-th].

[43] Paul M. Chesler. "Colliding shock waves and hydrodynamics in small systems". In: *Phys. Rev. Lett.* 115.24 (2015), p. 241602. DOI: 10.1103/PhysRevLett.115.241602. arXiv: 1506.02209 [hep-th].

[44] Paul M. Chesler and Wilke van der Schee. "Early thermalization, hydrodynamics and energy loss in AdS/CFT". In: *Int. J. Mod. Phys.* E24.10 (2015), p. 1530011. DOI: 10.1142/S0218301315300118. arXiv: 1501.04952 [nucl-th].

[45] Paul M. Chesler. "How big are the smallest drops of quark-gluon plasma?" In: (2016). arXiv: 1601.01583 [hep-th].

[46] Jan de Boer, Kyriakos Papadodimas, and Erik Verlinde. "Holographic Neutron Stars". In: *JHEP* 10 (2010), p. 020. DOI: 10.1007/JHEP10(2010)020. arXiv: 0907.2695 [hep-th].

[47] Carlos Hoyos, Niko Jokela, and Aleksi Vuorinen. "Holographic approach to compact stars and their binary mergers". In: (Dec. 2021). arXiv: 2112.08422 [hep-th].

[48] Carlos Hoyos et al. "Holographic approach to transport in dense QCD matter". In: (Sept. 2021). arXiv: 2109.12122 [hep-th].

[49] Carlos Hoyos et al. "Holographic quark matter and neutron stars". In: *Phys. Rev. Lett.* 117.3 (2016), p. 032501. DOI: 10.1103/PhysRevLett.117.032501. arXiv: 1603.02943 [hep-ph].

[50] Carlos Hoyos et al. "Breaking the sound barrier in AdS/CFT". In: *Phys. Rev. D* 94.10 (2016), p. 106008. DOI: 10.1103/PhysRevD.94.106008. arXiv: 1609.03480 [hep-th].

[51] Christian Ecker et al. "Stiff phases in strongly coupled gauge theories with holographic duals". In: *JHEP* 11 (2017), p. 031. DOI: 10.1007/JHEP11(2017)031. arXiv: 1707.00521 [hep-th].

[52] Eemeli Annala et al. "Holographic compact stars meet gravitational wave constraints". In: *JHEP* 12 (2018), p. 078. DOI: 10.1007/JHEP12(2018)078. arXiv: 1711.06244 [astro-ph.HE].

[53] Kazem Bitaghsir Fadafan, Jesús Cruz Rojas, and Nick Evans. "Deconfined, Massive Quark Phase at High Density and Compact Stars: A Holographic Study". In: *Phys. Rev. D* 101.12 (2020), p. 126005. DOI: 10.1103/PhysRevD.101.126005. arXiv: 1911.12705 [hep-ph].

[54] Takaaki Ishii, Matti Järvinen, and Govert Nijs. "Cool baryon and quark matter in holographic QCD". In: *JHEP* 07 (2019), p. 003. DOI: 10.1007/JHEP07(2019)003. arXiv: 1903.06169 [hep-ph].

[55] Niko Jokela and Javier G. Subils. "Is entanglement a probe of confinement?" In: *JHEP* 02 (2021), p. 147. DOI: 10.1007/JHEP02(2021)147. arXiv: 2010.09392 [hep-th].

[56] Anton F. Faedo et al. "Multiple mass hierarchies from complex fixed point collisions". In: *JHEP* 10 (2021), p. 246. DOI: 10.1007/JHEP10(2021)246. arXiv: 2106.01802 [hep-th].

[57] Antón F. Faedo et al. "Holographic Complex Conformal Field Theories". In: *Phys. Rev. Lett.* 124.16 (2020), p. 161601. DOI: 10.1103/PhysRevLett.124.161601. arXiv: 1909.04008 [hep-th].

[58] Yago Bea and David Mateos. "Heating up Exotic RG Flows with Holography". In: *JHEP* 08 (2018), p. 034. DOI: 10.1007/JHEP08(2018)034. arXiv: 1805.01806 [hep-th].

[59] Oliver DeWolfe, Steven S. Gubser, and Christopher Rosen. "A holographic critical point". In: *Phys. Rev. D* 83 (2011), p. 086005. DOI: 10.1103/PhysRevD.83.086005. arXiv: 1012.1864 [hep-th].

[60] J. Knaute, R. Yaresko, and B. Kämpfer. "Holographic QCD phase diagram with critical point from Einstein–Maxwell-dilaton dynamics". In: *Phys. Lett. B* 778 (2018), pp. 419–425. DOI: 10.1016/j.physletb.2018.01.053. arXiv: 1702.06731 [hep-ph].

[61] Maximilian Attems et al. "Phase Transitions, Inhomogeneous Horizons and Second-Order Hydrodynamics". In: *JHEP* 06 (2017), p. 129. DOI: 10.1007/JHEP06(2017)129. arXiv: 1703.02948 [hep-th].

[62] Richard A. Davison, Simon A. Gentle, and Blaise Goutéraux. "Slow relaxation and diffusion in holographic quantum critical phases". In: *Phys. Rev. Lett.* 123.14 (2019), p. 141601. DOI: 10.1103/PhysRevLett.123.141601. arXiv: 1808.05659 [hep-th].

[63] Maximilian Attems et al. "Dynamics of Phase Separation from Holography". In: *JHEP* 01 (2020), p. 106. DOI: 10.1007/JHEP01(2020)106. arXiv: 1905.12544 [hep-th].

[64] Gian Andrea Inkof et al. "Quantum critical scaling and holographic bound for transport coefficients near Lifshitz points". In: *JHEP* 11 (2020), p. 088. DOI: 10.1007/JHEP11(2020)088. arXiv: 1907.05744 [cond-mat.str-el].

[65] Daniel Arean et al. "Hydrodynamic Diffusion and Its Breakdown near AdS2 Quantum Critical Points". In: *Phys. Rev. X* 11.3 (2021), p. 031024. DOI: 10.1103/PhysRevX.11.031024. arXiv: 2011.12301 [hep-th].

[66] Steven S. Gubser. "Breaking an Abelian gauge symmetry near a black hole horizon". In: *Phys. Rev. D* 78 (2008), p. 065034. DOI: 10.1103/PhysRevD.78.065034. arXiv: 0801.2977 [hep-th].

[67] Sean A. Hartnoll, Christopher P. Herzog, and Gary T. Horowitz. "Building a Holographic Superconductor". In: *Phys. Rev. Lett.* 101 (2008), p. 031601. DOI: 10.1103/PhysRevLett.101.031601. arXiv: 0803.3295 [hep-th].

[68] Sean A. Hartnoll, Christopher P. Herzog, and Gary T. Horowitz. "Holographic Superconductors". In: *JHEP* 12 (2008), p. 015. DOI: 10.1088/1126-6708/2008/12/015. arXiv: 0810.1563 [hep-th].

[69] Tameem Albash and Clifford V. Johnson. "Vortex and Droplet Engineering in Holographic Superconductors". In: *Phys. Rev. D* 80 (2009), p. 126009. DOI: 10.1103/PhysRevD.80.126009. arXiv: 0906.1795 [hep-th].

[70] Marc Montull, Alex Pomarol, and Pedro J. Silva. "The Holographic Superconductor Vortex". In: *Phys. Rev. Lett.* 103 (2009), p. 091601. DOI: 10.1103/PhysRevLett.103.091601. arXiv: 0906.2396 [hep-th].

[71] Óscar J. C. Dias et al. "Vortices in holographic superfluids and superconductors as conformal defects". In: *JHEP* 04 (2014), p. 096. DOI: 10.1007/JHEP04(2014)096. arXiv: 1311.3673 [hep-th].

[72] Blaise Goutéraux and Eric Mefford. "Normal charge densities in quantum critical superfluids". In: *Phys. Rev. Lett.* 124.16 (2020), p. 161604. DOI: 10.1103/PhysRevLett.124.161604. arXiv: 1912.08849 [hep-th].

[73] Sean A. Hartnoll et al. "Diving into a holographic superconductor". In: *SciPost Phys.* 10.1 (2021), p. 009. DOI: 10.21468/SciPostPhys.10.1.009. arXiv: 2008.12786 [hep-th].

[74] Blaise Goutéraux and Eric Mefford. "Non-vanishing zero-temperature normal density in holographic superfluids". In: *JHEP* 11 (2020), p. 091. DOI: 10.1007/JHEP11(2020)091. arXiv: 2008.02289 [hep-th].

[75] Geoffrey Penington. "Entanglement Wedge Reconstruction and the Information Paradox". In: *JHEP* 09 (2020), p. 002. DOI: 10.1007/JHEP09(2020)002. arXiv: 1905.08255 [hep-th].

[76] Raphael Bousso and Marija Tomaŝević. "Unitarity From a Smooth Horizon?" In: *Phys. Rev. D* 102.10 (2020), p. 106019. DOI: 10.1103/PhysRevD.102.106019. arXiv: 1911.06305 [hep-th].

[77] Jean-Marc Schlenker and Edward Witten. "No Ensemble Averaging Below the Black Hole Threshold". In: (Feb. 2022). arXiv: 2202.01372 [hep-th].

[78] Roberto Emparan et al. "Black tsunamis and naked singularities in AdS". In: *JHEP* 02 (2022), p. 090. DOI: 10.1007/JHEP02(2022)090. arXiv: 2112.07967 [hep-th].

[79] Yago Bea et al. "Holographic Bubbles with Jecco: Expanding, Collapsing and Critical". In: (Feb. 2022). arXiv: 2202.10503 [hep-th].

[80] Yago Bea et al. "Crossing a large-N phase transition at finite volume". In: *JHEP* 02 (2021), p. 061. DOI: 10.1007/JHEP02(2021)061. arXiv: 2007.06467 [hep-th].

[81] Yago Bea et al. "Domain Collisions". In: (Nov. 2021). arXiv: 2111.03355 [hep-th].

[82] Yago Bea et al. "Bubble wall velocity from holography". In: *Phys. Rev. D* 104.12 (2021), p. L121903. DOI: 10.1103/PhysRevD.104.L121903. arXiv: 2104.05708 [hep-th].

[83] Yago Bea et al. "Spinodal Gravitational Waves". In: (Dec. 2021). arXiv: 2112.15478 [hep-th].

[84] Miguel Zilhao, Mikel Sanchez-Garitaonandia, and Thanasis Giannakopoulos. *Jecco.jl*. Version v0.9.1. Jan. 2022. DOI: 10.5281/zenodo.5907929. URL: https://doi.org/10.5281/zenodo.5907929.

[85] Paul M. Chesler and Laurence G. Yaffe. "Numerical solution of gravitational dynamics in asymptotically anti-de Sitter spacetimes". In: *JHEP* 1407 (2014), p. 086. DOI: 10.1007/JHEP07(2014)086. arXiv: 1309.1439 [hep-th].

[86] H. O. Kreiss and J. Oliger. *Methods for the Approximate Solution of Time Dependent Problems*. World Meteorological Organization, 1973.

[87] Aron Jansen. "Overdamped modes in Schwarzschild-de Sitter and a Mathematica package for the numerical computation of quasinormal modes". In: *Eur. Phys. J. Plus* 132.12 (2017), p. 546. DOI: 10.1140/epjp/i2017-11825-9. arXiv: 1709.09178 [gr-qc].

[88] Romuald A. Janik, Jakub Jankowski, and Hesam Soltanpanahi. "Real-Time dynamics and phase separation in a holographic first order phase transition". In: *Phys. Rev. Lett.* 119.26 (2017), p. 261601. DOI: 10.1103/PhysRevLett.119.261601. arXiv: 1704.05387 [hep-th].

[89] Loredana Bellantuono et al. "Dynamics near a first order phase transition". In: *JHEP* 10 (2019), p. 146. DOI: 10.1007/JHEP10(2019)146. arXiv: 1906.00061 [hep-th].

[90] Alex Buchel. "A Holographic perspective on Gubser-Mitra conjecture". In: *Nucl. Phys.* B731 (2005), pp. 109–124. DOI: 10.1016/j.nuclphysb.2005.10.014. arXiv: hep-th/0507275 [hep-th].

[91] Roberto Emparan et al. "World-Volume Effective Theory for Higher-Dimensional Black Holes". In: *Phys. Rev. Lett.* 102 (2009), p. 191301. DOI: 10.1103/PhysRevLett.102.191301. arXiv: 0902.0427 [hep-th].

[92] Roberto Emparan et al. "Essentials of Blackfold Dynamics". In: *JHEP* 03 (2010), p. 063. DOI: 10.1007/JHEP03(2010)063. arXiv: 0910.1601 [hep-th].

[93] R. Gregory and R. Laflamme. "Black strings and p-branes are unstable". In: *Phys. Rev. Lett.* 70 (1993), pp. 2837–2840. DOI: 10.1103/PhysRevLett.70.2837. arXiv: hep-th/9301052 [hep-th].

[94] Aristomenis Donos and Jerome P. Gauntlett. "The thermoelectric properties of inhomogeneous holographic lattices". In: *JHEP* 01 (2015), p. 035. DOI: 10.1007/JHEP01(2015)035. arXiv: 1409.6875 [hep-th].

[95] Donald Marolf and Jorge E. Santos. "Phases of Holographic Hawking Radiation on spatially compact spacetimes". In: *JHEP* 10 (2019), p. 250. DOI: 10.1007/JHEP10(2019)250. arXiv: 1906.07681 [hep-th].

[96] Massimo Bianchi, Daniel Z. Freedman, and Kostas Skenderis. "How to go with an RG flow". In: *JHEP* 08 (2001), p. 041. DOI: 10.1088/1126-6708/2001/08/041. arXiv: hep-th/0105276 [hep-th].

[97] Massimo Bianchi, Daniel Z. Freedman, and Kostas Skenderis. "Holographic renormalization". In: *Nucl. Phys.* B631 (2002), pp. 159–194. DOI: 10.1016/S0550-3213(02)00179-7. arXiv: hep-th/0112119 [hep-th].

[98] Oscar J.C. Dias, Jorge E. Santos, and Benson Way. "Lattice Black Branes: Sphere Packing in General Relativity". In: *JHEP* 05 (2018), p. 111. DOI: 10.1007/JHEP05(2018)111. arXiv: 1712.07663 [hep-th].

[99] Steven S. Gubser. "On nonuniform black branes". In: *Class. Quant. Grav.* 19 (2002), pp. 4825–4844. DOI: 10.1088/0264-9381/19/19/303. arXiv: hep-th/0110193 [hep-th].

[100] Toby Wiseman. "Static axisymmetric vacuum solutions and nonuniform black strings". In: *Class. Quant. Grav.* 20 (2003), pp. 1137–1176. DOI: 10.1088/0264-9381/20/6/308. arXiv: hep-th/0209051 [hep-th].

[101] Evgeny Sorkin. "A Critical dimension in the black string phase transition". In: *Phys. Rev. Lett.* 93 (2004), p. 031601. DOI: 10.1103/PhysRevLett.93.031601. arXiv: hep-th/0402216 [hep-th].

[102] Oscar J. C. Dias, Jorge E. Santos, and Benson Way. "Numerical Methods for Finding Stationary Gravitational Solutions". In: *Class. Quant. Grav.* 33.13 (2016), p. 133001. DOI: 10.1088/0264-9381/33/13/133001. arXiv: 1510.02804 [hep-th].

[103] Oscar J.C. Dias, Jorge E. Santos, and Benson Way. "Lumpy $AdS_5 \times S^5$ black holes and black belts". In: *JHEP* 04 (2015), p. 060. DOI: 10.1007/JHEP04(2015)060. arXiv: 1501.06574 [hep-th].

[104] Oscar J.C. Dias, Jorge E. Santos, and Benson Way. "Localised $AdS_5 \times S^5$ Black Holes". In: *Phys. Rev. Lett.* 117.15 (2016), p. 151101. DOI: 10.1103/PhysRevLett.117.151101. arXiv: 1605.04911 [hep-th].

[105] Oscar J.C. Dias, Jorge E. Santos, and Benson Way. "Localised and nonuniform thermal states of super-Yang-Mills on a circle". In: *JHEP* 06 (2017), p. 029. DOI: 10.1007/JHEP06(2017)029. arXiv: 1702.07718 [hep-th].

[106] Oscar J.C. Dias et al. "Mass-deformed M2 branes in Stenzel space". In: *JHEP* 11 (2017), p. 105. DOI: 10.1007/JHEP11(2017)105. arXiv: 1704.02323 [hep-th].

[107] Iosif Bena et al. "Holographic dual of hot Polchinski-Strassler quark-gluon plasma". In: *JHEP* 09 (2019), p. 033. DOI: 10.1007/JHEP09(2019)033. arXiv: 1805.06463 [hep-th].

[108] Gary T. Horowitz. "Playing with black strings". In: *The future of theoretical physics and cosmology: Celebrating Stephen Hawking's 60th birthday. Proceedings, Workshop and Symposium, Cambridge, UK, January 7-10, 2002*. 2002, pp. 310–329. arXiv: hep-th/0205069 [hep-th].

[109] Troels Harmark and Niels A. Obers. "Phase structure of black holes and strings on cylinders". In: *Nucl. Phys.* B684 (2004), pp. 183–208. DOI: 10.1016/j.nuclphysb.2004.02.022. arXiv: hep-th/0309230 [hep-th].

[110] Oscar J. C. Dias et al. "Multi-black hole configurations on the cylinder". In: *Phys. Rev.* D76 (2007), p. 104025. DOI: 10.1103/PhysRevD.76.104025. arXiv: 0706.3645 [hep-th].

[111] Paolo Benincasa, Alex Buchel, and Andrei O. Starinets. "Sound waves in strongly coupled non-conformal gauge theory plasma". In: *Nucl. Phys.* B733 (2006), pp. 160–187. DOI: 10.1016/j.nuclphysb.2005.11.005. arXiv: hep-th/0507026 [hep-th].

[112] Maximilian Attems et al. "Thermodynamics, transport and relaxation in non-conformal theories". In: *JHEP* 10 (2016), p. 155. DOI: 10.1007/JHEP10(2016)155. arXiv: 1603.01254 [hep-th].

[113] Maximilian Attems et al. "Holographic Collisions in Non-conformal Theories". In: *JHEP* 01 (2017), p. 026. DOI: 10.1007/JHEP01(2017)026. arXiv: 1604.06439 [hep-th].

[114] Steven S. Gubser and Abhinav Nellore. "Mimicking the QCD equation of state with a dual black hole". In: *Phys. Rev.* D78 (2008), p. 086007. DOI: 10.1103/PhysRevD.78.086007. arXiv: 0804.0434 [hep-th].

[115] Mikko Laine and Aleksi Vuorinen. *Basics of Thermal Field Theory*. Vol. 925. Springer, 2016. DOI: 10.1007/978-3-319-31933-9. arXiv: 1701.01554 [hep-ph].

[116] Oliver Gould and Joonas Hirvonen. "Effective field theory approach to thermal bubble nucleation". In: *Phys. Rev. D* 104.9 (2021), p. 096015. DOI: 10.1103/PhysRevD.104.096015. arXiv: 2108.04377 [hep-ph].

[117] Jose R. Espinosa et al. "Energy Budget of Cosmological First-order Phase Transitions". In: *JCAP* 06 (2010), p. 028. DOI: 10.1088/1475-7516/2010/06/028. arXiv: 1004.4187 [hep-ph].

[118] P. Kovtun, Dan T. Son, and Andrei O. Starinets. "Viscosity in strongly interacting quantum field theories from black hole physics". In: *Phys. Rev. Lett.* 94 (2005), p. 111601. DOI: 10.1103/PhysRevLett.94.111601. arXiv: hep-th/0405231.

[119] Christopher Eling and Yaron Oz. "A Novel Formula for Bulk Viscosity from the Null Horizon Focusing Equation". In: *JHEP* 06 (2011), p. 007. DOI: 10.1007/JHEP06(2011)007. arXiv: 1103.1657 [hep-th].

[120] Fëanor Reuben Ares et al. "Effective actions and bubble nucleation from holography". In: (Sept. 2021). arXiv: 2109.13784 [hep-th].

[121] Fëanor Reuben Ares et al. "Gravitational Waves at Strong Coupling from an Effective Action". In: (Oct. 2021). arXiv: 2110.14442 [hep-th].

[122] K. Enqvist et al. "Nucleation and bubble growth in a first order cosmological electroweak phase transition". In: *Phys. Rev. D* 45 (1992), pp. 3415–3428. DOI: 10.1103/PhysRevD.45.3415.

[123] Philip Candelas and Harald Skarke. "F theory, SO(32) and toric geometry". In: *Phys. Lett. B* 413 (1997), pp. 63–69. DOI: 10.1016/S0370-2693(97)01047-2. arXiv: hep-th/9706226.

[124] James Halverson and Washington Taylor. "$\mathbb{P}^1$-bundle bases and the prevalence of non-Higgsable structure in 4D F-theory models". In: *JHEP* 09 (2015), p. 086. DOI: 10.1007/JHEP09(2015)086. arXiv: 1506.03204 [hep-th].

[125] Washington Taylor and Yi-Nan Wang. "The F-theory geometry with most flux vacua". In: *JHEP* 12 (2015), p. 164. DOI: 10.1007/JHEP12(2015)164. arXiv: 1511.03209 [hep-th].

[126] Washington Taylor and Yi-Nan Wang. "Scanning the skeleton of the 4D F-theory landscape". In: *JHEP* 01 (2018), p. 111. DOI: 10.1007/JHEP01(2018)111. arXiv: 1710.11235 [hep-th].

[127] David H. Lyth and Ewan D. Stewart. "Cosmology with a TeV mass GUT Higgs". In: *Phys. Rev. Lett.* 75 (1995), pp. 201–204. DOI: 10.1103/PhysRevLett.75.201. arXiv: hep-ph/9502417.

[128] David H. Lyth and Ewan D. Stewart. "Thermal inflation and the moduli problem". In: *Phys. Rev. D* 53 (1996), pp. 1784–1798. DOI: 10.1103/PhysRevD.53.1784. arXiv: hep-ph/9510204.

[129] Yago Bea et al. "Quasi-particles in strongly coupled plasmas". In: in progress ().

[130] Umut Gürsoy, Aron Jansen, and Wilke van der Schee. "New dynamical instability in asymptotically anti–de Sitter spacetime". In: *Phys. Rev. D* 94.6 (2016), p. 061901. DOI: 10.1103/PhysRevD.94.061901. arXiv: 1603.07724 [hep-th].

[131] Yago Bea et al. "The holographic life of a single bubble". In: to appear ().

[132] Juan Garcia-Bellido, Daniel G. Figueroa, and Alfonso Sastre. "A Gravitational Wave Background from Reheating after Hybrid Inflation". In: *Phys. Rev. D* 77 (2008), p. 043517. DOI: 10.1103/PhysRevD.77.043517. arXiv: 0707.0839 [hep-ph].

[133] Alex Buchel. "Ringing in de Sitter spacetime". In: *Nucl. Phys. B* 928 (2018), pp. 307–320. DOI: 10.1016/j.nuclphysb.2018.01.021. arXiv: 1707.01030 [hep-th].

[134] Alex Buchel and Aleksandr Karapetyan. "de Sitter Vacua of Strongly Interacting QFT". In: *JHEP* 03 (2017), p. 114. DOI: 10.1007/JHEP03(2017)114. arXiv: 1702.01320 [hep-th].

[135] Alex Buchel. "Entanglement entropy of $\mathcal{N} = 2^*$ de Sitter vacuum". In: *Nucl. Phys. B* 948 (2019), p. 114769. DOI: 10.1016/j.nuclphysb.2019.114769. arXiv: 1904.09968 [hep-th].

[136] Alex Buchel. "χSB of cascading gauge theory in de Sitter". In: *JHEP* 05 (2020), p. 035. DOI: 10.1007/JHEP05(2020)035. arXiv: 1912.03566 [hep-th].

[137] Jorge Casalderrey-Solana et al. "Strong-coupling dynamics and entanglement in de Sitter space". In: *JHEP* 03 (2021), p. 181. DOI: 10.1007/JHEP03(2021)181. arXiv: 2011.08194 [hep-th].

[138] D. Giataganas and N. Tetradis. "Entanglement entropy in FRW backgrounds". In: *Phys. Lett. B* 820 (2021), p. 136493. DOI: 10.1016/j.physletb.2021.136493. arXiv: 2105.12614 [hep-th].

[139] Alex Buchel. "Dynamical fixed points in holography". In: (Nov. 2021). arXiv: 2111.04122 [hep-th].

[140] José Manuel Penín, Kostas Skenderis, and Benjamin Withers. "Massive holographic QFTs in de Sitter". In: (Dec. 2021). arXiv: 2112.14639 [hep-th].

[141] Christian Ecker et al. "Holographic Evolution with Dynamical Boundary Gravity". In: (Sept. 2021). arXiv: 2109.10355 [hep-th].